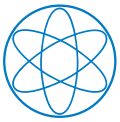

Technische Universität München

Fakultät für Physik

STRUPHY: a structure-preserving hybrid MHD-kinetic code for the interaction of energetic particles with Alfvén waves in magnetized plasmas

Florian Erich Holderied

Vollständiger Abdruck der von der Fakultät für Physik der Technischen Universität München zur Erlangung der akademischen Grades eines

Doktors der Naturwissenschaften

genehmigten Dissertation.

Vorsitz:	Prof. Dr. Katharina Krischer
Prüfer der Dissertation:	
	1. Hon.-Prof. Dr. Sibylle Günter
	2. Prof. Dr. Oliver Junge

Die Dissertation wurde am 10.05.2022 bei der Technischen Universität München eingereicht und durch die Fakultät für Physik am 27.07.2022 angenommen.

DEPARTMENT OF PHYSICS

TECHNISCHE UNIVERSITÄT MÜNCHEN

STRUPHY: a structure-preserving hybrid MHD-kinetic code for the interaction of energetic particles with Alfvén waves in magnetized plasmas

Author:	Florian Erich Holderied
Supervisor:	Hon.-Prof. Dr. Sibylle Günter
Advisors:	Dr. Xin Wang Dr. Stefan Possanner
Submission Date:	10.05.2022

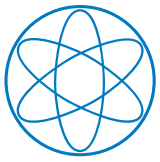

HELMHOLTZ
RESEARCH FOR GRAND CHALLENGES

EUROfusion

Das, wobei unsere Berechnungen versagen,
nennen wir Zufall

Albert Einstein

Zusammenfassung

Die vorliegende Arbeit befasst sich mit der Entwicklung und der Anwendung des neuen Simulationscodes STRUPHY (Structure-Preserving Hybrid Code) für die rechnerische Beschreibung der Wechselwirkung hochenergetischer geladener Teilchen mit niederfrequenten magnetohydrodynamischen Wellen in magnetisierten Hochtemperaturplasmen. Solche Szenarien treten üblicherweise in Kernfusionsexperimenten auf, wo es neben einem thermischen keV Hintergrundplasma aus ionisierten Wasserstoffisotopen eine Reihe hochenergetischer MeV Teilchenspezies gibt, die wegen ihrer geringen Kollisionalität über relativ lange Zeiträume fernab vom thermischen Gleichgewicht existieren können. Typische Beispiele sind eingeschossene Neutralteilchen zur externen Heizung des Hauptplasmas oder α-Teilchen, welche in einem gezündeten Plasma durch Fusionsprozesse entstehen und so zu einer selbsterhaltenden Heizung beitragen. Aufgrund thermischer Geschwindigkeiten von energetischen Teilchen in der Größenordnung der Phasengeschwindigkeiten von globalen magnetohydrodynamischen Eigenmoden im Hauptplasma, können energetische Teilchen und Plasmawellen resonant miteinander interagieren, was einen Energieaustausch zwischen Teilchen und Wellen ermöglicht. Durch nichtlineare Rückkopplungseffekte kann es dabei zu einem verstärkten Teilchen- und Energietransport kommen, was sich negativ auf die Fusionsleistung und die Belastung der Reaktorwände auswirken kann.

Aufgrund der komplexen Geometrie von modernen Fusionsexperimenten und der Tatsache dass die zugrunde liegenden partiellen Differentialgleichungen im Allgemeinen stark nichtlinear sind, ist in den meisten Fällen eine numerische Behandlung der oben beschriebenen physikalischen Phänomene nötig. Um den Ergebnissen einer numerischen Computersimulation vertrauen zu können, insbesondere im Fall von zeitlich langen Simulationen bis tief in die nichtlineare Phase, ist es dabei oft von Vorteil, bestimmte mathematische Eigenschaften des verwendeten Modells in der diskreten, d. h. numerischen Variante zu erhalten. Klassische Verfahren gehen hierbei von einem bestimmten Anfangszustand aus und berechnen den Zustand des Plasmas zu einem späteren Zeitpunkt unter Einhaltung numerischer Konsistenz und numerischer Stabilität. Dies trifft jedoch im Allgemeinen keinerlei Aussagen bezüglich der Einhaltung fundamentaler physikalischer Gesetze wie der Ladungserhaltung, der Energieerhaltung oder der Divergenzfreiheit des selbstkonsistenten Magnetfeldes. Dies kann die korrekte Interpretation von Simulationsergebnissen stark erschweren. Dagegen ermöglichen moderne numerische Verfahren, welche auf der Diskretisierung von Objekten aus der Differentialgeometrie basieren, die Erhaltung der dem Modell zugrunde liegenden geometrischen Struktur und damit die Erhaltung bestimmter Eigenschaften des kontinuierlichen Modells.

Diese Arbeit beschäftigt sich u. a. mit der Anwendung dieser Ideen auf ein Modell, welches ein Dreikomponentenplasma (thermische Ionen, thermische Elektronen und energetische Ionen) mittels gekoppelter magnetohydrodynamischer und kinetischer Gleichungen beschreibt (Hybridmodell). Das Resultat ist der neue Simulationscode STRUPHY, der im Vergleich zu bereits existierenden Hybridcodes Verbesserungen in zweierlei Hinsicht aufweist. Zum einen führt die erstmals auf ein magnetohydrodynamisch-kinetisches Hybridmodell angewandte Kombination aus konformen Finite-Elemente-Räumen für diskrete Differentialformen und einer Par-

tikeldiskretisierung der vollen Phasenraumverteilungsfunktion der energetischen Ionen zu einer diskreten Modellvariante mit exakter Energieerhaltung und divergenzfreiem Magnetfeld. Diese Eigenschaft ist dabei unabhängig von den verwendeten numerischen Parametern sowie der Geometrie (bzw. Krümmung) des Berechnungsgebietes. Zum anderen enthält STRUPHY ein in dieser Arbeit weiterentwickeltes Verfahren zur Behandlung der Singularität an der magnetischen Achse, welche bei der Verwendung von magnetischen Flusskoordinaten auftritt und bei bereits existierenden Codes häufig zu numerischen Problemen führt. Dies wird im Wesentlichen mit der Konstruktion neuer sog. „polarer“ Freiheitsgrade basierend auf an der magnetischen Achse kontinuierlich differenzierbaren Finite-Elemente Basisfunktionen erreicht.

STRUPHY wird in dieser Arbeit anhand mehrerer physikalischer Problemstellungen erfolgreich verifiziert. Dies geschieht zunächst durch den Vergleich numerischer Resultate mit einer eigens entwickelten linearen analytische Theorie für den Spezialfall eines unendlich ausgedehnten, im Gleichgewicht homogenen, magnetisierten Hintergrundplasmas, welches mit einer energetischen Teilchensorte mit verschobener, isotroper Maxwell-Boltzmannverteilung interagiert. Durch eine genaue Analyse der resonanten energetischen Teilchen wird auch der auf die lineare Anwachsphase folgende nichtlineare Sättigungsmechanismus näher untersucht. Dabei werden wiederum numerische Ergebnisse mit analytischen Erwartungen verglichen. Verbesserungen bzgl. der Singularität an der magnetischen Achse werden anhand von Berechnungen von globalen idealen MHD Eigenmoden in zylindrischer und toroidaler Geometrie demonstriert. Abschließend wird STRUPHY noch auf die Berechnung einer toroidalen Alfvén Eigenmode angewandt, welche durch energetische Teilchen mit einem radialen Druckgradienten destabilisiert wird. Dieser Fall stellt dahingehend eine Herausforderung dar, als dass STRUPHY in der hier verwendeten Version die volle sechsdimensionale Verteilungsfunktion der energetischen Ionen auflöst und damit die vollständigen Bahnen, inklusive der schnellen Gyrobewegung um die Magnetfeldlinien, darstellt.

Summary

This thesis is concerned with the development and application of the new simulation code STRUPHY (Structure-Preserving Hybrid Code) for the computational description of the interaction of highly energetic charged particles with low-frequency magnetohydrodynamic waves in magnetized high temperature plasmas. Such scenarios are typically found in nuclear fusion experiments, where highly energetic MeV particles exist alongside a thermal keV background plasma composed of ionized hydrogen isotopes. Due to their low collisionality, such particles can exist far away from thermal equilibrium for relative long times. Typical examples are injected neutral particles for external heating of the main plasma or fusion born α-particles in a burning plasma leading to plasma self-heating. Due to thermal velocities of energetic particles of the order of phase velocities of global magnetohydrodynamic eigenmodes, energetic particles and plasma waves can resonantly interact, which can ultimately lead to an energy transfer from particles to waves or vice versa. In this regard, subsequent non-linear feedback phenomena can result in enhanced particle and energy transport, which can have negative impacts on the reachable fusion power as well as on the load on the reactor walls.

Due to the complex geometry of modern fusion experiments and the fact that the underlying partial differential equations are in general strongly non-linear, a numerical treatment of the above described physical phenomena is in most cases necessary. To be able to trust the results of a numerical computer simulation, in particular in case of long-term simulations deep into the non-linear phase, it is often advantageous to preserve certain mathematical properties of the simulated model in the discrete, i.e. numerical version. In this context, classical methods advance the plasma state from some given initial state by adhering to numerical consistency and stability. However, this does not guarantee the preservation of fundamental physics laws like charge conservation, conservation of energy or the divergence-free constraint of the self-consistent magnetic field. This can make the correct interpretation of simulation results quite difficult. On the other hand, modern numerical methods that are based on the discretization of objects coming from differential geometry, enable the preservation of the model's underlying geometric structure and therefore the preservation of certain properties of the continuous model.

The present work is concerned, among others, with the application of these ideas to a model which describes a three-component plasma (thermal ions, thermal electrons and energetic ions) by means of coupled magnetohydrodynamic and kinetic equations (hybrid model). The result is the new simulation code STRUPHY, which exhibits significant improvements compared to already existing hybrid codes in two respects. On the one hand, the first-time application of a combination of conforming finite element spaces for discrete differential forms and a particle based discretization of the full energetic ion distribution function on a magnetohydrodynamic-kinetic hybrid model leads to a discrete model version with exact conservation of energy and a divergence-free magnetic field. Moreover, these properties are independent of the used numerical parameters as well as the geometry (resp. curvature) of the computational domain. On the other hand, STRUPHY contains a newly developed treatment of the singularity at the magnetic axis which usually arises when magnetic flux coordinates are in play and which often leads

to numerical problems in existing codes. This is achieved by the construction of new so-called "polar" degrees of freedom based on modified finite element basis functions that are continuously differentiable across the polar singularity.

In this thesis, STRUPHY is successfully verified by applying it to several physics problems. First, numerical results are compared to a linear analytical theory for the special case of an infinitely extended, homogeneously magnetized plasma that interacts with a single energetic ion species with a shifted, isotropic Maxwell-Boltzmann distribution function in velocity space. For this case, the non-linear saturation phase that follows the linear growth phase is additionally investigated in more detail by analyzing the motion of resonant particles. In this regard, numerical results are once more compared to analytical expectations. Improvements regarding the polar singularity at the magnetic axis are demonstrated by means of global ideal MHD eigenmode calculations in cylindrical and toroidal geometry. Finally, STRUPHY is applied to the computation of a toroidal Alfvén eigenmode that is destabilized by energetic particles with a radial pressure gradient. This case poses a major computational challenge which is due to the fact that in the version presented in this thesis, STRUPHY resolves the full six-dimensional energetic ion distribution function and therefore calculates the complete particle orbits, including the fast gyro-motion around the magnetic field lines.

Contents

List of Figures

Chapter 1

Introduction

1.1 Fusion research

Since the 1960s, the World has seen an unprecedented growth in terms of population size, economic performance and energy consumption per person. This has led to a revival of mankind's old dream of an abundant, safe and emission-free source of energy because of the severe problems that come along with this enormous thirst for energy. To these belong a still rapidly growing global population, the finite amount of fossil fuels like coal, oil and gas on Earth, the unsolved problem of storing the large amounts of long-living nuclear waste produced by conventional nuclear power plants and the advancing human made climate change caused by greenhouse gas emissions. Nuclear fusion, the process with which stars like the Sun gain their energy, has become a promising candidate for a future source of energy for mankind since it combines the advantages of having an almost infinite amount of the fuel on Earth and not producing harmful exhaust fumes and long-living nuclear waste. For a future fusion reactor, the above-mentioned fuel is intended to be a 50:50 mixture of the hydrogen isotopes deuterium (D) and tritium (T) [1], which are supposed to fuse according to the reaction

$$ {}^{2}_{1}\mathrm{D} + {}^{3}_{1}\mathrm{T} \rightarrow {}^{4}_{2}\mathrm{He} + {}^{1}_{0}\mathrm{n} + 17.6\,\mathrm{MeV}\,. \tag{1.1} $$

Deuterium can easily be extracted from seawater [2] whereas tritium, which is unstable and does therefore not exist in vast amounts in nature, can be generated by a reaction involving the neutrons in the reaction (1.1) and externally added lithium (also called *tritium breeding*) [3].

However, bringing two positively charged ions close enough together in order to overcome the repulsive Coulomb barrier by quantum tunneling requires much thermal energy of $T \gtrsim 10\,\mathrm{keV}$[1]. At such a high temperature, a gas can be considered to be completely ionized and shows a distinctly different behavior compared to a neutral gas due to the long-range nature of electromagnetic forces. Hence, such a gas, which gets the new name *plasma*, is a collection of freely movable ions and electrons showing collective behavior in contrast to a neutral gas [1, 4, 5]. Sometimes this state is called the *fourth state of matter* which is strictly speaking not true because there is no sharp phase transition at a certain temperature as it is the case for the phase transitions solid-liquid and liquid-gas.

The reason for the choice of the reaction (1.1) for controlled nuclear fusion on Earth is its relatively high probability to occur at fairly low temperatures compared to other reactions [6]. A measure for this is given by the so-called reaction parameter $\langle \sigma_{\mathrm{fus}} u \rangle$ which is the reaction cross-section σ_{fus} multiplied by the relative velocity u of the two reaction partners followed by

[1] The Boltzmann constant k_{B} is suppressed. The temperature T therefore actually denotes the energy $k_{\mathrm{B}}T$.

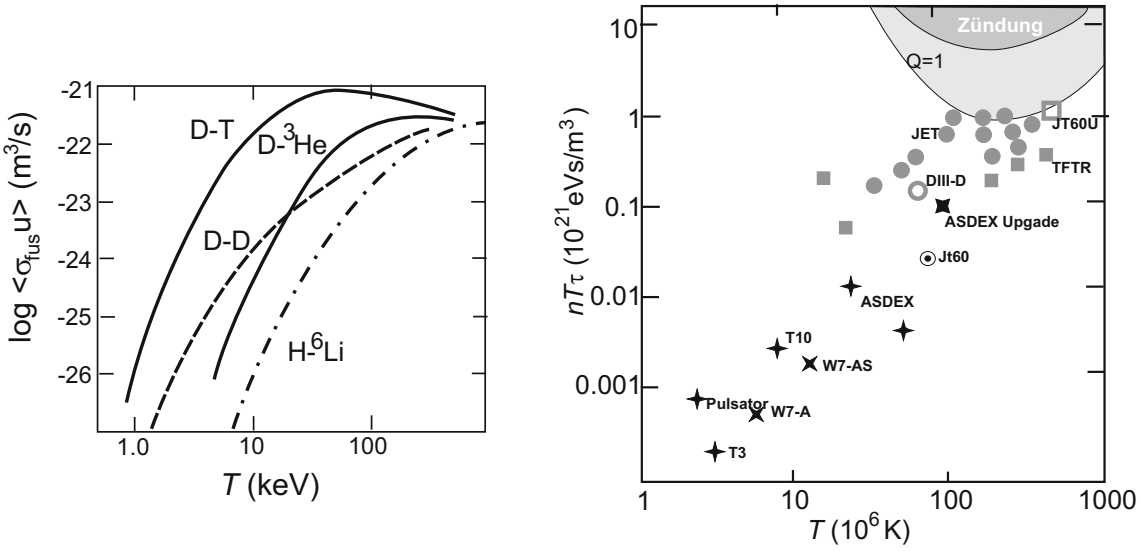

Figure 1.1: Left: temperature dependence of the reaction parameter $\langle \sigma_{\mathrm{fus}} u \rangle$ of some common fusion reactions. At $T \approx 10\,\mathrm{keV}$ one observes a two orders of magnitude larger reactivity of the D-T reaction compared to the other reactions. Right: fusion triple product and peak temperature of present and past fusion experiments. Both figures extracted from [4].

averaging over the Maxwell-Boltzmann distribution in velocity space if one assumes a plasma in thermal equilibrium. The number of reactions per volume and time unit for a 50:50 D-T mixture is then given by $n_{\mathrm{DT}}^2 \langle \sigma_{\mathrm{fus}} u \rangle / 4$, where $n_{\mathrm{DT}} = n_{\mathrm{D}} + n_{\mathrm{T}}$ is the D-T number density (number of particles per unit volume). The reaction parameter's temperature dependence for some common fusion reactions is shown in Figure 1.1 on the left. It is evident that in the range $T \gtrsim 10\,\mathrm{keV}$ the D-T reaction is the most dominant one by approximately two orders of magnitude.

Since neutrons are electrically neutral, they do not interact with the ambient plasma and therefore cannot contribute to a desired self-heating of the plasma caused by occurring fusion reactions. In order to achieve a self-sustained fusion plasma (*ignition*), the self-heating power due to Coulomb collisions must therefore be provided entirely by the formed α-particles which get one fifth of the released energy according to the mass ratio 1:4 (= 3.52 MeV). To reach ignition, this self-hating power $P_{\mathrm{fus},\alpha}$ must be larger than all the losses P_{loss} during a characteristic confinement time τ. For a homogeneous plasma in a volume V this condition reads

$$\frac{n_{\mathrm{DT}}^2 \, \langle \sigma_{\mathrm{fus}} u \rangle \, Q_{\mathrm{DT}} \, V}{20} = P_{\mathrm{fus},\alpha} \geq P_{\mathrm{loss}} = \frac{3}{2} \frac{T \, (n_{\mathrm{e}} + n_{\mathrm{DT}}) V}{\tau} \,, \tag{1.2}$$

where $Q_{\mathrm{DT}} = 17.6\,\mathrm{MeV}$ is the released energy per fusion reaction and $n_{\mathrm{e}} = n_{\mathrm{DT}}$ is the electron number density. Expression (1.2) is most easily satisfied for $T \approx 26\,\mathrm{keV}$ which leads to the famous *Lawson criterion* [7]

$$n_{\mathrm{DT}} \, \tau \geq 1.5 \times 10^{20} \, \frac{\mathrm{s}}{\mathrm{m}^3} \,, \tag{1.3}$$

for the case of the D-T reaction. This criterion means that one can in principle vary the fuel density n_{DT} and the confinement time τ over very wide ranges as long as the product $n_{\mathrm{DT}} \, \tau$ is large enough to overcome the lower limit. Two main concepts have been pursued in the past to reach this goal:

- The concept of *inertial confinement* is the approach of a large $n_{\mathrm{DT}} \approx 1 \times 10^{31}\,\mathrm{m}^{-3}$ and a low $\tau \approx 1 \times 10^{-10}\,\mathrm{s}$. The idea of this method is to heat a frozen D-T pellet on a time

scale where it is confined by its own inertia [8]. This can for instance be achieved with very strong and temporally short laser pulses [9].

- In contrast to that, the concept of *magnetic confinement* aims for a low $n_{\mathrm{DT}} \approx 1 \times 10^{20}\,\mathrm{m}^{-3}$ and a large $\tau \approx 5\,\mathrm{s}$. This method uses a strong helically shaped magnetic field ($B \approx 5\,\mathrm{T}$) that forces the charged particles of the fusion plasma on gyro-orbits around its field lines. The most advanced realizations of this concept are nowadays considered to be the tokamak and stellarator, both being toroidal devices characterized by a major radius R_0 and a minor radius a. While the helical magnetic field of the former is generated with a combination of external coils with a planar shape and a current flowing in the plasma, the magnetic field of the latter is generated completely by external coils with a complicated three-dimensional shape. An example for a tokamak is ITER [10] ($R_0 \approx 6\,\mathrm{m}$, $a \approx 2\,\mathrm{m}$), which is currently built in southern France, and an example for a stellarator is Wendelstein 7-X [11] ($R_0 \approx 5.5\,\mathrm{m}$, $a \approx 0.5\,\mathrm{m}$) in Greifswald, Germany.

It should of course be noted that the Lawson criterion in the form (1.3) is only valid for a best case scenario. In practice, the ignition criterion is more restrictive, e.g. due to energy losses caused by Bremsstrahlung at impurities coming from the wall surrounding the plasma or a dilution of the fusion plasma by helium ash. Reaching the ignition state is therefore a challenging task and has not been achieved until now. However, as shown in Figure 1.1 on the right, present and past fusion experiments have more and more approached this state. In this figure, the so-called *triple product* consisting of density, confinement time and temperature is used rather than just the product of density and confinement time. This is an alternative figure of merit used in fusion research. Compared to (1.3), it is more flexible in a sense that the temperature is not fixed.

1.2 The role of energetic particles in fusion plasmas

The more fusion experiments approach the desired ignition state, the more interest is attracted by the effects of highly energetic particles in the MeV range on the stability of the keV bulk plasma. Examples for such particles are the fusion-born 3.52 MeV α-particles in the reaction (1.1) or externally generated energetic ions which are used to heat the plasma beyond Ohmic heating. A prominent example for the latter is neutral beam injection (NBI), where ions are first accelerated externally, then neutralized in order to penetrate the magnetic field, and finally ionized via collisions with the bulk plasma particles. It is well-known that under certain conditions, low-frequency, large-scale (comparable to the system size) magnetohydrodynamic (MHD) waves propagating in the bulk plasma can resonantly interact with such particles. This can lead to a net energy transfer from the particles to the waves (destabilization) which can in turn lead to increased particle and energy transport followed by a degradation of the confinement time [12, 13, 14]. This effect has been observed especially for one type of MHD waves, namely the shear Alfvén wave (SAW) which shall be explained in more detail in the following.

1.2.1 Shear Alfvén waves

Shear Alfvén waves (named after Hannes Alfvén, † 1995) are low-frequency, transverse, electromagnetic plasma waves which propagate parallel to the magnetic field $\mathbf{B}$ [4]. Here, low-frequency means smaller than the ion cyclotron frequency $\Omega_{\mathrm{ci}} = q_{\mathrm{i}}B/m_{\mathrm{i}}$, where q_{i} is the ion charge, m_{i} its mass and $B = |\mathbf{B}|$ the absolute value of the magnetic field. Moreover, SAWs have the important property that they are incompressible, i.e. no plasma compression is involved in the propagation of the waves. This is why SAWs are generally considered to be more easily destabilizable than

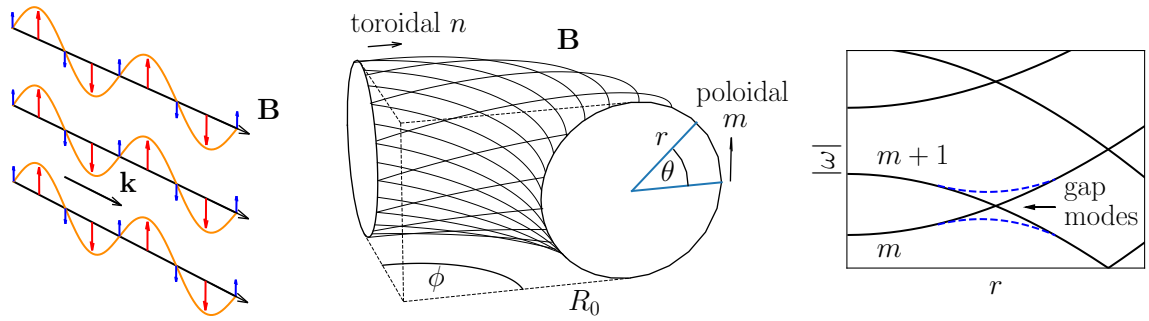

Figure 1.2: Basic shear Alfvén physics. Left: shear Alfvén waves in an homogeneous, infinitely extended magnetized plasma. Shown is the perturbed magnetic field in blue, the plasma displacement in red and the total magnetic field in orange. Middle: toroidal plasma confined by an helically shaped magnetic field. Right: continuous Alfvén spectra for fixed toroidal mode number n in the cylindrical limit (black lines) and the formation of a frequency gap if toroidal curvature is present (blue dashed lines).

compressible MHD waves. Their dispersion relation is given by the simple relation $\omega^2 = v_\mathrm{A}^2 k_\parallel^2$, where ω is the wave frequency, $k_\parallel = (\mathbf{k}\cdot\mathbf{B})/B$ the wave number parallel to the magnetic field and $v_\mathrm{A} = B/\sqrt{\mu_0 m_\mathrm{i} n_\mathrm{i}}$ the Alfvén velocity (μ_0 denotes the vacuum permeability and n_i the number density of the plasma ions). For typical fusion plasma parameters $v_\mathrm{A} \approx 6 \times 10^6\,\mathrm{m/s}$, i.e well below the speed of light. The physical mechanism behind SAWs is an interplay between the restoring force of bent magnetic field lines on the one hand and the inertia of the plasma ions on the other hand. This is shown in Figure 1.2 on the left for the simplest case of an homogeneously magnetized plasma. A remarkable, as well as non-trivial property of the dispersion relation $\omega^2 = v_\mathrm{A}^2 k_\parallel^2$ is that it is also valid for a cylindrical plasma with radial variations of the magnetic field and the plasma density. For a helical magnetic field $\mathbf{B} = B_\theta(r)\,\mathbf{e}_\theta + B_z(r)\,\mathbf{e}_z$ and a cylindrical plasma of length $2\pi R_0$ it is easily verified that

$$\omega^2 = v_\mathrm{A}^2\, k_\parallel^2 = \frac{B_z^2(r)}{\mu_0 m_\mathrm{i} n_\mathrm{i}(r)} \frac{1}{R_0^2} \left(n + \frac{m}{q(r)} \right)^2, \qquad q(r) = \frac{r B_z(r)}{R_0 B_\theta(r)}\,, \tag{1.4}$$

such that the wave frequency becomes a function of radius r. In (1.4), m and n are two integer mode numbers introduced by periodicity constraints in the azimuthal (m) and axial (n) direction. Moreover, q is the so-called safety factor commonly used in fusion research giving the number of axial turns of a magnetic field line per azimuthal turn. SAWs satisfying the dispersion relation (1.4) are part of the *Alfvén continuum* and are subjected to a phenomenon called *continuum damping* [15]. Qualitatively, this can be explained by imagining a radially extended wave packet which is rapidly dispersed due to different phase velocities at different radial positions. Hence, exciting waves which are part of the Alfvén continuum is generally difficult.

However, under certain conditions, additional discrete Alfvén eigenmodes (AEs) can exist outside of the continuous spectrum, and which are therefore not subjected to continuum damping. This is the case if, as shown in the middle of Figure 1.2, the cylinder is bent to a torus (tokamak geometry). Because the field is now stronger on the inside of the torus than on the outside, the toroidal (axial) magnetic field experiences a periodic modulation in the poloidal (azimuthal) direction. This can lead to a coupling of Alfvén waves with different poloidal mode numbers m which in turn can induce a frequency gap in the Alfvén continuum [16]. This is shown in Figure 1.2 on the right for a fixed toroidal mode number n. In the cylindrical limit (black lines), continuum branches $\omega = \omega(r)$ with different poloidal mode numbers may intersect.

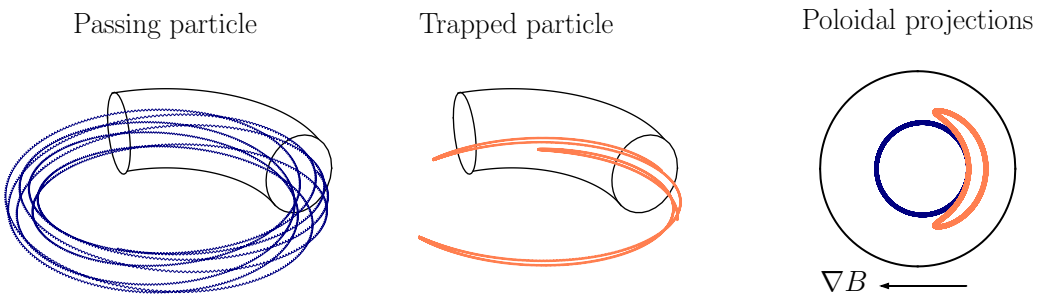

Figure 1.3: Particle orbits in a tokamak-like fusion plasma. Left: passing particle with $v_\parallel$ that is high enough to exceed the top of the magnetic hill on the inside of the torus (high-field side). Middle: trapped particle which is reflected at the high field side because of a too low $v_\parallel$. Right: poloidal projections give rise to a circular drift-orbit for the passing particle and a banana drift-orbit for the trapped particle.

If toroidal curvature and the associated symmetry breaking of the toroidal magnetic field is present, counter-propagating waves with the same frequency can couple together which results in the formation of a frequency gap (similar to the formation of band gaps in conductors). Inside gaps between m and $m+1$ branches, a discrete AE known as the toroidal Alfvén eigenmode (TAE) exists [16]. TAEs are just one example. In more realistic scenarios many other AEs exist. For instance, a non-monotonic safety factor q with a minimum at some radial location can give rise to reversed shear Alfvén eigenmodes (RSAEs) [17, 18] while geometries with elliptical instead of circular poloidal cross-sections can lead to coupling of m and $m+2$ modes resulting in ellipticity induced Alfvén eigenmodes (EAEs) [19, 20]. A list can be found for instance in Table 1 in [12].

1.2.2 Particle orbits and mode drive

In the pure MHD picture, the above explained AEs are stable and therefore in principle not problematic or dangerous. However, since these modes are not subjected to continuum damping, they can be driven unstable by e.g. an external antenna or by energetic particles via resonant wave-particle interaction processes [12, 14]. The reason why the latter is possible in a toroidal configuration is that this geometry gives rise to special ion orbits with new intrinsic frequencies apart from the cyclotron frequency which is always present in a magnetized plasma.

If the magnetic field variation scale $B/|\nabla B|$ is large compared to the gyro-radius $|v_\perp|/\Omega_{\mathrm{ci}}$ (which is usually the case in a tokamak), a particle's magnetic moment $\mu = m_i v_\perp^2/2B$ is an adiabatic invariant and it can therefore be assumed that it is a constant of motion. Since the particle's kinetic energy is also a conserved quantity, the following relation between the parallel velocity and the magnetic field strength holds:

$$\frac{1}{2}m_{\mathrm{i}}v_\parallel^2 + \mu B = const.. \tag{1.5}$$

Hence, if a particle in a tokamak-like magnetic field moves along a field line towards the inner side of the torus, the magnetic field gets stronger and the parallel velocity will therefore decrease. This gives rise to two main classes of orbits: First, if the parallel velocity is high enough to travel over the top of the magnetic hill on the inside of the torus, a particle is called a *passing* particle. Second, if the parallel velocity is too low, the particle gets reflected by a change of the sign in the parallel velocity (magnetic mirror). Such a particle is called a *trapped* particle.

In addition to the fast gyro-motion around the magnetic field lines and the free motion along the field lines, particles in an inhomogeneous magnetic field experience a slow drift motion perpendicular to field lines caused by gradient and curvature drifts (for details on single-particle motion see [1, 4, 5] for instance). This leads to orbits like the ones shown in Figure 1.3 for a passing (left) and trapped particle (middle). Moreover, a projection on a poloidal plane leads to the orbits shown on the right, where it is evident that the passing particle has an almost circular drift orbit while the trapped one has a banana orbit. The time to complete such orbits in the poloidal plane as well in the toroidal direction gives rise to the previously mentioned new frequencies besides the cyclotron frequency, namely the poloidal precision frequency ω_θ and the toroidal precision frequency ω_ϕ. Usually ω_θ, $\omega_\phi \ll \Omega_{\mathrm{ci}}$. In order to make energy transfer between a drifting particle and an Alfvén eigenmode possible, the following resonance condition must be satisfied [12]

$$\omega + (m + l\,)\,\omega_\theta - n\,\omega_\phi \simeq 0\,, \tag{1.6}$$

where $l = \pm 1$ in the simplest case of a tokamak with circular cross-section. It can be shown that keV particles of the thermal bulk plasma are usually too slow to meet condition (1.6). However, the opposite is true for MeV energetic particles. For a passing particle and a TAE introduced in the previous section, analytical approximations for all three frequencies in (1.6) can be derived. This leads to resonances for particles with $v_\parallel \approx v_{\mathrm{A}}$ and $v_\parallel \approx v_{\mathrm{A}}/3$.

Meeting a resonance condition of the form (1.6) does, however, not give any information whether a mode is damped (energy transfer wave $\rightarrow$ particles) or driven (energy transfer particles $\rightarrow$ wave). This depends on the specific distribution of the energetic particles both in velocity and real space. For instance, a radial gradient in the energetic particle pressure caused by e.g. fusion reactions in the hotter core of a fusion plasma is a driving mechanism while a negative gradient in velocity space around the resonant velocity is a damping mechanism [12].

1.2.3 Modeling approaches

A quantitative description of the linear and especially the non-linear dynamics of the above described phenomena in realistic geometries usually requires computer simulations of suitable model equations. The latter can be separated into two main classes: First, the more complete and accurate kinetic models which resolve the plasma behavior in a statistical sense in the six-dimensional phase space and second, fluid models which rely on averages in velocity space such that the problem dimensionality is reduced to the three-dimensional real space. Due to the fact that six-dimensional kinetic simulations are computationally expensive even on current supercomputers, one usually make use of reduced models which are easier to solve while still being able to describe the physical phenomena of interest. For instance, collision-less wave-particle interactions require a kinetic description because it is based on resonances in velocity space which cannot be captured if averages are taken beforehand. However, in strongly magnetized plasmas, the fast gyro-motion around the field lines is often not of interest and can be averaged out, thus eliminating one velocity degree of freedom. Examples for implementations of such so-called gyro-kinetic models [21, 22, 23, 24] of all involved plasma species (bulk and energetic particles) are the eigenvalue code LIGKA [25] and the initial-value codes ORB5 [26] and EUTERPE [27]. However, as explained in the previous section, electrons and ions of the bulk plasma are far away from resonating with Alfvén eigenmodes. Hence, if kinetic effects within the bulk plasma can be neglected or are not of interest, a fluid model for the bulk plasma can be used while retaining a kinetic description for the energetic particles. Such models are called *hybrid models* since they combine a fluid model for the bulk plasma and a kinetic model for the energetic particles (see [28] for an early work that suggests such a strategy). Current-coupling (CC) and pressure-coupling

(PC) schemes can be used in this regard, depending on how the coupling between the two models is achieved. Generally speaking, the notion of a hybrid code implies the following two crucial features:

1. Use of reduced model equations for the bulk plasma (for instance fluid equations instead of kinetic equations).

2. Fully self-consistent description of the non-linear dynamics (beyond the linear phase).

Examples of successful implementations of hybrid codes in fusion research are MEGA [29], M3D-K [30, 31], HMGC [32, 33] and the non-linear MHD code JOREK [34, 35, 36] which has recently been extended to be able to deal with hybrid fluid-kinetic models [37]. The appeal of hybrid codes can be summarized as follows:

1. Reduced numerical costs compared to fully kinetic simulations.

2. Inclusion of non-equilibrium dynamics (wave-particle resonances) compared to pure fluid simulations.

3. Possibility of direct comparison with analytical computations (for linear dynamics).

The drawback is the increased complexity of model equations compared to pure fluid models. For instance, while the mathematical geometric structure (Poisson bracket and/or Hamilton's variational principle) of MHD equations has been known for decades [38], the underlying structure of MHD-kinetic hybrid models has been discovered only very recently [39, 40]. This shows that the proper derivation of MHD-kinetic hybrid models that respect fundamental physics principles such as energy conservation is a non-trivial task. As a consequence, little attention had been paid to these issues during the design of the first generation of hybrid codes mentioned above. An example that the use of an energetically consistent model can be important in some situations is demonstrated in [41], where a comparison between a Hamiltonian and non-Hamiltonian hybrid MHD-kinetic model (pressure-coupling) has been performed. A linear stability analysis revealed a spurious, i.e. non-physical instability in the non-Hamiltonian model, which could be removed in the corresponding Hamiltonian, energy-preserving model.

1.3 Structure-preserving geometric numerical integration

In parallel to the theoretical discoveries regarding hybrid models came the advent of geometric (or structure-preserving) numerical methods for plasma equations, see [42] for a review. These methods obey many conservation properties implied by the geometric structure, such as conservation of energy, charge or momentum on the discrete level [43, 44]. This can be very helpful especially when it comes to long-term and strongly non-linear simulations because preserving such quantities improves long-term numerical stability and physical reliability. The main idea is to discretize directly the underlying Poisson structure or variational principle, thus transferring geometric properties to a finite-dimensional setting. For the discretization of kinetic equations, the most popular method is still the particle-in-cell (PIC) method because it is fairly simple to implement and it is inherently parallel [45]. That is why a lot of attention has been paid to the design of structure-preserving geometric PIC algorithms. The first one was designed and implemented by Squire et al. in 2012 [46]. Similar methods have later been successfully applied to Vlasov-Maxwell [47, 48, 49, 50], Vlasov-Darwin [51], Vlasov-Poisson [52, 53] and also to pure fluid models like ideal MHD [54] and Navier-Stokes equations [55]. The first structure-preserving

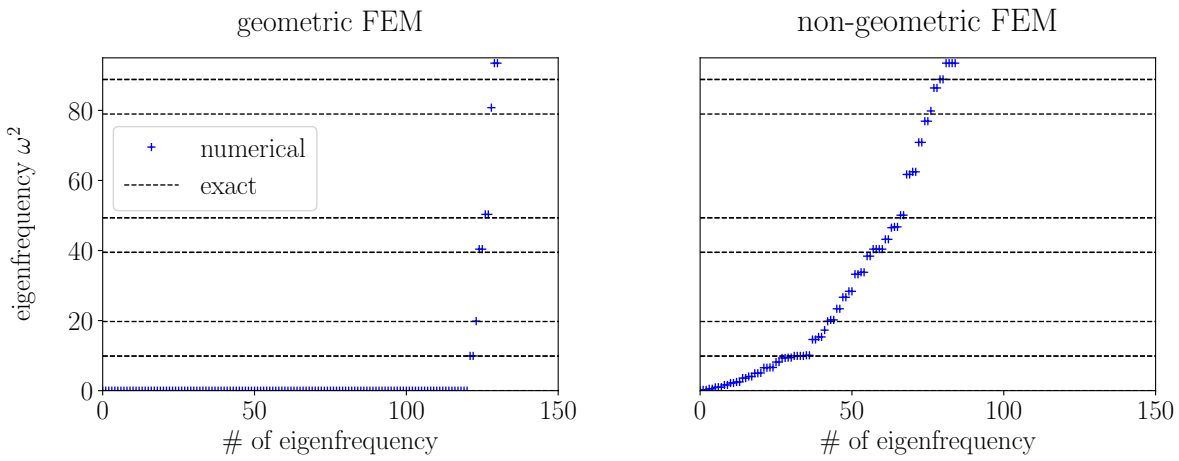

Figure 1.4: Numerical eigenspectrum of a geometric (left) and a non-geometric (right) finite element discretization of the Maxwell-type eigenvalue problem (1.8). While the geometric one reproduces the analytical spectrum very well, the non-geometric one produces a spectrum polluted with many spurious eigenfrequencies. Based on [63].

geometric PIC algorithm using the framework of finite element exterior calculus (FEEC) for solving field equations was designed by He et al. in 2016 [56]. The same approach has later been taken by Kraus et al. [57] who used FEEC based on tensor product B-spline basis functions constructed in [58, 59].

FEEC is a framework for the geometric discretization of partial differential equations which allows, among others, to encode the properties curl grad = 0 and div curl = 0 (*de Rham cochain complex*) into conforming finite element (FE) spaces. The theoretical foundation of FEEC has been laid by Arnold et al. [60, 61, 62]. From a physicist's or applied mathematician's point of view, FEEC is based on the notion of *discrete differential forms* leading to an exact (i.e. up to machine precision) preservation of the generalized Stokes theorem

$$\int_C \nabla\phi \cdot \mathrm{d}\mathbf{L} = \phi(P_1) - \phi(P_2)\,, \tag{1.7a}$$

$$\int_S (\nabla \times \mathbf{E}) \cdot \mathrm{d}\mathbf{S} = \oint_{\partial S} \mathbf{E} \cdot \mathrm{d}\mathbf{L}\,, \tag{1.7b}$$

$$\int_V (\nabla \cdot \mathbf{B})\,\mathrm{d}V = \oint_{\partial V} \mathbf{B} \cdot \mathrm{d}\mathbf{S}\,, \tag{1.7c}$$

on all parts of the discretized computational domain, independently of space curvature introduced by some coordinate transformation in the context of differential geometry (hence the name *geometric* methods). Consequently, if physical quantities such as the electric or magnetic field are not discretized as classical vector fields (usually contra-variant) but as differential forms (either 1-form or 2-form), this property can be extremely beneficial to preserve certain invariants like the divergence-free constraint $\nabla \cdot \mathbf{B} = 0$ of the magnetic field.

As simple example that demonstrates the power of using a geometric discretization for solving a PDE is the numerical solution of the vacuum, time-harmonic Maxwell's equations on the unit square $\Omega = [0, 1] \times [0, 1]$ which is surrounded by a perfectly conducting wall (vanishing tangential components of the electric field on the domain boundary). The problem can be

formulated as an eigenvalue problem and reads as follows: find $\omega^2 \in \mathbb{R}$ and non-vanishing functions $\mathbf{E}$ such that

$$\begin{cases} \nabla \times \nabla \times \mathbf{E} = \omega^2 \mathbf{E} & \text{in } \Omega\,, \quad (1.8a) \\ \nabla \cdot \mathbf{E} = 0 & \text{in } \Omega\,, \quad (1.8b) \\ \mathbf{E} \times \mathbf{n} = 0 & \text{on } \partial\Omega\,, \quad (1.8c) \end{cases}$$

where $\mathbf{E}$ is the electric field and $\mathbf{n}$ an outward-pointing unit vector normal to the surface of the computational domain. The homogeneous Dirichlet boundary condition (1.8c) for the tangential components leads to a quantized spectrum of eigenfrequencies $\omega^2 > 0$ with corresponding eigenfunctions. In this simple geometry, the eigenfrequencies are analytical and readily given by $\omega^2 = (\ell\pi)^2 + (m\pi)^2$ with ℓ and m being integer mode numbers. This makes a direct comparison to the numerically calculated eigenfrequencies possible.

In Figure 1.4, the resulting numerical eigenfrequencies of a geometric (left) and non-geometric (right) discretization are compared against the exact ones. On the one hand, the geometric discretization is clearly able to distinguish between zero and non-zero eigenfrequencies and, on the other hand, shows an excellent agreement with the analytical spectrum of non-zero eigenfrequencies (see Chapter 11 in [63] for more details on the meaning of zero eigenfrequencies). In contrast to that, the non-geometric discretization leads to a spectrum which is polluted with many spurious eigenfrequencies. This makes it almost impossible to judge whether an eigenfrequency is a true, physical one or a spurious one if the analytical spectrum is not known a priori (which is usually the case in realistic geometries).

1.4 Dissertation overview and outline

This thesis is concerned with a) the application of ideas of structure-preserving integration to a MHD-kinetic hybrid model (see [52, 64] for other conservative schemes for hybrid models), namely the Hamiltonian current-coupling (CC) scheme [39] and b) the verification and physical analysis of simulations performed with the resulting algorithms. The model equations consist of the three-dimensional, ideal MHD equations coupled to the collision-less, full-orbit Vlasov equation with three velocity degrees of freedom. The MHD part thus covers the entire set of MHD waves, namely shear Alfvén, slow- and fast magnetosonic waves. The kinetic equation contains the gyro-motion of the energetic species, enabling the description of wave-particle resonances in this regime. The overall motivation for this work stems from the need of stable and reliable long-time simulations of energetic particle physics in complex geometries such as tokamaks and stellarators. Since the model's field equations are strongly based on objects and operators coming from differential geometry (both vector- and scalar-valued functions, grad, curl and div operators etc.), the FEEC framework seems to be a natural candidate for a numerical treatment in order to avoid spurious modes that may pollute long-time simulations.

A result of this thesis is the new numerical code STRUPHY (Structure-Preserving Hybrid Code). In the version presented in this thesis, the MHD part is linearized and the focus is laid on the non-linear coupling to the kinetic species, which acts back on the bulk plasma via charge and current densities according to the used current-coupling scheme. FEEC is used for the discretization of the MHD part and PIC for the kinetic part. The concept is similar to the GEMPIC approach in [57, 65, 66], only that the role of Maxwell's equations is taken by the linear MHD equations. Another difference with respect to GEMPIC is that the discretization is performed directly on the equations rather than to the variational principle or the Poisson bracket. There are three reasons for this:

1. Linearized MHD equations lose their Hamiltonian structure if the magnetic background field is not chosen properly. In this case there is no such thing as a Poisson bracket or variational formulation, but the method presented in this thesis still applies.

2. Poisson structures of extended hybrid models with two-fluid MHD, drift-kinetic or gyrokinetic models are either not known or very cumbersome.

3. A high level of abstraction is avoided in the presentation of the scheme. In fact, the mere existence of a Poisson structure on the continuous level is sufficient to translate several important conservation properties to the discrete level by applying FEEC to the equations directly.

The resulting discretization of the CC hybrid model provably conserves the total energy, mass and the divergence-free constraint of the magnetic field, irrespective of metric (= space curvature), mesh parameters and chosen order of the scheme. This is, on the one hand, thanks to the separation between topological and metric properties in the theory of differential forms upon which FEEC is built and, on the other hand, due to the coupling with a particle-based kinetic solver. In the version presented in this thesis, the finite element spaces are constructed from two-dimensional tensor product B-splines in the poloidal plane and a single Fourier mode in the toroidal direction in order to reduce the computational costs. Consequently, the current version is only applicable to tokamak-like axisymmetric equilibria but an extension to fully three-dimensional equilibria is possible but needs further parallelization. During an entire simulation, position space is expressed in logical (curvilinear) coordinates, also for the kinetic species. Results in physical (Cartesian) space are obtained via post-processing using push-forward operations. Time stepping is implicit and based on the splitting of a skew-symmetric matrix into skew-symmetric sub-matrices. Most of the resulting substeps are solved with the semi-implicit Crank-Nicolson method [67]. The resulting time integrators are combined via splitting methods according to Lie-Trotter [68] and Strang [69]. However, higher-order splitting schemes would in principle be available, too [70].

If the coupling between the MHD bulk and the energetic ions is switched off (or if no energetic particles are present), the spatially discretized linear MHD equations can be directly used to run STRUPHY not only as an initial-value solver but also as an eigenvalue solver (similar to problem (1.8)). In this case, STRUPHY solves the following ideal MHD eigenvalue problem: find $\omega^2 \in \mathbb{R}$ and non-vanishing $\mathbf{U}$ (in some suitable space to be defined) in a domain $\Omega \subset \mathbb{R}^3$ such that

$$
\begin{cases}
\mathbf{F}(\mathbf{U}) = -\omega^2 \rho_{\text{eq}}\, \mathbf{U} \qquad \text{in } \Omega\,, & \text{(1.9a)} \\
\mathbf{F}(\mathbf{U}) = -\dfrac{1}{\mu_0}\big\{\nabla \times \big[\, \nabla \times (\mathbf{B}_{\text{eq}} \times \mathbf{U}\,)\,\big]\big\} \times \mathbf{B}_{\text{eq}} - \mathbf{J}_{\text{eq}} \times \big[\, \nabla \times (\mathbf{B}_{\text{eq}} \times \mathbf{U})\,\big] \\
\qquad\qquad + \nabla\big[\, \nabla \cdot (\, p_{\text{eq}}\, \mathbf{U}) + (\gamma - 1)\, p_{\text{eq}}\, \nabla \cdot \mathbf{U}\,\big]\,, & \text{(1.9b)} \\
\mathbf{U} \cdot \mathbf{n} = 0 \qquad \text{on } \partial\Omega\,, & \text{(1.9c)}
\end{cases}
$$

where ω^2 denotes the eigenfrequency, $\rho_{\text{eq}} = \rho_{\text{eq}}(\mathbf{x})$ the equilibrium mass density, $\mathbf{B}_{\text{eq}} = \mathbf{B}_{\text{eq}}(\mathbf{x})$ the equilibrium magnetic field, $p_{\text{eq}} = p_{\text{eq}}(\mathbf{x})$ the equilibrium pressure and $\gamma = 5/3$ the heat capacity ratio of an ideal gas. Moreover, $\mathbf{U} = \mathbf{U}(\mathbf{x})$ is the unknown perturbed velocity field and (1.9b) is the *MHD force operator* which is a self-adjoint differential operator such that the eigenvalues ω^2 are purely real [71]. The equilibrium about which the non-linear ideal MHD equations are linearized is characterized by zero flow $\mathbf{U}_{\text{eq}} = 0$ and the well-known MHD force balance $\mathbf{J}_{\text{eq}} \times \mathbf{B}_{\text{eq}} = \nabla p_{\text{eq}}$, where $\mathbf{J}_{\text{eq}} = (\nabla \times \mathbf{B}_{\text{eq}})/\mu_0$ is the equilibrium current. Finally, in

this thesis, a plasma surrounded by a perfectly conducting wall is considered (fixed boundary modes). This means that $\mathbf{U}$ must have vanishing normal components on the boundary according to (1.9c). A more realistic, yet mathematically more involved scenario would be to consider a vacuum region between the plasma and the wall [72].

There exist many sophisticated solvers for the solution of (1.9) in axisymmetric equilibria (where Fourier modes in the toroidal direction decouple), among the best-known being PEST [73], ERATO [74], GATO [75], as well as KINX [76] to include divertor configurations, the code in [77] and MARS [78] which include resistive effects, CASTOR [79] which can also handle 3d stellarator configurations. The conventional approach is to expand the eigen-solution $\mathbf{U}$ in a suitable, finite set of basis functions, usually Fourier basis in the poloidal direction and spline or polynomial basis in the radial direction of the poloidal plane, and to solve the ensuing discrete eigenvalue problem. If solved in magnetic flux coordinates a complication arises from the geometry of the problem, which has a polar point at the magnetic axis, where the Jacobian determinant of the mapping between logical and physical coordinates vanishes (see Section 5.1). This usually requires some kind of work-around when computing the push-forward of the solution to Cartesian coordinates. Regarding this problem, this thesis proposes a new framework based on an extension of FEEC and *smooth polar splines* that produces physical (i.e. pushed-forward) solutions which are continuous across the magnetic axis, the continuity being enforced directly through the basis functions in which $\mathbf{U}$ is represented. These polar splines were first introduced in [80] and are constructed as linear combinations of tensor product B-splines supported in the vicinity of the polar point (magnetic axis). Moreover, these splines must be used in the context of isogeometric-analysis (IGA) [81] being an approach in which the mapping (= coordinate transformation) describing the geometry of the problem is represented in the same set of basis functions as the solution fields. If the problem is solved in magnetic flux coordinates, these must first be constructed from a given numerical or experimental MHD equilibrium which usually results in a numerical description of the geometry. Hence, imposing the IGA constraint does not introduce additional difficulties.

Later, the polar spline framework (originally for scalar fields only) was used to construct the discrete de Rham complex (curl grad = 0 and div curl = 0) which is one of the two main ingredients of FEEC [82] from a practitioner's point of view. A contribution of this thesis is the second main ingredient, namely the formulation of a *commuting* diagram in case when the discrete complex is spanned by differential forms based on smooth polar splines. For this, new polar projection operators are defined that project from the continuous de Rham complex into the polar spline sub-complex in a way that the commuting property holds. This is achieved by the formulation of "polar degrees of freedom" (polar DOFs), i.e. linear functionals on functions from the de Rham complex that define the conforming polar sub-complex. Just as the polar basis functions are linear combinations of tensor product basis functions, the polar DOFs can be constructed as linear combinations of tensor product DOFs. Explicit expressions for all reduction matrices needed in the process are presented.

This thesis is organized as follows: Chapter 2 is concerned with the detailed derivation of the hybrid MHD-kinetic model considered in this thesis starting from a kinetic description of all involved plasma species (bulk electrons and ions and energetic ions). Once the model is obtained, some of its conservation properties are discussed. This is followed by the derivation of an analytical dispersion relation for a homogeneously magnetized, infinitely extended bulk plasma. Chapter 3 deals with first formulating the model equations in terms of differential forms, followed by the derivation of a weak formulation suitable for a spatial discretization with FEEC. The resulting semi-discrete system (discrete in space and continuous in time) will then be discretized in time. Finally, Chapter 3 also gives information on the implementation and code development and describes the main structure of STRUPHY. Next, Chapter 4 presents

simulations results in a simplified geometry without a polar point and toroidal curvature. The focus here lies on the one hand on the investigation of basic properties of the algorithm and on the other hand on physical effects like continuum damping and wave-particle interactions which do not require a cylindrical or toroidal geometry. Chapter 5 then extends the algorithm to such domains with a polar singularity at the magnetic axis. Finally, Chapter 6 presents numerical results in cylindrical and toroidal geometry with investigations on the behavior of MHD eigenmodes at the magnetic axis and benchmark studies with other codes.

Chapter 2

Hybrid MHD-kinetic current-coupling model

2.1 Model derivation and properties

The starting point of the derivation of the MHD-kinetic hybrid model used in this thesis is the kinetic equation

$$\frac{\partial f_s}{\partial t} + \mathbf{v} \cdot \nabla f_s + \frac{q_s}{m_s} \left(\mathbf{E} + \mathbf{v} \times \mathbf{B} \right) \cdot \nabla_{\mathbf{v}} f_s = \sum_{s'} C_{ss'}(f_s) \,, \tag{2.1}$$

describing the temporal evolution of the distribution function $f_s = f_s(\mathbf{x}, \mathbf{v}, t)$ of a charged particle species s in the six-dimensional phase space. The distribution function is a measure for the number of particles located in an infinitesimal phase space volume element $\mathrm{d}^3x\,\mathrm{d}^3v$ around the point $(\mathbf{x}, \mathbf{v}) \in \mathbb{R}^6$ at time $t \geq 0$. This description should be regarded as a *mesoscopic* one because it is obtained from the more general single particle *Klimontovich distribution function* by using a procedure called *ensemble averaging* which make use of the fact that one deals with indistinguishable particles from a statistical point of view [83]. As a result of this procedure, interactions on a microscopic scale are taken into account in the collision operator $C_{ss'}$ appearing on the right-hand side of (2.1). If, for some reason, collisions can be neglected, equation (2.1) is called the *Vlasov equation*. In what follows, we consider a plasma consisting of three species: thermal electrons ($s = \mathrm{e}$), thermal ions ($s = \mathrm{i}$) and energetic ions ($s = \mathrm{h}$ for "hot"). For the latter, we neglect collisions between themselves as well as between them and the other two species because, as explained in the introduction, energetic particles are weakly collisional on typical MHD time scales due to their low Rutherford cross-section. Hence, $C_{\mathrm{hs}} = C_{s\mathrm{h}} = 0$.

Again due to the averaging process, the electromagnetic fields $\mathbf{E}$ and $\mathbf{B}$ can be regarded as mesoscopic ones not containing fluctuations on a microscopic scale. They satisfy Maxwell's equations

$$\nabla \times \mathbf{B} = \frac{1}{c^2} \frac{\partial \mathbf{E}}{\partial t} + \mu_0 \mathbf{J} \,, \qquad \text{(Ampére)} \tag{2.2a}$$

$$\nabla \times \mathbf{E} = -\frac{\partial \mathbf{B}}{\partial t} \,, \qquad \text{(Faraday)} \tag{2.2b}$$

$$\nabla \cdot \mathbf{E} = \frac{\rho}{\epsilon_0} \,, \qquad \text{(Gauß 1)} \tag{2.2c}$$

$$\nabla \cdot \mathbf{B} = 0 \,, \qquad \text{(Gauß 2)} \tag{2.2d}$$

where ϵ_0 and μ_0 stand for the vacuum permittivity and vacuum permeability, respectively, and $\epsilon_0 \mu_0 = 1/c^2$ with c being the speed of light in vacuum. The sources in (2.2a) and (2.2c) are the

charge density ρ and the current density $\mathbf{J}$ which are obtained from the particles' distribution functions by taking the first two moments in velocity space and summing over all species:

$$\rho := \sum_s q_s \int_{\mathbb{R}^3} f_s \,\mathrm{d}^3 v\,, \qquad \mathbf{J} := \sum_s q_s \int_{\mathbb{R}^3} \mathbf{v} f_s \,\mathrm{d}^3 v\,. \tag{2.3}$$

Equations (2.1)-(2.3) form a closed system of partial differential equations in seven dimensions (the six-dimensional phase space + time) and is usually considered to be the most complete description of a plasma because it includes various spatial and temporal scales. It is strongly non-linear and numerically very expensive to solve. As already explained in the introduction, however, a hybrid model aims for a model simplification for the parts of the plasma for which a kinetic description is actually not needed. To obtain a simpler set of equations one therefore builds moments of (2.1) in velocity space for thermal electrons and ions ($s = \mathrm{e}, \mathrm{i}$) but not for energetic ions ($s = \mathrm{h}$). For this, we introduce the fluid quantities

$$n_s := \int_{\mathbb{R}^3} f_s \,\mathrm{d}^3 v\,, \qquad n_s \mathbf{u}_s := \int_{\mathbb{R}^3} \mathbf{v} f_s \,\mathrm{d}^3 v\,, \qquad n_s \,\mathcal{E}_s := \int_{\mathbb{R}^3} \frac{m_s v^2}{2} f_s \,\mathrm{d}^3 v\,, \tag{2.4}$$

that are, the particle number density, the particle flux density, and the energy density, respectively. The latter contains a contribution from the mean flow kinetic energy and the kinetic energy related to the stochastic velocity $\mathbf{v}' = \mathbf{v} - \mathbf{u}_s$ relative to the mean flow $\mathbf{u}_s$. The stochastic part can be related to the temperature by

$$\frac{3}{2} T_s = \mathcal{E}_s - \frac{m_s}{2}\, u_s^2\,. \tag{2.5}$$

By taking the first three moments of (2.1) in velocity space and using the fact that $f_\mathrm{h} \to 0$ for $|v| \to \infty$, one obtains three equations representing transport equations for mass, momentum and energy, respectively,

$$\frac{\partial}{\partial t}(m_s n_s) + \nabla \cdot (m_s n_s \mathbf{u}_s) = 0\,, \tag{2.6}$$

$$\frac{\partial}{\partial t}(m_s n_s \mathbf{u}_s) + \nabla \cdot (m_s n_s \mathbf{u}_s^\top \mathbf{u}_s) + \nabla \cdot \mathbb{P}_s - q_s n_s \left(\mathbf{E} + \mathbf{u}_s \times \mathbf{B} \right) = \mathbf{R}_s\,, \tag{2.7}$$

$$\begin{aligned} \frac{\partial}{\partial t}\left(n_s \frac{m_s}{2}\, u_s^2 + \frac{3}{2}\, n_s T_s \right) + \nabla \cdot \left(n_s \frac{m_s}{2}\, u_s^2\, \mathbf{u}_s + \frac{5}{2}\, n_s T_s \mathbf{u}_s + \mathbf{u}_s \cdot \mathbb{\Pi}_s + \mathbf{q}_s \right) - q_s n_s\, \mathbf{E} \cdot \mathbf{u}_s \\ = Q_s + \mathbf{R}_s \cdot \mathbf{u}_s\,, \end{aligned} \tag{2.8}$$

where $\mathbb{P}_s$ and $\mathbb{\Pi}_s$ denote the pressure and viscosity tensor, respectively, which are related to the scalar pressure p_s via

$$\mathbb{P}_s := m_s \int_{\mathbb{R}^3} \mathbf{v}' \left(\mathbf{v}'\right)^\top f_s \,\mathrm{d}^3 v = p_s \mathbb{1} + \mathbb{\Pi}_s\,, \tag{2.9}$$

and the third order moment

$$\mathbf{q}_s := \int_{\mathbb{R}^3} \frac{m_s \left(v'\right)^2}{2}\, \mathbf{v}' f_s \,\mathrm{d}^3 v\,, \tag{2.10}$$

is the heat flux density. Note that bold symbols normally represent column vectors which means that in (2.7) the operation $\mathbf{u}_s \mathbf{u}_s^\top$ results in a 3×3 matrix. In (2.6), the right-hand side (contribution from collision operator) is zero if we deal with collisions that do not change the number of particles, e.g. by ionization or recombination processes. In (2.7) and (2.8),

only collisions between different particle species play a role because elastic collisions between indistinguishable particles of the same species do not change momentum and energy. Hence, in the expressions for the collisional friction force and heat exchange

$$\mathbf{R}_s := \int_{\mathbb{R}^3} m_s \mathbf{v}' C_{ss'} \, \mathrm{d}^3 v \,, \qquad Q_s := \int_{\mathbb{R}^3} \frac{m_s (v')^2}{2} \, C_{ss'} \, \mathrm{d}^3 v \,, \tag{2.11}$$

respectively, only collision between unlike particles play a role ($s' \neq s$).

It is immediately clear that equations (2.6)-(2.8) do not form a closed system of equations consisting of as many unknowns as equations because the p-th moment equation depends explicitly on the $(p+1)$-th moment of the distribution function. Finding an appropriate *closure* is therefore needed if a macroscopic fluid description is desired. This *fluid closure* essentially consists of finding adequate relations for the pressure tensor (2.9) and the heat flux density (2.10) in terms of the lower order moments n_s, $\mathbf{u}_s$ and T_s. The way this is done essentially defines the accuracy of the used fluid model compared to the full kinetic description. In principle, there are two classes of closure schemes. The more systematic and rigorous one is the class of asymptotic schemes in which the existence of some small parameter $\epsilon \ll 1$ is exploited and the distribution function is written as $f_s = \mathcal{M}_s + \epsilon f_s^{(1)} + \mathcal{O}(\epsilon^2)$. The Maxwellian $\mathcal{M}_s$ is given by

$$\mathcal{M}_s(\mathbf{x}, \mathbf{v}, t) := n_s(\mathbf{x}, t) \left(\frac{m_s}{2\pi T_s(\mathbf{x}, t)} \right)^{3/2} \exp \left[- \frac{m_s (\mathbf{v} - \mathbf{u}_s(\mathbf{x}, t))^2}{2 T_s(\mathbf{x}, t)} \right] , \tag{2.12}$$

and satisfies the moment equations (2.4). The expansion around a Maxwellian is based upon the fact that any non-Maxwellian distribution function will relax to (2.12) for sufficiently long times due to thermalizing collisions. The next step is then to formulate a hierarchy of linearized kinetic equations with the aim to obtain approximate solutions for the higher-order corrections in the power series in terms of the lower-order ones [84]. A prominent example for this procedure is the one by Braginskii [85] who used an asymptotic scheme to systematically derive transport coefficients from a microscopic collisional theory.

The other class of closure schemes, which shall be used in the following, is the one of so-called truncation schemes, where higher-order moments of the distribution function are simply assumed to be small and therefore negligible. In fact, the assumption of local thermal equilibrium, meaning that the distribution function is essentially given by (2.12), greatly simplifies (2.6)-(2.8) because the viscosity tensor $\mathbb{\Pi}_s = 0$ such that the pressure tensor $\mathbb{P}_s = p_s \mathbb{1}$ is diagonal with the scalar pressure $p_s = n_s T_s$ being the well-known expression for the pressure of an ideal gas. Moreover, there is no heat flux density related to a Maxwellian. The concept of local thermal equilibrium is based on the assumption of high collisionality which is usually **not** justified in fusion plasmas. This is, however, in contradiction with the good agreement of fluid approximations with experimental results related to the macroscopic plasma behavior. Freidberg [71, 86] argues that at least perpendicular to the magnetic field, the high collisionality assumption is justified because charged particles are attached to the field lines according to their gyro-motion and therefore have a strongly reduced mobility in this direction. This is a similar effect as for collisions. Hence, high collisionality can be assumed in perpendicular direction but certainly not in parallel direction where particles can move freely and usually have much larger mean free paths than the system size. After some straightforward manipulations, while using

the just stated simplifications, (2.6)-(2.8) reduce to

$$\frac{\partial n_s}{\partial t} + \nabla \cdot (n_s \mathbf{u}_s) = 0\,, \tag{2.13}$$

$$m_s n_s \left[\frac{\partial \mathbf{u}_s}{\partial t} + (\mathbf{u}_s \cdot \nabla)\,\mathbf{u}_s\right] + \nabla p_s = \rho_s\,(\mathbf{E} + \mathbf{u}_s \times \mathbf{B}) + \mathbf{R}_s\,, \tag{2.14}$$

$$\frac{\partial p_s}{\partial t} + \nabla \cdot (p_s \mathbf{u}_s) + (\gamma - 1)\, p_s \nabla \cdot \mathbf{u}_s = Q_s\,, \tag{2.15}$$

which has the form of Euler equations in hydrodynamics for neutral fluids supplemented with the Lorentz force due to the existence of electromagnetic fields. In (2.15), $\gamma = 5/3$ is the heat capacity ratio of an ideal gas with three spatial degrees of freedom.

As a next step, the two-fluid description for thermal electrons and ions is transformed to a one-fluid description combined with contributions from the energetic ion species. The first important assumption in this regard is the one of quasineutrality, meaning that the total charge density $\rho = \rho_\mathrm{e} + \rho_\mathrm{i} + \rho_\mathrm{h} = 0$. This assumption is satisfied if the wave frequencies of interest are much smaller than the electron plasma frequency ($\omega \ll \Omega_\mathrm{pe}$) such that the electrons have enough time to respond to any charge separation leading to a formation of an electric field which tries to cancel the formed charged separation. The second assumption is that the phase velocities of the considered waves are much smaller than the speed of light ($\omega/k \ll c$). This results in a simplification of Ampère's law (2.2a) by neglecting the displacement current. To obtain a one-fluid description, we define the bulk mass density and the bulk velocity

$$\rho_\mathrm{b} := \sum_{s=\mathrm{e,i}} m_\mathrm{s} n_\mathrm{s} \approx m_\mathrm{i} n_\mathrm{i}\,, \qquad \rho_\mathrm{b}\mathbf{U} := \sum_{s=\mathrm{e,i}} m_\mathrm{s} n_\mathrm{s} \mathbf{u}_s \approx m_\mathrm{i} n_\mathrm{i} \mathbf{u}_\mathrm{i}\,, \tag{2.16}$$

respectively, where the approximations are due to the smallness of the electron mass compared to the ion mass ($m_\mathrm{e} \ll m_\mathrm{i}$). Taking now the sum of each equation for $s = \mathrm{e,i}$ and neglecting the electron inertia ($m_\mathrm{e} \to 0$) in the momentum equation (2.14) yields

$$\frac{\partial \rho_\mathrm{b}}{\partial t} + \nabla \cdot (\rho_\mathrm{b} \mathbf{U}) = 0\,, \tag{2.17}$$

$$\rho_\mathrm{b} \left[\frac{\partial \mathbf{U}}{\partial t} + (\mathbf{U} \cdot \nabla)\,\mathbf{U}\right] + \nabla p = -\rho_\mathrm{h}\mathbf{E} + (\mathbf{J} - \mathbf{J}_\mathrm{h}) \times \mathbf{B}\,, \tag{2.18}$$

$$\frac{\partial p}{\partial t} + \nabla \cdot (p\,\mathbf{U}) + (\gamma - 1)\, p \nabla \cdot \mathbf{U} = 0\,, \tag{2.19}$$

where $p = p_\mathrm{e} + p_\mathrm{i}$ is the bulk pressure, $\mathbf{J} = \rho_\mathrm{e}\mathbf{u}_\mathrm{e} + \rho_\mathrm{i}\mathbf{u}_\mathrm{i} + \rho_\mathrm{h}\mathbf{u}_\mathrm{h}$ the total current and $\mathbf{R}_\mathrm{e} = -\mathbf{R}_\mathrm{i}$ and $Q_\mathrm{e} = -Q_\mathrm{i}$ has been used; a consequence of momentum and energy conservation in elastic collisions. To close the system of equations, a defining equation for the electric field is needed. This is obtained from the momentum balance equation for electrons upon neglecting once more the electron inertia. This leads to a generalized Ohm's law of the form

$$\begin{aligned} \mathbf{E} = -\mathbf{u}_\mathrm{e} \times \mathbf{B} + \frac{1}{\rho_\mathrm{e}} \nabla p_\mathrm{e} - \frac{1}{\rho_\mathrm{e}} \mathbf{R}_\mathrm{e} \\ = -\left(\frac{\rho_\mathrm{i}\mathbf{u}_\mathrm{i} + \rho_\mathrm{h}\mathbf{u}_\mathrm{h}}{q_\mathrm{i} n_\mathrm{i} + q_\mathrm{h} n_\mathrm{h}}\right) \times \mathbf{B} - \frac{1}{\rho_\mathrm{e}} (\mathbf{J} \times \mathbf{B}) + \frac{1}{\rho_\mathrm{e}} \nabla p_\mathrm{e} - \frac{1}{\rho_\mathrm{e}} \mathbf{R}_\mathrm{e}\,. \end{aligned} \tag{2.20}$$

The assumption made in ideal MHD is that the last three terms (Hall term, electron pressure gradient and resistive term) are small compared to the first one. Regarding the first term, we

have an additional contribution from the energetic ions compared to classical ideal MHD. This means that the magnetic field is not frozen into the bulk mean velocity but actually into the center-of mass mean velocity of bulk plasma and energetic ions. However, if one assumes that the energetic ion mean velocity $\mathbf{u}_\mathrm{h}$ is smaller or at most comparable to the bulk ion mean velocity $\mathbf{u}_\mathrm{i}$ and that energetic ions are a minority species such that $\rho_\mathrm{h} \ll \rho_\mathrm{i}$, these two velocities are almost the same. This leads to the simplified form

$$\mathbf{E} = -\mathbf{U} \times \mathbf{B}\,, \tag{2.21}$$

which is the well-known Ohm's law used in ideal MHD. Together with the Vlasov equation for the energetic ions and Maxwell's equations (2.2) without the displacement current, we finally end up with the hybrid MHD-Vlasov model

$$\text{Ideal MHD} \begin{cases} \dfrac{\partial \rho_\mathrm{b}}{\partial t} + \nabla \cdot (\rho_\mathrm{b} \mathbf{U}) = 0\,, & \text{(2.22a)} \\ \rho_\mathrm{b} \left[\dfrac{\partial \mathbf{U}}{\partial t} + (\mathbf{U} \cdot \nabla)\, \mathbf{U} \right] + \nabla p = \rho_\mathrm{h} (\mathbf{U} \times \mathbf{B}) + \left[\dfrac{1}{\mu_0} (\nabla \times \mathbf{B}) - \mathbf{J}_\mathrm{h} \right] \times \mathbf{B}\,, & \text{(2.22b)} \\ \dfrac{\partial p}{\partial t} + \nabla \cdot (p\, \mathbf{U}) + (\gamma - 1)\, p \nabla \cdot \mathbf{U} = 0\,, & \text{(2.22c)} \\ \dfrac{\partial \mathbf{B}}{\partial t} = \nabla \times (\mathbf{U} \times \mathbf{B})\,, \qquad \nabla \cdot \mathbf{B} = 0\,, & \text{(2.22d)} \end{cases}$$

$$\text{EPs} \begin{cases} \dfrac{\partial f_\mathrm{h}}{\partial t} + \mathbf{v} \cdot \nabla f_\mathrm{h} + \dfrac{q_\mathrm{h}}{m_\mathrm{h}} (\mathbf{B} \times \mathbf{U} + \mathbf{v} \times \mathbf{B}) \cdot \nabla_\mathbf{v} f_\mathrm{h} = 0\,, & \text{(2.22e)} \\ \rho_\mathrm{h} = q_\mathrm{h} \displaystyle\int_{\mathbb{R}^3} f_\mathrm{h}\, \mathrm{d}^3 v\,, \qquad \mathbf{J}_\mathrm{h} = q_\mathrm{h} \int_{\mathbb{R}^3} \mathbf{v} f_\mathrm{h}\, \mathrm{d}^3 v\,, & \text{(2.22f)} \end{cases}$$

composed of ideal MHD for the bulk plasma and Vlasov equations for the energetic ions (EPs). This model belongs to the class of current-coupling hybrid models which is evident from the fact that the hot current density $\mathbf{J}_\mathrm{h}$ appears explicitly in the momentum balance equation (2.22b). Moreover, it was shown that this model possesses a non-canonical Hamiltonian structure meaning that it can be derived from a Poisson bracket together with a suitable Hamiltonian [39]. As already mentioned in the introduction, an alternative modeling approach is formed by the class of pressure-coupling hybrid models, where a three-species plasma is modeled as a single charged fluid such that the sums in (2.16) would include the energetic species $s = \mathrm{h}$. This has the consequence that in the momentum balance equation (2.22b) one would find the gradient of the EP pressure tensor $\nabla \cdot \mathbb{P}_\mathrm{h}$ instead of ρ_h and $\mathbf{J}_\mathrm{h}$.

As a next step, let us note some important properties of the model (2.22):

- Conservation of divergence-free constraint for the magnetic field:

$$\frac{\partial}{\partial t} (\nabla \cdot \mathbf{B}) = 0\,. \tag{2.23}$$

- Conservation of the total mass:

$$\frac{\mathrm{d}}{\mathrm{d}t} M(t) = \frac{\mathrm{d}}{\mathrm{d}t} \left(\int_\Omega \rho_\mathrm{b}\, \mathrm{d}^3 x + m_\mathrm{h} \int_\Omega \int_{\mathbb{R}^3} f_\mathrm{h}\, \mathrm{d}^3 v\, \mathrm{d}^3 x \right) = 0\,. \tag{2.24}$$

- Conservation of the total momentum:

$$\frac{\mathrm{d}}{\mathrm{d}t} \mathbf{P}(t) = \frac{\mathrm{d}}{\mathrm{d}t} \left(\int_\Omega \rho_\mathrm{b}\, \mathbf{U}\, \mathrm{d}^3 x + m_\mathrm{h} \int_\Omega \int_{\mathbb{R}^3} \mathbf{v} f_\mathrm{h}\, \mathrm{d}^3 v\, \mathrm{d}^3 x \right) = 0\,. \tag{2.25}$$

- Conservation of the total energy:

$$\frac{\mathrm{d}}{\mathrm{d}t}\mathcal{H}(t) = \frac{\mathrm{d}}{\mathrm{d}t}\left(\frac{1}{2}\int_\Omega \rho_\mathrm{b}\, U^2\,\mathrm{d}^3x + \frac{1}{\gamma-1}\int_\Omega p\,\mathrm{d}^3x \right. \\ \left. + \frac{1}{2\mu_0}\int_\Omega B^2\,\mathrm{d}^3x + \frac{1}{2}\,m_\mathrm{h}\int_\Omega\int_{\mathbb{R}^3} v^2 f_\mathrm{h}\,\mathrm{d}^3v\,\mathrm{d}^3x\right) = 0\,. \tag{2.26}$$

The integrations are performed over some domain $\Omega \subset \mathbb{R}^3$. The first conservation property is straightforwardly given by Faraday's law (2.22d) because

$$\frac{\partial}{\partial t}\left(\nabla\cdot\mathbf{B}\right) = 0 = \nabla\cdot\frac{\partial\mathbf{B}}{\partial t} = \nabla\cdot\left[\,\nabla\times\left(\mathbf{U}\times\mathbf{B}\right)\right] = 0\,, \tag{2.27}$$

which is due to the well-known vector calculus identity $\mathrm{div}\,\mathrm{curl} = 0$. Hence, if the magnetic field is divergence-free at time $t = 0$ it will remain divergence-free for all times. In order to proof the energy theorem (2.26), we write the total energy $\mathcal{H}$ as the sum of the bulk kinetic energy $\mathcal{H}_U$, the bulk internal energy $\mathcal{H}_p$, the magnetic field energy $\mathcal{H}_B$ and the energetic ion energy $\mathcal{H}_\mathrm{h}$ and calculate the respective time evolutions separately. Terms of the form $\int_\Omega \nabla\cdot(\cdots)\,\mathrm{d}^3x$ will vanish because such integrals can be transformed to surface integrals via the divergence theorem which then vanish if we assume that either nothing flows in or out at the boundary $\partial\Omega$ or if we let the surface go to infinity where all fields must converge to zero. Let us start with the energies $\mathcal{H}_p$ and $\mathcal{H}_B$ for which we employ integration by parts (IP):

$$\frac{\mathrm{d}}{\mathrm{d}t}\mathcal{H}_p = \frac{1}{\gamma-1}\int_\Omega\frac{\partial p}{\partial t}\,\mathrm{d}^3x = -\int_\Omega p\,\nabla\cdot\mathbf{U}\,\mathrm{d}^3x \overset{\mathrm{IP}}{=} \int_\Omega \mathbf{U}\cdot\nabla p\,\mathrm{d}^3x\,, \tag{2.28}$$

$$\frac{\mathrm{d}}{\mathrm{d}t}\mathcal{H}_B = \frac{1}{\mu_0}\int_\Omega \mathbf{B}\cdot\frac{\partial\mathbf{B}}{\partial t}\,\mathrm{d}^3x = \frac{1}{\mu_0}\int_\Omega \mathbf{B}\cdot\left[\,\nabla\times\left(\mathbf{U}\times\mathbf{B}\right)\right]\mathrm{d}^3x \\ \overset{\mathrm{IP}}{=} -\frac{1}{\mu_0}\int_\Omega\left[\,\left(\nabla\times\mathbf{B}\right)\times\mathbf{B}\,\right]\cdot\mathbf{U}\,\mathrm{d}^3x\,. \tag{2.29}$$

In the last step we used the fact that the triple product $(\mathbf{U}\times\mathbf{B})\cdot(\nabla\times\mathbf{B})$ is invariant under cyclic permutations. For the bulk kinetic energy we use the identity $(\mathbf{U}\cdot\nabla)\,\mathbf{U} = \nabla U^2/2 - \mathbf{U}\times(\nabla\times\mathbf{U})$ and the fact that terms of the form $[\,\mathbf{U}\times(\cdots)\,]\cdot\mathbf{U}$ are equal to zero:

$$\frac{\mathrm{d}}{\mathrm{d}t}\mathcal{H}_U = \frac{1}{2}\int_\Omega\frac{\partial\rho_\mathrm{b}}{\mathrm{d}t}\,U^2\,\mathrm{d}^3x + \int_\Omega\left(\rho_\mathrm{b}\,\frac{\partial\mathbf{U}}{\partial t}\right)\cdot\mathbf{U}\,\mathrm{d}^3x \\ = -\frac{1}{2}\int_\Omega U^2\,\nabla\cdot\left(\rho_\mathrm{b}\mathbf{U}\right)\mathrm{d}^3x - \frac{1}{2}\int_\Omega\rho_\mathrm{b}\nabla U^2\,\mathrm{d}^3x - \int_\Omega\mathbf{U}\cdot\nabla p\,\mathrm{d}^3x \\ + \frac{1}{\mu_0}\int_\Omega\left[\,\left(\nabla\times\mathbf{B}\right)\times\mathbf{B}\,\right]\cdot\mathbf{U}\,\mathrm{d}^3x - \int_\Omega\left(\mathbf{J}_\mathrm{h}\times\mathbf{B}\right)\cdot\mathbf{U}\,\mathrm{d}^3x\,. \tag{2.30}$$

The first two terms cancel each other if integration by part is performed on the first term. The third and fourth term cancel with (2.28) and (2.29), respectively, which means that we obtain the intermediate result

$$\frac{\mathrm{d}}{\mathrm{d}t}\left(\mathcal{H}_U + \mathcal{H}_p + \mathcal{H}_B\right) = -\int_\Omega\left(\mathbf{J}_\mathrm{h}\times\mathbf{B}\right)\cdot\mathbf{U}\,\mathrm{d}^3x\,, \tag{2.31}$$

which represents the energy exchange between the bulk plasma and the energetic ions. Lastly, the time evolution of the energetic ion energy is given by the Vlasov equation and reads

$$\begin{aligned}\frac{\mathrm{d}}{\mathrm{d}t}\mathcal{H}_\mathrm{h} &= \frac{1}{2}\,m_\mathrm{h}\int_\Omega\int_{\mathbb{R}^3} v^2\frac{\partial f_\mathrm{h}}{\partial t}\,\mathrm{d}^3v\,\mathrm{d}^3x \\ &= -\frac{1}{2}\,m_\mathrm{h}\int_\Omega\int_{\mathbb{R}^3} v^2\left[\mathbf{v}\cdot\nabla f_\mathrm{h} + \frac{q_\mathrm{h}}{m_\mathrm{h}}(\,\mathbf{B}\times\mathbf{U}+\mathbf{v}\times\mathbf{B})\cdot\nabla_\mathbf{v} f_\mathrm{h}\right]\mathrm{d}^3v\,\mathrm{d}^3x\,.\end{aligned} \tag{2.32}$$

The first term $v^2\,\mathbf{v}\cdot\nabla f_\mathrm{h}$ can be written as $\nabla\cdot(v^2\,\mathbf{v}f_\mathrm{h})$ ($\mathbf{x}$ and $\mathbf{v}$ are independent variables) and therefore vanishes after integrating over $\mathbf{x}$. The third terms vanishes after integration by parts in $\mathbf{v}$ because $\nabla_\mathbf{v}\cdot(\mathbf{v}\times\mathbf{B})=0$. Performing integration by parts in $\mathbf{v}$ as well on the second term and noting that $\nabla_\mathbf{v}\cdot[\,v^2\,(\mathbf{B}\times\mathbf{U})\,] = 2\,\mathbf{v}\,(\mathbf{B}\times\mathbf{U})$ leads to

$$\frac{\mathrm{d}}{\mathrm{d}t}\mathcal{H}_\mathrm{h} = q_\mathrm{h}\int_\Omega\int_{\mathbb{R}^3}(\mathbf{B}\times\mathbf{U})\cdot\mathbf{v}f_\mathrm{h}\,\mathrm{d}^3v\,\mathrm{d}^3x = \int_\Omega(\mathbf{J}_\mathrm{h}\times\mathbf{B})\cdot\mathbf{U}\,\mathrm{d}^3x\,, \tag{2.33}$$

where the definition of the current density (2.22f) and once more the invariance of the vector triple product under cyclic permutation has been used in the last step. Hence, (2.33) cancels (2.31) and in summary we showed that

$$\frac{\mathrm{d}}{\mathrm{d}t}\mathcal{H} = \frac{\mathrm{d}}{\mathrm{d}t}\left(\mathcal{H}_U+\mathcal{H}_p+\mathcal{H}_B+\mathcal{H}_\mathrm{h}\right) = 0\,. \tag{2.34}$$

The proofs for the conservation of the total mass (2.24) and the total momentum (2.25) work in a similar fashion which is why they are not presented explicitly.

2.2 Normalization

In order to "eliminate" physical constants like the vacuum permeability μ_0 and because in numerical simulations that are based on floating point operations it is beneficial to work with quantities that are of order one, we normalize all unknowns in (2.22) to some characteristic value which we denote by bars. In particular, length scales are normalized to some characteristic length $\bar{L}$ and time scales to the Alfvén time $\bar{\tau}_\mathrm{A} = \bar{L}/\bar{v}_\mathrm{A}$:

$$\begin{aligned}&\mathbf{x} = \mathbf{x}'\,\bar{L} \quad\Rightarrow\quad \nabla = \frac{1}{\bar{L}}\nabla'\,,\\ &t = t'\,\bar{\tau}_\mathrm{A} \quad\Rightarrow\quad \frac{\partial}{\partial t} = \frac{1}{\bar{\tau}_\mathrm{A}}\frac{\partial}{\partial t'}\,, \qquad \bar{v}_\mathrm{A} = \frac{\bar{B}}{\sqrt{\mu_0 A_\mathrm{b} m_\mathrm{p}\bar{n}_\mathrm{b}}}\,,\\ &\mathbf{B} = \mathbf{B}'\bar{B}\,, \qquad \rho_\mathrm{b} = n'_\mathrm{b}A_\mathrm{b}m_\mathrm{p}\bar{n}_\mathrm{b}\,, \qquad p = p'\frac{\bar{B}^2}{\mu_0}\,, \qquad \mathbf{U} = \mathbf{U}'\bar{v}_\mathrm{A}\,,\\ &f_\mathrm{h} = f'_\mathrm{h}\frac{\bar{n}_\mathrm{h}}{\bar{v}_\mathrm{A}^3}\,, \qquad \rho_\mathrm{h} = Z_\mathrm{h}e\,n'_\mathrm{h}\bar{n}_\mathrm{h} =: Z_\mathrm{h}e\,\rho'_\mathrm{h}\bar{n}_\mathrm{h}\,, \qquad \mathbf{J}_\mathrm{h} = Z_\mathrm{h}e\,n'_\mathrm{h}\,\boldsymbol{U}'_\mathrm{h}\,\bar{n}_\mathrm{h}\bar{v}_\mathrm{A} =: Z_\mathrm{h}e\,\mathbf{J}'_\mathrm{h}\,\bar{n}_\mathrm{h}\bar{v}_\mathrm{A}\,.\end{aligned}$$

More specifically, we choose $\bar{L} = 1\,\mathrm{m}$ and $\bar{B} = 1\,\mathrm{T}$ which are typical orders of magnitude of present fusion devices. Other works often use $\bar{L} = R_0$ and $\bar{B} = B_{\mathrm{T}0}$ instead, where R_0 is the major radius of the considered toroidal device and $B_{\mathrm{T}0}$ the magnetic field at the magnetic axis. However, in this work, we do not want to restrict ourselves to toroidal geometries and hence keep

the former choice. Plugging the given normalizations in (2.22) yields the normalized version

$$\text{Ideal MHD}\begin{cases} \dfrac{\partial n_{\mathrm{b}}'}{\partial t'} + \nabla' \cdot (n_{\mathrm{b}}' \mathbf{U}') = 0\,, & \text{(2.35a)} \\ n_{\mathrm{b}}' \left[\dfrac{\partial \mathbf{U}'}{\partial t'} + (\mathbf{U}' \cdot \nabla')\,\mathbf{U}' \right] + \nabla' p' = \nu_{\mathrm{h}} \dfrac{Z_{\mathrm{h}}}{A_{\mathrm{b}}} \kappa\, \rho_{\mathrm{h}}' \,(\mathbf{U}' \times \mathbf{B}') \\ \qquad\qquad + \left[(\nabla' \times \mathbf{B}') - \nu_{\mathrm{h}} \dfrac{Z_{\mathrm{h}}}{A_{\mathrm{b}}} \kappa\, \mathbf{J}_{\mathrm{h}}' \right] \times \mathbf{B}'\,, & \text{(2.35b)} \\ \dfrac{\partial p'}{\partial t'} + \nabla' \cdot (p'\,\mathbf{U}') + (\gamma - 1)\, p'\, \nabla' \cdot \mathbf{U}' = 0\,, & \text{(2.35c)} \\ \dfrac{\partial \mathbf{B}'}{\partial t'} = \nabla' \times (\mathbf{U}' \times \mathbf{B}')\,, \qquad \nabla' \cdot \mathbf{B}' = 0\,, & \text{(2.35d)} \end{cases}$$

$$\text{EPs}\begin{cases} \dfrac{\partial f_{\mathrm{h}}'}{\partial t'} + \mathbf{v}' \cdot \nabla' f_{\mathrm{h}}' + \dfrac{Z_{\mathrm{h}}}{A_{\mathrm{h}}} \kappa\, (\mathbf{B}' \times \mathbf{U}' + \mathbf{v}' \times \mathbf{B}') \cdot \nabla_{\mathbf{v}'} f_{\mathrm{h}}' = 0\,, & \text{(2.35e)} \\ \rho_{\mathrm{h}}' = \displaystyle\int_{\mathbb{R}^3} f_{\mathrm{h}}'\, \mathrm{d}^3 v'\,, \qquad \mathbf{J}_{\mathrm{h}}' = \int_{\mathbb{R}^3} f_{\mathrm{h}}' \mathbf{v}'\, \mathrm{d}^3 v'\,, & \text{(2.35f)} \end{cases}$$

i.e. the mass continuity, pressure and induction equation in the MHD system remain "unchanged". In the momentum balance equation (2.35b) and the Vlasov equation (2.35e), the two new important dimensionless parameters $\nu_{\mathrm{h}} := \bar{n}_{\mathrm{h}}/\bar{n}_{\mathrm{b}}$ and $\kappa := \bar{\Omega}_{\mathrm{cp}}\, \bar{\tau}_{\mathrm{A}}$ ($\kappa \sim \sqrt{A_{\mathrm{b}}\, \bar{n}_{\mathrm{b}}}$) are the ratio of characteristic hot/bulk number densities and the product of proton cyclotron frequency $\bar{\Omega}_{\mathrm{cp}} = e\bar{B}/m_{\mathrm{p}}$ with the Alfvén time, respectively. For fusion plasmas one typically has $\nu_{\mathrm{h}} \ll 1$ (low-density energetic particles) and $\kappa \gg 1$ (Alfvén frequencies much smaller than ion cyclotron frequency). Moreover, if the conserved Hamiltonian $\mathcal{H} = \mathcal{H}'\bar{\mathcal{H}}$ in (2.26) is normalized to the characteristic energy $\bar{\mathcal{H}} = A_{\mathrm{b}} m_{\mathrm{p}}\, \bar{n}_{\mathrm{b}}\, \bar{L}^3\, \bar{v}_{\mathrm{A}}^2$, we find the normalized Hamiltonian

$$\mathcal{H}'(t) = \frac{1}{2} \int_{\Omega'} n_{\mathrm{b}}' \,(U')^2\, \mathrm{d}^3 x' + \frac{1}{\gamma - 1} \int_{\Omega'} p'\, \mathrm{d}^3 x' + \frac{1}{2} \int_{\Omega'} (B')^2\, \mathrm{d}^3 x' + \frac{1}{2}\, \nu_{\mathrm{h}} \frac{A_{\mathrm{h}}}{A_{\mathrm{b}}} \int_{\Omega'} \int_{\mathbb{R}^3} f_{\mathrm{h}}'(v')^2\, \mathrm{d}^3 v'\, \mathrm{d}^3 x'\,. \tag{2.36}$$

In what follows, we shall work with the dimension-less equations (2.35)-(2.36). We therefore drop all primes in order to improve readability (e.g. $\mathbf{U}' \to \mathbf{U}$ or $f_{\mathrm{h}}' \to f_{\mathrm{h}}$). As a consequence of the chosen normalization, if ones wants to convert back to physical (SI) units, one just has to specify values for the bulk mass number A_{b} (e.g. $A_{\mathrm{b}} = 1$ for a hydrogen bulk plasma or $A_{\mathrm{b}} = 2$ for a deuterium bulk plasma) and the characteristic bulk number density $\bar{n}_{\mathrm{b}}$ since this sets the value for the characteristic Alfvén velocity $\bar{v}_{\mathrm{A}}$.

2.3 Linearization of the MHD part

As mentioned in the introduction, we shall neglect MHD non-linearities in this thesis and focus on the coupling to the kinetic ions since this is enough to describe Alfvén eigenmodes and their linear and non-linear interactions with EPs. Therefore, the MHD equations are linearized about a zero-flow equilibrium characterized by the ansatzes $n_{\mathrm{b}} = n_{\mathrm{b,eq}} + \tilde{n}_{\mathrm{b}}$, $\mathbf{U} = \tilde{\mathbf{U}}$, $p = p_{\mathrm{eq}} + \tilde{p}$ and $\mathbf{B} = \mathbf{B}_{\mathrm{eq}} + \tilde{\mathbf{B}}$, where the quantities with tildes are small perturbations of the equilibrium state denoted by the subscript $(\cdot)_{\mathrm{eq}}$. Plugging these ansatzes into the normalized model equations

and neglecting MHD non-linearities yields

$$\text{Ideal MHD} \begin{cases} n_{\mathrm{b,eq}} \dfrac{\partial \tilde{\mathbf{U}}}{\partial t} + \nabla \tilde{p} = (\nabla \times \tilde{\mathbf{B}}) \times \mathbf{B}_{\mathrm{eq}} + \mathbf{J}_{\mathrm{eq}} \times \tilde{\mathbf{B}} \\ \qquad\qquad + \nu_{\mathrm{h}} \dfrac{Z_{\mathrm{h}}}{A_{\mathrm{b}}} \kappa \, (\rho_{\mathrm{h}} \tilde{\mathbf{U}} - \mathbf{J}_{\mathrm{h}}) \times (\mathbf{B}_{\mathrm{eq}} + \tilde{\mathbf{B}}) \,, & \text{(2.37a)} \\ \dfrac{\partial \tilde{p}}{\partial t} + (\gamma - 1) \, \nabla \cdot (p_{\mathrm{eq}} \, \tilde{\mathbf{U}}) + p_{\mathrm{eq}} \nabla \cdot \tilde{\mathbf{U}} = 0 \,, & \text{(2.37b)} \\ \dfrac{\partial \tilde{\mathbf{B}}}{\partial t} = \nabla \times (\, \tilde{\mathbf{U}} \times \mathbf{B}_{\mathrm{eq}} \,) \,, \qquad \nabla \cdot \tilde{\mathbf{B}} = 0 \,, & \text{(2.37c)} \end{cases}$$

$$\text{EPs} \begin{cases} \dfrac{\partial f_{\mathrm{h}}}{\partial t} + \mathbf{v} \cdot \nabla f_{\mathrm{h}} + \dfrac{Z_{\mathrm{h}}}{A_{\mathrm{h}}} \kappa \Big[(\mathbf{B}_{\mathrm{eq}} + \tilde{\mathbf{B}}) \times \tilde{\mathbf{U}} \\ \qquad\qquad + \mathbf{v} \times (\mathbf{B}_{\mathrm{eq}} + \tilde{\mathbf{B}}) \Big] \cdot \nabla_{\mathbf{v}} f_{\mathrm{h}} = 0 \,, & \text{(2.37d)} \\ \rho_{\mathrm{h}} = \displaystyle\int_{\mathbb{R}^3} f_{\mathrm{h}} \, \mathrm{d}^3 v \,, \qquad \mathbf{J}_{\mathrm{h}} = \int_{\mathbb{R}^3} f_{\mathrm{h}} \mathbf{v} \, \mathrm{d}^3 v \,, & \text{(2.37e)} \end{cases}$$

where $\mathbf{J}_{\mathrm{eq}} = \nabla \times \mathbf{B}_{\mathrm{eq}}$ is the equilibrium current. The mass continuity equation (2.35a) is removed from the system because in the linearized momentum balance equation (2.37a) only the equilibrium number density $n_{\mathrm{b,eq}}$ appears. A consequence of the linarization is, however, that the Hamiltonian $\mathcal{H}$ given in (2.36) is no longer a conserved quantity. Instead, the new quantity

$$\tilde{\mathcal{H}}(t) := \frac{1}{2} \int_\Omega n_{\mathrm{b,eq}} \, \tilde{U}^2 \, \mathrm{d}^3 x + \frac{1}{\gamma - 1} \int_\Omega \tilde{p} \, \mathrm{d}^3 x + \frac{1}{2} \int_\Omega \tilde{B}^2 \, \mathrm{d}^3 x + \frac{1}{2} \, \nu_{\mathrm{h}} \frac{A_{\mathrm{h}}}{A_{\mathrm{b}}} \int_\Omega \int_{\mathbb{R}^3} f_{\mathrm{h}} v^2 \, \mathrm{d}^3 v \, \mathrm{d}^3 x \,, \tag{2.38}$$

evolves in time as

$$\frac{\mathrm{d}\tilde{\mathcal{H}}}{\mathrm{d}t} = \int_\Omega (\mathbf{J}_{\mathrm{eq}} \times \mathbf{B}) \cdot \mathbf{U} \, \mathrm{d}^3 x - \int_\Omega (p_{\mathrm{eq}} - \tilde{p}) \nabla \cdot \mathbf{U} \, \mathrm{d}^3 x \,. \tag{2.39}$$

Consequently, $\tilde{\mathcal{H}}$ is only conserved for incompressible waves ($\nabla \cdot \mathbf{U} = 0$) and if additionally, there is no equilibrium current ($\mathbf{J}_{\mathrm{eq}} = 0$) or the perturbed velocity field is directed perpendicular to the Hall term $\mathbf{J}_{\mathrm{eq}} \times \mathbf{B}$. The former is particularly true for shear Alfvén waves. It should be noted, however, that the energy balance of the energy exchange between the bulk and the energetic ions is still intact. Finally, as in Section 2.2, the tildes shall be dropped in what follows in order to improve readability ($\tilde{\mathbf{U}} \to \mathbf{U}$, $\tilde{p} \to p$ and $\tilde{\mathbf{B}} \to \mathbf{B}$). Model (2.37) is the final model which is considered in this thesis.

2.4 Linear dispersion relation for a uniform plasma

To better understand the basics physics contained in the hybrid model (2.37), we derive in the following a linear dispersion relation for the case of an infinitely extended, uniform, homogeneously magnetized bulk plasma and a spatially uniform energetic ion distribution function. The result will also serve for code verification by comparing simulations results with the analytical expectations obtained from the dispersion relation.

For this purpose, all remaining non-linear terms in (2.37) are linearized in the same manner as in Section 2.3, i.e. we set $f_\mathrm{h} = f_\mathrm{h,eq} + \tilde{f}_\mathrm{h}$ and neglect non-linear terms in (2.37a) and (2.37d). Moreover, because we consider a spatially uniform energetic ion distribution function, $f_\mathrm{h,eq} = f_\mathrm{h,eq}(\mathbf{v})$ is a function of velocity coordinates only. Finally, since all the information regarding the bulk and energetic number densities is encoded in the ν_h parameter in case of spatially homogeneous densities, we can set without loss of generality $n_\mathrm{b,eq} = 1$ and $\rho_\mathrm{h,eq} = \int_{\mathbb{R}^3} f_\mathrm{h,eq}\,\mathrm{d}^3v = 1$. The fully normalized momentum balance equation (2.37a) and Vlasov equation (2.37d) then read

$$\frac{\partial \mathbf{U}}{\partial t} + \nabla p = (\nabla \times \mathbf{B}) \times \mathbf{B}_\mathrm{eq} + \nu_\mathrm{h} \frac{Z_\mathrm{h}}{A_\mathrm{b}} \kappa \,(\mathbf{U} \times \mathbf{B}_\mathrm{eq}) - \nu_\mathrm{h} \frac{Z_\mathrm{h}}{A_\mathrm{b}} \kappa \,(\mathbf{J}_\mathrm{h,eq} \times \mathbf{B} + \mathbf{J}_\mathrm{h} \times \mathbf{B}_\mathrm{eq})\,, \tag{2.40}$$

$$\frac{\partial f_\mathrm{h}}{\partial t} + \mathbf{v} \cdot \nabla f_\mathrm{h} + \frac{Z_\mathrm{h}}{A_\mathrm{h}} \kappa \,(\mathbf{v} \times \mathbf{B}_\mathrm{eq}\,) \cdot \nabla_\mathbf{v} f_\mathrm{h} = -\frac{Z_\mathrm{h}}{A_\mathrm{h}} \kappa \,(\,\mathbf{B}_\mathrm{eq} \times \mathbf{U} + \mathbf{v} \times \mathbf{B}\,) \cdot \nabla_\mathbf{v} f_\mathrm{h,eq}\,, \tag{2.41}$$

$$\mathbf{J}_\mathrm{h} = \int_{\mathbb{R}^3} \mathbf{v} f_\mathrm{h}\,\mathrm{d}^3v\,, \tag{2.42}$$

where the tilde for the perturbed distribution function has been dropped ($\tilde{f}_\mathrm{h} \to f_\mathrm{h}$). Regarding the equilibrium EP current, the assumptions made up to this point imply $\mathbf{J}_\mathrm{h,eq} = const. \equiv \mathbf{v}_0$. However, if we align the coordinate system in a way that the magnetic field points in the z-direction ($\mathbf{B}_\mathrm{eq} = B_0\,\mathbf{e}_z$), the equilibrium EP current must also point in z-direction ($\mathbf{J}_\mathrm{h,eq} = v_0\,\mathbf{e}_z$) in order to satisfy the equilibrium condition $\mathbf{J}_\mathrm{h,eq} \times \mathbf{B}_\mathrm{eq} = 0$. Lastly, we only consider wave propagation parallel to the magnetic field. Hence, the ansatz for all perturbed quantities is $\hat{A}\,\mathrm{e}^{i(kz-\omega t)}$ for $A = \mathbf{U}$, p, $\mathbf{B}$ and f_h such that derivatives can be replaced according to $\partial/\partial t \to -i\omega$ and $\nabla \to ik\,\mathbf{e}_z$.

The first step in the derivation of the dispersion relation is to note that the equilibrium distribution function $f_\mathrm{h,eq}$ must be rotationally symmetric around the magnetic field in velocity space, i.e. $f_\mathrm{h,eq} = f_\mathrm{h,eq}(v_\perp, v_\parallel)$ if cylindrical coordinates $\mathbf{v} = (v_\perp \cos v_\theta, v_\perp \sin v_\theta, v_\parallel)$ are used. This is a direct consequence of the equilibrium Vlasov equation $(\mathbf{v} \times \mathbf{B}_\mathrm{eq}) \cdot \nabla_\mathbf{v} f_\mathrm{h,eq} = 0$ which can only be satisfied for $\partial f_\mathrm{h,eq}/\partial v_\theta = 0$. Then the solution of the linearized Vlasov equation (2.41) is given by

$$\begin{aligned}
\hat{f}_\mathrm{h} = &-\frac{Z_\mathrm{h}}{A_\mathrm{h}} \kappa \frac{\hat{G} f_\mathrm{h,eq}}{\Omega_+ \Omega_-} \left[i(\omega - k v_\parallel) \cos v_\theta + \frac{B_0 Z_\mathrm{h}}{A_\mathrm{h}} \kappa \sin v_\theta \right] \hat{E}_x \\
&-\frac{Z_\mathrm{h}}{A_\mathrm{h}} \kappa \frac{\hat{G} f_\mathrm{h,eq}}{\Omega_+ \Omega_-} \left[i(\omega - k v_\parallel) \sin v_\theta - \frac{B_0 Z_\mathrm{h}}{A_\mathrm{h}} \kappa \cos v_\theta \right] \hat{E}_y \\
&-\frac{Z_\mathrm{h}}{A_\mathrm{h}} \kappa i \frac{1}{\omega - k v_\parallel} \frac{\partial f_\mathrm{h,eq}}{\partial v_\parallel} \hat{E}_z\,,
\end{aligned} \tag{2.43}$$

where $\Omega_\pm = \omega - k v_\parallel \pm B_0 Z_\mathrm{h} \kappa / A_\mathrm{h}$ and $\hat{\mathbf{E}} = \mathbf{B}_\mathrm{eq} \times \hat{\mathbf{U}}$. For a detailed derivation of this result see [83] for instance. The differential operator

$$\hat{G} := \frac{\partial}{\partial v_\perp} + \frac{k}{\omega} \left(v_\perp \frac{\partial}{\partial v_\parallel} - v_\parallel \frac{\partial}{\partial v_\perp} \right)\,, \tag{2.44}$$

can be seen as a measure for the anisotropy of the distribution function in velocity space with respect to the direction of the magnetic field $\mathbf{B}_\mathrm{eq}$.

Our aim is to express the linearized momentum balance equation (2.40) solely in terms of the perturbed velocity $\hat{\mathbf{U}}$. Therefore, we have to calculate the current $\hat{\mathbf{J}}_\mathrm{h}$ induced by the

perturbed distribution function (2.43) which can then again be used to calculate the interaction with the magnetic field (both background and perturbed) in the momentum balance equation. Using $\mathrm{d}^3v = v_\perp \mathrm{d}v_\perp \mathrm{d}v_\theta \, \mathrm{d}v_\parallel$ in cylindrical coordinates, we obtain from (2.42) and (2.43) the three EP current components

$$\hat{J}_{\mathrm{h},x} = -\frac{Z_\mathrm{h}}{A_\mathrm{h}} \kappa \pi i \int \frac{v_\perp \hat{G} f_{\mathrm{h,eq}}(\omega - k v_\parallel)}{\Omega_+ \Omega_-} \, \mathrm{d}^2v \, \hat{E}_x + \frac{Z_\mathrm{h}^2}{A_\mathrm{h}^2} \, \kappa^2 \pi B_0 \int \frac{v_\perp \hat{G} f_{\mathrm{h,eq}}}{\Omega_+ \Omega_-} \, \mathrm{d}^2v \, \hat{E}_y \,, \tag{2.45}$$

$$\hat{J}_{\mathrm{h},y} = -\frac{Z_\mathrm{h}}{A_\mathrm{h}} \kappa \pi i \int \frac{v_\perp \hat{G} f_{\mathrm{h,eq}}(\omega - k v_\parallel)}{\Omega_+ \Omega_-} \, \mathrm{d}^2v \, \hat{E}_y - \frac{Z_\mathrm{h}^2}{A_\mathrm{h}^2} \, \kappa^2 \pi B_0 \int \frac{v_\perp \hat{G} f_{\mathrm{h,eq}}}{\Omega_+ \Omega_-} \, \mathrm{d}^2v \, \hat{E}_x \,, \tag{2.46}$$

$$\hat{J}_{\mathrm{h},z} = -\frac{Z_\mathrm{h}}{A_\mathrm{h}} \kappa 2 \pi i \int \frac{1}{\omega - k v_\parallel} \frac{\partial f_{\mathrm{h,eq}}}{\partial v_\parallel} \, \mathrm{d}^2v \, \hat{E}_z \,, \tag{2.47}$$

where the integration over v_θ has been carried out such that $\mathrm{d}^2v = v_\perp \mathrm{d}v_\perp \mathrm{d}v_\parallel$ in (2.45)-(2.47). By introducing the anti-symmetric conductivity tensor σ_h this can be written in a compact way similar to classical Ohm's law:

$$\begin{bmatrix} \hat{J}_{\mathrm{h},x} \\ \hat{J}_{\mathrm{h},y} \\ \hat{J}_{\mathrm{h},z} \end{bmatrix} = \begin{bmatrix} \sigma_{\mathrm{h},xx} & \sigma_{\mathrm{h},xy} & 0 \\ -\sigma_{\mathrm{h},xy} & \sigma_{\mathrm{h},xx} & 0 \\ 0 & 0 & \sigma_{\mathrm{h},zz} \end{bmatrix} \begin{bmatrix} \hat{E}_x \\ \hat{E}_y \\ \hat{E}_z \end{bmatrix} = B_0 \begin{bmatrix} \sigma_{\mathrm{h},xy} & -\sigma_{\mathrm{h},xx} & 0 \\ \sigma_{\mathrm{h},xx} & \sigma_{\mathrm{h},xy} & 0 \\ 0 & 0 & 0 \end{bmatrix} \begin{bmatrix} \hat{U}_x \\ \hat{U}_y \\ \hat{U}_z \end{bmatrix} . \tag{2.48}$$

Consequently, there is no parallel current which is due to the fact that there is no parallel electric field in ideal MHD ($\hat{E}_z = 0$).

Besides the induced current density $\hat{\mathbf{J}}_\mathrm{h}$, we also need the responses of the bulk pressure and the magnetic field on the velocity field perturbation. These are given by the pressure equation (2.37b) and Faraday's law (2.37c), respectively, and read

$$\hat{p} = \frac{\gamma p_0 k}{\omega} \, \hat{U}_z \equiv \frac{\gamma p_0 k}{\omega} \, \hat{U}_\parallel \,, \qquad \hat{\mathbf{B}} = -\frac{B_0 k}{\omega} \begin{bmatrix} \hat{U}_x \\ \hat{U}_y \\ 0 \end{bmatrix} \equiv -\frac{B_0 k}{\omega} \, \hat{\mathbf{U}}_\perp \,, \tag{2.49}$$

where $p_\mathrm{eq} = p_0 = const.$. Plugging (2.48) and (2.49) in the linearized momentum balance equation (2.40) finally leads to

$$\begin{aligned} \omega^2 \, \hat{\mathbf{U}} - \gamma p_0 \, k^2 \, \hat{U}_\parallel - B_0^2 \, k^2 \, \hat{\mathbf{U}}_\perp = {} & i \, \nu_\mathrm{h} \, \omega \frac{Z_\mathrm{h} B_0}{A_\mathrm{b}} \kappa \, (\hat{\mathbf{U}} \times \mathbf{e}_z) \\ & - i \, \nu_\mathrm{h} \, \omega \frac{Z_\mathrm{h} B_0}{A_\mathrm{b}} \kappa \, \mathbf{e}_z \times \left(\frac{v_0}{B_0} \hat{\mathbf{B}} - \hat{\mathbf{J}}_\mathrm{h} \right) . \end{aligned} \tag{2.50}$$

Here, the contributions from the energetic ions are written on the right-hand side in order to highlight the differences compared to the "standard" MHD terms on the left hand side that represent sound and shear Alfvén waves. In (2.50) $\hat{\mathbf{B}}$ and $\hat{\mathbf{J}}_\mathrm{h}$ can be eliminated with relations (2.49) and (2.45)-(2.47), respectively, which yields the linear system

$$\begin{bmatrix} A & i\,C & 0 \\ -i\,C & A & 0 \\ 0 & 0 & S \end{bmatrix} \begin{bmatrix} \hat{U}_x \\ \hat{U}_y \\ \hat{U}_z \end{bmatrix} = 0 \,, \qquad \begin{aligned} A &= \omega^2 - B_0^2 \, k^2 + i \nu_\mathrm{h} \, \omega \frac{Z_\mathrm{h} B_0^2}{A_\mathrm{b}} \kappa \sigma_{\mathrm{h},xx} \,, \\ C &= -\nu_\mathrm{h} \, \omega \frac{Z_\mathrm{h} B_0}{A_\mathrm{b}} \kappa \\ &\quad + \nu_\mathrm{h} \frac{Z_\mathrm{h} B_0}{A_\mathrm{b}} \kappa \, v_0 \, k + \nu_\mathrm{h} \, \omega \frac{Z_\mathrm{h} B_0^2}{A_\mathrm{b}} \kappa \sigma_{\mathrm{h},xy} \,, \\ S &= \omega^2 - \gamma p_0 \, k^2 \,. \end{aligned} \tag{2.51}$$

The structure of this linear system reveals three types of waves: First, longitudinal sound waves with the same dispersion relation $\omega^2 = \gamma p_0 \, k^2$ as for the case without energetic ions. Second, right-handed circularly polarized waves characterized by $i\,\hat{U}_x/\hat{U}_y = +1$ and third, left-handed circularly polarized waves characterized by $i\,\hat{U}_x/\hat{U}_y = -1$. The latter two constitute a modification of the "standard" shear Alfvén waves whose dispersion relation $\omega^2 = B_0^2 k^2$ is recovered for $\nu_\mathrm{h} = 0$. In this case, $C = 0$ in (2.51) such that there is no coupling between different velocity components. However, the presence of energetic ions leads to the dispersion relation $D^\pm(k,\omega) = 0$, where

$$\begin{aligned} D^\pm(k,\omega) &= \omega^2 - B_0^2 k^2 \pm \nu_\mathrm{h}\,\omega \frac{Z_\mathrm{h} B_0}{A_\mathrm{b}}\kappa \mp \nu_\mathrm{h} \frac{Z_\mathrm{h} B_0}{A_\mathrm{b}}\kappa\, v_0\, k + \nu_\mathrm{h}\,\omega \frac{Z_\mathrm{h} B_0^2}{A_\mathrm{b}}\kappa\,(i\sigma_{\mathrm{h},xx} \mp \sigma_{\mathrm{h},xy}) \\ &= \omega^2 - B_0^2 k^2 \pm \nu_\mathrm{h}\,\omega \frac{Z_\mathrm{h} B_0}{A_\mathrm{b}}\kappa \mp \nu_\mathrm{h} \frac{Z_\mathrm{h} B_0}{A_\mathrm{b}}\kappa\, v_0\, k + \nu_\mathrm{h} \frac{\omega Z_\mathrm{h}^2 B_0^2}{A_\mathrm{h} A_\mathrm{b}}\kappa^2 \pi \int \frac{v_\perp \hat{G} f_{\mathrm{h,eq}}}{\Omega_\pm}\,\mathrm{d}^2 v\,. \end{aligned} \tag{2.52}$$

This results is still fairly general because we have not further specified the distribution function yet. In order to make predictions about stability we proceed the calculation for the case of an isotropic Maxwellian distribution function with a shift along the magnetic field:

$$f_{\mathrm{h,eq}} = \frac{1}{\pi^{3/2} v_\mathrm{th}^3} \exp\left[-\frac{(v_\parallel - v_0)^2 + v_\perp^2}{v_\mathrm{th}^2}\right] \qquad \Rightarrow \qquad \hat{G} f_{\mathrm{h,eq}} = \frac{2 v_\perp}{v_\mathrm{th}^2}\left(\frac{k v_0}{\omega} - 1\right) f_{\mathrm{h,eq}}\,. \tag{2.53}$$

This distribution function could for instance model a beam of energetic ions that is injected externally into the bulk plasma. Plugging (2.53) in the last term in (2.52) and carrying out the integral over the perpendicular velocity components results in

$$\begin{aligned} \pi \int_{-\infty}^{\infty}\int_0^{\infty} \frac{v_\perp^2 \hat{G} f_{\mathrm{h,eq}}}{\Omega_\pm}\,\mathrm{d}v_\perp \mathrm{d}v_\parallel &= \frac{2}{v_\mathrm{th}^2}\left(\frac{k v_0}{\omega} - 1\right)\pi \int_{-\infty}^{\infty}\int_0^{\infty} \frac{v_\perp^3}{\Omega_\pm} f_{\mathrm{h,eq}}\,\mathrm{d}v_\perp \mathrm{d}v_\parallel \\ &= \frac{1}{v_\mathrm{th}}\left(\frac{k v_0}{\omega} - 1\right)\frac{1}{\sqrt{\pi}} \int_{-\infty}^{\infty} \frac{1}{\Omega_\pm} \exp\left[-\frac{(v_\parallel - v_0)^2}{v_\mathrm{th}^2}\right]\mathrm{d}v_\parallel\,. \end{aligned} \tag{2.54}$$

For the remaining integral over the parallel velocity we make the substitution $u = (v_\parallel - v_0)/v_\mathrm{th}$ such that (2.54) becomes

$$\frac{1}{\omega}\frac{\omega - k v_0}{k v_\mathrm{th}}\frac{1}{\sqrt{\pi}}\int_{-\infty}^{\infty} \mathrm{e}^{-u^2} \frac{1}{u - \underbrace{(\omega - k v_0 \pm B_0 Z_\mathrm{h}\kappa/A_\mathrm{h})/k v_\mathrm{th}}_{=:\xi^\pm}}\,\mathrm{d}u \equiv \frac{1}{\omega}\frac{\omega - k v_0}{k v_\mathrm{th}} Z(\xi^\pm)\,, \tag{2.55}$$

where Z is the plasma dispersion function [87] defined by

$$Z(\xi) = \sqrt{\pi}\mathrm{e}^{-\xi^2}(i - \mathrm{erfi}(\xi))\,, \tag{2.56}$$

and erfi denotes the complex error function. This finally leads to the dispersion relation

$$D^\pm(k,\omega) = \omega^2 - B_0^2 k^2 \pm \nu_\mathrm{h}\,\omega \frac{Z_\mathrm{h} B_0}{A_\mathrm{b}}\kappa \mp \nu_\mathrm{h} \frac{Z_\mathrm{h} B_0}{A_\mathrm{b}}\kappa\, v_0\, k + \nu_\mathrm{h} \frac{Z_\mathrm{h}^2 B_0^2}{A_\mathrm{h} A_\mathrm{b}}\kappa^2 \frac{\omega - k v_0}{k v_\mathrm{th}} Z(\xi^\pm) = 0\,. \tag{2.57}$$

For fixed k, this equation must be solved for the complex frequency $\omega = \omega_\mathrm{r} + i\gamma$, where $\omega_\mathrm{r} = \mathrm{Re}(\omega) \in \mathbb{R}$ is the real oscillation frequency and $\gamma = \mathrm{Im}(\omega) \in \mathbb{R}$ is the corresponding growth rate ($\gamma > 0$), respectively damping rate ($\gamma < 0$).

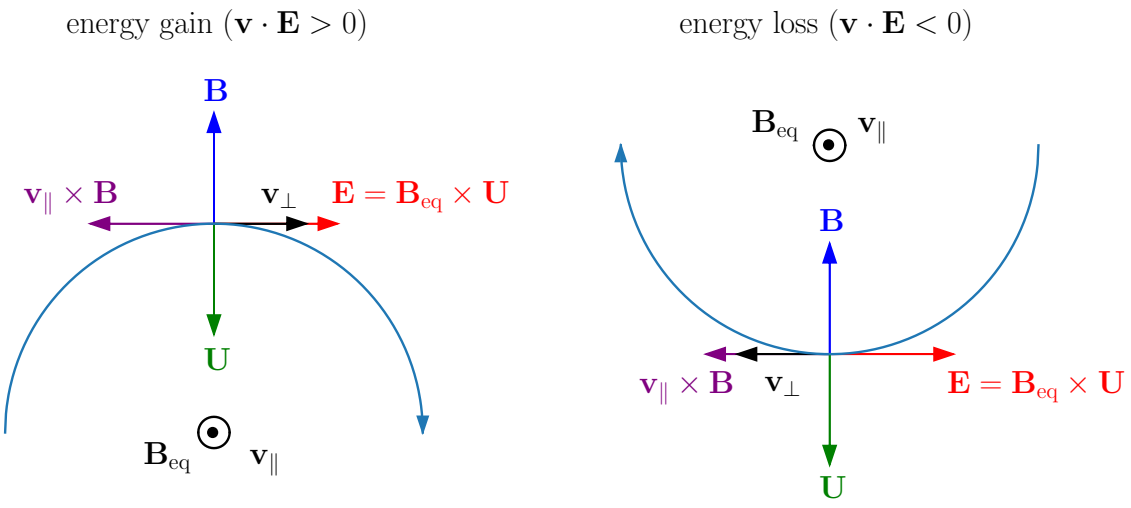

Figure 2.1: Wave-particle interaction between a circularly polarized wave and an ion that moves at the resonance velocity $v_\parallel = v_\mathrm{R}$ along the background magnetic field $\mathbf{B}_\mathrm{eq}$. Due to a Doppler-shift, there is a constant phase between the particle and the wave fields. On the left, the phase is such that a particle gains energy ($\mathbf{v} \cdot \mathbf{E} > 0$) while on the right, the particle losses energy ($\mathbf{v} \cdot \mathbf{E} < 0$).

One approach is to solve (2.57) numerically. In this work, this is achieved with the classical Newton method for root finding because calculating the analytical derivative of (2.57) is unproblematic. This is due to the fact that the analytical derivative of the plasma dispersion function Z is available [83]. However, in actual applications of the Newton method, it was observed that reaching convergence and finding a solution is quite sensitive to the chosen initial guess. The following algorithm is proposed to deal with this issue: one starts with a rather large value for the wave number k in a region where it is assumed that the additional terms in (2.57) due to the energetic ions are small (far away from resonance) and thus takes as an initial guess the solution of the "standard" shear Alfvén wave which is simply given by $\omega = B_0\, k$. If a solution is found (which is usually the case), k is reduced by a small step and the solution of (2.57) from the previous k is taken as an initial guess. This procedure is then repeated for arbitrary small wave numbers $k \to 0$.

An alternative approach is to solve (2.57) analytically in an approximate way under the assumption of weak growth or damping ($|\,\gamma\,| \ll \omega_\mathrm{r}$). This is expected to be the case for low EP densities ($\nu_\mathrm{h} \ll 1$). Performing a Taylor expansion of the dispersion function $D^\pm(k, \omega_\mathrm{r} + i\gamma)$ around ω_r then yields the explicit solution for the growth/damping rate

$$\gamma(k) \approx -\frac{D_\mathrm{i}^\pm(k,\omega_\mathrm{r})}{\partial D_\mathrm{r}^\pm(k,\omega_\mathrm{r})/\partial\omega_\mathrm{r}} = -\frac{1}{2B_0 k}\nu_\mathrm{h}\frac{Z_\mathrm{h}^2 B_0^2}{A_\mathrm{h} A_\mathrm{b}}\kappa^2\frac{B_0 - v_0}{v_\mathrm{th}}\sqrt{\pi}\exp\left(-\frac{(v_\mathrm{R}(k) - v_0)^2}{v_\mathrm{th}^2}\right), \qquad (2.58)$$

where $D_\mathrm{r}^\pm$ and $D_\mathrm{i}^\pm$ are the real and imaginary part of (2.57), respectively. Moreover, $\omega_\mathrm{r} \approx B_0\, k$ has been used. It was observed in practice that this analytical result agrees well with numerical solutions of (2.57) for $\nu_\mathrm{h} \lesssim 1\%$.

Looking at (2.58), it is immediately evident that there is a stability transition at $v_0 = B_0$, i.e. waves are damped ($\gamma < 0$) for $v_0 < B_0$ and growing ($\gamma > 0$) for $v_0 > B_0$. Moreover, in above

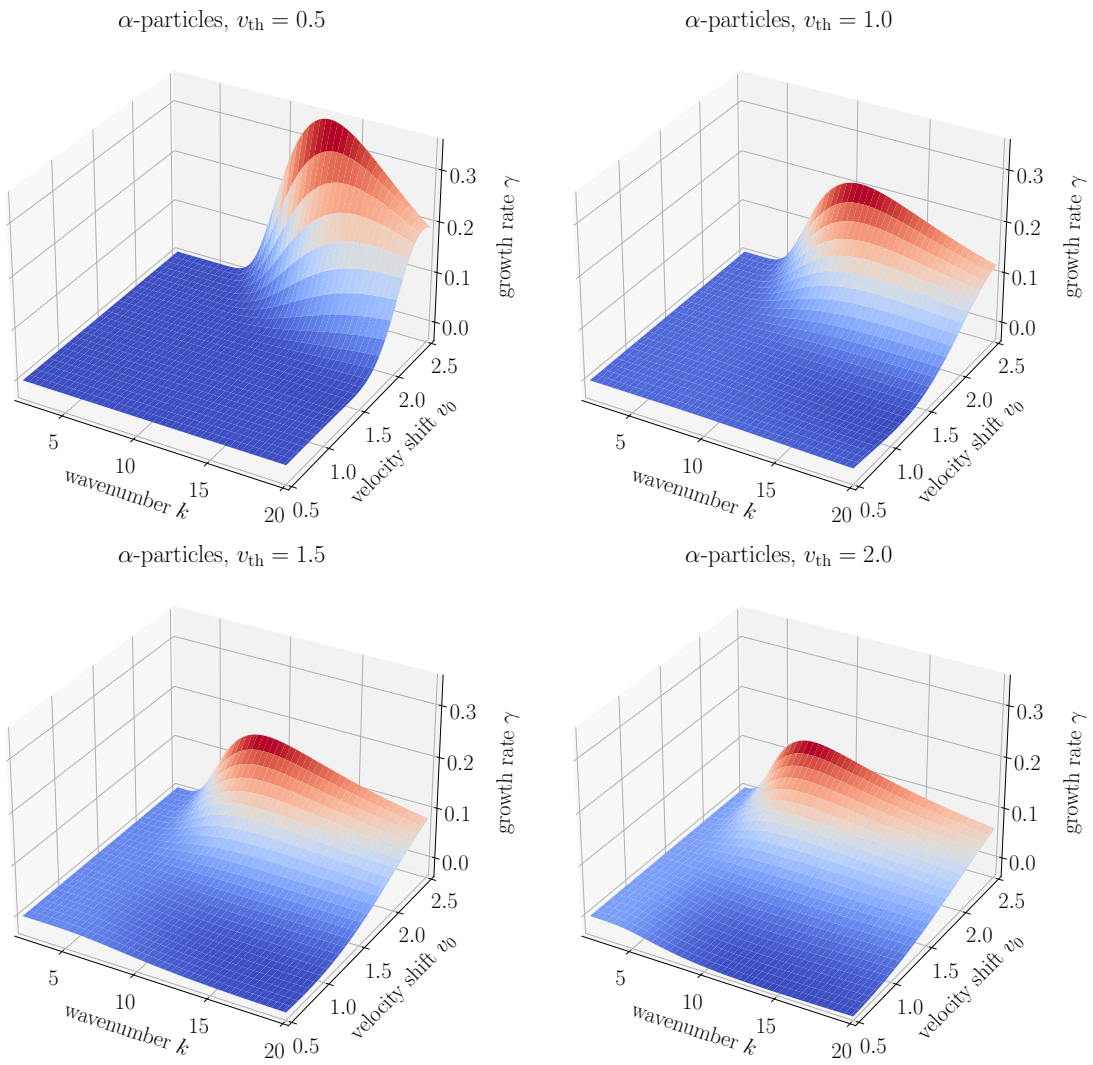

Figure 2.2: Solution of the dispersion relation (2.57) for right-handed circularly polarized waves (+) and four different thermal velocities. Fixed parameters are $A_\mathrm{b} = 2$ (deuterium bulk plasma), $\bar{n}_\mathrm{b} = 1 \times 10^{19}\,\mathrm{m}^{-3}$, $B_0 = 1.5$, $A_\mathrm{h} = 4$, $Z_\mathrm{h} = 2$ (α-particles) and $\nu_\mathrm{h} = 1\,\%$.

expression the velocity

$$v_\mathrm{R}(k) = B_0 \left(1 \pm \frac{Z_\mathrm{h}\kappa}{A_\mathrm{h}k}\right) , \tag{2.59}$$

is the velocity of resonant particles which is essentially states that the Doppler-shifted wave frequency $\omega_\mathrm{r} - kv_\mathrm{R}$ matches the EP cyclotron frequency $\Omega_\mathrm{ch} = Z_\mathrm{h}B_0\kappa/A_\mathrm{h}$. Qualitatively, this can be understood as follows: in order for a particle to efficiently resonate with a circularly polarized wave, there must be a constant phase between the wave magnetic field and the perpendicular velocity of the particle. Since a positively charged ion gyrates in a left-handed sense around a magnetic field line, this is only possible if the ion "sees" a left-handed circularly polarized wave. This in turn is the case if either the ion is slower than a left-handed circularly polarized wave ($v_\mathrm{R} < v_\mathrm{ph} \approx B_0$) or faster than a right-handed circularly polarized wave ($v_\mathrm{R} > v_\mathrm{ph} \approx B_0$) because an ion that is faster than the wave "sees" the wave field circulating in an opposite sense compared to an observer in the laboratory frame. The latter is also called *anomalous* cyclotron interaction because a left-handed ion interacts with a right-handed circularly polarized wave

[88]. If the resonance condition is satisfied, the principle wave-particle interaction mechanisms are shown in Figure 2.1. Depending on the phase shift between the wave's electric field and and the particle's perpendicular velocity, there is either a gain in energy (left-hand side) or a loss in energy (right-hand side). Depending on the gradients of the EP distribution function in velocity space, this then either leads to a net energy transfer from the wave to the particles or vice versa. By plugging (2.59) in (2.58), it is also easily verified that in case of instability ($v_0 > B_0$), the growth rate of the R-wave (+) is always larger than the one of the L-wave (-).

Finally, Figure 2.2 shows the growth/damping rate of numerical solutions of (2.57) in the k-v_0-plane for the case of a deuterium bulk plasma ($A_\mathrm{b} = 2$, $\bar{n}_\mathrm{b} = 1 \times 10^{19}\,\mathrm{m}^{-3}$), α-particles ($A_\mathrm{h} = 4$ and $Z_\mathrm{h} = 2$) as the energetic component and right-handed circulary polarized waves (+). Moreover, $B_0 = 1.5$ and the thermal velocity of the α-particles is taken to be $v_\mathrm{th} = \{0.5, 1.0, 1.5, 2.0\}$. One can show that it is quite difficult to satisfy (2.59) for typical fusion parameters ($A_\mathrm{b} = 2$, $\bar{n}_\mathrm{b} = 1 \times 10^{20}\,\mathrm{m}^{-3} \Rightarrow \bar{v}_\mathrm{A} \approx 1.5 \times 10^{6}\,\mathrm{m/s}$) because in this case, the coupling parameter $\kappa \approx 62$, which shows the strong separation of Alfvénic time scales and gyromotion times scales (recall that $\kappa = \bar{\Omega}_{cp}\,\bar{\tau}_\mathrm{A}$, see Section 2.2). Hence, for a typical magnetic field strength $B_0 = 3.0$ and for reasonable k-values for which the corresponding wavelength $2\pi/k$ is well above the α-particles gyro-radius ($k < 10$), the resonance velocity $v_\parallel \approx 12$ is very large and almost in the relativistic regime. Hence, satisfying (2.59) requires a reduction of the bulk number density $\bar{n}_\mathrm{b}$ down to a point where reasonable values for k lead to reasonable values for the resonance velocity $v_\parallel$ well within the Maxwellian. Reducing $\bar{n}_\mathrm{b}$ by one order of magnitude to $\bar{n}_\mathrm{b} = 1 \times 10^{19}\,\mathrm{m}^{-3}$, as in Figure 2.2, leads to $\kappa \approx 20$ such that the resonance velocity $v_\parallel \approx 2B_0$ for $k = 10$.

Chapter 3

Model discretization and implementation

3.1 Basic concepts of differential geometry in 3d

Since the framework of finite element exterior calculus is highly based on concepts form differential geometry, we shall first give an overview about the needed notions and terminologies. We choose a physicist's point of view rather than the rigorous one of a mathematician because in this thesis we are mainly interested in the applications of these concepts. However, we refer the interested reader to e.g. [89] for a thorough introduction to differential geometry.

In principle, we are concerned with an initial-boundary-value problem on a subset of the three-dimensional space which we call the *physical domain* $\Omega \subset \mathbb{R}^3$. Standard Cartesian coordinates on this domain are denoted by $\mathbf{x} := (x, y, z) \in \Omega$. However, especially when it comes to complicated geometries, it is much more convenient to work with more general curvilinear coordinates $\boldsymbol{\eta} := (s, \chi, \varphi) \in \hat{\Omega}$. The domain $\hat{\Omega}$ on which these coordinates live we call the *logical* domain and the associated coordinates $\boldsymbol{\eta}$ the logical coordinates. We choose the logical domain to be the unit cube $\hat{\Omega} = [0, 1]^3$. The physical domain is the image of the logical domain under the mapping

$$F : \hat{\Omega} \to \Omega, \ (s, \chi, \varphi) \mapsto (x, y, z) = F(s, \chi, \varphi)\,, \tag{3.1}$$

which we assume for the moment to be smooth and invertible everywhere. The latter is not strictly true for polar-like coordinates. However, this difficulty and a proposed solution will be the topic of Chapter 5. Examples for (3.1) are classical cylindrical or spherical coordinates but much more general (even not analytical) mappings are possible. An example which is of special interest in fusion research in depicted in Figure 3.1, where the the logical domain is shown on the left and the physical domain on the right. In this example, the coordinates (s, χ) parameterize the poloidal cross-section of a toroidal domain such that s can be identified with a radial-like coordinate, χ with an angle-like coordinate in the poloidal plane and φ with the (normalized) toroidal angle. In fact, for the remainder of this thesis, we assume the χ and φ coordinate to be angle-like, i.e. periodic.

The most basic objects related to the mapping (3.1) are the Jacobian matrix DF, the metric tensor G and its determinant g defined as

$$DF := \begin{bmatrix} \dfrac{\partial x}{\partial s} & \dfrac{\partial x}{\partial \chi} & \dfrac{\partial x}{\partial \varphi} \\ \dfrac{\partial y}{\partial s} & \dfrac{\partial y}{\partial \chi} & \dfrac{\partial y}{\partial \varphi} \\ \dfrac{\partial z}{\partial s} & \dfrac{\partial z}{\partial \chi} & \dfrac{\partial z}{\partial \varphi} \end{bmatrix}, \qquad G := DF^\top DF\,, \qquad g := \det G\,, \tag{3.2}$$

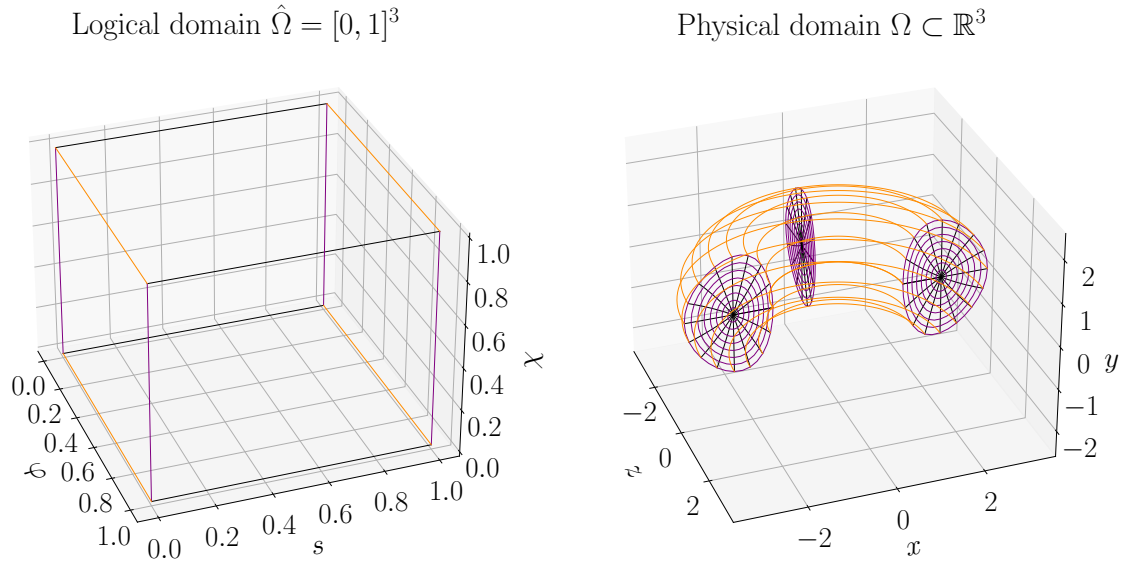

Figure 3.1: Illustration of the mapping $F : \hat{\Omega} \to \Omega$ (3.1) form the logical unit cube to the computational domain of interest (physical domain). For better visibility only half of the torus is shown.

respectively. It is easily verified that $\sqrt{g} = |\det DF|$ and the assumption on the mapping being invertible everywhere implies $\sqrt{g} > 0$ everywhere. The columns of DF can be used to define local basis vectors which are tangent to the mapping's coordinate lines. A vector field expressed in this basis is called a *contra-variant* representation. Hence, the three components

$$\mathbf{V} = \mathbf{V}(\mathbf{x}) = [\, V_x(\mathbf{x}),\, V_y(\mathbf{x}),\, V_z(\mathbf{x})\,]^\top , \tag{3.3}$$

of a vector field written in the standard Cartesian basis $\{\mathbf{e}_x, \mathbf{e}_y, \mathbf{e}_z\}$ can be represented as well as $\mathbf{V}(F(\boldsymbol{\eta})) = DF\,\hat{\mathbf{V}}(\boldsymbol{\eta})$, where $\hat{\mathbf{V}}$ are contra-variant components which are functions of the logical coordinates $\boldsymbol{\eta}$ rather than the Cartesian coordinates $\mathbf{x}$. In what follows, whenever we talk about vector fields, we shall use the hat notation in combination with upper-case bold roman characters to denote contra-variant components which are functions of the logical coordinates. In contrast to that, from now on, upper-case bold roman characters without a hat denote Cartesian components which are functions of the Cartesian coordinates as in (3.3) (the only exception is the lower-case bold roman character $\mathbf{n} = \mathbf{n}(\mathbf{x})$ for a surface normal vector. The contra-variant representation if of course not the only possible one. Another option is to represent a vector field in the dual basis composed of the rows of the inverse Jacobian matrix DF^{-1}. This representation is called *co-variant* and we have $\mathbf{V}(F(\boldsymbol{\eta})) = DF^{-\top}\,\mathbf{V}^1(\boldsymbol{\eta})$, where $DF^{-\top}$ denotes the inverse transposed Jacobian matrix and $\mathbf{V}^1$ are co-variant components or components of a differential 1-form. A third representation is given by $\mathbf{V}(F(\boldsymbol{\eta})) = DF\,\mathbf{V}^2(\boldsymbol{\eta})/\sqrt{g}$, where $\mathbf{V}^2$ are the components of a pseudo-vector or components of a differential 2-form. We shall use the superscripts $()^1$ and $()^2$ in combination with capital bold roman symbols to denote components of differential 1-forms and 2-forms, respectively, which are **always** functions of the logical coordinates. Scalar fields $f = f(\mathbf{x})$ in turn can be represented in two ways: First, a scalar field can be transformed via $f(F(\boldsymbol{\eta})) = \hat{f}(\boldsymbol{\eta}) = f^0(\boldsymbol{\eta})$ yielding a differential 0-form f^0. Second, a scalar field can be transformed via $f(F(\boldsymbol{\eta})) = f^3(\boldsymbol{\eta})/\sqrt{g}$ yielding the component of a differential 3-form f^3. Hence, scalar fields without a hat are functions of the Cartesian coordinates whereas scalar field with a hat are functions of the logical coordinates. Moreover,

Table 3.1: Summary of pull-back and push-forward transformations between generic scalar- and vector-valued functions $f = f(\mathbf{x})$ and $\mathbf{V} = \mathbf{V}(\mathbf{x})$, respectively, and differential k-forms $(0 \leq k \leq 3)$ under the map $F : \hat{\Omega} \to \Omega,\ \boldsymbol{\eta} \mapsto \mathbf{x} = F(\boldsymbol{\eta})$.

	pull-back	push-forward
0-form	$f^0(\boldsymbol{\eta}) = f(F(\boldsymbol{\eta}))$	$f(F(\boldsymbol{\eta})) = f^0(\boldsymbol{\eta})$
1-form (co-variant)	$\mathbf{V}^1 = \begin{bmatrix} V_1^1(\boldsymbol{\eta}) \\ V_2^1(\boldsymbol{\eta}) \\ V_3^1(\boldsymbol{\eta}) \end{bmatrix} = DF^\top \begin{bmatrix} V_x(F(\boldsymbol{\eta})) \\ V_y(F(\boldsymbol{\eta})) \\ V_z(F(\boldsymbol{\eta})) \end{bmatrix}$	$\begin{bmatrix} V_x(F(\boldsymbol{\eta})) \\ V_y(F(\boldsymbol{\eta})) \\ V_z(F(\boldsymbol{\eta})) \end{bmatrix} = DF^{-\top} \begin{bmatrix} V_1^1(\boldsymbol{\eta}) \\ V_2^1(\boldsymbol{\eta}) \\ V_3^1(\boldsymbol{\eta}) \end{bmatrix}$
2-form (pseudo-vector)	$\mathbf{V}^2 = \begin{bmatrix} V_1^2(\boldsymbol{\eta}) \\ V_2^2(\boldsymbol{\eta}) \\ V_3^2(\boldsymbol{\eta}) \end{bmatrix} = \sqrt{g}\, DF^{-1} \begin{bmatrix} V_x(F(\boldsymbol{\eta})) \\ V_y(F(\boldsymbol{\eta})) \\ V_z(F(\boldsymbol{\eta})) \end{bmatrix}$	$\begin{bmatrix} V_x(F(\boldsymbol{\eta})) \\ V_y(F(\boldsymbol{\eta})) \\ V_z(F(\boldsymbol{\eta})) \end{bmatrix} = \frac{1}{\sqrt{g}}\, DF \begin{bmatrix} V_1^2(\boldsymbol{\eta}) \\ V_2^2(\boldsymbol{\eta}) \\ V_3^2(\boldsymbol{\eta}) \end{bmatrix}$
3-form	$f^3(\boldsymbol{\eta}) = \sqrt{g}\, f(F(\boldsymbol{\eta}))$	$f(F(\boldsymbol{\eta})) = \frac{1}{\sqrt{g}}\, f^3(\boldsymbol{\eta})$
vector field (contra-variant)	$\hat{\mathbf{V}} = \begin{bmatrix} \hat{V}_1(\boldsymbol{\eta}) \\ \hat{V}_2(\boldsymbol{\eta}) \\ \hat{V}_3(\boldsymbol{\eta}) \end{bmatrix} = DF^{-1} \begin{bmatrix} V_x(F(\boldsymbol{\eta})) \\ V_y(F(\boldsymbol{\eta})) \\ V_z(F(\boldsymbol{\eta})) \end{bmatrix}$	$\begin{bmatrix} V_x(F(\boldsymbol{\eta})) \\ V_y(F(\boldsymbol{\eta})) \\ V_z(F(\boldsymbol{\eta})) \end{bmatrix} = DF \begin{bmatrix} \hat{V}_1(\boldsymbol{\eta}) \\ \hat{V}_2(\boldsymbol{\eta}) \\ \hat{V}_3(\boldsymbol{\eta}) \end{bmatrix}$

we use the superscripts $()^0$ and $()^3$ to denote a differential 0-form and the component of a differential 3-forms, respectively, which are **always** functions of the logical coordinates. Table 3.1 summarizes the most important transformation formulae between components of differential k-forms. We refer to them as *pull-back* $(\Omega \to \hat{\Omega})$ and *push-forward* $(\hat{\Omega} \to \Omega)$ operations.

We remark that although the distinction between the components of differential k-forms on the one hand and their basis on the other hand is an important concept in differential geometry, we shall sometimes use the term "differential k-form" for quantities which are strictly speaking just the components and not the entire form consisting of the components **and** the basis. This is because the relevant information needed to perform actual calculations is encoded entirely in the components.

The introduced transformation formulae of differential k-forms are of course not random but follow from the fact that k-forms can be integrated over a k-dimensional manifold, i.e. components of differential k-forms can be used to conveniently calculate line integrals (1-forms), surface integrals (2-forms) and volume integrals (3-forms) because

$$\int_{C_\mu} \mathbf{V} \cdot \mathrm{d}\boldsymbol{L} = \begin{cases} \displaystyle\int_{s_1}^{s_2} V_1^1(s, \chi_0, \varphi_0)\, \mathrm{d}s\,, \\ \displaystyle\int_{\chi_1}^{\chi_2} V_2^1(s_0, \chi, \varphi_0)\, \mathrm{d}\chi\,, \\ \displaystyle\int_{\varphi_1}^{\varphi_2} V_3^1(s_0, \chi_0, \varphi)\, \mathrm{d}\varphi\,, \end{cases} \qquad \int_{S_\mu} \mathbf{V} \cdot \mathrm{d}\mathbf{S} = \begin{cases} \displaystyle\int_{\chi_1}^{\chi_2} \int_{\varphi_1}^{\varphi_2} V_1^2(s_0, \chi, \varphi)\, \mathrm{d}\chi\, \mathrm{d}\varphi\,, \\ \displaystyle\int_{s_1}^{s_2} \int_{\varphi_1}^{\varphi_2} V_2^2(s, \chi_0, \varphi)\, \mathrm{d}s\, \mathrm{d}\varphi\,, \\ \displaystyle\int_{s_1}^{s_2} \int_{\chi_1}^{\chi_2} V_3^2(s, \chi, \varphi_0)\, \mathrm{d}s\, \mathrm{d}\chi\,. \end{cases} \tag{3.4}$$

In (3.4), C_μ ($\mu = 1, 2, 3$) are curves along the coordinate lines which result if the μ-th logical coordinate is varied while the other two are fixed, S_μ ($\mu = 1, 2, 3$) are surfaces which result if the μ-th logical coordinate is fixed while the other two are varied. For volume integrals over scalar fields we similarly have

$$\int_V f \,\mathrm{d}V = \int_{s_1}^{s_2} \int_{\chi_1}^{\chi_2} \int_{\varphi_1}^{\varphi_2} f^3(s, \chi, \varphi) \,\mathrm{d}s \,\mathrm{d}\chi \,\mathrm{d}\varphi \,, \tag{3.5}$$

where V is a finite volume which results if all three logical coordinates are varied in some finite interval. Consequently, differential forms "swallow" the geometric information introduced by the coordinate transformation (3.1) in its components in a way that integrals can be calculated in the same way as in Cartesian space.

The differential operators grad, curl and div transform as

$$\nabla f = DF^{-\top} \hat{\nabla} f^0 \,, \tag{3.6a}$$

$$\nabla \times \mathbf{V} = \frac{1}{\sqrt{g}} DF \,\hat{\nabla} \times (G \,\hat{\mathbf{V}}) = \frac{1}{\sqrt{g}} DF \,\hat{\nabla} \times \mathbf{V}^1 \,, \tag{3.6b}$$

$$\nabla \cdot \mathbf{V} = \frac{1}{\sqrt{g}} \,\hat{\nabla} \cdot (\sqrt{g} \,\hat{\mathbf{V}}) = \frac{1}{\sqrt{g}} \,\hat{\nabla} \cdot \mathbf{V}^2 \,, \tag{3.6c}$$

where the operators

$$\nabla := \begin{bmatrix} \dfrac{\partial}{\partial x} & \dfrac{\partial}{\partial y} & \dfrac{\partial}{\partial z} \end{bmatrix}^\top , \qquad \hat{\nabla} := \begin{bmatrix} \dfrac{\partial}{\partial s} & \dfrac{\partial}{\partial \chi} & \dfrac{\partial}{\partial \varphi} \end{bmatrix}^\top , \tag{3.7}$$

act on Cartesian and logical coordinates, respectively. From (3.6) it is immediately evident that the gradient acts on 0-forms and transforms as a 1-form, the curl acts on 1-forms and transforms as a 2-form, and the divergence acts on 2-forms and transforms as a 3-form (compare the right-hand sides of (3.6) with the push-forward operations in Table 3.1).

Finally, we define the L^2-scalar products

$$(\, f^0, h^0 \,)_0 := \int_{\hat{\Omega}} f^0 \, h^0 \, \sqrt{g} \,\mathrm{d}s \,\mathrm{d}\chi \,\mathrm{d}\varphi \,, \tag{3.8a}$$

$$(\mathbf{V}^1, \mathbf{W}^1)_1 := \int_{\hat{\Omega}} (\mathbf{V}^1)^\top G^{-1} \,\mathbf{W}^1 \,\sqrt{g} \,\mathrm{d}s \,\mathrm{d}\chi \,\mathrm{d}\varphi \,, \tag{3.8b}$$

$$(\mathbf{V}^2, \mathbf{W}^2)_2 := \int_{\hat{\Omega}} (\mathbf{V}^2)^\top G \,\mathbf{W}^2 \frac{1}{\sqrt{g}} \,\mathrm{d}s \,\mathrm{d}\chi \,\mathrm{d}\varphi \,, \tag{3.8c}$$

$$(\, f^3, h^3 \,)_3 := \int_{\hat{\Omega}} f^3 \, h^3 \, \frac{1}{\sqrt{g}} \,\mathrm{d}s \,\mathrm{d}\chi \,\mathrm{d}\varphi \,, \tag{3.8d}$$

which take the components of two k-forms as an input and produce a real number. The metric coefficients in (3.8) result from pulling back the two input functions to logical space and transforming the volume element $\mathrm{d}V = \mathrm{d}x \,\mathrm{d}y \,\mathrm{d}z$ according to $\mathrm{d}V = \sqrt{g} \,\mathrm{d}s \,\mathrm{d}\chi \,\mathrm{d}\varphi$. The scalar

products (3.8) allow for the definition of Sobolev spaces of differential forms:

$$V^0 := \left\{ f^0 = \sum_{k=0}^{1} f_k^0(s,\chi)\,\mathcal{F}_k^n(\varphi)\,, \quad (\,f^0, f^0\,)_0 < \infty\,, \quad (\,\hat{\nabla} f^0, \hat{\nabla} f^0\,)_1 < \infty \right\}, \tag{3.9a}$$

$$V^1 := \left\{ \mathbf{V}^1 = \sum_{k=0}^{1} \mathbf{V}_k^1(s,\chi)\,\mathcal{F}_k^n(\varphi)\,, \quad (\,\mathbf{V}^1, \mathbf{V}^1\,)_1 < \infty\,, \quad (\,\hat{\nabla}\times\mathbf{V}^1, \hat{\nabla}\times\mathbf{V}^1\,)_2 < \infty \right\}, \tag{3.9b}$$

$$V^2 := \left\{ \mathbf{V}^2 = \sum_{k=0}^{1} \mathbf{V}_k^2(s,\chi)\,\mathcal{F}_k^n(\varphi)\,, \quad (\,\mathbf{V}^2, \mathbf{V}^2\,)_2 < \infty\,, \quad (\,\hat{\nabla}\cdot\mathbf{V}^2, \hat{\nabla}\cdot\mathbf{V}^2\,)_3 < \infty \right\}, \tag{3.9c}$$

$$V^3 := \left\{ f^3 = \sum_{k=0}^{1} f_k^3(s,\chi)\,\mathcal{F}_k^n(\varphi)\,, \quad (\,f^3, f^3\,)_3 < \infty \right\}, \tag{3.9d}$$

where we already restricted ourselves to a single Fourier mode in toroidal (φ) direction. This is the case treated throughout this thesis. Functions with more general dependencies in toroidal direction are in principle possible in the definition of the spaces (3.9), but here we only allow for functions which are a linear combination of the real Fouier basis functions $\mathcal{F}_0^n = \cos(2\pi n\varphi)$ and $\mathcal{F}_1^n = \sin(2\pi n\varphi)$ with $n \in \mathbb{Z}$ being the toroidal mode number.

In the literature, these spaces are often referred to as $H^1(\hat{\Omega})$, $H(\mathrm{curl}, \hat{\Omega})$, $H(\mathrm{div}, \hat{\Omega})$ and $L^2(\hat{\Omega})$, respectively and have the meaning of minimal regularity constraints in different directions. For instance, a function to be an element of V^1 must not have tangential discontinuities while a function to be an element of V^2 must not have normal discontinuities (relative to the coordinate lines). In contrast to that, an element in V^3 can in principle have discontinuities in all directions. Finally, the spaces (3.9) form a so-called differential cochain complex (de Rham complex):

$$V^0 \xrightarrow{\text{grad}} V^1 \xrightarrow{\text{curl}} V^2 \xrightarrow{\text{div}} V^3\,. \tag{3.10}$$

This means that the previous operator maps into the kernel of the next operator which is due to the well-known vector calculus identities curl grad = 0 and div curl = 0, where grad = $\hat{\nabla}$, curl = $\hat{\nabla}\times$ and div = $\hat{\nabla}\cdot$.

3.2 Model weak formulation with differential forms

The first step to obtain a weak formulation which is suitable for a discretization within the FEEC framework is to write the model equations in terms of components of differential forms. This is obtained by using the push-forward transformation formulae in Table 3.1 and the transformation formulae for differential operators (3.6). An important question is, however, which form to choose for which physical quantity. Here, we choose to express $n_{\mathrm{b,eq}}$, p_{eq} and p as 3-forms and $\mathbf{J}_{\mathrm{eq}}$, $\mathbf{B}_{\mathrm{eq}}$, $\mathbf{B}$ and $\mathbf{U}$ as a 2-forms. The choices for the 3-forms, the current density and the magnetic fields are motivated by the fact that these quantities are (flux) densities which are naturally integrated over some volume (surface) to get the total mass, internal energy, current and magnetic flux, respectively, inside this volume (surface). In contrast to that, the choice of $\mathbf{U}$ being a 2-form is somewhat more questionable. A more natural choice would be to express it as a vector field since all operations in the MHD equations involving the velocity field can be written independently of the metric if $\mathbf{U}$ is chosen to be a vector field. This is due to the fact that all other quantities are transported along $\mathbf{U}$. However, all finite element spaces in FEEC are subspaces of Sobolev spaces of differential forms (3.9) and an additional space for vector fields is not existing in the current framework. The reason for then choosing $\mathbf{U}$ to be a 2-form rather than a 1-form is the

fixed wall boundary condition $\mathbf{U} \cdot \mathbf{n} = 0$. It is easily understood that the second and the third basis vector of 2-forms (columns of $DF/\sqrt{g}$) are always tangential to the boundary surfaces at $s = 0$ and $s = 1$. Therefore, forcing the first component of a 2-form to zero at the boundary directly leads to the desired boundary condition. To properly account this fact as well as for natural boundary for other forms, we define the following subspaces of (3.9):

$$V_0^0 := \left\{ f^0 \in V^0,\ f_k^0(0,\chi) = f_k^0(1,\chi) = 0 \quad \forall\, \chi,\, k \right\} , \tag{3.11a}$$

$$V_0^1 := \left\{ \mathbf{V}^1 \in V^1,\ V_{2,k}^2(0,\chi) = V_{2,k}^2(1,\chi) = V_{3,k}^2(0,\chi) = V_{3,k}^2(1,\chi) = 0 \quad \forall\, \chi,\, k \right\} , \tag{3.11b}$$

$$V_0^2 := \left\{ \mathbf{V}^2 \in V^2,\ V_{1,k}^2(0,\chi) = V_{1,k}^2(1,\chi) = 0 \quad \forall\, \chi,\, k \right\} , \tag{3.11c}$$

$$V_0^3 := V^3 . \tag{3.11d}$$

These spaces are constructed in a way that elements in V_0^1 that are pushed-forward according to Table 3.1 have vanishing tangential components on $\partial\Omega$ and elements in V_0^2 that are pushed-forward have vanishing normal components on $\partial\Omega$. These spaces once more form a de Rham complex:

$$V_0^0 \xrightarrow{\text{grad}} V_0^1 \xrightarrow{\text{curl}} V_0^2 \xrightarrow{\text{div}} V_0^3 . \tag{3.12}$$

We choose to write the MHD momentum conservation law in weak form and the pressure and induction equation in strong from. This leads to strong conservation of $\nabla \cdot \mathbf{B} = 0$ and the preservation of the symmetry between the Alfvénic force term in the momentum conservation law and the induction equation which is important for energy conservation. Moreover, since both coupling terms to the Vlasov equation appear in the momentum conservation law, this facilitates the evaluation of these coupling terms via Monte-Carlo integration. To finally obtain the weak formulation, we take the L^2 scalar product (3.8c) of (2.37a) with the test function $\mathbf{K}^2 \in V_0^2$ and perform integration by parts in the first and second term on the right-hand side of the MHD momentum balance equation. This is followed by transformation to differential forms (with the help of Table 3.1 and (3.6)). This leads to the following weak formulation: find $(\mathbf{U}^2,\, p^3,\, \mathbf{B}^2) \in V_0^2 \times V_0^3 \times V_0^2$ such that

$$\begin{aligned} \left(\frac{1}{\sqrt{g}}\, n_{\mathrm{b,eq}}^3\, \frac{\partial \mathbf{U}^2}{\partial t},\, \mathbf{K}^2 \right)_2 &= \left(p^3,\, \hat{\nabla} \cdot \mathbf{K}^2 \right)_3 - \left(\mathbf{B}^2,\, \hat{\nabla} \times \left(\frac{1}{\sqrt{g}}\, \mathbf{K}^2 \times \mathbf{B}_{\mathrm{eq}}^2 \right) \right)_2 \\ &\quad + \left(G^{-1} \left(\mathbf{J}_{\mathrm{eq}}^2 \times \mathbf{B}^2 \right), \mathbf{K}^2 \right)_2 + \mathrm{CC}(\rho_{\mathrm{h}}^3) + \mathrm{CC}(\mathbf{J}_{\mathrm{h}}^2) \qquad \forall\ \mathbf{K}^2 \in V_0^2 , \end{aligned} \tag{3.13a}$$

$$\frac{\partial p^3}{\partial t} = -\hat{\nabla} \cdot \left(\frac{1}{\sqrt{g}}\, p_{\mathrm{eq}}^3\, \mathbf{U}^2 \right) - (\gamma - 1)\, \frac{1}{\sqrt{g}}\, p_{\mathrm{eq}}^3\, \hat{\nabla} \cdot \mathbf{U}^2 \qquad \text{in } V_0^3 , \tag{3.13b}$$

$$\frac{\partial \mathbf{B}^2}{\partial t} = \hat{\nabla} \times \left(\frac{1}{\sqrt{g}}\, \mathbf{U}^2 \times \mathbf{B}_{\mathrm{eq}}^2 \right) \qquad \text{in } V_0^2 , \tag{3.13c}$$

where we used the formula $M\mathbf{V} \times M\mathbf{W} = (\det M)\, M^{-\top}(\mathbf{V} \times \mathbf{W})$ for some invertible matrix $M \in \mathbb{R}^{3\times 3}$ to transform cross products of 2-forms components according to

$$\mathbf{V} \times \mathbf{W} = \frac{1}{\sqrt{g}}\, DF^{-\top} \left(\mathbf{V}^2 \times \mathbf{W}^2 \right) , \tag{3.14}$$

and we introduced the abbreviations $\mathrm{CC}(\rho_{\mathrm{h}}^3)$ and $\mathrm{CC}(\mathbf{J}_{\mathrm{h}}^2)$ for the two coupling terms for which explicit expression will be given in a moment. Moreover, the two boundary terms appearing on

the right-hand side of (3.13a) when integrating by parts vanish due to the choice $\mathbf{K}^2 \in V_0^2$ and the assumption that the equilibrium magnetic field has vanishing normal components on the boundary, i.e. $\mathbf{B}_{\rm eq} \cdot \mathbf{n} = 0$ (perfectly conduction wall).

The two coupling terms in (3.13) read

$$\mathrm{CC}(\rho_{\rm h}^3) = \nu_{\rm h} \frac{Z_{\rm h}}{A_{\rm b}} \kappa \left(\frac{1}{\sqrt{g}} \rho_{\rm h}^3 \, G^{-1} \left(\mathbf{U}^2 \times \mathbf{B}_{\rm tot}^2 \right), \mathbf{K}^2 \right)_2 , \tag{3.15}$$

$$\mathrm{CC}(\mathbf{J}_{\rm h}^2) = -\nu_{\rm h} \frac{Z_{\rm h}}{A_{\rm b}} \kappa \left(G^{-1} \left(\mathbf{J}_{\rm h}^2 \times \mathbf{B}_{\rm tot}^2 \right), \mathbf{K}^2 \right)_2 , \tag{3.16}$$

where $\mathbf{B}_{\rm tot}^2 = \mathbf{B}_{\rm eq}^2 + \mathbf{B}^2$ is the total magnetic field (equilibrium + perturbed). Finally, the transformed Vlasov equation is given by

$$\begin{aligned} \frac{\partial f_{\rm h}^0}{\partial t} + (DF^{-1}\mathbf{v}) \cdot \hat{\nabla} f_{\rm h}^0 + \frac{Z_{\rm h}}{A_{\rm h}} \kappa \Bigg[\frac{1}{\sqrt{g}} DF^{-\top} (\mathbf{B}_{\rm tot}^2 \times \mathbf{U}^2) \\ + DF^{-\top} \left(DF^{-1}\mathbf{v} \times \mathbf{B}_{\rm tot}^2 \right) \cdot \nabla_{\mathbf{v}} f_{\rm h}^0 \Bigg] = 0 , \end{aligned} \tag{3.17}$$

if velocity space is expressed with Cartesian coordinates $\mathbf{v} = (v_x, v_y, v_z)$, i.e. the distribution function $f_{\rm h}^0 = f_{\rm h}^0(\boldsymbol{\eta}, \mathbf{v}, t)$.

3.3 Discrete differential forms based on B-splines

The goal of this section is to construct finite-dimensional subspaces of (3.9) resp. (3.11) based on 2d tensor product B-splines in the poloidal (s, χ)-plane [58]. Furthermore, the spaces shall be constructed in a way to preserve the de Rham complex property (3.10).

B-splines (from *basis* spline) are piecewise polynomials with a compact support (see Figure 3.2) and are commonly used in computer-aided design. Compared to classical Lagrange polynomial basis functions, B-splines are characterized by higher smoothness which makes them particularly popular in PIC codes. For details on B-splines, see [90, 91].

To construct uni-variant B-splines in s- and χ-direction, let $\hat{\Omega}^s = \hat{\Omega}^\chi = [0, 1]$ be two unit intervals partitioned by cell interfaces $0 = c_0^s < c_1^s \ldots < c_{n_s - p_s}^s = 1$ and $0 = c_0^\chi < c_1^\chi \ldots < c_{n_\chi}^\chi = 1$ such that the number of cells (or *elements*) is $N_{\rm el}^s = n_s - p_s$ and $N_{\rm el}^\chi = n_\chi$, respectively. The k-th element in s-direction is denoted by $\hat{\Omega}_k^s = [\, c_k^s, c_{k+1}^s \,]$ and accordingly $\hat{\Omega}_k^\chi = [\, c_k^\chi, c_{k+1}^\chi \,]$ in χ-direction. B-splines of degree $p_s \geq 1$ denoted by $N_i^{p_s}(s)$ and B-splines of degree $p_\chi \geq 1$ denoted by $N_i^{p_\chi}(\chi)$ are then defined via the knot sequences

$$\mathbf{T}^s := (\underbrace{0, \ldots, 0}_{p_s \text{ times}}, c_0^s, c_1^s, \ldots, c_{n_s - p_s - 1}^s, c_{n_s - p_s}^s, \underbrace{1, \ldots, 1}_{p_s \text{ times}}) , \tag{3.18}$$

$$\mathbf{T}^\chi := (\underbrace{c_{-p_\chi}^\chi, \ldots, c_{-1}^\chi}_{p_\chi \text{ points}}, c_0^\chi, c_1^\chi, \ldots, c_{n_\chi - 1}^\chi, c_{n_\chi}^\chi, \underbrace{c_{n_\chi + 1}^\chi, \ldots, c_{n_\chi + p_\chi}^\chi}_{p_\chi \text{ points}}) , \tag{3.19}$$

together with the recursion formula

$$N_i^{p_s}(s) := w_i^{p_s}(s) \, N_i^{p_s - 1}(s) + (1 - w_{i+1}^{p_s}(s)) \, N_{i+1}^{p_s - 1}(s) , \qquad w_i^{p_s}(s) := \frac{s - T_i^s}{T_{i+p_s}^s - T_i^s} , \tag{3.20}$$

$$N_i^0(s) := \begin{cases} 1 & \text{for} \quad s \in [\, T_i^s, T_{i+1}^s \,) , \\ 0 & \text{else} . \end{cases} \tag{3.21}$$

and accordingly for $N_i^{p_\chi}(\chi)$. The knot sequence (3.18) results in a family *clamped* B-splines in $\hat{\Omega}^s$ and the knot sequence (3.19) results in a family of *periodic* B-splines in $\hat{\Omega}^\chi$. In the periodic case, we have $c^\chi_{-i} = c^\chi_{n_\chi - i} - 1$ and $c^\chi_{n_\chi+i} = c^\chi_i + 1$ for $0 < i \leq p_\chi$ and the multiplicity of each knot is 1. The knot sequence $\mathbf{T}^\chi$ containing $n_\chi + 2p_\chi + 1$ distinct points results in $n_\chi + p_\chi$ shifted B-splines of identical shape that are $\mathcal{C}^{p_\chi - 1}$ everywhere. To ensure periodicity, the last p_χ B-splines are identified with the first p_χ B-splines which yields the final number of n_χ linearly independent periodic B-spline basis functions in $\hat{\Omega}^\chi$. In the clamped case, the knot sequence $\mathbf{T}^s$ containing $n_s + p_s + 1$ points yields n_s B-splines, where all B-splines are $\mathcal{C}^{p_s - 1}$ everywhere. Hence, we obtain n_s linearly independent clamped B-spline basis functions in $\hat{\Omega}^s$. The consequence of the first and the last knot having multiplicity $p_s + 1$ is that the first and the last B-spline are interpolatory at $s = 0$ and $s = 1$, respectively:

$$N_0^{p_s}(0) = N_{n_s-1}^{p_s}(1) = 1\,, \qquad N_{i>0}^{p_s}(0) = N_{i<n_s-1}^{p_s}(1) = 0\,. \tag{3.22}$$

This allows for an efficient construction of spaces of the form (3.11) by simply removing contributions from the first and the last spline. The derivatives of B-splines $N_i^{p_s}(s)$ and $N_i^{p_\chi}(\chi)$ can be expressed as

$$\frac{\mathrm{d}}{\mathrm{d}s} N_i^{p_s}(s) = p_s \left(\frac{N_i^{p_s-1}(s)}{T^s_{i+p_s} - T^s_i} - \frac{N_{i+1}^{p_s-1}(s)}{T^s_{i+p_s+1} - T^s_{i+1}} \right), \qquad N_0^{p_s-1}(s) = N_{n_s}^{p_s-1}(s) = 0\,, \tag{3.23}$$

$$\frac{\mathrm{d}}{\mathrm{d}\chi} N_i^{p_\chi}(\chi) = p_\chi \left(\frac{N_i^{p_\chi-1}(\chi)}{T^\chi_{i+p_\chi} - T^\chi_i} - \frac{N_{i+1}^{p_\chi-1}(\chi)}{T^\chi_{i+p_\chi+1} - T^\chi_{i+1}} \right), \quad N_0^{p_\chi-1}(\chi) = N_{n_\chi}^{p_\chi-1}(\chi)\,, \tag{3.24}$$

where $N_i^{p_s-1}(s)$ and $N_i^{p_\chi-1}(\chi)$ are lower degree B-splines created from the same knot sequences (3.18) and (3.19), respectively. It is convenient to define the lower degree, re-scaled B-splines (also called M-splines)

$$D_i^{p_s}(s) := p_s \, \frac{N_{i+1}^{p_s-1}(s)}{T^s_{i+p_s+1} - T^s_{i+1}}\,, \qquad D_i^{p_\chi}(\chi) := p_\chi \, \frac{N_{i+1}^{p_\chi-1}(\chi)}{T^\chi_{i+p_\chi+1} - T^\chi_{i+1}}\,, \tag{3.25}$$

where $0 \leq i < d_s$ with $d_s = n_s - 1$ for $D_i^{p_s}(s)$. In the periodic case, the last $p_\chi - 1$ M-splines that have a non-vanishing support in Ω_χ are once more identified with the first $p_\chi - 1$ M-splines. This yields the total number of $d_\chi = n_\chi$ linearly independent periodic M-splines. Using (3.25) the recursion formulae for the derivatives (3.23) and (3.24) become

$$\frac{\mathrm{d}}{\mathrm{d}s} N_i^{p_s}(s) = D_{i-1}^{p_s}(s) - D_i^{p_s}(s)\,, \qquad D_{-1}^{p_s}(s) = D_{n_s-1}^{p_s}(s) = 0\,, \tag{3.26}$$

$$\frac{\mathrm{d}}{\mathrm{d}\chi} N_i^{p_\chi}(\chi) = D_{i-1}^{p_\chi}(\chi) - D_i^{p_\chi}(\chi)\,, \qquad D_{-1}^{p_\chi}(\chi) = D_{n_\chi-1}^{p_\chi}(\chi)\,. \tag{3.27}$$

Finally, we define the so-called Greville points [92], denoted by $(\mathfrak{s}_i)_{i=0}^{n_s-1}$ and $(\mathfrak{t}_i)_{i=0}^{n_\chi-1}$:

$$\mathfrak{s}_i := \frac{1}{p_s} \sum_{j=i+1}^{i+p_s} T_j^s\,, \qquad \mathfrak{t}_i := \frac{1}{p_\chi} \sum_{j=i+1}^{i+p_\chi} T_j^\chi\,. \tag{3.28}$$

These points will serve as interpolation points in Section 5.3 when projection operators on B-spline bases are introduced. A Greville point is generally located close the maximum of the

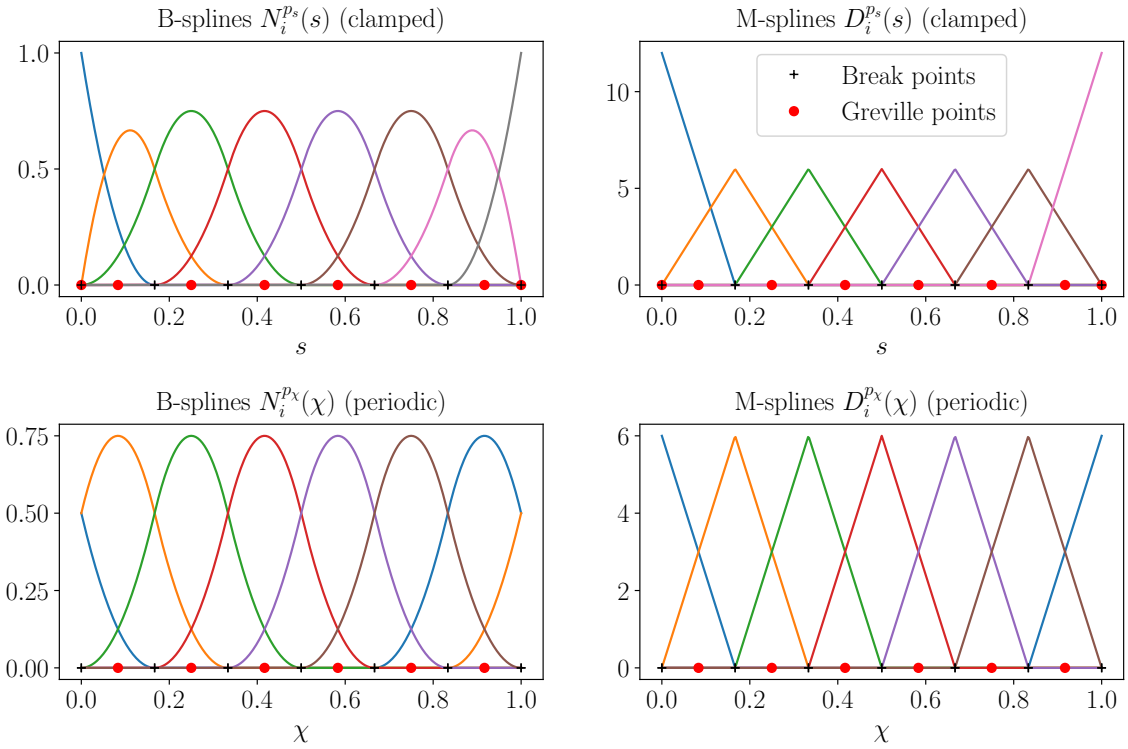

Figure 3.2: B-spline basis functions of degree $p_s = p_\chi = 2$ on a uniform grid with $n_s - p_s = n_\chi = 6$ cells defined by equally spaced break points (black crosses). Shown are clamped (top left) and periodic (bottom left) B-splines. The corresponding lower degree ($p_s - 1 = p_\chi - 1 = 1$), re-scaled B-splines (here called M-splines) are plotted for the clamped (top right) and the periodic (bottom right) case. The corresponding Greville points (3.28) are shown as well (red dots).

B-spline with the same index. Typical examples of uni-variate B-spline bases are plotted in Figure 3.2 for the clamped (top left) and the periodic (bottom left) case. The corresponding lower degree, re-scaled B-splines (here called M-splines) are plotted in the right column. The splines are created from equally spaced cell interfaces (here called break points) and the Greville points (3.28) are shown as well (red dots).

An arbitrary B-spline function is now given as a linear combination of B-spline basis functions with real coefficients. Hence, we define the following function spaces:

$$V_h^{s,0} := \operatorname{span}\left(N_0^{p_s}, \dots, N_{n_s-1}^{p_s}\right), \qquad \dim V_h^{s,0} = n_s, \tag{3.29a}$$

$$V_h^{s,1} := \operatorname{span}\left(D_0^{p_s}, \dots, D_{d_s-1}^{p_s}\right), \qquad \dim V_h^{s,1} = d_s = n_s - 1, \tag{3.29b}$$

$$V_h^{\chi,0} := \operatorname{span}\left(N_0^{p_\chi}, \dots, N_{n_\chi-1}^{p_\chi}\right), \qquad \dim V_h^{\chi,0} = n_\chi, \tag{3.29c}$$

$$V_h^{\chi,1} := \operatorname{span}\left(D_0^{p_\chi}, \dots, D_{d_\chi-1}^{p_\chi}\right), \qquad \dim V_h^{\chi,1} = d_\chi = n_\chi. \tag{3.29d}$$

The subscript "h" is used to denote spline spaces and spline functions and should not be confused with the non-italic subscript "h", which is used to label quantities related to the energetic particle species. With regards to derivatives, we have for $f_h \in V_h^{s,0}$ and $g_h \in V_h^{\chi,0}$, thanks to (3.26) and

(3.27),

$$f_h = \sum_{i=0}^{n_s-1} f_i N_i^{p_s} \quad \Rightarrow \quad f_h' = \sum_{i=0}^{n_s-1} f_i (D_{i-1}^{p_s} - D_i^{p_s}) = \sum_{i=0}^{d_s-1} (f_{i+1} - f_i) D_i^{p_s} \qquad \in V_h^{s,1}\,, \tag{3.30}$$

$$g_h = \sum_{i=0}^{n_\chi-1} g_i N_i^{p_\chi} \quad \Rightarrow \quad g_h' = \sum_{i=0}^{n_\chi-1} g_i (D_{i-1}^{p_\chi} - D_i^{p_\chi}) = \sum_{i=0}^{d_\chi-1} (g_{i+1} - g_i) D_i^{p_\chi} \qquad \in V_h^{\chi,1}\,. \tag{3.31}$$

Hence, we can define the derivative matrices $\mathbb{G}^s \in \mathbb{R}^{d_s \times n_s}$ and $\mathbb{G}^\chi \in \mathbb{R}^{d_\chi \times n_\chi}$ with entries

$$\mathbb{G}_{ij}^s := \begin{cases} -1 & \text{for} \quad j = i\,, \\ 1 & \text{for} \quad j = i+1\,, \\ 0 & \text{else}\,, \end{cases} \qquad\qquad \mathbb{G}_{ij}^\chi := \begin{cases} -1 & \text{for} \quad j = i\,, \\ 1 & \text{for} \quad j = \mathrm{mod}(i+1, n_\chi)\,, \\ 0 & \text{else}\,, \end{cases} \tag{3.32}$$

respectively. By additionally stacking FE coefficients and basis functions on top of each other (bold symbols),

$$\mathbf{f} := (f_i)_{i=0}^{n_s-1}\,, \qquad \mathbf{N}^s := (N_i^{p_s})_{i=0}^{n_s-1}\,, \qquad \mathbf{D}^s := (D_i^{p_s})_{i=0}^{d_s-1}\,, \tag{3.33}$$

$$\mathbf{g} := (g_i)_{i=0}^{n_\chi-1}\,, \qquad \mathbf{N}^\chi := (N_i^{p_\chi})_{i=0}^{n_\chi-1}\,, \qquad \mathbf{D}^\chi := (D_i^{p_\chi})_{i=0}^{d_\chi-1}\,, \tag{3.34}$$

functions $f_h \in V_h^{s,0}$ and $g_h \in V_h^{\chi,0}$ and their derivatives $f_h' \in V_h^{s,1}$ and $g_h' \in V_h^{\chi,1}$ can compactly be written as

$$f_h = \mathbf{f}^\top \mathbf{N}^s\,, \qquad\qquad f_h' = (\mathbb{G}^s\,\mathbf{f})^\top \mathbf{D}^s\,, \tag{3.35}$$

$$g_h = \mathbf{g}^\top \mathbf{N}^\chi\,, \qquad\qquad g_h' = (\mathbb{G}^\chi\,\mathbf{g})^\top \mathbf{D}^\chi\,, \tag{3.36}$$

respectively. We remark that here and in the following, when we deal with sets of FE coefficients, basis functions etc. (bold symbols), we always assume them to be **column** vectors when actual calculations are performed. **Row** vectors therefore always appear with the transposed sign $(\cdot)^\top$.

To represent three-dimensional functions, we use a 2d tensor product representation of the introduced clamped B-splines in s-direction and periodic B-splines in χ-direction, supplemented with a Fourier harmonic in toroidal (φ-) direction. A discrete 0-form is therefore written as

$$f_h^0(s,\chi,\varphi) = \sum_{k=0}^{1} f_{h,k}^0(s,\chi)\,\mathcal{F}_k^n(\varphi) = \sum_{i=0}^{n_s-1} \sum_{j=0}^{n_\chi-1} \sum_{k=0}^{1} f_{(ijk)} N_i^{p_s}(s)\, N_j^{p_\chi}(\chi)\,\mathcal{F}_k^n(\varphi)\,. \tag{3.37}$$

Multi-indices ijk are "flattened" in row-major ordering (last index runs first). In (3.37), we therefore introduced the *flattened-index notation* $(ijk) := 2\,(j_{\max}+1)\,i + 2j + k$ which allows us to stack tensor product basis functions (and FE coefficients) as

$$\mathbf{\Lambda}^0 := \left(\Lambda_{(ijk)}^0\right) \in \mathbb{R}^{2 n_s n_\chi}\,, \qquad \Lambda_{(ijk)}^0 := N_i^{p_s} N_j^{p_\chi} \mathcal{F}_k^n\,. \tag{3.38}$$

A few words regarding the notation: and indexed object inside a parenthesis, e.g. $(\Lambda_{(ijk)}^0)$, denotes the ordered set of all objects resulting from all possible indices. In the 1d case, we have always explicitly given the range for the indices (e.g. in (3.33)) but in higher dimensions we simply assume the ranges to be known in order to improve readability. If a range is not clear, we

shall still give it explicitly. To represent discrete 1-forms and 2-forms we introduce the following sets of vector-valued basis functions:

$$\vec{\mathbf{\Lambda}}^1 := \left(\vec{\mathbf{\Lambda}}^1_1,\, \vec{\mathbf{\Lambda}}^1_2,\, \vec{\mathbf{\Lambda}}^1_3\right) \quad \begin{cases} \vec{\mathbf{\Lambda}}^1_1 := \left(\vec{\Lambda}^1_{1,(ijk)}\right) \in \mathbb{R}^{2d_s n_\chi}\,, & \vec{\Lambda}^1_{1,(ijk)} := \begin{bmatrix} D_i^{p_s} N_j^{p_\chi} \mathcal{F}_k^n \\ 0 \\ 0 \end{bmatrix}, \\ \vec{\mathbf{\Lambda}}^1_2 := \left(\vec{\Lambda}^1_{2,(ijk)}\right) \in \mathbb{R}^{2n_s d_\chi}\,, & \vec{\Lambda}^1_{2,(ijk)} := \begin{bmatrix} 0 \\ N_i^{p_s} D_j^{p_\chi} \mathcal{F}_k^n \\ 0 \end{bmatrix}, \\ \vec{\mathbf{\Lambda}}^1_3 := \left(\vec{\Lambda}^1_{3,(ijk)}\right) \in \mathbb{R}^{2n_s n_\chi}\,, & \vec{\Lambda}^1_{3,(ijk)} := \begin{bmatrix} 0 \\ 0 \\ N_i^{p_s} N_j^{p_\chi} \mathcal{F}_k^n \end{bmatrix}, \end{cases} \tag{3.39}$$

$$\vec{\mathbf{\Lambda}}^2 := \left(\vec{\mathbf{\Lambda}}^2_1,\, \vec{\mathbf{\Lambda}}^2_2,\, \vec{\mathbf{\Lambda}}^2_3\right) \quad \begin{cases} \vec{\mathbf{\Lambda}}^2_1 := \left(\vec{\Lambda}^2_{1,(ijk)}\right) \in \mathbb{R}^{2n_s d_\chi}\,, & \vec{\Lambda}^2_{1,(ijk)} := \begin{bmatrix} N_i^{p_s} D_j^{p_\chi} \mathcal{F}_k^n \\ 0 \\ 0 \end{bmatrix}, \\ \vec{\mathbf{\Lambda}}^2_2 := \left(\vec{\Lambda}^2_{2,(ijk)}\right) \in \mathbb{R}^{2d_s n_\chi}\,, & \vec{\Lambda}^2_{2,(ijk)} := \begin{bmatrix} 0 \\ D_i^{p_s} N_j^{p_\chi} \mathcal{F}_k^n \\ 0 \end{bmatrix}, \\ \vec{\mathbf{\Lambda}}^2_3 := \left(\vec{\Lambda}^2_{3,(ijk)}\right) \in \mathbb{R}^{2d_s d_\chi}\,, & \vec{\Lambda}^2_{3,(ijk)} := \begin{bmatrix} 0 \\ 0 \\ D_i^{p_s} D_j^{p_\chi} \mathcal{F}_k^n \end{bmatrix}, \end{cases} \tag{3.40}$$

where the arrow notation is used to highlight the fact that $\vec{\mathbf{\Lambda}}^1$ and $\vec{\mathbf{\Lambda}}^2$ contain vector-valued basis functions. Finally, a basis for discrete 3-forms is given by

$$\mathbf{\Lambda}^3 := \left(\Lambda^3_{(ijk)}\right) \in \mathbb{R}^{2d_s d_\chi}\,, \qquad \Lambda^3_{(ijk)} := D_i^{p_s} D_j^{p_\chi} \mathcal{F}_k^n\,. \tag{3.41}$$

The bases (3.38)-(3.41) allow for a straightforward definition of finite-dimensional subspaces of (3.9):

$$V_h^0 := \operatorname{span}\left(\mathbf{\Lambda}^0\right), \quad V_h^1 := \operatorname{span}\left(\vec{\mathbf{\Lambda}}^1\right), \quad V_h^2 := \operatorname{span}\left(\vec{\mathbf{\Lambda}}^2\right), \quad V_h^3 := \operatorname{span}\left(\mathbf{\Lambda}^3\right), \tag{3.42}$$

with dimensions $n^k := \dim V_h^k$. Similar to (3.35) and (3.36), elements of these spaces can be written compactly as

$$V_h^0 \ni f_h^0 = \mathcal{S}_0[\,\mathbf{f}\,] = \mathbf{f}^\top \mathbf{\Lambda}^0\,, \qquad \mathbf{f} := \left(f_{(ijk)}\right), \tag{3.43}$$

$$V_h^1 \ni \mathbf{E}_h^1 = \mathcal{S}_1[\,\vec{\mathbf{e}}\,] = \vec{\mathbf{e}}^\top \vec{\mathbf{\Lambda}}^1\,, \qquad \vec{\mathbf{e}} := \left(\mathbf{e}_1 := (e_{1,(ijk)}),\, \mathbf{e}_2 := (e_{2,(ijk)}),\, \mathbf{e}_3 := (e_{3,(ijk)})\right), \tag{3.44}$$

$$V_h^2 \ni \mathbf{B}_h^2 = \mathcal{S}_2[\,\vec{\mathbf{b}}\,] = \vec{\mathbf{b}}^\top \vec{\mathbf{\Lambda}}^2\,, \qquad \vec{\mathbf{b}} := \left(\mathbf{b}_1 := (b_{1,(ijk)}),\, \mathbf{b}_2 := (b_{2,(ijk)}),\, \mathbf{b}_3 := (b_{3,(ijk)})\right), \tag{3.45}$$

$$V_h^3 \ni p_h^3 = \mathcal{S}_3[\,\mathbf{p}\,] = \mathbf{p}^\top \mathbf{\Lambda}^3\,, \qquad \mathbf{p} := \left(p_{(ijk)}\right), \tag{3.46}$$

where the operators $\mathcal{S}_k : \mathbb{R}^{n^k} \to V_h^k$ $(0 \leq k \leq 3)$ map FE coefficients to the corresponding spline space V_h^k. With regards to derivatives (grad, curl and div), let us introduce the tensor product

matrices

$$\mathbb{D}^s := \mathbb{G}^s \otimes \mathbb{1}^\chi \otimes \mathbb{1}_2\,, \qquad \mathbb{D}^\chi := \mathbb{1}^s \otimes \mathbb{G}^\chi \otimes \mathbb{1}_2\,, \qquad \mathbb{D}^\varphi := \mathbb{1}^s \otimes \mathbb{1}^\chi \otimes \mathbb{G}^\varphi\,, \tag{3.47}$$

where $\otimes$ denotes the Kronecker product of two matrices. The size of the identity matrices $\mathbb{1}^s$ and $\mathbb{1}^\chi$ will be adapted to the corresponding space it acts on; hence $\mathbb{1}^s = \mathbb{1}_{n_s}$ or $\mathbb{1}^s = \mathbb{1}_{d_s}$ and accordingly for $\mathbb{1}^\chi$. The derivative matrices $\mathbb{G}^s$ and $\mathbb{G}^\chi$ are given in (3.32). The derivative matrix $\mathbb{G}^\varphi \in \mathbb{R}^{2\times 2}$ is obtained by noting that

$$\frac{\partial}{\partial\varphi}\sum_{k=0}^{1} f^0_{h,k}\mathcal{F}^n_k(\varphi) = -2\pi n\sum_{k=0}^{1}\operatorname{sgn}\left(k-\frac{1}{2}\right) f^0_{h,k+1}\mathcal{F}^n_k(\varphi) \quad\Rightarrow\quad \mathbb{G}^\varphi := \begin{bmatrix} 0 & 2\pi n \\ -2\pi n & 0 \end{bmatrix}, \tag{3.48}$$

where $\operatorname{sgn}(\cdot)$ is the sign function such that $\operatorname{sgn}(k-1/2) = -1$ for $k = 0$ and $\operatorname{sgn}(k-1/2) = +1$ for $k = 1$. Thus, the following derivatives are easily computed in view of (3.30) and (3.31),

$$\hat\nabla f^0_h = (\mathbb{G}\,\mathbf{f})^\top \vec{\mathbf{\Lambda}}^1 \in V^1_h\,, \qquad \mathbb{G} := \begin{bmatrix} \mathbb{D}^s \\ \mathbb{D}^\chi \\ \mathbb{D}^\varphi \end{bmatrix}, \tag{3.49}$$

$$\hat\nabla \times \mathbf{E}^1_h = (\mathbb{C}\,\vec{\mathbf{e}})^\top \vec{\mathbf{\Lambda}}^2 \in V^2_h\,, \qquad \mathbb{C} := \begin{bmatrix} 0 & -\mathbb{D}^\varphi & \mathbb{D}^\chi \\ \mathbb{D}^\varphi & 0 & -\mathbb{D}^s \\ -\mathbb{D}^\chi & \mathbb{D}^s & 0 \end{bmatrix}, \tag{3.50}$$

$$\hat\nabla \cdot \mathbf{B}^2_h = (\mathbb{D}\,\vec{\mathbf{b}})^\top \mathbf{\Lambda}^3 \in V^3_h\,, \qquad \mathbb{D} := \left[\begin{array}{c|c|c} \mathbb{D}^s & \mathbb{D}^\chi & \mathbb{D}^\varphi \end{array}\right], \tag{3.51}$$

By construction, it is immediately evident that $\mathbb{C}\,\mathbb{G} = 0$ and $\mathbb{D}\,\mathbb{C} = 0$ which allows the construction of the discrete de Rham complex

$$V^0_h \xrightarrow{\text{grad}\,/\,\mathbb{G}} V^1_h \xrightarrow{\text{curl}\,/\,\mathbb{C}} V^2_h \xrightarrow{\text{div}\,/\,\mathbb{D}} V^3_h\,, \tag{3.52}$$

in the same way as in the continuous case (3.10). Finally, we define mass matrices $\mathbb{M}^k$ related to each space V^k_h. They are obtained by replacing the continuous fields in the L^2-scalar products (3.8) with their discrete counterparts:

$$\mathbb{M}^0_{(ijk)(mno)} := \int_{\hat\Omega} \Lambda^0_{(ijk)}\,\Lambda^0_{(mno)}\sqrt{g}\,\mathrm{d}s\,\mathrm{d}\chi\,\mathrm{d}\varphi\,, \tag{3.53a}$$

$$\mathbb{M}^1 := [\mathbb{M}^1_{\mu\nu}]\,, \qquad \left(\mathbb{M}^1_{\mu\nu}\right)_{(ijk)(mno)} := \int_{\hat\Omega} (\vec\Lambda^1_{\mu,(ijk)}\cdot\vec{\mathbf{e}}_\mu)\,G^{-1}_{\mu\nu}\,(\vec\Lambda^1_{\nu,(mno)}\cdot\vec{\mathbf{e}}_\nu)\sqrt{g}\,\mathrm{d}s\,\mathrm{d}\chi\,\mathrm{d}\varphi\,, \tag{3.53b}$$

$$\mathbb{M}^2 := [\mathbb{M}^2_{\mu\nu}]\,, \qquad \left(\mathbb{M}^2_{\mu\nu}\right)_{(ijk)(mno)} := \int_{\hat\Omega} (\vec\Lambda^2_{\mu,(ijk)}\cdot\vec{\mathbf{e}}_\mu)\,G_{\mu\nu}\,(\vec\Lambda^2_{\nu,(mno)}\cdot\vec{\mathbf{e}}_\nu)\frac{1}{\sqrt{g}}\,\mathrm{d}s\,\mathrm{d}\chi\,\mathrm{d}\varphi\,, \tag{3.53c}$$

$$\mathbb{M}^3_{(ijk)(mno)} := \int_{\hat\Omega} \Lambda^3_{(ijk)}\,\Lambda^3_{(mno)}\frac{1}{\sqrt{g}}\,\mathrm{d}s\,\mathrm{d}\chi\,\mathrm{d}\varphi\,. \tag{3.53d}$$

Here, $\mathbf{e}_1 := [\,1,0,0\,]$, $\mathbf{e}_2 := [\,0,1,0\,]$ and $\mathbf{e}_3 := [\,0,0,1\,]$. Moreover, $\mathbb{M}^1$ and $\mathbb{M}^2$ are 3×3 block matrices ($\mu,\nu = 1,2,3$ in (3.53b) and (3.53c)). In what follows, we shall use the square bracket notation $[\,\mathbb{A}_{\mu\nu}\,]$ to denote 3×3 block matrices.

To incorporate the boundary conditions in the same way as in (3.11), we finally introduce *boundary operators* $\mathbb{B}^k$ ($0 \le k \le 3$) whose application on the complete set of basis functions

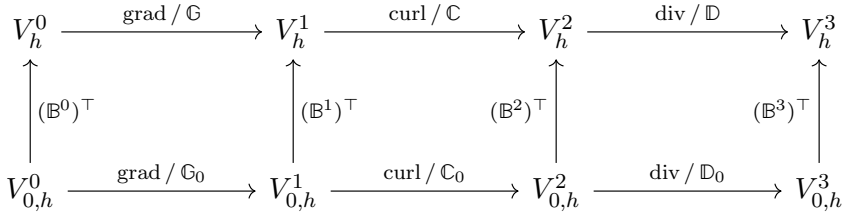

Figure 3.3: Commuting diagram for full spline spaces (3.42) (upper line) and reduced boundary spaces (3.54) (lower line). Both sequences form discrete de Rham complexes and are connected via the transposed boundary operators (3.56) and (3.57).

spanning the spaces V_h^k (3.42) form reduced bases spanning subspaces $V_{0,h}^k$ satisfying the same boundary conditions as in (3.11):

$$V_{0,h}^k := \operatorname{span}\left(\boldsymbol{\Lambda}_0^k := \mathbb{B}^k \boldsymbol{\Lambda}^k \right) \quad k = 0, 3\,, \qquad V_{0,h}^k := \operatorname{span}\left(\vec{\boldsymbol{\Lambda}}_0^k := \mathbb{B}^k \vec{\boldsymbol{\Lambda}}^k \right) \quad k = 1, 2\,. \tag{3.54}$$

Thanks to the property of clamped B-splines being interpolatory at the boundaries (3.22), the operators $\mathbb{B}^k$ have a simple form and just have to make sure that basis functions of V_h^k having contributions from $N_0^{p_s}$ and $N_{n_s-1}^{p_s}$ are eliminated. This can be achieved with the help of the matrix

$$\mathbb{B}^s := \begin{bmatrix} 0 & 1 & 0 & \cdots & 0 & 0 \\ 0 & 0 & 1 & & 0 & 0 \\ \vdots & \vdots & & \ddots & \vdots & \vdots \\ 0 & 0 & 0 & \cdots & 1 & 0 \end{bmatrix} \in \mathbb{R}^{(n_s-2)\times n_s}\,, \tag{3.55}$$

which is the identity matrix of size $(n_s - 2) \times (n_s - 2)$ supplemented with two columns of zeros at the beginning and the end. The dimensions $n_0^k := \dim V_{0,h}^k$ are thus $n_0^0 := n^0 - 4n_\chi$, $n_0^1 := n^1 - 4n_\chi - 4d_\chi$, $n_0^2 := n^2 - 4d_\chi$ and $n_0^3 := n^3$ and the boundary operators read

$$\mathbb{B}^0 := \mathbb{B}^s \otimes \mathbb{1}_{n_\chi} \otimes \mathbb{1}_2\,, \quad \mathbb{B}^1 := \begin{bmatrix} \mathbb{B}_1^1 := \mathbb{1}_{d_s} \otimes \mathbb{1}_{n_\chi} \otimes \mathbb{1}_2 & 0 & 0 \\ 0 & \mathbb{B}_2^1 := \mathbb{B}^s \otimes \mathbb{1}_{d_\chi} \otimes \mathbb{1}_2 & 0 \\ 0 & 0 & \mathbb{B}_3^1 := \mathbb{B}^0 \end{bmatrix}, \tag{3.56}$$

$$\mathbb{B}^3 := \mathbb{1}_{n^3}\,, \qquad \mathbb{B}^2 := \begin{bmatrix} \mathbb{B}_1^2 := \mathbb{B}^s \otimes \mathbb{1}_{d_\chi} \otimes \mathbb{1}_2 & 0 & 0 \\ 0 & \mathbb{B}_1^2 := \mathbb{1}_{d_s} \otimes \mathbb{1}_{n_\chi} \otimes \mathbb{1}_2 & 0 \\ 0 & 0 & \mathbb{B}_3^2 := \mathbb{B}^3 \end{bmatrix}. \tag{3.57}$$

Since the boundary spaces $V_{0,h}^k$ are subspaces of V_h^k, it is always possible to express an element in $V_{0,h}^k$ in the basis of V_h^k because

$$V_{0,h}^k \ni f_h^0 = \mathbf{f}^\top \boldsymbol{\Lambda}_0^0 = \mathbf{f}^\top \mathbb{B}^0 \boldsymbol{\Lambda}^0 = \left[(\mathbb{B}^0)^\top \mathbf{f} \right]^\top \boldsymbol{\Lambda}^0\,, \tag{3.58}$$

and similarly for $k > 0$. Consequently, for given FE coefficient $\mathbf{f}$ of an element in $V_{0,h}^k$, the corresponding FE coefficients in the full space V_h^k are obtained via $(\mathbb{B}^k)^\top \mathbf{f}$. This allows for a straightforward incorporation of boundary conditions into the mass matrices (3.53):

$$\mathbb{M}_0^0 := \mathbb{B}^0\, \mathbb{M}^0 (\mathbb{B}^0)^\top\,, \quad \mathbb{M}_0^1 := \mathbb{B}^1\, \mathbb{M}^1 (\mathbb{B}^1)^\top\,, \quad \mathbb{M}_0^2 := \mathbb{B}^2\, \mathbb{M}^2 (\mathbb{B}^2)^\top\,, \quad \mathbb{M}_0^3 := \mathbb{B}^3\, \mathbb{M}^3 (\mathbb{B}^3)^\top\,. \tag{3.59}$$

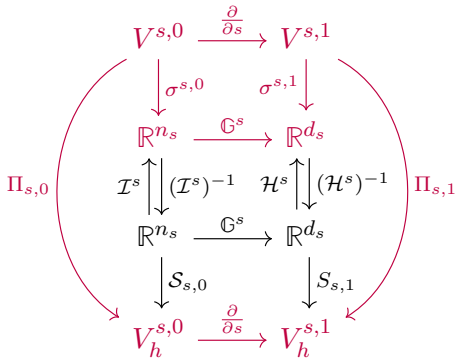

Figure 3.4: Commuting diagram in 1d using the notions of degrees of freedom (DOFs) $\sigma^{s,0}$ and $\sigma^{s,1}$ and finite element (FE) coefficients.

Moreover, we aim for new discrete derivatives $\mathbb{G}_0$, $\mathbb{C}_0$ and $\mathbb{D}_0$ acting on FE coefficients in the reduced spaces $V_{0,h}^k$ in a way that we obtain the commuting diagram shown in Figure 3.3. This is because one should obtain the same result no matter if e.g. one first prolongs the FE coefficients to the full space V_h^0 and then takes the discrete gradient $\mathbb{G}$ or if one first takes a (yet to define) discrete gradient $\mathbb{G}_0$ and then prolongs to the full space V_h^1. Hence, the defining relations for the new discrete derivatives are the commutativity relations

$$\mathbb{G}\,(\mathbb{B}^0)^\top = (\mathbb{B}^1)^\top\,\mathbb{G}_0\,, \qquad \mathbb{C}\,(\mathbb{B}^1)^\top = (\mathbb{B}^2)^\top\,\mathbb{C}_0\,, \qquad \mathbb{D}\,(\mathbb{B}^2)^\top = (\mathbb{B}^3)^\top\,\mathbb{D}_0\,, \tag{3.60}$$

which lead to the simple definitions

$$\mathbb{G}_0 := \mathbb{B}^1\,\mathbb{G}\,(\mathbb{B}^0)^\top\,, \qquad \mathbb{C}_0 := \mathbb{B}^2\,\mathbb{C}\,(\mathbb{B}^1)^\top\,, \qquad \mathbb{D}_0 := \mathbb{B}^3\,\mathbb{D}\,(\mathbb{B}^2)^\top\,. \tag{3.61}$$

for the new discrete derivatives. Going from (3.60) to (3.61) is due to the fact that $\mathbb{B}^k(\mathbb{B}^k)^\top = \mathbb{1}_{n_0^k}$. Finally, a direct consequence of the commutativity relations (3.60) is that the reduced spaces $V_{0,h}^k$ once more form a discrete de Rham complex as shown in the lower line of the diagram in Figure 3.3.

3.4 Degrees of freedom and commuting diagram

Now that we have infinite-dimensional function spaces and finite-dimensional subspaces which both form de Rham complexes, the next question is how to connect these two complexes, i.e. for given functions in V^k, what are good approximations that live in V_0^k? In the framework of FEEC, this connection is obtained via so-called *commuting projectors*. We shall first introduce the basic notions and notations in 1d and subsequently extend to 3d. These constructions are based on [59].

A good understanding of the commuting projectors can be obtained in terms of the 1d diagram in Figure 3.4. We choose the s-space in this example, the χ-direction is treated in full analogy (even though the spaces are slightly different because of the boundaries). The upper row of the diagram contains the continuous function spaces $V^{s,0} = H^1(\hat{\Omega}^s)$ and $V^{s,1} = L^2(\hat{\Omega}^s)$ with $\hat{\Omega}^s = [0,1]$. The *degrees of freedom* (DOFs) $\sigma^{s,0} : V^{s,0} \to \mathbb{R}^{n_s}$ and $\sigma^{s,1} : V^{s,1} \to \mathbb{R}^{d_s}$ are linear functionals on the continuous spaces, with their image in the second row. The third row contains the *finite element (FE) coefficients* (in the spline bases) and the fourth row the FE spaces $V_h^{s,0} \subset V^{s,0}$ and $V_h^{s,1} \subset V^{s,1}$ spanned by the 1d spline bases and introduced in (3.29).

When dealing with inter-/histopolation, the DOFs can be defined as

$$f \in V^{s,0}: \qquad \boldsymbol{\sigma}^{s,0} := (\sigma_i^{s,0})_{i=0}^{n_s-1}\,, \qquad \sigma_i^{s,0}(f) := f(\mathfrak{s}_i)\,, \tag{3.62a}$$

$$g \in V^{s,1}: \qquad \boldsymbol{\sigma}^{s,1} := (\sigma_i^{s,1})_{i=0}^{d_s-1}\,, \qquad \sigma_i^{s,1}(g) := \int_{\mathfrak{s}_i}^{\mathfrak{s}_{i+1}} g(s)\,\mathrm{d}s\,. \tag{3.62b}$$

Here, $\mathfrak{s} = (\mathfrak{s}_i)_{i=0}^{n_s-1}$ are the interpolation points in $\hat{\Omega}^s$, for example the Greville points of a spline basis (3.28), and $d_s = n_s - 1$ is the number of histopolation intervals. The bases of the FE spaces $V_h^{s,0}$ and $V_h^{s,1}$ appear in the inter-/histopolation matrices

$$\mathcal{I}_{ij}^s := N_j^{p_s}(\mathfrak{s}_i)\,, \qquad \mathcal{H}_{ij}^s := \int_{\mathfrak{s}_i}^{\mathfrak{s}_{i+1}} D_j^{p_s}(s)\,\mathrm{d}s\,, \tag{3.63}$$

respectively. The interpolation points $\mathfrak{s}$ have to be chosen such that $\mathcal{I}^s$ and $\mathcal{H}^s$ are invertible (that is the reason for Greville points with splines, usually). When using, for instance, a quadrature rule of sufficient order for computing integrals, the matrix $\mathcal{H}^s$ is exact since M-splines are piecewise polynomials.

The operators $\mathcal{S}_{s,0} : \mathbb{R}^{n_s} \to V_h^{s,0}$ and $\mathcal{S}_{s,1} : \mathbb{R}^{d_s} \to V_h^{s,1}$ map FE coefficients to the corresponding spline function:

$$V_h^{s,0} \ni f_h = S_{s,0}[\,\mathbf{f}\,](s) = \sum_{j=0}^{n_s-1} f_j\, N_j^{p_s}(s)\,, \qquad \mathbf{f} = (f_j)_{j=0}^{n_s-1}\,, \tag{3.64a}$$

$$V_h^{s,1} \ni g_h = S_{s,1}[\,\mathbf{g}\,](s) = \sum_{j=0}^{d_s-1} g_j\, D_j^{p_s}(s)\,, \qquad \mathbf{g} = (g_j)_{j=0}^{d_s-1}\,. \tag{3.64b}$$

For the DOFs (3.62) this means

$$\sigma_i^{s,0}(f_h) = \sum_{j=0}^{n_s-1} f_j\, N_j^{p_s}(\mathfrak{s}_i) = \sum_j \mathcal{I}_{ij}^s\, f_j \qquad \Rightarrow \quad \sigma^{s,0}(f_h) = \mathcal{I}^s\,\mathbf{f}\,, \tag{3.65a}$$

$$\sigma_i^{s,1}(g_h) = \sum_{j=0}^{d_s-1} g_j \int_{\mathfrak{s}_i}^{\mathfrak{s}_{i+1}} D_j^{p_s}(s)\,\mathrm{d}s = \sum_j \mathcal{H}_{ij}^s\, g_j \quad \Rightarrow \quad \sigma^{s,1}(g_h) = \mathcal{H}^s\,\mathbf{g}\,, \tag{3.65b}$$

such that it is evident that the DOFs (3.62) uniquely define an element in $V_h^{s,0}$ and $V_h^{s,1}$ provided that $\mathcal{I}^s$ and $\mathcal{H}^s$ are invertible.

Definition 1. *The projectors $\Pi_{s,0} : V^{s,0} \to V_h^{s,0}$ and $\Pi_{s,1} : V^{s,1} \to V_h^{s,1}$ are defined via the DOFs:*

$$\sigma^{s,0}(\Pi_{s,0}(f)) = \sigma^{s,0}(f)\,, \qquad \sigma^{s,1}(\Pi_{s,1}(g)) = \sigma^{s,1}(g)\,. \tag{3.66}$$

Proposition 1. *Provided that the histopolation matrix $\mathcal{H}^s$ is exact, the projectors* (3.66) *satisfy*

$$\Pi_{s,1}\left(\frac{\partial f}{\partial s}\right) = \frac{\partial}{\partial s}\Pi_{s,0}(f). \tag{3.67}$$

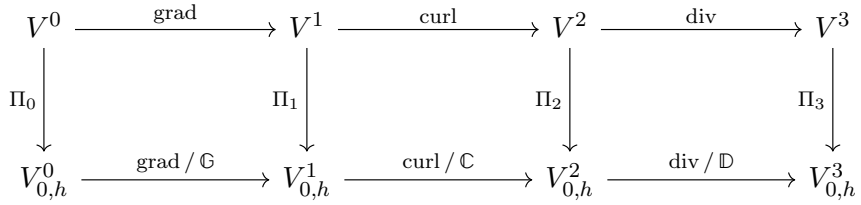

Figure 3.5: Commuting diagram for infinite-dimensional Sobolev spaces of differential forms (upper line) and finite-dimensional subspaces (lower line). Both sequences form discrete de Rham complexes and are connected via commuting projectors.

Proof. By definition both sides of the equality are in $V_h^{s,1}$. Since an element in $V_h^{s,1}$ is uniquely defined by its DOFs, we can apply $\sigma_i^{s,1}$ on both sides and show the results to be equal:

$$\sigma_i^{s,1}\left(\Pi_{s,1}\left(\frac{\partial f}{\partial s}\right)\right) \overset{(3.66)}{=} \sigma_i^{s,1}\left(\frac{\partial f}{\partial s}\right) = f(\mathfrak{s}_{i+1}) - f(\mathfrak{s}_i) = \sigma_{i+1}^{s,0}(f) - \sigma_i^{s,0}(f)\,,$$

$$\sigma_i^{s,1}\left(\frac{\partial}{\partial s}\Pi_{s,0}(f)\right) = \Pi_{s,0}(f)(\mathfrak{s}_{i+1}) - \Pi_{s,0}(f)(\mathfrak{s}_i) = \sigma_{i+1}^{s,0}(\Pi_{s,0}(f)) - \sigma_i^{s,0}(\Pi_{s,0}(f))$$

$$\overset{(3.66)}{=} \sigma_{i+1}^{s,0}(f) - \sigma_i^{s,0}(f)\,.$$

□

We note that this proof did not rely on the choice of basis functions. The DOFs defined by (3.62) and projectors defined in Definition 1 are *sufficient conditions* for the commuting property.

Let us now shift to the spaces V^k $(0 \leq k \leq 3)$ defined in (3.9). The corresponding commuting diagram is depicted in Figure 3.5. To define the DOFs, we consider the tensor product grid $(\mathfrak{s}_i, \mathfrak{t}_j)$ built from the additional 1d set of Greville points $\mathfrak{t} = (\mathfrak{t}_j)_{j=0}^{n_\chi - 1}$ in χ-direction. The DOFs can then be defined as

$$f^0 \in V^0: \qquad \sigma^0_{(ijk)}(f^0) := f^0_k(\mathfrak{s}_i, \mathfrak{t}_j)\,, \tag{3.68a}$$

$$\mathbf{E}^1 \in V^1: \quad \begin{cases} \sigma^1_{1,(ijk)}(\mathbf{E}^1) := \displaystyle\int_{\mathfrak{s}_i}^{\mathfrak{s}_{i+1}} E^1_{1,k}(s, \mathfrak{t}_j)\,\mathrm{d}s\,, \\ \sigma^1_{2,(ijk)}(\mathbf{E}^1) := \displaystyle\int_{\mathfrak{t}_j}^{\mathfrak{t}_{j+1}} E^1_{2,k}(\mathfrak{s}_i, \chi)\,\mathrm{d}\chi\,, \\ \sigma^1_{3,(ijk)}(\mathbf{E}^1) := E^1_{3,k}(\mathfrak{s}_i, \mathfrak{t}_j)\,, \end{cases} \tag{3.68b}$$

$$\mathbf{B}^2 \in V^2: \quad \begin{cases} \sigma^2_{1,(ijk)}(\mathbf{B}^2) := \displaystyle\int_{\mathfrak{t}_j}^{\mathfrak{t}_{j+1}} B^2_{1,k}(\mathfrak{s}_i, \chi)\,\mathrm{d}\chi\,, \\ \sigma^2_{2,(ijk)}(\mathbf{B}^2) := \displaystyle\int_{\mathfrak{s}_i}^{\mathfrak{s}_{i+1}} B^2_{2,k}(s, \mathfrak{t}_j)\,\mathrm{d}s\,, \\ \sigma^2_{3,(ijk)}(\mathbf{B}^2) := \displaystyle\int_{\mathfrak{s}_i}^{\mathfrak{s}_{i+1}} \int_{\mathfrak{t}_j}^{\mathfrak{t}_{j+1}} B^2_{3,k}(s, \chi)\,\mathrm{d}s\,\mathrm{d}\chi\,, \end{cases} \tag{3.68c}$$

$$p^3 \in V^3 : \qquad \sigma^3_{(ijk)}(p^3) := \int_{\mathfrak{s}_i}^{\mathfrak{s}_{i+1}} \int_{\mathfrak{t}_j}^{\mathfrak{t}_{j+1}} p^3_k(s,\chi)\,\mathrm{d}s\,\mathrm{d}\chi\,. \tag{3.68d}$$

Similar to (3.65) we have for discrete functions

$$f^0_h = \mathcal{S}_0[\,\mathbf{f}\,] \in V^0_h : \quad \sigma^0(f^0_h) = \mathcal{I}^0\,\mathbf{f}\,, \qquad \mathbf{E}^1_h = \mathcal{S}_1[\,\vec{\mathbf{e}}\,] \in V^1_h : \quad \sigma^1(\mathbf{E}^1_h) = \mathcal{I}^1\,\vec{\mathbf{e}}\,, \tag{3.69a}$$

$$p^3_h = \mathcal{S}_3[\,\mathbf{p}\,] \in V^3_h : \quad \sigma^3(p^3_h) = \mathcal{I}^3\,\mathbf{p}\,, \qquad \mathbf{B}^2_h = \mathcal{S}_2[\,\vec{\mathbf{b}}\,] \in V^2_h : \quad \sigma^2(\mathbf{B}^2_h) = \mathcal{I}^2\,\vec{\mathbf{b}}\,, \tag{3.69b}$$

where the mixed inter-/histopolation matrices $\mathcal{I}^k$ are given by

$$\mathcal{I}^0 := \mathcal{I}^s \otimes \mathcal{I}^\chi \otimes \mathbb{1}_2\,, \qquad \mathcal{I}^1 := \begin{bmatrix} \mathcal{H}^s \otimes \mathcal{I}^\chi \otimes \mathbb{1}_2 & 0 & 0 \\ 0 & \mathcal{I}^s \otimes \mathcal{H}^\chi \otimes \mathbb{1}_2 & 0 \\ 0 & 0 & \mathcal{I}^s \otimes \mathcal{I}^\chi \otimes \mathbb{1}_2 \end{bmatrix}, \tag{3.70a}$$

$$\mathcal{I}^3 := \mathcal{H}^s \otimes \mathcal{H}^\chi \otimes \mathbb{1}_2\,, \qquad \mathcal{I}^2 := \begin{bmatrix} \mathcal{I}^s \otimes \mathcal{H}^\chi \otimes \mathbb{1}_2 & 0 & 0 \\ 0 & \mathcal{H}^s \otimes \mathcal{I}^\chi \otimes \mathbb{1}_2 & 0 \\ 0 & 0 & \mathcal{H}^s \otimes \mathcal{H}^\chi \otimes \mathbb{1}_2 \end{bmatrix}. \tag{3.70b}$$

Definition 2. *The projectors $\Pi_k : V^k \to V^k_h$ $(0 \le k \le 3)$ are defined via the DOFs* (3.68)*:*

$$\sigma^0(\Pi_0(f^0)) = \sigma^0(f^0)\,, \qquad \sigma^1(\Pi_1(\mathbf{E}^1)) = \sigma^1(\mathbf{E}^1)\,, \tag{3.71a}$$

$$\sigma^3(\Pi_3(p^3)) = \sigma^3(p^3)\,, \qquad \sigma^2(\Pi_2(\mathbf{B}^2)) = \sigma^2(\mathbf{B}^2)\,. \tag{3.71b}$$

Proposition 2. *Provided that the integrals in* (3.68) *are exact, the projectors* (3.71) *satisfy the commutation relations*

$$\Pi_1\,\mathrm{grad} = \mathrm{grad}\,\Pi_0\,, \qquad \Pi_2\,\mathrm{curl} = \mathrm{curl}\,\Pi_1\,, \qquad \Pi_3\,\mathrm{div} = \mathrm{div}\,\Pi_2\,. \tag{3.72}$$

Proof. We only prove the first relation $\Pi_1\,\mathrm{grad} = \mathrm{grad}\,\Pi_0$ explicitly, the other two relations can be proven accordingly. By definition both sides are in V^1_h. Since an element in V^1_h is uniquely defined by its DOFs, we can apply σ^1 on both sides:

$$\sigma^1_{1,(ijk)}\left(\Pi_1(\hat{\nabla} f^0)\right) \overset{(3.71)}{=} \sigma^1_{1,(ijk)}\left(\hat{\nabla} f^0\right) = f^0_k(\mathfrak{s}_{i+1},\mathfrak{t}_j) - f^0_k(\mathfrak{s}_i,\mathfrak{t}_j) = \sigma^0_{(i+1jk)}\left(f^0\right) - \sigma^0_{(ijk)}\left(f^0\right)\,,$$

$$\sigma^1_{2,(ijk)}\left(\Pi_1(\hat{\nabla} f^0)\right) \overset{(3.71)}{=} \sigma^1_{2,(ijk)}\left(\hat{\nabla} f^0\right) = f^0_k(\mathfrak{s}_i,\mathfrak{t}_{j+1}) - f^0_k(\mathfrak{s}_i,\mathfrak{t}_j) = \sigma^0_{(ij+1k)}\left(f^0\right) - \sigma^0_{(ijk)}\left(f^0\right)\,,$$

$$\begin{aligned}\sigma^1_{3,(ijk)}\left(\Pi_1(\hat{\nabla} f^0)\right) \overset{(3.71)}{=} \sigma^1_{3,(ijk)}\left(\hat{\nabla} f^0\right) &= -2\pi n\,\mathrm{sgn}\left(k-\frac{1}{2}\right) f^0_{k+1}(\mathfrak{s}_i,\mathfrak{t}_j) \\ &= -2\pi n\,\mathrm{sgn}\left(k-\frac{1}{2}\right)\sigma^0_{(ijk+1)}(f^0)\,.\end{aligned}$$

On the other hand

$$\begin{aligned}\sigma^1_{1,(ijk)}\left(\hat{\nabla}\,\Pi_0(f^0)\right) &= [\Pi_0(f^0)]_k(\mathfrak{s}_{i+1},\mathfrak{t}_j) - [\Pi_0(f^0)]_k(\mathfrak{s}_i,\mathfrak{t}_j)\\ &= \sigma^0_{(i+1jk)}(\Pi_0(f^0)) - \sigma^0_{(ijk)}(\Pi_0(f^0)) \overset{(3.71)}{=} \sigma^0_{(i+1jk)}(f^0) - \sigma^0_{(ijk)}(f^0)\,,\\ \sigma^1_{2,(ijk)}\left(\hat{\nabla}\,\Pi_0(f^0)\right) &= [\Pi_0(f^0)]_k(\mathfrak{s}_i,\mathfrak{t}_{j+1}) - [\Pi_0(f^0)]_k(\mathfrak{s}_i,\mathfrak{t}_j)\\ &= \sigma^0_{(ij+1k)}(\Pi_0(f^0)) - \sigma^0_{(ijk)}(\Pi_0(f^0)) \overset{(3.71)}{=} \sigma^0_{(ij+1k)}(f^0) - \sigma^0_{(ijk)}(f^0)\,,\\ \sigma^1_{3,(ijk)}\left(\hat{\nabla}\,\Pi_0(f^0)\right) &= -2\pi n\,\mathrm{sgn}\left(k-\frac{1}{2}\right)[\Pi_0(f^0)]_{k+1}(\mathfrak{s}_i,\mathfrak{t}_j)\\ &= -2\pi n\,\mathrm{sgn}\left(k-\frac{1}{2}\right)\sigma^0_{ijk+1}(\Pi_0(f^0)) \overset{(3.71)}{=} -2\pi n\,\mathrm{sgn}\left(k-\frac{1}{2}\right)\sigma^0_{(ijk+1)}(f^0)\,.\end{aligned}$$

Because this holds for any (ijk) the first relation in (3.72) is proven. The proofs for the second and third relation work in full analogy. □

By identifying the projected functions with their spline coefficients as in (3.69),

$$\Pi_0(f^0) = \mathcal{S}_0[\,\mathbf{f}\,]\,, \qquad \Pi_1(\mathbf{E}^1) = \mathcal{S}_1[\,\vec{\mathbf{e}}\,]\,, \qquad \Pi_2(\mathbf{B}^2) = \mathcal{S}_2[\,\vec{\mathbf{b}}\,]\,, \qquad \Pi_3(p^3) = \mathcal{S}_3[\,\mathbf{p}\,]\,, \tag{3.73}$$

the projection problems (3.71) can be written as linear systems

$$\mathcal{I}^0\,\mathbf{f} = \sigma^0(f^0)\,, \qquad \mathcal{I}^1\,\vec{\mathbf{e}} = \sigma^1(\mathbf{E}^1)\,, \qquad \mathcal{I}^2\,\vec{\mathbf{b}} = \sigma^2(\mathbf{B}^2)\,, \qquad \mathcal{I}^3\,\mathbf{p} = \sigma^3(p^3)\,. \tag{3.74}$$

The solution of these linear systems can be done very efficiently because of the tensor product structure of the matrices $\mathcal{I}^k$, e.g. $(\mathcal{I}^0)^{-1} = (\mathcal{I}^s \otimes \mathcal{I}^\chi \otimes \mathbb{1}_2)^{-1} = (\mathcal{I}^s)^{-1} \otimes (\mathcal{I}^\chi)^{-1} \otimes \mathbb{1}_2$, and the costs for inverting the matrices $\mathcal{I}^s$ and $\mathcal{I}^\chi$ corresponding to 1d spline bases are negligible.

3.5 Spatial discretization

In this section, we perform the spatial discretization of the weak formulation (3.13) in order to arrive at a semi-discrete system with continuous time variable. We shall first focus on the MHD part followed by kinetic coupling terms and the Vlasov equation.

3.5.1 MHD equations

The spatial discretization of (3.13) is achieved by projecting the strong equations (3.13b) and (3.13c) onto the finite-dimensional subspaces $V^3_{0,h}$ and $V^2_{0,h}$ using the projectors Π_3 and Π_2, respectively, and replacing the trail and test functions in the weak momentum balance equation (3.13a) by their discrete counterparts. The time dependence is put into the FE coefficients such that

$$\mathbf{U}^2 \approx \mathbf{U}^2_h = \mathcal{S}_{2,0}[\,\vec{\mathbf{u}}(t)\,]\,, \qquad \mathbf{K}^2 \approx \mathbf{K}^2_h = \mathcal{S}_{2,0}[\,\vec{\mathbf{k}}(t)\,]\,, \tag{3.75}$$

$$\mathbf{B}^2 \approx \mathbf{B}^2_h = \mathcal{S}_{2,0}[\,\vec{\mathbf{b}}(t)\,]\,, \qquad p^3 \approx p^3_h = \mathcal{S}_{3,0}[\,\mathbf{p}(t)\,]\,, \tag{3.76}$$

where the operators $\mathcal{S}_{k,0} : \mathbb{R}^{n^k_0} \to V^k_{0,h}$ map FE coefficients of size n^k_0 to the corresponding boundary spline space $V^k_{0,h}$. Performing the above described discretization yields the semi-

discrete system

$$\mathbb{M}_0^{n_\mathrm{b}} \frac{\mathrm{d}\vec{\mathbf{u}}}{\mathrm{d}t} = \mathbb{D}_0^\top \mathbb{M}_0^3 \mathbf{p} + \mathcal{T}_0^\top (\mathcal{I}_0^1)^{-\top} \mathbb{C}_0^\top \mathbb{M}_0^2 \vec{\mathbf{b}} + \mathbb{M}_0^J \vec{\mathbf{b}}\,, \tag{3.77a}$$

$$\frac{\mathrm{d}\mathbf{p}}{\mathrm{d}t} = -\mathbb{D}_0 (\mathcal{I}_0^2)^{-1} \mathcal{F}_0 \vec{\mathbf{u}} - (\gamma - 1) (\mathcal{I}_0^3)^{-1} \mathcal{K}_0 \mathbb{D}_0 \vec{\mathbf{u}}\,, \tag{3.77b}$$

$$\frac{\mathrm{d}\vec{\mathbf{b}}}{\mathrm{d}t} = -\mathbb{C}_0 (\mathcal{I}_0^1)^{-1} \mathcal{T}_0 \vec{\mathbf{u}}\,. \tag{3.77c}$$

As stated before, the last two equations are obtained by applying the projectors Π_2 and Π_3 on the continuous equations (3.13b) and (3.13c), respectively. Where possible, the commuting diagram property (3.72) has been used to exchange projectors and differential operators. In particular, in (3.13b), we used $\Pi_3 \operatorname{div} = \operatorname{div} \Pi_2$ and in (3.13b) we used $\Pi_2 \operatorname{curl} = \operatorname{curl} \Pi_1$. In the first equation it is important to note that we applied the projector Π_2 to the second argument of the term

$$\left(\mathbf{B}^2, \hat{\nabla} \times \left(\frac{1}{\sqrt{g}} \mathbf{K}^2 \times \mathbf{B}^2_\mathrm{eq} \right) \right)_2\,, \tag{3.78}$$

in the weak momentum balance equation (3.13a). This is necessary to keep the symmetry with the induction equation which is important for energy conservation. Among the new matrices in (3.77) are the two weighted mass matrices

$$\mathbb{M}_0^{n_\mathrm{b}} := \mathbb{B}^2 \mathbb{M}^{n_\mathrm{b}} (\mathbb{B}^2)^\top\,, \qquad \left(\mathbb{M}^{n_\mathrm{b}}_{\mu\nu}\right)_{(ijk)(mno)} := \int_{\hat{\Omega}} \Lambda^2_{\mu,(ijk)} G_{\mu\nu} \Lambda^2_{\nu,(mno)} n^3_{\mathrm{b,eq}} \frac{1}{g} \,\mathrm{d}s\,\mathrm{d}\chi\,\mathrm{d}\varphi\,, \tag{3.79a}$$

$$\mathbb{M}_0^{J} := \mathbb{B}^2 \mathbb{M}^{J} (\mathbb{B}^2)^\top\,, \qquad \left(\mathbb{M}^{J}_{\mu\nu}\right)_{(ijk)(mno)} := \int_{\hat{\Omega}} \Lambda^2_{\mu,(ijk)} \epsilon_{\mu\alpha\nu} \Lambda^2_{\nu,(mno)} J^2_{\mathrm{eq},\alpha} \frac{1}{\sqrt{g}} \,\mathrm{d}s\,\mathrm{d}\chi\,\mathrm{d}\varphi\,, \tag{3.79b}$$

where $\mathbb{M}^{n_\mathrm{b}} = [\,\mathbb{M}^{n_\mathrm{b}}_{\mu\nu}\,]$ and $\mathbb{M}^{J} = [\,\mathbb{M}^{J}_{\mu\nu}\,]$ are 3×3 block matrices ($\mu, \nu = 1, 2, 3$ in (3.79)). Moreover, $\epsilon_{\mu\alpha\nu}$ are the components of the Levi-Civita tensor and $\Lambda^2_{\mu,(ijk)} = \vec{\Lambda}^2_{\mu,(ijk)} \cdot \vec{\mathbf{e}}_\mu$. Furthermore, we introduced the matrices

$$\mathcal{T}_0 := \mathbb{B}^1 \mathcal{T} (\mathbb{B}^2)^\top\,, \qquad \mathcal{T}_{\mu\nu,(ijk)(mno)} := \sigma^1_{\mu,(ijk)} \left[\frac{1}{\sqrt{g}} \left(\mathbf{B}^2_\mathrm{eq} \times \vec{\Lambda}^2_{\nu,(mno)} \right) \right]\,, \tag{3.80a}$$

$$\mathcal{F}_0 := \mathbb{B}^2 \mathcal{F} (\mathbb{B}^2)^\top\,, \qquad \mathcal{F}_{\mu\nu,(ijk)(mno)} := \sigma^2_{\mu,(ijk)} \left[\frac{p^3_\mathrm{eq}}{\sqrt{g}} \vec{\Lambda}^2_{\nu,(mno)} \right]\,, \tag{3.80b}$$

$$\mathcal{K}_0 := \mathbb{B}^3 \mathcal{K} (\mathbb{B}^2)^\top\,, \qquad \mathcal{K}_{(ijk)(mno)} := \sigma^3_{(ijk)} \left[\frac{p^3_\mathrm{eq}}{\sqrt{g}} \Lambda^3_{(mno)} \right]\,, \tag{3.80c}$$

which appear in (3.77) at places where a projector $\overline{\Pi}_k$ is applied. Finally, the modified inter-/histopolation matrices $\mathcal{I}_0^k := \mathbb{B}^k \mathcal{I}^k (\mathbb{B}^k)^\top$ in (3.77). They account for the boundary conditions and result from removing DOFs which are related to interpolation points on the domain boundaries at $s = 0$ and $s = 1$.

The initial-value problem (3.77) can be directly transferred to an eigenvalue problem by assuming a time variation $\sim \mathrm{e}^{-i\omega t}$ for all unknowns such that time derivatives can be replaced by $-i\omega$. Using an eigenvalue formulation instead of an initial-value one is simpler in a way that a) no initial conditions need to be prescribed and b) one obtains frequencies/growth rates $\omega \in \mathbb{C}$ for each eigenfunction (*normal mode*) which usually allows for a quicker insight into the underlying physics of the considered system. Performing the substitution $\mathrm{d}/\mathrm{d}t \to -i\omega$ in (3.77) followed by eliminating $\mathbf{p}$ and $\vec{\mathbf{b}}$ in (3.77a) with the help of (3.77b) and (3.77c) yields the

following eigenvalue problem which can be thought of as a discrete version of (1.9): find $\omega \in \mathbb{C}$ and $\vec{\mathbf{u}} \in \mathbb{R}^{n_0^2}$ such that

$$\begin{cases} \mathbb{F}\,\vec{\mathbf{u}} = -\omega^2\,\mathbb{M}^{n_\mathrm{b}}\,\vec{\mathbf{u}}\,, & \text{(3.81a)} \\ \mathbb{F} := -\mathbb{D}_0^\top\,\mathbb{M}^3\,[\,\mathbb{D}_0\,(\mathcal{I}_0^2)^{-1}\,\mathcal{F}_0 + (\gamma-1)\,(\mathcal{I}_0^3)^{-1}\,\mathcal{K}_0\,\mathbb{D}_0\,] - \mathbb{A} - \mathbb{M}_0^J\,\mathbb{C}_0\,(\mathcal{I}_0^1)^{-1}\,\mathcal{T}_0\,, & \text{(3.81b)} \\ \mathbb{A} := \mathcal{T}_0^\top\,(\mathcal{I}_0^1)^{-\top}\,\mathbb{C}_0^\top\,\mathbb{M}_0^2\,\mathbb{C}_0\,(\mathcal{I}_0^1)^{-1}\,\mathcal{T}_0\,, & \text{(3.81c)} \end{cases}$$

where $\mathbb{F}$ is the discretized MHD force operator (1.9b) and $\mathbb{A} = \mathbb{A}^\top$ is a symmetric operator representing shear Alfvén physics. Consequently, the eigenvalues ω^2 and eigenfunctions $\mathbf{u}$ of the matrix $-(\mathbb{M}_0^{n_\mathrm{b}})^{-1}\,\mathbb{F}$ constitute the complete ideal MHD spectrum corresponding to some given equilibrium. $\omega^2 > 0$ correspond to stability and $\omega^2 < 0$ to instability.

3.5.2 Kinetic equations

We solve the Vlasov equation (3.17) with classical particle-in-cell techniques [45]. We therefore assume a particle-like distribution function which, for the moment in physical space Ω, takes the form

$$f_\mathrm{h}^0 = f_\mathrm{h}^0(\boldsymbol{\eta}, \mathbf{v}, t) \approx \sum_{i=1}^{N_\mathrm{p}} \frac{w_i}{\sqrt{g}(\boldsymbol{\eta}_i(t))}\,\delta(\boldsymbol{\eta} - \boldsymbol{\eta}_i(t))\,\delta(\mathbf{v} - \mathbf{v}_i(t))\,, \tag{3.82}$$

where N_p is the total number of simulation markers (to which we simply refer to as *particles*), w_i is the weight of the i-th particle and $(\boldsymbol{\eta}_i = \boldsymbol{\eta}_i(t), \mathbf{v}_i = \mathbf{v}_k(t)) \in \mathbb{R}^6$ its position in phase space at time $t \geq 0$. The Jacobian determinant $\sqrt{g}$ in the denominator of (3.82) is due to the transformation of the Dirac-delta from physical space Ω to logical space $\hat{\Omega}$. The particles satisfy the equations of motion

$$\frac{\mathrm{d}\boldsymbol{\eta}_i}{\mathrm{d}t} = DF^{-1}\mathbf{v}_i, \qquad \boldsymbol{\eta}_i(t=0) =: \boldsymbol{\eta}_i^0\,, \tag{3.83a}$$

$$\frac{\mathrm{d}\mathbf{v}_k}{\mathrm{d}t} = \frac{Z_\mathrm{h}}{A_\mathrm{h}}\kappa\left[\frac{1}{\sqrt{g}}DF^{-\top}(\mathbf{B}_\mathrm{tot}^2 \times \mathbf{U}^2) + DF^{-\top}\left(DF^{-1}\mathbf{v}_i \times \mathbf{B}_\mathrm{tot}^2\right)\right], \quad \mathbf{v}_i(t=0) =: \mathbf{v}_i^0\,, \tag{3.83b}$$

which can be identified from the Vlasov equation (3.17) by noting that a particle must "see" a constant distribution function during its motion:

$$\frac{\mathrm{d}}{\mathrm{d}t} f_\mathrm{h}^0(\boldsymbol{\eta}(t), \mathbf{v}(t), t) = \frac{\partial f_\mathrm{h}^0}{\partial t} + \frac{\mathrm{d}\boldsymbol{\eta}}{\mathrm{d}t} \cdot \hat{\nabla} f_\mathrm{h}^0 + \frac{\mathrm{d}\mathbf{v}}{\mathrm{d}t} \cdot \nabla_\mathbf{v} f_\mathrm{h}^0 = 0\,. \tag{3.84}$$

Hence, a simulation particle satisfies the same equations of motion as a real (or physical) particle.

We now turn our attention to the two coupling terms $\mathrm{CC}(\rho_\mathrm{h}^3)$ (3.15) and $\mathrm{CC}(\mathbf{J}_\mathrm{h}^2)$ (3.16) involving the energetic ion charge and current density, respectively. Following classical PIC techniques, the resulting integrals (both in logical position space and velocity space) are evaluated by Monte-Carlo estimates using the particle positions in phase space (see [93] for a thorough overview about this topic). The field are replaced by their finite element approximations. This

leads to

$$\begin{aligned}
\mathrm{CC}(\rho_\mathrm{h}^3) &\approx -\nu_\mathrm{h}\frac{Z_\mathrm{h}}{A_b n}\kappa \int_\Omega (\mathbf{K}^2)^\top \frac{1}{\sqrt{g}}\,\rho_\mathrm{h}^3\,(\,\mathbf{B}^2_\mathrm{tot}\times\mathbf{U}^2\,)\frac{1}{\sqrt{g}}\,\mathrm{d}^3\eta \\
&= -\nu_\mathrm{h}\frac{Z_\mathrm{h}}{A_\mathrm{b}}\kappa \int_\Omega\int_{\mathbb{R}^3}\left[(\mathbf{K}^2)^\top\frac{1}{g}\,\frac{f_\mathrm{h}^0}{\zeta_\mathrm{h}^0}\,(\,\mathbf{B}^2_\mathrm{tot}\times\mathbf{U}^2\,)\right]\sqrt{g}\,\zeta_\mathrm{h}^0\,\mathrm{d}^3\eta\,\mathrm{d}^3v \\
&\approx -\nu_\mathrm{h}\frac{Z_\mathrm{h}}{A_\mathrm{b}}\kappa \sum_{i=0}^{N_\mathrm{p}} \underbrace{\frac{1}{N_\mathrm{p}}\frac{f_\mathrm{h}^0(\boldsymbol{\eta}_i^0,\mathbf{v}_i^0,t=0)}{\zeta_\mathrm{h}^0(\boldsymbol{\eta}_i^0,\mathbf{v}_i^0,t=0)}}_{=:\,w_i}\mathbf{K}^2(\boldsymbol{\eta}_i)^\top\frac{1}{g(\boldsymbol{\eta}_i)}\,(\,\mathbf{B}^2_\mathrm{tot}(\boldsymbol{\eta}_i)\times\mathbf{U}^2(\boldsymbol{\eta}_i)\,)\,,
\end{aligned} \tag{3.85}$$

where we introduced the probability density function (PDF) $\zeta_\mathrm{h}^0 = \zeta_\mathrm{h}^0(\boldsymbol{\eta},\mathbf{v},t) = \zeta_\mathrm{h}(F(\boldsymbol{\eta}),\mathbf{v},t)$ from which we demand to satisfy the Vlasov equation. In order for ζ_h to be a PDF, it must be normalized in a way that

$$1 = \int_\Omega\int_{\mathbb{R}^3}\zeta_\mathrm{h}(\mathbf{x},\mathbf{v},t)\,\mathrm{d}^3v\,\mathrm{d}^3x = \int_{\hat\Omega}\int_{\mathbb{R}^3}\zeta_\mathrm{h}^0(\boldsymbol{\eta},\mathbf{v},t)\,\sqrt{g}(\boldsymbol{\eta})\,\mathrm{d}^3v\,\mathrm{d}^3\eta \qquad \forall\, t\geq 0\,, \tag{3.86}$$

such that the PDF on the logical domain is given by the 3-form $\zeta_\mathrm{h}^3 = \sqrt{g}\,\zeta_\mathrm{h}^0$. The second line of (3.85) can then be interpreted as the expectation value of the random variable inside the square brackets distributed under the PDF ζ_h^3 with the third line being its estimator using the particle positions in phase space. Finally, we made use of the fact that the distribution function f_h^0 and the PDF ζ_h^0 are constant along a particle trajectory according to the Vlasov equation: $\mathrm{d}f_\mathrm{h}^0/\mathrm{d}t = 0$ in a Lagrangian frame. Therefore, $f_\mathrm{h}^0(\boldsymbol{\eta}_i(t),\mathbf{v}_i(t),t) = f_\mathrm{h}^0(\boldsymbol{\eta}_i^0,\mathbf{v}_i^0,t=0)$, where $(\boldsymbol{\eta}_i^0,\mathbf{v}_i^0)$ is the initial phase space position of the i-th particle drawn from the initial PDF $\zeta_\mathrm{h}^0(\boldsymbol{\eta},\mathbf{v},t=0)$. It is important to keep in mind that if one defines a PDF which is normalized to one on the logical domain (which is usually the case), one essentially samples from the 3-form ζ_h^3. Hence, one must not forget the Jacobian determinant in the definition of the weights because there the 0-form $\zeta_\mathrm{h}^0 = \zeta_\mathrm{h}^3/\sqrt{g}$ is needed. A simple example for this is shown in Figure 3.7 for the case of the standard square-to-disc mapping for which the Jacobian determinant $\sqrt{g}\sim s$. If one samples uniformly on the logical domain (upper left), there will be a larger particle density around the center of the disc (upper right). Therefore, if one wants to have a uniform density of particles on the disc (lower right), particles must be sampled according to the (normalized) Jacobian determinant on the logical domain (lower left).

In order to write (3.85) as well as the equations of motion (3.83) in a compact matrix-vector form, we stack the particles' logical coordinates and velocities according to

$$\boldsymbol{\Upsilon} := (s_1,\,\cdots,\,s_{N_\mathrm{p}},\chi_1,\,\cdots,\,\chi_{N_\mathrm{p}},\varphi_1,\,\cdots,\varphi_{N_\mathrm{p}}) \qquad \in\mathbb{R}^{3N_\mathrm{p}}\,, \tag{3.87}$$

$$\mathbf{V} := (v_{1,x},\,\cdots,v_{N_\mathrm{p},x},v_{1,y},\,\cdots,v_{N_\mathrm{p},y},v_{1,z},\,\cdots,v_{N_\mathrm{p},z}) \in\mathbb{R}^{3N_\mathrm{p}}\,, \tag{3.88}$$

and define the matrices

$$\mathbb{R}^{n^2\times 3N_\mathrm{p}} \ni \mathbb{\Lambda}^2(\boldsymbol{\Upsilon}) := \begin{bmatrix}\mathbb{\Lambda}_1^2(\boldsymbol{\Upsilon}) & 0 & 0\\ 0 & \mathbb{\Lambda}_2^2(\boldsymbol{\Upsilon}) & 0\\ 0 & 0 & \mathbb{\Lambda}_3^2(\boldsymbol{\Upsilon})\end{bmatrix}\,,\quad \left(\mathbb{\Lambda}_\mu^2\right)_{(ijk)m} := \Lambda^2_{\mu,(ijk)}(\boldsymbol{\eta}_m)\,, \tag{3.89a}$$

$$\mathbb{R}^{3N_\mathrm{p}\times 3N_\mathrm{p}} \ni \mathbb{W} := \mathbb{1}_3\otimes\mathrm{diag}\,(w_1,\,\cdots,w_{N_\mathrm{p}})\,, \tag{3.89b}$$

$$\mathbb{R}^{3N_\mathrm{p}\times 3N_\mathrm{p}} \ni \mathbb{N}_{DF}(\boldsymbol{\Upsilon}) := [\,\mathbb{N}_{DF,\mu\nu}(\boldsymbol{\Upsilon})\,]\,, \tag{3.89c}$$

$$\mathbb{R}^{N_\mathrm{p}\times N_\mathrm{p}} \ni \mathbb{N}_{DF,\mu\nu}(\boldsymbol{\Upsilon}) := \mathrm{diag}\,\left(DF_{\mu\nu}(\boldsymbol{\eta}_1),\,\cdots,DF_{\mu\nu}(\boldsymbol{\eta}_{N_\mathrm{p}})\right)\,, \tag{3.89d}$$

$$\mathbb{R}^{3N_\mathrm{p}\times 3N_\mathrm{p}} \ni \mathbb{N}_{DF^{-1}}(\boldsymbol{\Upsilon}) := [\,\mathbb{N}_{DF^{-1},\mu\nu}(\boldsymbol{\Upsilon})\,], \tag{3.89e}$$

$$\mathbb{R}^{N_\mathrm{p}\times N_\mathrm{p}} \ni \mathbb{N}_{DF^{-1},\mu\nu}(\boldsymbol{\Upsilon}) := \mathrm{diag}\left((DF^{-1})_{\mu\nu}(\boldsymbol{\eta}_1),\cdots,(DF^{-1})_{\mu\nu}(\boldsymbol{\eta}_{N_\mathrm{p}})\right), \tag{3.89f}$$

$$\mathbb{R}^{3N_\mathrm{p}\times 3N_\mathrm{p}} \ni \mathbb{N}_{g^{-1}}(\boldsymbol{\Upsilon}) := \mathbb{1}_3 \otimes \mathrm{diag}\left(\frac{1}{g(\boldsymbol{\eta}_1)},\cdots,\frac{1}{g(\boldsymbol{\eta}_{N_\mathrm{p}})}\right), \tag{3.89g}$$

$$\mathbb{R}^{3N_\mathrm{p}\times 3N_\mathrm{p}} \ni \mathbb{N}_{\sqrt{g}^{-1}}(\boldsymbol{\Upsilon}) := \mathbb{1}_3 \otimes \mathrm{diag}\left(\frac{1}{\sqrt{g}(\boldsymbol{\eta}_1)},\cdots,\frac{1}{\sqrt{g}(\boldsymbol{\eta}_{N_\mathrm{p}})}\right), \tag{3.89h}$$

$$\mathbb{R}^{3N_\mathrm{p}\times 3N_\mathrm{p}} \ni \mathbb{B}_0^\times(\,\vec{\mathbf{b}},\boldsymbol{\Upsilon}\,) := [\,\mathbb{B}_{0,\mu\nu}^\times(\,\vec{\mathbf{b}},\boldsymbol{\Upsilon}\,)\,], \tag{3.89i}$$

$$\mathbb{R}^{N_\mathrm{p}\times N_\mathrm{p}} \ni \mathbb{B}_{0,\mu\nu}^\times(\,\vec{\mathbf{b}},\boldsymbol{\Upsilon}\,) := \epsilon_{\mu\alpha\nu}\,\mathrm{diag}\left((\mathbf{b}_\alpha+\mathbf{b}_{\mathrm{eq},\alpha})^\top \mathbb{B}_\alpha^2\,\mathbb{\Lambda}_\alpha^2(\boldsymbol{\Upsilon})\right), \tag{3.89j}$$

where $\mu,\nu=1,2,3$ as usual and $\vec{\mathbf{b}}_\mathrm{eq}=(\,\mathbf{b}_{\mathrm{eq},1},\mathbf{b}_{\mathrm{eq},2},\mathbf{b}_{\mathrm{eq},3}\,)$ are the FE coefficient of the projected equilibrium magnetic field. One could in principle also use the exact equilibrium field in (3.89j) but for efficiency reasons we use the FE coefficients. The anti-symmetric matrix $\mathbb{B}_0^\times=-(\mathbb{B}_0^\times)^\top$ essentially performs for each particle the cross product of the discrete magnetic field evaluated at the particle position with some other vector it is applied to. With this (3.85) can be compactly written as

$$\mathrm{CC}(\rho_\mathrm{h}^3) \approx -\nu_\mathrm{h}\frac{Z_\mathrm{h}}{A_\mathrm{b}}\kappa\,\vec{\mathbf{k}}^\top\,\mathbb{\Lambda}_0^2\,\mathbb{W}\,\mathbb{N}_{g^{-1}}\,\mathbb{B}_0^\times\,(\mathbb{\Lambda}_0^2)^\top\,\vec{\mathbf{u}}\,, \tag{3.90}$$

where $\mathbb{\Lambda}_0^2:=\mathbb{B}^2\mathbb{\Lambda}^2\in\mathbb{R}^{n_0^2\times 3N_\mathrm{p}}$ to take into account boundary conditions. It should be noted, however, that in actual simulations, matrices of size $N_\mathrm{p}\times N_\mathrm{p}$ or $3N_\mathrm{p}\times 3N_\mathrm{p}$ are never explicitly assembled. Instead, only the non-zero contributions to the final matrix $\mathbb{\Lambda}_0^2\,\mathbb{W}\,\mathbb{N}_{g^{-1}}\,\mathbb{B}^\times\,(\mathbb{\Lambda}_0^2)^\top$, which has the size of the mass matrix $\mathbb{M}_0^2$, are calculated separately for each particle and then added to the final matrix. However, for the further analysis of the semi-discrete system of equations and for the sake of compact notations we shall still use the matrices (3.87)-(3.89j) in the following. Performing the exact same steps as in (3.85), the second coupling terms involving the energetic ion current density amounts to

$$\mathrm{CC}(\mathbf{J}_\mathrm{h}^2) \approx \nu_\mathrm{h}\frac{Z_\mathrm{h}}{A_\mathrm{b}}\kappa\,\vec{\mathbf{k}}^\top\,\mathbb{\Lambda}_0^2\,\mathbb{W}\,\mathbb{N}_{\sqrt{g}^{-1}}\,\mathbb{B}_0^\times\,\mathbb{N}_{DF^{-1}}\,\mathbf{V}\,. \tag{3.91}$$

Writing also the particles' equations of motion (3.83) in a compact matrix-vector form finally yields the semi-discrete system of equations

$$\begin{cases}
\mathbb{M}_0^{n_\mathrm{b}}\dfrac{\mathrm{d}\vec{\mathbf{u}}}{\mathrm{d}t} = \mathbb{D}_0^\top\,\mathbb{M}_0^3\,\mathbf{p} + \mathcal{T}_0^\top(\mathcal{I}_0^1)^{-\top}\,\mathbb{C}_0^\top\,\mathbb{M}_0^2\,\vec{\mathbf{b}} + \mathbb{M}_0^J\,\vec{\mathbf{b}} \\
\qquad\qquad - \nu_\mathrm{h}\dfrac{Z_\mathrm{h}}{A_\mathrm{b}}\kappa\,\mathbb{\Lambda}_0^2\,\mathbb{W}\,\mathbb{N}_{g^{-1}}\,\mathbb{B}_0^\times\,(\mathbb{\Lambda}_0^2)^\top\,\vec{\mathbf{u}} + \nu_\mathrm{h}\dfrac{Z_\mathrm{h}}{A_\mathrm{b}}\kappa\,\mathbb{\Lambda}_0^2\,\mathbb{W}\,\mathbb{N}_{\sqrt{g}^{-1}}\,\mathbb{B}_0^\times\,\mathbb{N}_{DF^{-1}}\,\mathbf{V}\,, & \text{(3.92a)}\\
\dfrac{\mathrm{d}\mathbf{p}}{\mathrm{d}t} = -\mathbb{D}_0\,(\mathcal{I}_0^2)^{-1}\,\mathcal{F}_0\,\vec{\mathbf{u}} - (\gamma-1)\,(\mathcal{I}_0^3)^{-1}\,\mathcal{K}_0\,\mathbb{D}_0\,\vec{\mathbf{u}}\,, & \text{(3.92b)}\\
\dfrac{\mathrm{d}\vec{\mathbf{b}}}{\mathrm{d}t} = -\mathbb{C}_0\,(\mathcal{I}_0^1)^{-1}\,\mathcal{T}_0\,\vec{\mathbf{u}}\,, & \text{(3.92c)}\\
\dfrac{\mathrm{d}\boldsymbol{\Upsilon}}{\mathrm{d}t} = \mathbb{N}_{DF^{-1}}\,\mathbf{V}\,, & \text{(3.92d)}\\
\dfrac{\mathrm{d}\mathbf{V}}{\mathrm{d}t} = \dfrac{Z_\mathrm{h}}{A_\mathrm{h}}\kappa\left[\,\mathbb{N}_{\sqrt{g}^{-1}}\,\mathbb{N}_{DF^{-1}}^\top\,\mathbb{B}_0^\times\,(\mathbb{\Lambda}_0^2)^\top\vec{\mathbf{u}} - \mathbb{N}_{DF^{-1}}^\top\,\mathbb{B}_0^\times\,\mathbb{N}_{DF^{-1}}\mathbf{V}\,\right], & \text{(3.92e)}
\end{cases}$$

where, once more, the matrices in (3.92d) and (3.92e) are just used for a compact notation. In an actual simulation, the equations of motion are solved separately for each particle.

3.6 Temporal discretization

Before discussing the actual temporal discretization of the semi-discrete system (3.92), let us first define the discrete version of the energy-like quantity $\tilde{\mathcal{H}}$ introduced in (2.38):

$$\begin{aligned}\tilde{\mathcal{H}}_h &:= \frac{1}{2}\int_{\hat{\Omega}} \frac{1}{\sqrt{g}}\, n_{\mathrm{b,eq}}^3\, (\mathbf{U}_h^2)^\top G\, \mathbf{U}_h^2 \frac{1}{\sqrt{g}}\, \mathrm{d}^3\eta + \frac{1}{2}\int_{\hat{\Omega}} (\mathbf{B}_h^2)^\top G\, \mathbf{B}_h^2 \frac{1}{\sqrt{g}}\, \mathrm{d}^3\eta \\ &\qquad + \frac{1}{\gamma-1}\int_{\hat{\Omega}} p_h^3\, \mathrm{d}^3\eta + \frac{1}{2}\nu_\mathrm{h}\frac{A_\mathrm{h}}{A_\mathrm{b}}\int_{\hat{\Omega}}\int_{\mathbb{R}^3} v^2 f_\mathrm{h}\, \mathrm{d}^3 v\, \mathrm{d}^3\eta \\ &= \frac{1}{2}\vec{\mathbf{u}}^\top \mathbb{M}_0^{n_\mathrm{b}}\, \vec{\mathbf{u}} + \frac{1}{2}\vec{\mathbf{b}}^\top \mathbb{M}_0^2\, \vec{\mathbf{b}} + \frac{1}{\gamma-1}\mathbf{p}^\top \mathbf{1}^3 + \frac{1}{2}\nu_\mathrm{h}\frac{A_\mathrm{h}}{A_\mathrm{b}}\mathbf{V}^\top \mathbb{W}\, \mathbf{V} \\ &=: \tilde{\mathcal{H}}_U + \tilde{\mathcal{H}}_B + \tilde{\mathcal{H}}_p + \tilde{\mathcal{H}}_\mathrm{h}\,.\end{aligned} \tag{3.93}$$

It is obtained from (2.38) by first performing pull-backs from the physical to the logical domain followed by replacing the continuous fields by their discrete counterparts. The distribution function is replaced by its particle approximation (3.82). Moreover, $\mathbf{1}^3 := (1\,, \cdots, 1) \in \mathbb{R}^{n_0^3}$ is a vector filled with ones. If we collect as a next step all FE coefficients and particle positions in phase space in a single vector $\mathbf{R} := (\vec{\mathbf{u}},\, \mathbf{p},\, \vec{\mathbf{b}},\, \boldsymbol{\Upsilon},\, \mathbf{V})$, we can write the semi-discrete system (3.92) in the following compact form:

$$\frac{\mathrm{d}\mathbf{R}}{\mathrm{d}t} = \mathbb{J}\,\nabla_{\mathbf{R}}\tilde{\mathcal{H}}_1 + \mathbb{K}\,\mathbf{R}\,, \tag{3.94}$$

$$\Leftrightarrow \quad \frac{\mathrm{d}\mathbf{R}}{\mathrm{d}t} = \overbrace{\begin{bmatrix} \mathbb{J}_{11}(\vec{\mathbf{b}}, \boldsymbol{\Upsilon}) & 0 & \mathbb{J}_{13} & 0 & \mathbb{J}_{15}(\vec{\mathbf{b}}, \boldsymbol{\Upsilon}) \\ 0 & 0 & 0 & 0 & 0 \\ -\mathbb{J}_{13}^\top & 0 & 0 & 0 & 0 \\ 0 & 0 & 0 & 0 & \mathbb{J}_{45}(\boldsymbol{\Upsilon}) \\ -\mathbb{J}_{15}^\top(\vec{\mathbf{b}}, \boldsymbol{\Upsilon}) & 0 & 0 & -\mathbb{J}_{45}^\top(\boldsymbol{\Upsilon}) & \mathbb{J}_{55}(\vec{\mathbf{b}}, \boldsymbol{\Upsilon}) \end{bmatrix}}^{=:\mathbb{J}} \overbrace{\begin{bmatrix} \mathbb{M}_0^{n_\mathrm{b}}\, \vec{\mathbf{u}} \\ \mathbf{1}^3/(\gamma-1) \\ \mathbb{M}_0^2\, \vec{\mathbf{b}} \\ 0 \\ v_\mathrm{h} A_\mathrm{h} \mathbb{W}\mathbf{V}/A_\mathrm{b} \end{bmatrix}}^{=\nabla_{\mathbf{R}}\tilde{H}_h} \tag{3.95}$$

$$+ \underbrace{\begin{bmatrix} 0 & \mathbb{D}_0^\top\, \mathbb{M}_0^3 & \mathbb{M}_0^J & 0 & 0 \\ -\mathbb{D}_0\,(\mathcal{I}_0^2)^{-1}\,\mathcal{F}_0 - (\gamma-1)\,(\mathcal{I}_0^3)^{-1}\,\mathcal{K}_0\,\mathbb{D}_0 & 0 & 0 & 0 & 0 \\ 0 & 0 & 0 & 0 & 0 \\ 0 & 0 & 0 & 0 & 0 \\ 0 & 0 & 0 & 0 & 0 \end{bmatrix}}_{=:\mathbb{K}} \underbrace{\begin{bmatrix} \vec{\mathbf{u}} \\ \mathbf{p} \\ \vec{\mathbf{b}} \\ \boldsymbol{\Upsilon} \\ \mathbf{V} \end{bmatrix}}_{=\mathbf{R}}.$$

We find that the spatial discretizations performed in the previous sections results in a system of ordinary differential equations in time that can be written as the sum of a part with an anti-symmetric matrix $\mathbb{J}$ and an additional part with a matrix $\mathbb{K}$. It is intuitive to call the former the "Hamiltonian part" and the latter the "non-Hamiltonian part", although we do not prove the Jacobi identity of the matrix $\mathbb{J}$. Nevertheless, we stick to this notation in the following to make a clear distinction between the energy conserving and non-conserving part. The latter

only plays a role for compressible waves and if there is an equilibrium current $\mathbf{J}_{\text{eq}} \neq 0$ (then $\mathbb{M}_0^J = 0$). In particular, we remark that obtaining the Hamiltonian part relies on the symmetry of all mass matrices and the weight matrix $\mathbb{W}$. In this case $\nabla_{\mathbf{R}}\tilde{\mathcal{H}}_h$ takes the simple form given in the first line of (3.95) and only then the semi-discrete system of equations can be written in the form (3.95). The anti-symmetry $\mathbb{J}^\top = -\mathbb{J}$ immediately implies conservation of $\tilde{\mathcal{H}}_h$ for the Hamiltonian part of (3.95) because

$$\frac{\mathrm{d}}{\mathrm{d}t}\tilde{\mathcal{H}}_h(\mathbf{R}(t)) = (\nabla_{\mathbf{R}}\tilde{\mathcal{H}}_h)^\top \mathbb{J}\,\frac{\mathrm{d}\mathbf{R}}{\mathrm{d}t} = (\nabla_{\mathbf{R}}\tilde{\mathcal{H}}_h)^\top \mathbb{J}\,\nabla_{\mathbf{R}}\tilde{\mathcal{H}}_h = -(\nabla_{\mathbf{R}}\tilde{\mathcal{H}}_h)^\top \mathbb{J}\,\nabla_{\mathbf{R}}\tilde{\mathcal{H}}_h = 0. \tag{3.96}$$

The single blocks of $\mathbb{J}$ are given by

$$\mathbb{J}_{11}(\vec{\mathbf{b}}, \boldsymbol{\Upsilon}) := -\nu_{\mathrm{h}}\frac{Z_{\mathrm{h}}}{A_{\mathrm{b}}}\kappa\,(\mathbb{M}_0^{n_{\mathrm{b}}})^{-1}\,\mathbb{A}_0^2(\boldsymbol{\Upsilon})\,\mathbb{W}\,\mathbb{N}_{g^{-1}}(\boldsymbol{\Upsilon})\,\mathbb{B}_0^{\times}(\vec{\mathbf{b}}, \boldsymbol{\Upsilon})\,\mathbb{A}_0^2(\boldsymbol{\Upsilon})^\top\,(\mathbb{M}_0^{n_{\mathrm{b}}})^{-1}, \tag{3.97a}$$

$$\mathbb{J}_{13} := (\mathbb{M}_0^{n_{\mathrm{b}}})^{-1}\,\mathcal{T}_0^\top\,(\mathcal{I}_0^1)^{-\top}\,\mathbb{C}_0^\top, \tag{3.97b}$$

$$\mathbb{J}_{15}(\vec{\mathbf{b}}, \boldsymbol{\Upsilon}) := \frac{Z_{\mathrm{h}}}{A_{\mathrm{h}}}\kappa\,(\mathbb{M}_0^{n_{\mathrm{b}}})^{-1}\,\mathbb{A}_0^2(\boldsymbol{\Upsilon})\,\mathbb{N}_{\sqrt{g}^{-1}}(\boldsymbol{\Upsilon})\,\mathbb{B}_0^{\times}(\vec{\mathbf{b}}, \boldsymbol{\Upsilon})\,\mathbb{N}_{DF^{-1}}(\boldsymbol{\Upsilon}), \tag{3.97c}$$

$$\mathbb{J}_{45}(\boldsymbol{\Upsilon}) := \frac{A_{\mathrm{b}}}{\nu_{\mathrm{h}}A_{\mathrm{h}}}\,\mathbb{N}_{DF^{-1}}(\boldsymbol{\Upsilon})\,\mathbb{W}^{-1}, \tag{3.97d}$$

$$\mathbb{J}_{55}(\vec{\mathbf{b}}, \boldsymbol{\Upsilon}) := -\frac{A_{\mathrm{b}}Z_{\mathrm{h}}}{\nu_{\mathrm{h}}A_{\mathrm{h}}^2}\kappa\,\mathbb{N}_{DF^{-1}}(\boldsymbol{\Upsilon})^\top\,\mathbb{B}_0^{\times}(\vec{\mathbf{b}}, \boldsymbol{\Upsilon})\,\mathbb{N}_{DF^{-1}}(\boldsymbol{\Upsilon})\,\mathbb{W}^{-1}. \tag{3.97e}$$

In order to keep the energy conservation property of the Hamiltonian part, we propose two splitting steps: First, to take advantage of (3.96), we split apart the non-Hamiltonian part and solve successively the Hamiltonian part $\mathrm{d}\mathbf{R}/\mathrm{d}t = \mathbb{J}\,\nabla_{\mathbf{R}}\tilde{\mathcal{H}}_h$ and non-Hamiltonian part $\mathrm{d}\mathbf{R}/\mathrm{d}t = \mathbb{K}\,\mathbf{R}$, and second, we apply a skew-symmetric splitting to the Hamiltonian part and solve each (still skew-symmetric) substep in an energy conserving way. We recall the Hamiltonian part:

$$\frac{\mathrm{d}}{\mathrm{d}t}\begin{bmatrix}\vec{\mathbf{u}}\\ \vec{\mathbf{b}}\\ \boldsymbol{\Upsilon}\\ \mathbf{V}\end{bmatrix} = \begin{bmatrix}\mathbb{J}_{11}(\vec{\mathbf{b}}, \boldsymbol{\Upsilon}) & \mathbb{J}_{13} & 0 & \mathbb{J}_{15}(\vec{\mathbf{b}}, \boldsymbol{\Upsilon})\\ -\mathbb{J}_{13}^\top & 0 & 0 & 0\\ 0 & 0 & 0 & \mathbb{J}_{45}(\boldsymbol{\Upsilon})\\ -\mathbb{J}_{15}^\top(\vec{\mathbf{b}}, \boldsymbol{\Upsilon}) & 0 & -\mathbb{J}_{45}^\top(\boldsymbol{\Upsilon}) & \mathbb{J}_{55}(\vec{\mathbf{b}}, \boldsymbol{\Upsilon})\end{bmatrix}\begin{bmatrix}\mathbb{M}_0^{n_{\mathrm{b}}}\,\vec{\mathbf{u}}\\ \mathbb{M}_0^2\,\vec{\mathbf{b}}\\ 0\\ v_{\mathrm{h}}A_{\mathrm{h}}\mathbb{W}\mathbf{V}/A_{\mathrm{b}}\end{bmatrix}. \tag{3.98}$$

Splitting the matrix $\mathbb{J}$ into five separate matrices containing only equally colored blocks and introducing a temporal grid $t^n = n\Delta t$ with $n \in \mathbb{N}_0$ leads to the following substeps:

Substep 1 The first subsystem reads

$$\frac{\mathrm{d}\vec{\mathbf{u}}}{\mathrm{d}t} = \mathbb{J}_{11}(\vec{\mathbf{b}}, \boldsymbol{\Upsilon})\,\mathbb{M}_0^{n_{\mathrm{b}}}\,\vec{\mathbf{u}}, \qquad \frac{\mathrm{d}\vec{\mathbf{b}}}{\mathrm{d}t} = 0, \qquad \frac{\mathrm{d}\boldsymbol{\Upsilon}}{\mathrm{d}t} = 0, \qquad \frac{\mathrm{d}\mathbf{V}}{\mathrm{d}t} = 0. \tag{3.99}$$

We solve the only non-trivial equation for $\vec{\mathbf{u}}$ with the energy-preserving, implicit Crank-Nicolson method [67]. Note that the matrix $\mathbb{J}_{11}$ does not change in this step since $\vec{\mathbf{b}}$ and $\boldsymbol{\Upsilon}$ do not change in this step:

$$\vec{\mathbf{u}}^{n+1} = \vec{\mathbf{u}}^n + \frac{\Delta t}{2}\mathbb{J}_{11}(\vec{\mathbf{b}}^n, \boldsymbol{\Upsilon}^n)\,\mathbb{M}_0^{n_{\mathrm{b}}}\,(\vec{\mathbf{u}}^n + \vec{\mathbf{u}}^{n+1}), \tag{3.100}$$

$$\Leftrightarrow \quad \left(\mathbb{M}_0^{n_{\mathrm{b}}} - \frac{\Delta t}{2}\,\mathbb{M}_0^{n_{\mathrm{b}}}\,\mathbb{J}_{11}(\vec{\mathbf{b}}^n, \boldsymbol{\Upsilon}^n)\,\mathbb{M}_0^{n_{\mathrm{b}}}\right)\vec{\mathbf{u}}^{n+1} = \left(\mathbb{M}_0^{n_{\mathrm{b}}} + \frac{\Delta t}{2}\,\mathbb{M}_0^{n_{\mathrm{b}}}\,\mathbb{J}_{11}(\vec{\mathbf{b}}^n, \boldsymbol{\Upsilon}^n)\,\mathbb{M}_0^{n_{\mathrm{b}}}\right)\vec{\mathbf{u}}^n. \tag{3.101}$$

Hence, in every time step, one first needs to assemble the matrix $\mathbb{M}_0^{n_\mathrm{b}}\,\mathbb{J}_{11}(\,\vec{\mathbf{b}}^n,\boldsymbol{\Upsilon}^n\,)\,\mathbb{M}_0^{n_\mathrm{b}}$ followed by solving the linear system (3.101) for the new FE coefficients $\vec{\mathbf{u}}^{n+1}$. We dote the corresponding time integrator that performs these steps by $\Phi^1_{\Delta t}:\mathbb{R}^{n_0^2}\to\mathbb{R}^{n_0^2}$, $\vec{\mathbf{u}}^n\mapsto\vec{\mathbf{u}}^{n+1}$.

Substep 2 The second subsystem reads

$$\frac{\mathrm{d}\vec{\mathbf{u}}}{\mathrm{d}t}=\mathbb{J}_{13}\,\mathbb{M}_0^2\,\vec{\mathbf{b}},\qquad\frac{\mathrm{d}\vec{\mathbf{b}}}{\mathrm{d}t}=-\mathbb{J}_{13}^\top\,\mathbb{M}_0^{n_\mathrm{b}}\,\vec{\mathbf{u}},\qquad\frac{\mathrm{d}\boldsymbol{\Upsilon}}{\mathrm{d}t}=0,\qquad\frac{\mathrm{d}\mathbf{V}}{\mathrm{d}t}=0.\tag{3.102}$$

As before, this system is solved with the Crank-Nicolson method:

$$\mathbb{M}_0^{n_\mathrm{b}}\,\vec{\mathbf{u}}^{n+1}=\mathbb{M}_0^{n_\mathrm{b}}\,\vec{\mathbf{u}}^n+\frac{\Delta t}{2}\,\mathcal{T}_0^\top\,(\mathcal{I}_0^1)^{-\top}\,\mathbb{C}_0^\top\,\mathbb{M}_0^2\,(\vec{\mathbf{b}}^n+\vec{\mathbf{b}}^{n+1})\,,\tag{3.103}$$

$$\vec{\mathbf{b}}^{n+1}=\vec{\mathbf{b}}^n-\frac{\Delta t}{2}\,\mathbb{C}_0\,(\mathcal{I}_0^1)^{-1}\,\mathcal{T}_0\,(\vec{\mathbf{u}}^n+\vec{\mathbf{u}}^{n+1})\,.\tag{3.104}$$

These equations can be decoupled by plugging the second equation in the first equation and solving for $\vec{\mathbf{u}}^{n+1}$:

$$\mathbb{S}_2\,\vec{\mathbf{u}}^{n+1}=\left[\mathbb{M}_0^{n_\mathrm{b}}-\frac{\Delta t^2}{4}\,\mathcal{T}_0^\top\,(\mathcal{I}_0^1)^{-\top}\,\mathbb{C}_0^\top\,\mathbb{M}_0^2\,\mathbb{C}_0\,(\mathcal{I}_0^1)^{-1}\,\mathcal{T}_0\right]\vec{\mathbf{u}}^n+\Delta t\,\mathcal{T}_0^\top\,(\mathcal{I}_0^1)^{-\top}\,\mathbb{C}_0^\top\,\mathbb{M}_0^2\,\vec{\mathbf{b}}^n\,.\tag{3.105}$$

The matrix $\mathbb{S}_2:=\mathbb{M}_0^{n_\mathrm{b}}+\Delta t^2\,\mathcal{T}_0^\top\,(\mathcal{I}_0^1)^{-\top}\,\mathbb{C}_0^\top\,\mathbb{M}_0^2\,\mathbb{C}_0\,(\mathcal{I}_0^1)^{-1}\,\mathcal{T}_0/4$ on the left-hand side is symmetric and does not change in time. Moreover, we note that the explicit update rule (3.104) preserves the divergence of the magnetic field, i.e. $\mathbb{D}_0\,\vec{\mathbf{b}}^{n+1}=\mathbb{D}_0\,\vec{\mathbf{b}}^n$ due to the discrete de Rham complex property $\mathbb{D}_0\,\mathbb{C}_0=0$. Hence, if the initial magnetic field is divergence-free (which can exactly be translated to the discrete level via the commuting diagram property $\Pi_2\,(\hat{\nabla}\cdot\mathbf{B}^2)=\hat{\nabla}\cdot(\Pi_2\mathbf{B}^2)$, it will remain divergence-free for all times. We denote the second time integrator by $\Phi^2_{\Delta t}:\mathbb{R}^{n_0^2}\times\mathbb{R}^{n_0^2}\to\mathbb{R}^{n_0^2}\times\mathbb{R}^{n_0^2}$, $\vec{\mathbf{u}}^n,\vec{\mathbf{b}}^n\mapsto\vec{\mathbf{u}}^{n+1},\vec{\mathbf{b}}^{n+1}$.

Substep 3 The third subsystem reads

$$\frac{\mathrm{d}\vec{\mathbf{u}}}{\mathrm{d}t}=\nu_\mathrm{h}\frac{A_\mathrm{h}}{A_\mathrm{b}}\mathbb{J}_{15}(\,\vec{\mathbf{b}},\boldsymbol{\Upsilon}\,)\,\mathbb{W}\,\mathbf{V},\qquad\frac{\mathrm{d}\vec{\mathbf{b}}}{\mathrm{d}t}=0,\qquad\frac{\mathrm{d}\boldsymbol{\Upsilon}}{\mathrm{d}t}=0,\qquad\frac{\mathrm{d}\mathbf{V}}{\mathrm{d}t}=-\mathbb{J}_{15}^\top(\,\vec{\mathbf{b}},\boldsymbol{\Upsilon}\,)\,\mathbb{M}_0^{n_\mathrm{b}}\,\vec{\mathbf{u}}.\tag{3.106}$$

We solve this system in the same way as in the previous step by noting that $\vec{\mathbf{b}}$ and Υ do not change in this step such that the same is true for the matrix $\mathbb{J}_{15}=\mathbb{J}_{15}(\,\vec{\mathbf{b}}^n,\boldsymbol{\Upsilon}^n\,)$. Applying the Crank-Nicolson scheme yields

$$\vec{\mathbf{u}}^{n+1}=\vec{\mathbf{u}}^n+\nu_\mathrm{h}\frac{A_\mathrm{h}}{A_\mathrm{b}}\frac{\Delta t}{2}\,\mathbb{J}_{15}\,\mathbb{W}\,(\mathbf{V}^n+\mathbf{V}^{n+1})\,,\tag{3.107}$$

$$\mathbf{V}^{n+1}=\mathbf{V}^n-\frac{\Delta t}{2}\,\mathbb{J}_{15}^\top\,\mathbb{M}_0^{n_\mathrm{b}}\,(\vec{\mathbf{u}}^n+\vec{\mathbf{u}}^{n+1})\,,\tag{3.108}$$

which can once more by be decoupled by plugging the second equation in the first equation and solving for $\vec{\mathbf{u}}^{n+1}$:

$$\mathbb{S}_3\,\vec{\mathbf{u}}^{n+1}=\left(\mathbb{M}_0^{n_\mathrm{b}}-\nu_\mathrm{h}\frac{A_\mathrm{h}}{A_\mathrm{b}}\,\frac{\Delta t^2}{4}\,\mathbb{M}_0^{n_\mathrm{b}}\,\mathbb{J}_{15}\,\mathbb{W}\mathbb{J}_{15}^\top\,\mathbb{M}_0^{n_\mathrm{b}}\right)\vec{\mathbf{u}}^n+\Delta t\,\nu_\mathrm{h}\frac{A_\mathrm{h}}{A_\mathrm{b}}\,\mathbb{J}_{15}\,\mathbb{W}\,\mathbf{V}^n\,.\tag{3.109}$$

The matrix $\mathbb{S}_3:=\mathbb{M}_0^{n_\mathrm{b}}+\nu_\mathrm{h}\frac{A_\mathrm{h}}{A_\mathrm{b}}\,\Delta t^2\,\mathbb{M}_0^{n_\mathrm{b}}\,\mathbb{J}_{15}\,\mathbb{W}\mathbb{J}_{15}^\top\,\mathbb{M}_0^{n_\mathrm{b}}/4$ on the left-hand side is symmetric and needs to be assembled in every time step. The update (3.108) for the particle velocities can be done for a single particle independently from all the other particles. We denote the third time integrator by $\Phi^3_{\Delta t}:\mathbb{R}^{n_0^2}\times\mathbb{R}^{3N_\mathrm{p}}\to\mathbb{R}^{n_0^2}\times\mathbb{R}^{3N_\mathrm{p}}$, $\vec{\mathbf{u}}^n,\mathbf{V}^n\mapsto\vec{\mathbf{u}}^{n+1},\mathbf{V}^{n+1}$.

Substep 4 The fourth subsystem reads

$$\frac{\mathrm{d}\vec{\mathbf{u}}}{\mathrm{d}t} = 0, \qquad \frac{\mathrm{d}\vec{\mathbf{b}}}{\mathrm{d}t} = 0, \qquad \frac{\mathrm{d}\boldsymbol{\Upsilon}}{\mathrm{d}t} = \mathbb{N}_{DF^{-1}}(\boldsymbol{\Upsilon})\,\mathbf{V}, \qquad \frac{\mathrm{d}\mathbf{V}}{\mathrm{d}t} = 0. \tag{3.110}$$

This step does not play a role for conservation of energy because the Hamiltonian (3.93) does not depend on the particles' spatial positions. Due to the fact that the Crank-Nicolson method from the previous steps is of second order, we use a method of equal or higher order for the solution of this step. To additionally avoid another implicit method, we choose the classical fourth order Runge-Kutta method which reads

$$\mathbf{k}_1 = \mathbb{N}_{DF^{-1}}(\boldsymbol{\Upsilon}^n)\,\mathbf{V}^n\,, \tag{3.111a}$$

$$\mathbf{k}_2 = \mathbb{N}_{DF^{-1}}(\boldsymbol{\Upsilon}^n + \frac{\Delta t}{2}\,\mathbf{k}_1)\,\mathbf{V}^n\,, \tag{3.111b}$$

$$\mathbf{k}_3 = \mathbb{N}_{DF^{-1}}(\boldsymbol{\Upsilon}^n + \frac{\Delta t}{2}\,\mathbf{k}_2)\,\mathbf{V}^n\,, \tag{3.111c}$$

$$\mathbf{k}_4 = \mathbb{N}_{DF^{-1}}(\boldsymbol{\Upsilon}^n + \Delta t\,\mathbf{k}_3)\,\mathbf{V}^n\,, \tag{3.111d}$$

$$\boldsymbol{\Upsilon}^{n+1} = \boldsymbol{\Upsilon}^n + \frac{\Delta t}{6}(\mathbf{k}_1 + 2\mathbf{k}_2 + 2\mathbf{k}_3 + \mathbf{k}_4)\,. \tag{3.111e}$$

As in (3.108), this update rule applies to every particle independently from all the other particles. We denote the fourth time integrator by $\Phi^4_{\Delta t} : \mathbb{R}^{3N_\mathrm{p}} \to \mathbb{R}^{3N_\mathrm{p}}$, $\boldsymbol{\Upsilon}^n \mapsto \boldsymbol{\Upsilon}^{n+1}$.

Substep 5 The fifth subsystem reads

$$\frac{\mathrm{d}\vec{\mathbf{u}}}{\mathrm{d}t} = 0, \qquad \frac{\mathrm{d}\vec{\mathbf{b}}}{\mathrm{d}t} = 0, \qquad \frac{\mathrm{d}\boldsymbol{\Upsilon}}{\mathrm{d}t} = 0, \qquad \frac{\mathrm{d}\mathbf{V}}{\mathrm{d}t} = \nu_\mathrm{h}\frac{A_\mathrm{h}}{A_\mathrm{b}}\,\mathbb{J}_{55}(\,\vec{\mathbf{b}}, \boldsymbol{\Upsilon}\,)\,\mathbf{V}. \tag{3.112}$$

Since the magnetic field FE coefficients $\vec{\mathbf{b}}$ and the particle positions $\boldsymbol{\Upsilon}$ due not change in this step, the matrix $\mathbb{J}_{55}) = \mathbb{J}_{55}(\,\vec{\mathbf{b}}^n, \boldsymbol{\Upsilon}^n\,)$ does not change as well. It is then possible to solve system (3.112) in an exact analytical way because the ODE for the velocity effectively constitutes a rotation around the direction of the constant magnetic field vector. Moreover, since this system can be solved again for each particle separately, we just consider a single particle with index i in the following. The exact solution is then given by

$$\mathbf{v}_i^{n+1} = v_{i,\parallel}^n \frac{\mathbf{B}_h}{|\mathbf{B}_h|} + \cos\left(\frac{Z_\mathrm{h}|\mathbf{B}_h|}{A_\mathrm{h}}\,\kappa\,\Delta t\right)\mathbf{v}_{i,\perp}^n + \sin\left(\frac{Z_\mathrm{h}|\mathbf{B}_h|}{A_\mathrm{h}}\,\kappa\,\Delta t\right)\left(\mathbf{v}_{i,\perp}^n \times \frac{\mathbf{B}_h}{|\mathbf{B}_h|}\right), \tag{3.113}$$

$$v_{i,\parallel}^n := (\mathbf{v}_i^n \cdot \mathbf{B}_h/|\mathbf{B}_h|)\,, \tag{3.114}$$

$$\mathbf{v}_{i,\perp}^n := \mathbf{B}_h \times (\mathbf{v}_i^n \times \mathbf{B}_h)/|\mathbf{B}_h|^2\,, \tag{3.115}$$

where $\mathbf{B}_h = \mathbf{B}_h(\boldsymbol{\eta}_i^n) = DF(\boldsymbol{\eta}_i^n)\,\mathbf{B}_\mathrm{h}^2(\boldsymbol{\eta}_i^n)/\sqrt{g}(\boldsymbol{\eta}_i^n)$ are the Cartesian components of the magnetic field at the particle position η_i^n, $v_{i,\parallel}^n :=$ is the parallel velocity with respect to the magnetic field and $\mathbf{v}_{i,\perp}^n$ the perpendicular one. We denote the fifth time integrator by $\Phi^5_{\Delta t} : \mathbb{R}^{3N_\mathrm{p}} \to \mathbb{R}^{3N_\mathrm{p}}$, $\mathbf{V}^n \mapsto \mathbf{V}^{n+1}$.

Substep 6 The sixth subsystem (non-Hamiltonian part) reads

$$\mathbb{M}_0^{n_\mathrm{b}}\,\frac{\mathrm{d}\vec{\mathbf{u}}}{\mathrm{d}t} = \mathbb{D}_0^\top\,\mathbb{M}_0^3\,\mathbf{p} + \mathbb{M}_0^J\,\vec{\mathbf{b}}\,, \qquad \frac{\mathrm{d}\mathbf{p}}{\mathrm{d}t} = \left[\,-\mathbb{D}_0\,(\mathcal{I}_0^2)^{-1}\,\mathcal{F}_0 - (\gamma-1)\,(\mathcal{I}_0^3)^{-1}\,\mathcal{K}_0\,\mathbb{D}_0\,\right]\vec{\mathbf{u}}\,, \tag{3.116}$$

for constant $\vec{\mathbf{b}} = \vec{\mathbf{b}}^n$. Although this step does not conserve the total energy, we still solve it implicitly to circumvent possible Courant-Friedrichs-Lewy (CFL) constraints on the time step because this step contains pressure perturbations which can excite fast magnetosonic waves. We once more choose the Crank-Nicolson method. Defining $\mathbb{L} := -\mathbb{D}_0 \, (\mathcal{I}_0^2)^{-1} \, \mathcal{F}_0 - (\gamma - 1) \, (\mathcal{I}_0^3)^{-1} \, \mathcal{K}_0 \, \mathbb{D}_0$ for a shorter notation leads to

$$\mathbb{M}_0^{n_\flat} \, \vec{\mathbf{u}}^{n+1} = \mathbb{M}_0^{n_\flat} \, \vec{\mathbf{u}}^n + \frac{\Delta t}{2} \, \mathbb{D}_0^\top \, \mathbb{M}_0^3 \, (\mathbf{p}^n + \mathbf{p}^{n+1}) + \Delta t \, \mathbb{M}_0^J \, \vec{\mathbf{b}}^n \,, \tag{3.117}$$

$$\mathbf{p}^{n+1} = \mathbf{p}^n + \frac{\Delta t}{2} \, \mathbb{L} \, (\vec{\mathbf{u}}^n + \vec{\mathbf{u}}^{n+1}) \,. \tag{3.118}$$

As in substeps 1-3, these equations can be decoupled by plugging the second equation in the first one followed by solving for $\mathbb{u}^{n+1}$:

$$\mathbb{S}_6 \, \vec{\mathbf{u}}^{n+1} = \left(\mathbb{M}_0^{n_\flat} + \frac{\Delta t^2}{4} \, \mathbb{D}_0^\top \, \mathbb{M}_0^3 \, \mathbb{L} \right) \vec{\mathbf{u}}^n + \Delta t \, \mathbb{D}_0^\top \, \mathbb{M}_0^3 \, \mathbf{p}^n + \Delta t \, \mathbb{M}_0^J \, \vec{\mathbf{b}}^n \,. \tag{3.119}$$

The matrix $\mathbb{S}_6 := \mathbb{M}_0^{n_\flat} - \Delta t^2 \, \mathbb{D}_0^\top \, \mathbb{M}_0^3 \, \mathbb{L}/4$ is constant in time. We denote the sixth time integrator by $\Phi_{\Delta t}^6 : \mathbb{R}^{n_0^2} \times \mathbb{R}^{n_0^3} \to \mathbb{R}^{n_0^2} \times \mathbb{R}^{n_0^3}$, $\vec{\mathbf{u}}^n, \mathbf{p}^n \mapsto \vec{\mathbf{u}}^{n+1}, \mathbf{p}^{n+1}$.

In summary, in order to go from time t^n to time t^{n+1}, we successively apply the six integrators, where it is important to note that the input of the next integrator must be the output of the previous integrator:

$$\Phi_{\Delta t}^{\mathrm{L}} := \Phi_{\Delta t}^6 \circ \Phi_{\Delta t}^5 \circ \Phi_{\Delta t}^4 \circ \Phi_{\Delta t}^3 \circ \Phi_{\Delta t}^2 \circ \Phi_{\Delta t}^1 \,, \tag{3.120}$$

$$\Phi_{\Delta t}^{\mathrm{S}} := \Phi_{\Delta t/2}^{\mathrm{L}} \circ (\Phi_{\Delta t/2}^{\mathrm{L}})^{-1} \,. \tag{3.121}$$

This first-order composition (3.120) is known as the Lie-Trotter splitting [68] and consists of applying each integrator one after the other. In contrast to that, the second-order decomposition (3.121) known as the Strang splitting consists of first applying the Lie-Trotter decomposition with a half time step and in reverse order followed by applying the Lie-Trotter decomposition with a half time step in "normal" order. Higher-order compositions are in principle available [70] but become computationally more expensive which is why only these two compositions have been implemented so far. In all simulation results presented in this thesis, the second-order Strang splitting (3.121) was used.

3.7 Implementation and code description

The implementation of the methodologies introduced in the previous sections was realized with the help of the programming language Python in combination with automatically generated Fortran kernels for acceleration. The latter is achieved with the tool Pyccel which can be regarded as a Python-to-Fortran converter from a user point of view and which is currently being developed at the Max Planck Institute for Plasma Physics in Garching, Germany. The result of these implementations is the newly developed code STRUPHY which stands for Structure-Preserving Hybrid Code to highlight both the numerical methods being used (structure-preserving methods) as well as the physics models in play (hybrid MHD-kinetic models). The overall structure of STRUPHY is depicted in Figure 3.6, where each node represents a class and the arrows between the nodes indicate dependencies among different classes. In the following, we shall give a description of the most important low-level classes where the focus shall be laid on its basic contents and functionalities instead of a detailed and complete code description. For instance, when listing input parameters or methods of classes, we will use pseudo-code and not define data types of input and output variables etc..

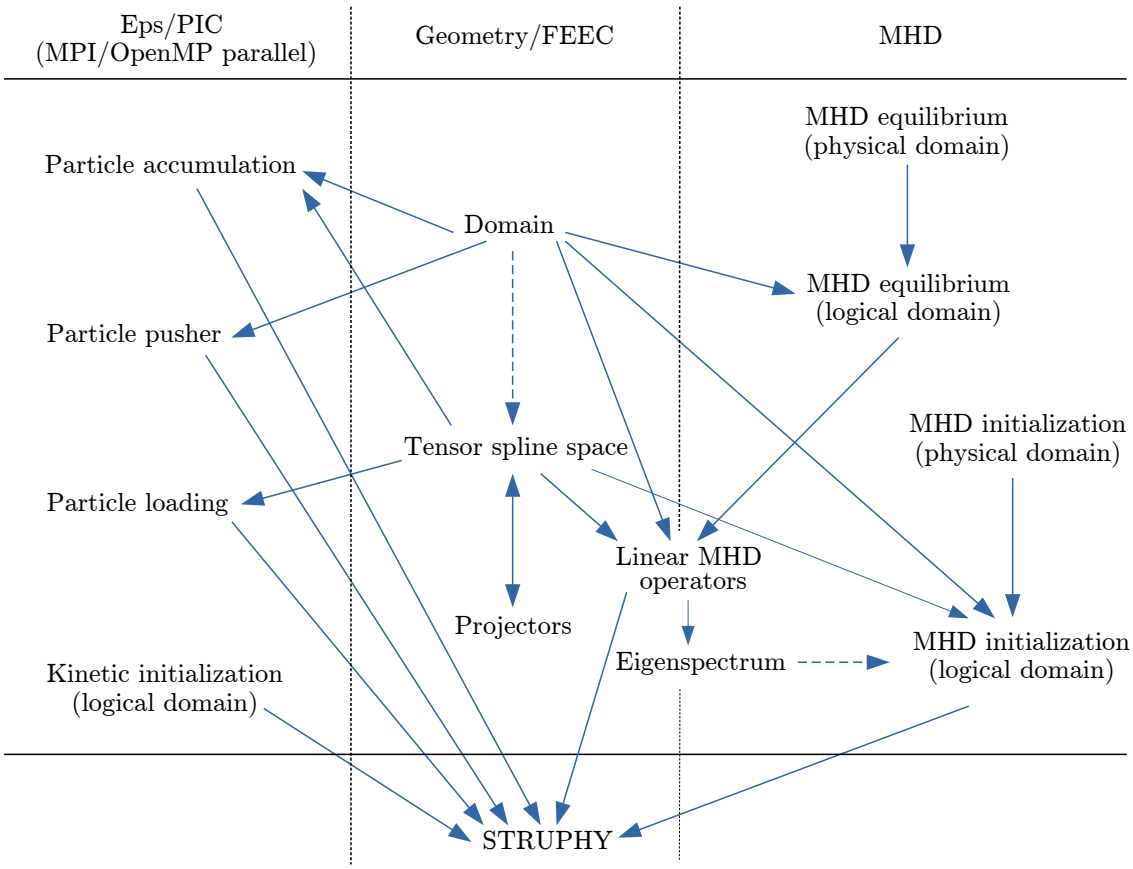

Figure 3.6: Schematic structure of the new hybrid MHD-kinetic code STRUPHY. Each nodes represents a Python class and arrows indicate dependencies among them. The classes can be grouped into 1) classes related to energetic particles (EPs) and particle-in-cell (PIC) routines (left column), 2) classes related to differential geometry and finite element exterior calculus (FEEC) and 3) classes related to magnetohydrodynamics (MHD).

3.7.1 Domain class

At the heart of STRUPHY lies the class `Domain` which is independent of the model being solved and does not require input data from any of the other classes. Therefore, when STRUPHY is executed, among the first things being performed is to create an object from this class. `Domain` handles all differential geometry related operations, in particular evaluation of metric coefficients and pull-back and push-forward operations according to Table 3.1. As shown in the beginning of this chapter, all these operations are based on the mapping $F : \hat{\Omega} \to \Omega$ from the logical domain $\hat{\Omega} = [0, 1]^3$ to the physical domain $\Omega \subset \mathbb{R}^3$. Among others, the following analytical mappings are available in the class `Domain`:

$$\text{Cuboid}: \qquad F(s,\chi,\varphi) = \begin{bmatrix} as \\ 2\pi a\chi \\ 2\pi R_0\,\varphi \end{bmatrix}, \tag{3.122}$$

$$\text{Cylinder}: \qquad F(s,\chi,\varphi) = \begin{bmatrix} R(s,\chi) \\ Y(s,\chi) \\ 2\pi R_0\,\varphi \end{bmatrix}, \quad \begin{matrix} R(s,\chi) = as\cos(2\pi\chi) + R_0 \\ Y(s,\chi) = as\sin(2\pi\chi) \end{matrix}, \tag{3.123}$$

$$\text{Circular torus (with straight field line angle)} \; : \; \begin{cases} F(s,\chi,\varphi) = \begin{bmatrix} R(s,\chi)\cos(2\pi\varphi) \\ Y(s,\chi) \\ R(s,\chi)\sin(2\pi\varphi) \end{bmatrix}, \\ R(s,\chi) = as\cos(\theta(s,\chi)) + R_0\,, \\ Y(s,\chi) = as\sin(\theta(s,\chi))\,, \\ \theta(s,\chi) = 2\arctan\left(\sqrt{\dfrac{1+as/R_0}{1-as/R_0}}\tan(\pi\chi)\right). \end{cases} \tag{3.124}$$

The first mapping (3.122) results in a cuboid with side lengths a, $2\pi a$ and $2\pi R_0$ and is supposed to mimic a torus with minor radius a and major radius R_0 in slab geometry. The second mapping (3.123) results in a cylinder where $r = as$ is the geometric distance from the pole at (R_0, Y_0) and $\theta = 2\pi\chi$ is the geometric polar angle. Finally, the mapping (3.123) describes a torus with circular concentric s-isolines and curved χ-isolines (both for fixed toroidal angle φ). Hence, $2\pi\chi$ is **not** equal to the geometric poloidal angle θ as opposed to (3.123) but is rather chosen in a way that magnetic field lines corresponding to an ad hoc tokamak-like magnetic field are straight when plotted in the (χ,φ)-plane for a fixed s. This means that the safety factor $q = (\mathbf{B}_{\text{eq}}\cdot\nabla\varphi)/(\mathbf{B}_{\text{eq}}\cdot\nabla\chi)$ is a function of s only [94]. More details, in particular the explicit form of the ad hoc magnetic field $\mathbf{B}_{\text{eq}}$, shall be given in Section 3.7.3 when talking about MHD equilibria.

Besides the analytical mappings (3.122)-(3.124), the class `Domain` also supports isogeometric (IGA) mappings in the poloidal plane, i.e. the "poloidal mapping" $F_{\text{pol}} : (s,\chi) \mapsto (R,Y)$ is more generally given by B-spline representations of the form

$$R_h(s,\chi) = R_0 + \sum_{i=1}^{n_s-1}\sum_{j=0}^{n_\chi-1} c^R_{(ij)}\, N_i^{p_s}(s) N_j^{p_\chi}(\chi)\,, \tag{3.125a}$$

$$Y_h(s,\chi) = Y_0 + \sum_{i=1}^{n_s-1}\sum_{j=0}^{n_\chi-1} c^Y_{(ij)}\, N_i^{p_s}(s) N_j^{p_\chi}(\chi)\,, \tag{3.125b}$$

where $(ij) := i\,(j_{\max}+1)+j$. The FE coefficients $\mathbf{c}^R := (c^R_{(ij)})$ and $\mathbf{c}^Y := (c^Y_{(ij)})$ are called the *control points* of the poloidal mapping F_{pol}; they can be obtained either by interpolation of given analytical expressions for $R = R(s,\chi)$ and $Y = Y(s,\chi)$ like in (3.124) or by interpolation of a given poloidal magnetic flux function $\psi = \psi(R,Y)$, e.g. obtained from an MHD equilibrium code, in a way that (s,χ) become *magnetic flux coordinates*. This means that for fixed $s = s_0$, the curve $\mathbf{L}(\chi) = (R(s_0,\chi), Y(s_0,\chi))$ defines a closed magnetic flux surface of arbitrary shape corresponding to some given MHD equilibrium. As in (3.124), a common choice for the angle-like coordinate χ is then to define it in a way that magnetic field lines become straight when plotted in the (χ,φ)-plane. Other choices for χ, however, can be made as well.

Table 3.2 summarizes the most important contents of the class `Domain_3d`. The input parameters essentially specify the desired mapping together with its parameters in case of the analytical mappings (3.122)-(3.124) (minor radius a and major radius R_0) or together with the required B-spline parameters (spline degrees etc.) in case of the IGA mappings (3.125). Once an instance of `Domain` is created, it allows the evaluation of all metric coefficients via the method `evaluation(s, chi, phi, what)`, where the parameter `what` selects the metric coefficient. For instance, `what='x'` evaluates the x-component of the chosen mapping and `what='g_23'` evaluates the 23-component of the metric tensor G. Finally, the two methods `pull(fun, s, chi,`

Table 3.2: Main contents and functionalities of the class `Domain` for handling 3d mapped domains. For analytical mappings, only the input parameters `kind_map` and `params_map` must be passed while for IGA mappings in the poloidal plane also the number of elements `Nel`, spline degrees `p`, kind of splines `spl` (clamped or periodic) and control points `cR` and `cY` must be passed. In case of IGA mappings, the attributes contain the number of B-splines `n` in s- and χ-direction and the respective spline knot vectors `T` needed for B-spline evaluations. The abbreviation "opt." stands for "optional".

Class: `Domain`		
Input parameters	Attributes	Methods
`kind_map`	`kind_map`	`evaluate(s, chi, phi, what)`
`params_map=(a, R0)`	`params_map`	`pull(fun, s, chi, phi, to_what)`
`Nel=(Nel_s, Nel_chi)` (opt.)	`n=(n_s, n_chi)`	`push(fun, s, chi, phi, to_what)`
`p=(p_s, p_chi)` (opt.)	`p=(p_s, p_chi)`	
`spl=(spl_s, spl_chi)` (opt.)	`T=(T_s, T_chi)`	
`cR`, `cY` (opt.)	`cR`, `cY`	

`phi, to_what)` and `push(fun, s, chi, phi, to_what)` implement the pull-back and push-forward operations listed in Table 3.1, where `fun` is the input function and `to_what` specifies the destination function. For example a scalar function on the physical domain can be pulled-back either to a 0-form (`to_what='0_form'`) or to a 3-form (`to_what='3_form'`).

3.7.2 FEM and projectors class

Everything related to FEEC is handled within the class `TensorSplineSpace`. It implements the commuting diagram both with and without boundary conditions in s-direction and contains routines for evaluating elements of the spaces V_h^k and $V_{0,h}^k$ for given FE coefficients. Therefore, input parameters are the number of elements, spline degrees and kind of splines (clamped or periodic) in each direction as well as the toroidal mode number and boundary conditions in s-direction. The latter is done via the parameter `bc=(bc_0, bc_1)`, where `bc_0` is the boundary condition at $s = 0$ and `bc_1` the boundary condition at $s = 1$. An object created from `TensorSplineSpace` then contains as attributes the four boundary operators $\mathbb{B}^k$ (3.56)-(3.57), the discrete derivatives $\mathbb{G}$, $\mathbb{C}$ and $\mathbb{D}$ for the de Rham complex of the full spaces V_h^k as well as the discrete derivatives $\mathbb{G}_0$, $\mathbb{C}_0$ and $\mathbb{D}_0$ for the de Rham complex of the reduced spaces $V_{0,h}^k$ that take into account boundary conditions. In order to calculate the integrals needed in the mass matrices, we employ a Gauss-Legendre quadrature in each element of the discretized poloidal plane. Contributions in toroidal direction are analytical and decoupled from the poloidal ones because in axisymmetric configurations equilibrium quantities, the Jacobian determinant $\sqrt{g}$ and metric tensor G are independent of the toroidal angle. Therefore, a generic entry of the mass matrix $\mathbb{M}^0$ (3.53a) is calculated as

$$\begin{aligned}\int_{\hat{\Omega}} \Lambda^0_{(ijk)}\, \Lambda^0_{(mno)} \sqrt{g}\, \mathrm{d}s\, \mathrm{d}\chi\, \mathrm{d}\varphi &= \left(\int_0^1 \int_0^1 N_i^{p_s} N_j^{p_\chi} N_m^{p_s} N_n^{p_\chi} \sqrt{g}\, f\, \mathrm{d}s\, \mathrm{d}\chi \right) \int_0^1 \mathcal{F}_k^n \mathcal{F}_o^n\, \mathrm{d}\varphi \\ &= \left(\int_0^1 \int_0^1 N_i^{p_s} N_j^{p_\chi} N_m^{p_s} N_n^{p_\chi} \sqrt{g}\, \mathrm{d}s\, \mathrm{d}\chi \right) \frac{1}{2}\, \delta_{ko}\,.\end{aligned} \tag{3.126}$$

Table 3.3: Main contents and functionalities of the class `TensorSplineSpace` for handling FEEC related operations. Input parameters are the number of elements `Nel`, spline degrees `p` and kind of splines `spl` (clamped or periodic) in s- and χ-direction as well as the toroidal mode number `n_tor` and boundary conditions `bc` in s-direction. The parameter `nq` is the number of Gauss-Legendre quadrature points per element for calculating integrals over the entire logical domain $\hat{\Omega}$.

Class: `TensorSplineSpace`		
Input parameters	Attributes	Methods
`Nel=(Nel_s, Nel_chi)`	`n=(n_s, n_chi)`	`eval_NN(s, chi, phi, coeff, space)`
`p=(p_s, p_chi)`	`d=(d_s, d_chi)`	`eval_DN(s, chi, phi, coeff, space)`
`spl=(spl_s, spl_chi)`	`T=(T_s, T_chi)`	`eval_ND(s, chi, phi, coeff, space)`
`n_tor`	`G`, `C`, `D`	`eval_DD(s, chi, phi, coeff, space)`
`bc=(bc_0, bc_1)`	`M0`, `M1`, `M2`, `M3`	`assemble_Mk(domain, space)`
`nq=(nq_s, nq_chi)`	`B0`, `B1`, `B2`, `B3`	`set_projectors(nq)`
	`G0`, `C0`, `D0`	
	`M0_0`, `M1_0`,	
	`M2_0`, `M3_0`	
	`projectors`	

Splitting the remaining two integrals into contributions from integrals over elements and subsequently applying the Gauss-Legendre quadrature yields

$$\begin{aligned}\int_{\hat{\Omega}} \Lambda^0_{(ijk)}\,\Lambda^0_{(mno)}\sqrt{g}\,\mathrm{d}s\,\mathrm{d}\chi\,\mathrm{d}\varphi &= \frac{1}{2}\,\delta_{ok}\left(\sum_{e_1,e_2}\int_{\hat{\Omega}^s_{e_1}}\int_{\hat{\Omega}^\chi_{e_2}} N_i^{p_s}N_j^{p_\chi}N_m^{p_s}N_n^{p_\chi}\sqrt{g}\,\mathrm{d}s\,\mathrm{d}\chi\right) \\ &\approx \frac{1}{2}\,\delta_{ko}\sum_{e_1,e_2}\sum_{q_1,q_2} w^s_{e_1q_1}w^\chi_{e_2q_2}N_i^{p_s}(s_{e_1q_1})N_j^{p_\chi}(\chi_{e_2q_2})N_m^{p_s}(s_{e_1q_1})N_n^{p_\chi}(\chi_{e_2q_2})\sqrt{g}(s_{e_1q_1},\chi_{e_2q_2})\,,\end{aligned} \tag{3.127}$$

where $w^s_{e_1q_1}$ is the q_1-th Gauss-Legendre quadrature weight and $s_{e_1q_1}$ the corresponding quadrature point; both mapped from the interval $[-1,1]$ (where quadrature rules are usually defined) to the element $\hat{\Omega}^s_{e_1} = [c^s_{e_1}, c^s_{e_1+1}]$ (accordingly for the χ-direction). The number of quadrature points per element in each of the two directions is set with the input parameter `nq=(nq_s, nq_chi)` which is set to the default value $(6,6)$ in the following if not specified differently. The computations (3.126)-(3.127) for the mass matrices (3.53) are then performed upon calling the method `assemble_mk(domain, space)`, where `domain` is an object crated from the class `Domain` and `space` specifies which mass matrix one wants to assemble (e.g. `space='V0'` for the mass matrix $\mathbb{M}^0$). A summary of the most important contents and functionalities of the class `TensorSplineSpace` is given in Table 3.3.

The commuting projectors Π_k are set with the method `set_projectors(nq)`, where `nq` are the number of quadrature points per integration interval in the computation of the degrees of freedom (3.68). The projectors are implemented in a separate class `ProjectorsGlobal3D`. Hence, after calling `set_projectors(nq)`, a projectors object becomes an attribute of the tensor spline space object on which the method is called. The class `ProjectorsGlobal3D` implements

Table 3.4: Main contents and functionalities of the class `ProjectorsGlobal3D` for handling commuting projections. Input parameters are an object `tensorspace` created from the `TensorSplineSpace` class and the number of Gauss-Legendre quadrature points per integration interval `nq` for computing the geometric degrees of freedom.

Class: `ProjectorsGlobal3D`		
Input parameters	Attributes	Methods
`tensorspace`	`I0`, `I1`, `I2`, `I3`	`dofs_0(fun, bc)`
`nq=(nq_s,nq_chi)`	`I0_0`, `I1_0`, `I2_0`, `I3_0`	`dofs_1(fun, bc)`
	`I0_lu`, `I1_lu`, `I2_lu`, `I3_lu`	`dofs_2(fun, bc)`
	`I0_0_lu`, `I1_0_lu`, `I2_0_lu`, `I3_0_lu`	`dofs_3(fun, bc)`
	`I0_0_t_lu`, `I1_0_t_lu`, `I2_0_t_lu`, `I3_0_t_lu`	

the evaluation of the degrees of freedom (3.68) via Gauss-Legendre quadrature in each histopolation interval $[\mathfrak{s}_k, \mathfrak{s}_{k+1}]$ between two successive Greville points (accordingly for the χ-direction) as well as the final projections using the interpolation matrices $\mathcal{I}^k$ (3.70) resp. $\mathcal{I}_0^k = \mathbb{B}^k \mathcal{I}^k \left(\mathbb{B}^k\right)^\top$. Since the inverse interpolation matrices are needed for this, LU decompositions are computed when a projectors object is created. With that, the application of an inverse interpolation matrix to some vector becomes very efficient. As before, if not stated differently, the number of quadrature points is set to $(6, 6)$. A summary of the most important contents and functionalities of the class `ProjectorsGlobal3D` is given in Table 3.4. Attributes are the interpolation matrices $\mathcal{I}^k$ and $\mathcal{I}_0^k$ as well as their LU decompositions. Besides this, LU decompositions of the transposed interpolation matrices $(\mathcal{I}_0^k)^\top$ are calculated because for instance $(\mathcal{I}_0^2)^{-\top}$ is needed in the MHD momentum balance equation (3.77a). The most important methods of the `ProjectorsGlobal3D` class are the ones for computing the geometric degrees of freedom needed for the commuting projectors. They take as an input the components of some analytical differential form and return the function evaluated at the interpolation point resp. the integrals between the interpolation points. The latter is once more performed with Gauss-Legendre quadrature. The parameter `bc` states whether to include (`bc=True`) or not include (`bc=False`) the degrees of freedom corresponding to interpolation points on the domain boundaries at $s = 0$ and $s = 1$.

3.7.3 MHD equilibrium classes

Three analytical MHD equilibria corresponding to slab, cylindrical and toroidal geometry were implemented in the class `EquilibriumMhdPhysical`. It enables the evaluation of the magnetic field $\mathbf{B}_{\text{eq}}$, the pressure p_{eq}, the number density $n_{\text{b,eq}}$ and the current density $\mathbf{J}_{\text{eq}} = \nabla \times \mathbf{B}_{\text{eq}}$; all on the physical domain Ω. It is important to note that this is a priori independent of the mapping F being used in the class `Domain` because different coordinates can be used to represent the same geometry.

The first equilibrium corresponds to a so-called "sheared slab" and is supposed to mimic the sheared magnetic field property of a tokamak in a simplified slab geometry. Hence, similar to a tokamak, there is a safety factor $q = q(x)$ which defines the magnetic shear along a radial-like coordinate (x in this case). The role of the radial, "poloidal" and "toroidal" coordinates are taken

Table 3.5: Main contents and functionalities of the class `EquilibriumMhdPhysical` for loading analytical MHD equilibria. Input parameters are the kind of MHD equilibrium one wants to load (e.g. `kind='torus'` for (3.130)) and the corresponding parameters `params_mhd` needed to define the profiles.

Class: `EquilibriumMhdPhysical`		
Input parameters	Attributes	Methods

`kind`
`params_mhd=(a,`
`R0, B0, q0, q1,`
`beta, p1, p2,`
`na, n1, n2)`
	`kind`
	`params_mhd`
		`B_eq_x(x, y, z)`, `B_eq_y(x, y, z)`, `B_eq_z(x, y, z)`
		`J_eq_x(x, y, z)`, `J_eq_y(x, y, z)`, `J_eq_z(x, y, z)`
		`p_eq(x, y, z)`
		`n_eq(x, y, z)`

by x, y and z, respectively, such that the equilibrium fields depend on x only:

$$\text{Sheared slab} : \begin{cases} \mathbf{B}_{\text{eq}} = B_0 \left(\mathbf{e}_z + \dfrac{a}{q(x) R_0} \mathbf{e}_y \right) , \quad q(x) = q_0 + (q_1 - q_0) \dfrac{x^2}{a^2} , \\ p_{\text{eq}} = \dfrac{\beta B_0^2}{2} \left(1 + \dfrac{a^2}{q^2 R_0^2} \right) + \dfrac{B_0^2 a^2}{R_0^2} \left(\dfrac{1}{q_0^2} - \dfrac{1}{q^2} \right) , \\ n_{\text{b,eq}} = 1 . \end{cases} \tag{3.128}$$

It is easily verified that (3.128) constitutes a MHD equilibrium according to $\nabla p_{\text{eq}} = (\nabla \times \mathbf{B}_{\text{eq}}) \times \mathbf{B}_{\text{eq}}$. The integration constant for the pressure is set in a way that $\beta = 2p_{\text{eq}}(x = 0)/(B_0^2 + B_{\text{ey},y}(x = 0)^2)$, i.e. the parameter β is the plasma beta (ratio kinetic and magnetic pressure) at $x = 0$.

The second equilibrium corresponds to a straight tokamak configurations with circular flux surfaces (screw pinch). In the same way as for the sheared slab, a strictly monotonically increasing safety factor $q = q(r)$ in radial direction together with a constant toroidal (axial) magnetic field $\mathbf{B}_{\text{eq}} \cdot \mathbf{e}_z = B_0$ is prescribed which results in the following profiles:

$$\begin{array}{l} \text{Straight tokamak} \\ x = r\cos\theta + R_0 \\ y = r\sin\theta \end{array} : \begin{cases} \mathbf{B}_{\text{eq}} = B_0 \left(\mathbf{e}_z + \dfrac{r}{q(r) R_0} \mathbf{e}_\theta \right) , \quad q(r) = q_0 + (q_1 - q_0) \dfrac{r^2}{a^2} , \\ p_{\text{eq}} = \begin{cases} \dfrac{B_0^2 a^2 q_0}{2R_0^2 (q_1 - q_0)} \left(\dfrac{1}{q^2} - \dfrac{1}{q_1^2} \right) & \text{if } q_1 \neq q_0 , \\ \dfrac{\beta B_0^2}{2} & \text{else} , \end{cases} \\ n_{\text{b,eq}} = (1 - n_a) \left(1 - \left(\dfrac{r}{a} \right)^{n_1} \right)^{n_2} + n_a . \end{cases} \tag{3.129}$$

For non-constant q-profiles ($q_0 \neq q_1$), the integration constant for the pressure is set in a way that the pressure drops to zero at the boundary, i.e. $p_{\text{eq}}(r = a) = 0$. For a constant q-profile ($q_0 = q_1$), the resulting constant pressure is defined by the plasma beta. Moreover, a strictly monotonically decreasing number density with a maximum at $r = 0$ and some non-zero value

n_a at $r = a$ is prescribed. As before, it is easily verified that (3.129) constitutes an exact MHD equilibrium.

The third equilibrium represents a tokamak with circular concentric flux surfaces. The profiles are given by

$$\text{Tokamak (ad hoc)} \quad \begin{aligned} x &= R\cos\theta\cos\phi \\ y &= r\sin\theta \\ z &= R\cos\theta\sin\phi \\ R &= R_0 + r\cos\theta \end{aligned} \quad : \quad \begin{cases} \mathbf{B}_{\text{eq}} = \dfrac{B_0 R_0}{R}\left(\mathbf{e}_\phi + \dfrac{r}{\bar{q}(r)R_0}\,\mathbf{e}_\theta\right), \quad \bar{q}(r) = q(r)\sqrt{1-\dfrac{r^2}{R_0^2}}\,, \\ \qquad\qquad\qquad\qquad q(r) = q_0 + (q_1 - q_0)\dfrac{r^2}{a^2}\,, \\ p_{\text{eq}} = \dfrac{\beta B_0^2}{2}\left(1 - p_1\dfrac{r^2}{a^2} - p_2\dfrac{r^4}{a^4}\right), \\ n_{\text{b,eq}} = (1-n_a)\left(1-\left(\dfrac{r}{a}\right)^{n_1}\right)^{n_2} + n_a\,, \end{cases} \tag{3.130}$$

where the ad hoc pressure profile is such that $\beta = 2p_{\text{eq}}(r=0)/B_0^2$, which means that the parameter β is the on-axis plasma beta. The relation between the "true" safety factor q and the modified one $\bar{q}$ used in the definition of the poloidal magnetic field component can be seen as a toroidal correction and results from averaging along a flux surface:

$$q := \frac{\mathbf{B}_{\text{eq}}\cdot\nabla\phi}{\mathbf{B}_{\text{eq}}\cdot\nabla\theta} = \frac{R_0}{R}\,\bar{q} \quad \Rightarrow \quad q(r) = R_0\,\bar{q}(r)\frac{1}{2\pi}\int_0^{2\pi}\frac{1}{R(r,\theta)}\,\mathrm{d}\theta = \frac{\bar{q}(r)}{\sqrt{1-r^2/R_0^2}}\,. \tag{3.131}$$

It should be noted that (3.130) is not an exact MHD equilibrium and should rather be seen as an approximation of a cylindrical equilibrium in toroidal geometry.

The profiles (3.128)-(3.130) are accessible via an object created from the class `EquilibriumMhdPhysical` whose contents are summarized in Table 3.5. Once an object is crated, it enables the evaluation of the magnetic field, current density, pressure and number density on the physical domain, i.e. with respect to Cartesian coordinates. The corresponding differential forms obtained by pull-back operations according to Table 3.1 are then accessible via an object created from the class `EquilibriumMhdLogical` whose contents and functionalities are summarized in Table 3.6. It enables the evaluation of components of differential forms according to expressions like `domain.pull([eq_mhd_phy.B_eq_x, eq_mhd_phy.B_eq_y, eq_mhd_phy.B_eq_z], s, chi, phi, '2_form_1')` for e.g. the evaluation of the first component of the 2-form equilibrium magnetic field.

3.7.4 Linear MHD operators class

Once the computational domain and an MHD equilibrium is created, the class `MhdOperators` handles all operations related to the linear MHD part of STRUPHY and thus brings together the chosen MHD equilibrium on the logical domain created from `EquilibriumMhdLogical` and the FEM spaces created from `TensorSplineSpace`. In particular, it implements the weighted mass matrices $\mathbb{M}_0^{n_\text{b}}$ and $\mathbb{M}_0^J$ (3.87) and the matrices $\mathcal{T}_0$, $\mathcal{F}_0$ and $\mathcal{K}_0$ (3.80) resulting from applications of one of the commuting projectors. As in the case of the mass matrices $\mathbb{M}^k$ $(0 \leq k \leq 3)$, this is done in an efficient way by taking into account the compact support of the basis functions, i.e. only matrix entries which are known to be non-zero are computed. The two weighted mass matrices are assembled by calling the methods `assemble_Mn()` and `assemble_MJ()`, respectively, while the degrees of freedom matrices are assembled by calling `assemble_dofs(which)`, where `which='T','F','K'` specifies the matrix to be assembled. Moreover, `MhdOperators` implements

Table 3.6: Main contents and functionalities of the class `EquilibriumMhdLogical` for pull-backs of MHD equilibrium profiles on the physical domain Ω to the logical domain $\hat{\Omega}$. Input parameters are an object `domain` created from the class `Domain` and an object `eq_mhd_phy` created from the class `EquilibriumMhdPhysical`.

Class: `EquilibriumMhdLogical`		
Input parameters	Attributes	Methods
`domain`	`domain`	`B2_eq_1(s, chi, phi)`, `B2_eq_2(s, chi, phi)`,
`eq_mhd_phy`	`eq_mhs_phy`	`B2_eq_3(s, chi, phi)`
		`J2_eq_1(s, chi, phi)`, `J2_eq_2(s, chi, phi)`,
		`J2_eq_3(s, chi, phi)`
		`p3_eq(s, chi, phi)`
		`n3_eq(s, chi, phi)`

preconditioners for the linear systems in (3.105) and (3.119) defined by the matrices $\mathbb{S}_2$ and $\mathbb{S}_6$, respectively. In STRUPHY, all linear systems are solved iteratively with a Krylov subspace method for solving large linear systems. The default solver for systems defined by a positive-definite matrix (substeps 2 and 3) is the conjugate gradient method (CG) [95] while the default solver for the other systems (substeps 1 and 6) is the generalized minimal residual method (GMRES) [96]. The usage of iterative methods has the advantage that inverse matrices do not have to be computed explicitly but only the results of matrix-vector products such as $\mathbb{S}_2\mathbf{u}^{n+1}$ need to be available. This is useful because the matrices $\mathbb{S}_2$ and $\mathbb{S}_6$ are **not** sparse because they involve inverse interpolation matrices with are dense. Saving these matrices explicitly would require about $(3\times100\times100\times2)^2\times8\,\mathrm{B} = 28.8\,\mathrm{GB}$ of memory on a 100×100 grid in case of double precision. Therefore, in order to save memory (especially when going to fully three-dimensional stellarator-like problems in the future), the matrices $\mathbb{S}_2$ and $\mathbb{S}_6$ are never assembled explicitly. However, it was observed that effective preconditioning is needed to reach convergence after a reasonable amount of iteration steps such that the overall simulation time does not become too large. Different preconditioning strategies were investigated for this purpose.

A first simple way is to approximate the system matrices in the substeps 1, 2, 3 and 6 by $\mathbb{M}_0^{n_\mathrm{b}}$ because all matrices are of the form $\mathbb{M}_0^{n_\mathrm{b}} \pm \Delta t \ldots$ (substep 1) or $\mathbb{M}_0^{n_\mathrm{b}} \pm \Delta t^2 \ldots$ (substeps 2, 3 and 6). Hence, if Δt is small ($\Delta t < 1$), $\mathbb{M}_0^{n_\mathrm{b}}$ seems to be a reasonable approximation and inverting the sparse matrix $\mathbb{M}_0^{n_\mathrm{b}}$ is easy (e.g. via sparse LU decomposition). Indeed, it was found that this method works well for the two kinetic coupling substeps 1 and 3. In all simulation results presented in this thesis, convergence was reached after a maximum of ~ 10 iteration steps even for larger times steps $\Delta t \lesssim 0.32$. In contrast to that, in the pure MHD systems in substeps 2 and 6 (especially substep 2) this method only worked reasonably well for very small time steps. For larger times steps a good preconditioning was obtained by computing approximations of $\mathbb{S}_2$ and $\mathbb{S}_6$ by approximating the inverse interpolation matrices. The latter is achieved by noting that many entries of the inverse interpolation matrices are close to zero. Hence, values smaller than some tolerance can be set to zero. The resulting sparse approximations are then used to compute approximations for $\mathbb{S}_2$ and $\mathbb{S}_6$ which are again sparse. For these matrices, sparse LU decompositions can be used as preconditioners. Since in linear MHD, $\mathbb{S}_2$ and $\mathbb{S}_6$ do not change in time, this needs to be done only once in the beginning of a simulation.

Table 3.7: Main contents and functionalities of the class `MhdOperators` for assembling MHD related weighted mass matrices, degree of freedom matrices and preconditioners for linear systems in substep 2 (3.105) and substep 6 (3.119). Input parameters are an object `tensorspace` created with the class `TensorSplineSpace` and an object `eq_mhd_log` created with the class `EquilibriumMhdLogical`.

Class: `MhdOperators`		
Input parameters	Attributes	Methods
`tensorspace`	`Mn_0, MJ_0`	`assemble_Mn()`, `assemble_MJ()`
`eq_mhd_log`	`T_0, F_0, K_0`	`assemble_dofs(which)`
	`S2_PRE`	`set_preconditioner_S2(which, tol_inv)`
	`S6_PRE`	`set_preconditioner_S6(which, tol_inv)`

3.7.5 Particle loading class

Currently, STRUPHY loads particles on the logical domain according to the general probability density function (PDF)

$$\begin{aligned} \zeta^3_{\rm h} &= \zeta_s(s)\frac{1}{\pi^{3/2}v^3_{\rm th}(s)}\exp\left[\frac{(v_x-v_{0x})^2+(v_y-v_{0y})^2+(v_z-v_{0z})^2}{v_{\rm th}(s)^2}\right], \\ &\int_0^1 \zeta_s(s)\,{\rm d}s = 1\,, \end{aligned} \tag{3.132}$$

which means that particles are loaded uniformly in the two periodic spatial directions χ and φ. In radial (s) direction particles are loaded according to some arbitrary function $\zeta_s(s)$ (the only restriction is that it must be normalized to one). The reason for this choice is that we want to have the possibility to obtain, for instance, a uniform distribution of particles on the physical domain or to have more particle in regions where a a higher numerical resolution is desired. The former is due to the fact that a uniform distribution of particles on the logical domain does in general **not** result in a uniform distribution of particles on the physical domain. A simple example for this is shown in Figure 3.7 for the case of the standard two-dimensional square-to-disc mapping $x = as\cos(2\pi\chi)$ and $y = as\sin(2\pi\chi)$ for which the Jacobian determinant is readily given by $\sqrt{g} = 2a^2\pi s \sim s$. If one loads particle uniformly on the logical domain according to $\zeta^3_{\rm h} = 1$ (upper left), this will result in a larger particle density around the center of the disc (upper right picture). Consequently, if one wants to end up with a uniform density of particles on the mapped domain (lower right), particles must be sampled according to the (normalized) Jacobian determinant $\zeta^3_{\rm h} = 2s$ on the logical domain (lower left).

In order to sample from the general PDF (3.132), it is first written conditionally in the form

$$\begin{aligned} \zeta^3_{\rm h} &= \iiint \zeta^3_{\rm h}\,{\rm d}v_x\,{\rm d}v_y\,{\rm d}v_z \frac{\iint \zeta^3_{\rm h}\,{\rm d}v_y\,{\rm d}v_z}{\iiint \zeta^3_{\rm h}\,{\rm d}v_x\,{\rm d}v_y\,{\rm d}v_z}\frac{\int \zeta^3_{\rm h}{\rm d}v_z}{\iint \zeta^3_{\rm h}\,{\rm d}v_y\,{\rm d}v_z}\frac{\zeta^3_{\rm h}}{\int \zeta^3_{\rm h}{\rm d}v_z} \\ &=: \zeta_s(s)\,\zeta_{sx}(s,v_x)\,\zeta_{sy}(s,v_y)\,\zeta_{sz}(s,v_z)\,, \end{aligned} \tag{3.133}$$

which allows to successively sample from $\zeta_s(s)$ (which yields some value s_0), from $\zeta_{sx}(s_0,v_x)$ (which yields some value v^0_x), from $\zeta_{sy}(s_0,v_y)$ (which yields some value v^0_y) and finally from

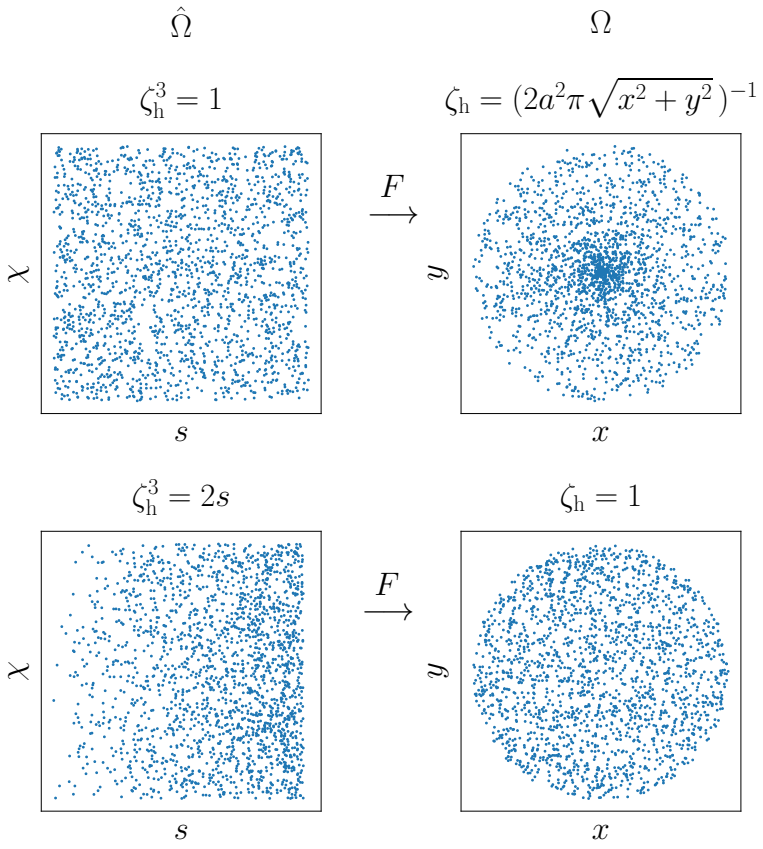

Figure 3.7: Different particle samplings on the logical domain $\hat{\Omega}$ (left column) for the standard square-to-disc mapping $x = as\cos(2\pi\chi)$ and $y = as\sin(2\pi\chi)$ and the resulting particle distribution on the physical domain Ω (right column). If the particles are sampled uniformly on $\hat{\Omega}$ ($\zeta_{\mathrm{h}}^3 = 1$), there will be more particles close to the center of Ω, while if the they are sampled according to the normalized Jacobian determinant ($\zeta_{\mathrm{h}}^3 = \sqrt{g}/\int_{\hat{\Omega}}\sqrt{g}\,\mathrm{d}s\,\mathrm{d}\chi = 2s$), there will be a uniform distribution on Ω.

$\zeta_{sz}(s_0, v_z)$ (which yields some value v_z^0). Since the PDF in s-direction is a priori not known and to therefore ensure maximum flexibility, STRUPHY uses the acceptance-rejection algorithm [97] in this direction. This method allows for sampling from arbitrary functions $\zeta_s(s)$ provided that uniform sampling in the unit interval $(0, 1)$ is possible (e.g. with Python's numpy.random.rand). In velocity space, inverse transform sampling [97] is used because it is more efficient than the acceptance-rejection method from a computational point of view. For this, the cumulative distribution function

$$\int_{-\infty}^{v_\mu} \zeta_{s\mu}(s, v'_\mu)\,\mathrm{d}v'_\mu = \frac{1}{2}\left[1 + \mathrm{erf}\left(\frac{v_\mu - v_{0\mu}}{v_{\mathrm{th}}(s)}\right)\right], \tag{3.134}$$

is needed ($\mu = x, y, z$), where erf denotes the error function. Setting this equal to a random number $u \in \mathcal{U}(0, 1)$ obtained from a uniform distribution in the unit interval and solving for v_μ yields

$$v_\mu = \mathrm{erfinv}(2u - 1)\,v_{\mathrm{th}}(s) + v_{0\mu}\,, \tag{3.135}$$

where erfinv is the inverse error function. The PDF (3.132) as well as the particle loading with the combined acceptance-rejection and inverse transform sampling method is implemented in

Table 3.8: Main contents and functionalities of the class `ParticleLoader`. The only input parameter is a list of parameters `params` which specifies the probability density function (3.132).

Class: `ParticleLoader`		
Input parameters	Attributes	Methods
`params`	`params`	`zeta_h(s, chi, phi, vx, vy, vz)` `load_particles(mpi_comm, seed)`

the class `ParticleLoader` (see Table 3.8). The particle loading is implemented in a way that MPI parallelization results in the same particles compared to the case without parallelization if the total number of particles is unchanged. This is in particular important to check if a parallel code gives the same results as the serial version.

Chapter 4

Simulation results in slab geometry

As a first verification and application of STRUPHY, this chapter is concerned with numerical results obtained in slab geometry given by the mapping (3.122), i.e. a cuboid with side lengths $L_x = a$ (a "minor radius"), $L_y = 2\pi a$ and $L_z = 2\pi R_0$ (R_0 "major radius") such that the x-direction can be identified with the "radial" direction, the y-direction with the "poloidal" direction and the z-direction with the "toroidal" direction of a torus. In the following, we set $a = 1$ and $R_0 = 3$. Moreover, we consider the sheared slab equilibrium (3.128) given by

$$\text{Sheared slab}: \quad \begin{cases} \mathbf{B}_{\text{eq}} = B_0 \left(\mathbf{e}_z + \dfrac{a}{q(x) R_0} \mathbf{e}_y \right), \quad q(x) = q_0 + (q_1 - q_0) \dfrac{x^2}{a^2}, \\ p_{\text{eq}} = \dfrac{\beta B_0^2}{2} \left(1 + \dfrac{a^2}{q^2 R_0^2} \right) + \dfrac{B_0^2 a^2}{R_0^2} \left(\dfrac{1}{q_0^2} - \dfrac{1}{q^2} \right), \\ n_{\text{b,eq}} = 1 . \end{cases} \tag{4.1}$$

In all simulations shown, the constant toroidal magnetic field $B_0 = 1$ and the on-axis ($x = 0$) plasma beta $\beta = 0$. Two classes of numerical tests are performed: The first section is concerned with pure MHD, i.e. the contribution from the kinetic ions is set to zero for all times ($f_{\text{h}} = 0$). The second section deals with non-linear simulations of the interaction of a small population of kinetic ions with shear Alfvén waves. This is the case for which the linear dispersion relation (2.57) was derived and which is expected to be valid as long as the field amplitudes of the perturbations are much smaller than the corresponding equilibrium quantities.

4.1 Continuous spectra and phase mixing

As already mentioned in the introduction, a typical ideal MHD spectrum consists of discrete eigenmodes with corresponding eigenfrequencies on the one hand and singular solutions with eigenfrequencies corresponding to a continuous spectrum on the other hand ($\omega^2 = \omega^2(x)$ in the present case). The latter can be further divided into the shear Alfvén continuum and the slow sound continuum. For the sheared slab equilibrium (4.1), the following analytical expressions for the two continuous spectra can be derived [72]:

$$\text{Alfvén continuum}: \quad \omega^2(x) = \frac{B_0^2}{n_{\text{b,eq}}(x)} \frac{1}{R_0^2} \left(n + \frac{m}{q(x)} \right)^2 , \tag{4.2}$$

$$\text{Sound continuum}: \quad \omega^2(x) = \frac{\gamma p_{\text{eq}}(x)}{n_{\text{b,eq}}(x)(\gamma p_{\text{eq}}(x) + B_{\text{eq},y}^2(x) + B_0^2)} \frac{1}{R_0^2} \left(n + \frac{m}{q(x)} \right)^2 . \tag{4.3}$$

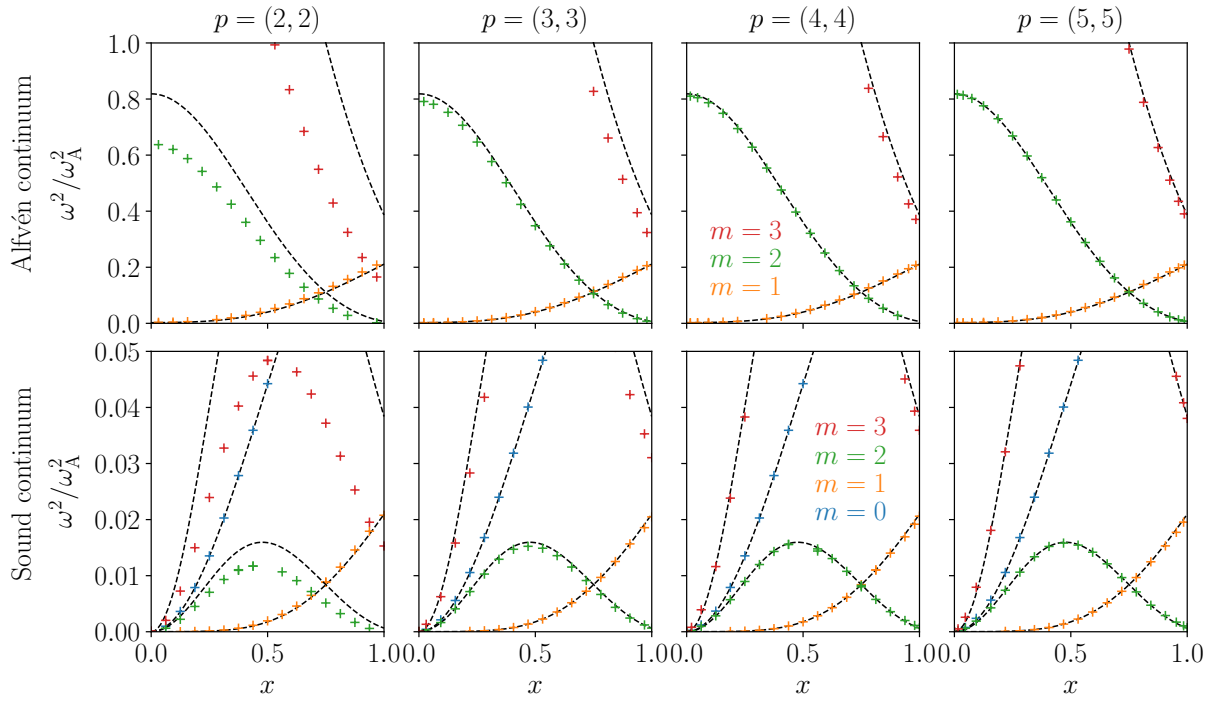

Figure 4.1: Numerical eigenfrequencies ω^2/ω_A^2 ($\omega_A = B_0/R_0$) corresponding to the shear Alfvén continuum (upper row) and slow sound continuum (lower row) for different spline degrees $p = (p_s, p_\chi)$. The toroidal mode number $n = -1$ and the black dashed lines are the analytical expectations according to (4.2) and (4.3). The different frequency ranges indicate that slow sound continuum modes have much smaller frequencies than Alfvénic modes.

In (4.2) and (4.3), $m = ak_y$ is the poloidal mode number in y-direction and $n = R_0\, k_z$ the toroidal mode number in z-direction. For a safety factor profile with parameters $q_0 = 1.05$ and $q_1 = 1.85$ and a numerical resolution of $N_{\text{el}} = (16, 12)$, the resulting continuous spectra calculated with the eigenvalue version of STRUPHY are shown in Figure 4.1 for four different splines degrees $p = (p_s, p_\chi)$. Since the eigenvalue solver currently computes the complete MHD spectrum including compressible modes, the divergence of an eigenfunction $\mathbf{U}_h^2$ is taken as a measure to distinguish between incompressible Alfvénic modes ($\nabla \cdot \mathbf{U}_{\text{h}} \approx 0$) and compressible magnetosonic modes ($\nabla \cdot \mathbf{U} \neq 0$). Moreover, the radial location of a continuum mode is identified by searching for the singularity (or discontinuity) in the corresponding eigenfunction. Once this location is found, the poloidal mode number m is finally identified by analyzing the Fourier spectrum along the poloidal direction at the previously found singular point in radial direction. From Figure 4.1 it is evident that the used spline degree has a strong impact on the correct representation of the continuous spectra. While $p = (2, 2)$ is not able to resolve modes with $m > 1$ properly (upper left plot), $p = (5, 5)$ results in an excellent agreement with the analytical expectation. This is because higher spline degrees are able to better approximate Fourier modes due to their larger support compared to smaller degrees (the support of B-splines is $p + 1$ elements).

Based on the result that STRUPHY calculates continuous spectra in a very satisfactory way, as a next step, continuum damping is investigated. As already mentioned in the introduction, continuum damping can be understood by imagining a radially extended wave packet which is dispersed due to different local Alfvén velocities at different radial positions. Hence, after some time, adjacent fluid elements loose their phase coherence which will lead to an effective damping. To model this feature with the initial-value run mode of STRUPHY, it is initialized

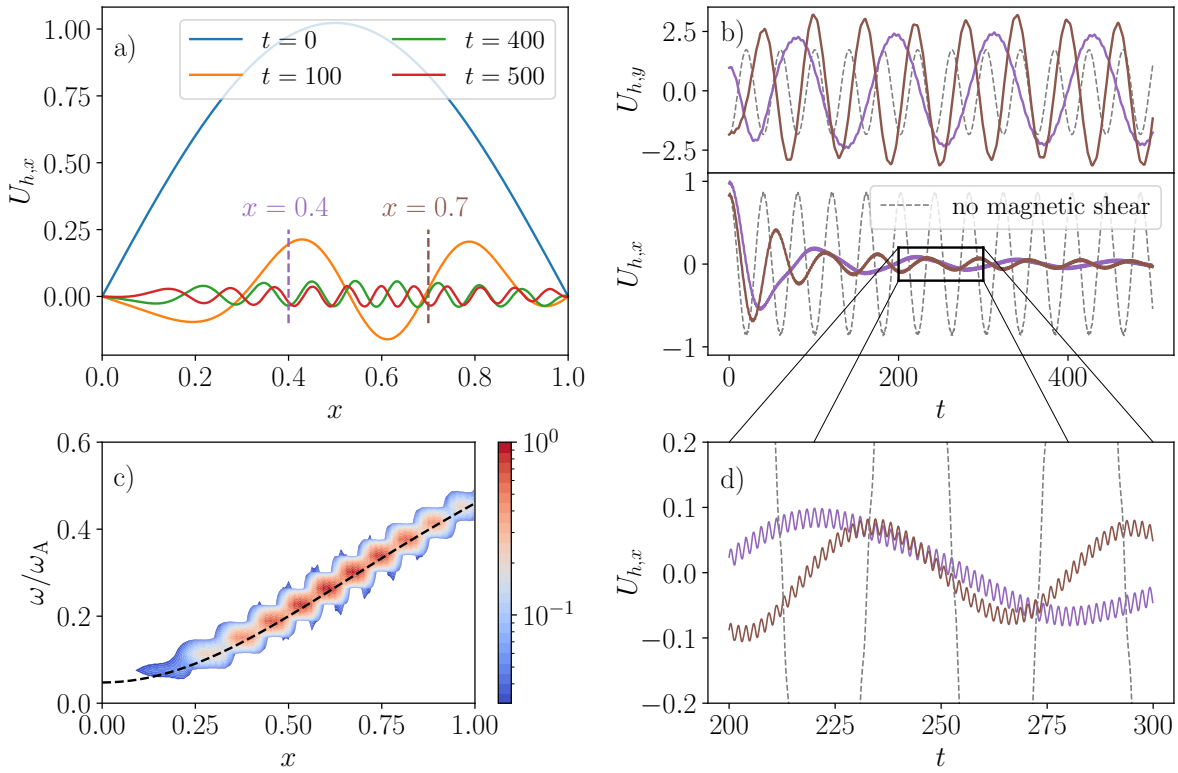

Figure 4.2: Phase mixing in sheared slab geometry with initial condition (4.4) and mode numbers $(m, n) = (1, -1)$: a) Radial velocity component $U_{h,x}$ at different times. b) Time traces of the radial ($U_{h,x}$) and poloidal ($U_{h,y}$) velocity components, respectively, at two radial positions $x = 0.4$ and $x = 0.7$ and comparison to the case without magnetic shear (dashed line). c) Spatially resolved Fourier spectrum of the undamped poloidal velocity component $U_{h,y}$ and comparison to the analytical expectation (dashed line). d) Zoom into time traces of $U_{h,x}$ reveals fast, small amplitude oscillations caused by fast magnetosonic modes.

with a radially extended $(m, n) = (1, -1)$ mode of the form

$$\mathbf{U}(t=0,\mathbf{x}): \quad \begin{cases} U_x(t=0,\mathbf{x}) = \sin\left(\frac{\pi x}{a}\right) \sin\left(\frac{my}{a} + \frac{nz}{a}\right), \\ U_y(t=0,\mathbf{x}) = \cos\left(\frac{\pi x}{a}\right) \cos\left(\frac{my}{a} + \frac{nz}{a}\right) \frac{\pi}{m}, \\ U_z(t=0,\mathbf{x}) = 0, \end{cases} \tag{4.4}$$

where the poloidal component is chosen in a way that $\nabla \cdot \mathbf{U}(t=0) = 0$ in order to suppress compressible modes. For the same safety factor profile that was used in Figure 4.1 ($q_0 = 1.05$ and $q_1 = 1.85$) and numerical parameters $N_{\text{el}} = (64, 12)$, $p = (2, 2)$ and $\Delta t = 0.1$, Figure 4.2 a) shows the radial component $U_{h,x}$ at different times. It can be seen that the initially extended radial mode structure decays towards smaller and smaller scales ($k_x \to \infty$) leading to an eventual break down of the ideal MHD model. The effective damping is visible in Figure 4.2 b) where time traces of $U_{h,x}$ (bottom) and $U_{h,y}$ (top) at two different radial locations $x = 0.4$ and $x = 0.7$ are shown. While the radial component goes roughly like $\sim 1/t$ and is therefore damped, the poloidal component remains undamped. Moreover, both components oscillate with their local Alfvén velocity which is better visible in Figure 4.2 c), where the spatially resolved Fourier

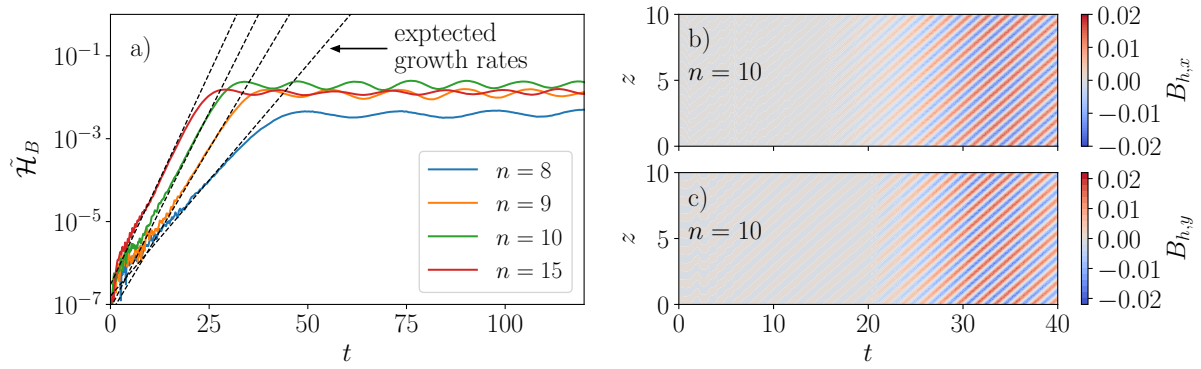

Figure 4.3: Cyclotron interaction of a shear Alfvén wave with full-orbit energetic ions: a) Time evolution of the wave magnetic field energy $\tilde{\mathcal{H}}_B$ (see (3.93) for its definition) for different toroidal mode numbers n and comparisons to the analytical growth rates obtained from the dispersion relation (2.57) (dashed lines). b), c) Corresponding evolution of the wave magnetic field components $B_{h,x}(t,z)$ and $B_{h,y}(t,z)$ for the toroidal mode number $n = 10$.

spectrum of the undamped component is shown and compared to the analytical expectation according to (4.2). To check that magnetic shear is indeed responsible for the damping, an additional run with a flat safety factor profile ($q_0 = q_1 = 1.85$) was performed. The resulting time traces of the radial and toroidal component are once more plotted in Figure 4.2 b) (grey dashed lines). Compared to the case with magnetic shear, both components now oscillate with the radially constant Alfvén frequency and are undamped. Finally, in Figure 4.2 d) a zoom into the time traces of the radial component reveals fast, small amplitude oscillations which is probably caused by fast magnetosonic modes which are excited. This means that although the initial condition was chosen in a way that $\nabla \cdot \mathbf{U}_h = 0$, the numerical scheme in STRUPHY leads to a finite velocity divergence as time evolves. However, since all substeps in the time integration scheme are solved implicitly, there is no Courant-Friedrichs-Lewy (CFL) constraint in STRUPHY. If this were the case, one would always have to choose a time step which properly resolves the fast magnetosonic waves.

4.2 Cyclotron wave-particle interaction

In this section, a beam of energetic deuterons ($A_\mathrm{h} = 2$ and $Z_\mathrm{h} = 1$) with an initially Maxwellian distribution function of the form

$$f_\mathrm{h}(\mathbf{x}, \mathbf{v}, t = 0) = \frac{1}{\pi^{3/2} v_\mathrm{th}^3} \exp\left[-\frac{v_x^2 + v_y^2 + (v_z - v_0)^2}{v_\mathrm{th}^2} \right], \tag{4.5}$$

with parameters $v_\mathrm{th} = 1$ and $v_0 = 2$ is injected into a bulk plasma composed of hydrogen ions ($A_\mathrm{b} = 1$). Moreover, magnetic field inhomogeneities are switched off ($q_0 = q_1 \to \infty$), i.e. the magnetic field $\mathbf{B}_\mathrm{eq} = B_0\, \mathbf{e}_z$, and periodic boundary conditions in s-direction are used. For this physical setup, the linear dispersion relation (2.57) was derived. Other physical parameters are the characteristic bulk number density $\bar{n}_\mathrm{b} = 8 \times 10^{18}\,\mathrm{m}^{-3}$ and the EP number density $\bar{n}_\mathrm{h} = 1.6 \times 10^{17}\,\mathrm{m}^{-3}$ resulting in the ratio $\nu_\mathrm{h} = \bar{n}_\mathrm{h}/\bar{n}_\mathrm{b} = 2\,\%$. Numerical mesh parameters are $N_\mathrm{el} = (2, 2)$ and $p = (1, 1)$ and for the time being a rather small time step $\Delta t = 0.02$ and a very large number of particles $N_\mathrm{p} = 8 \times 10^6$ is used in order to make sure that numerical convergence is reached (convergence tests will be presented at the end of the section). Moreover, no field

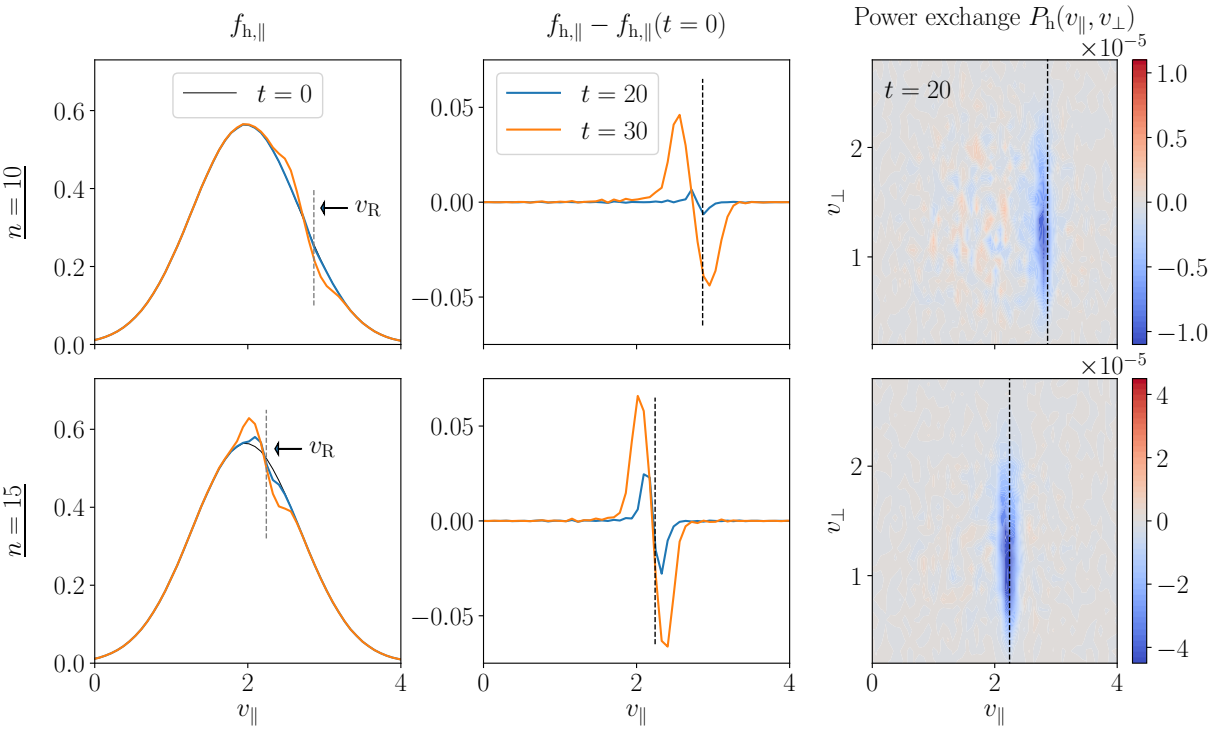

Figure 4.4: Cyclotron interaction of a shear Alfvén wave with full-orbit energetic ions: EP distribution function in parallel velocity space (4.6) at different times (first column), the corresponding differences to the initial distribution function (second column) and the wave-particle power exchange (4.7) resolved in $v_\parallel$-$v_\perp$-space (third column). All for the two mode numbers $n = 10$ (upper row) and $n = 15$ (lower row). For the present setup, the parallel velocity $v_\parallel = v_z$ and the perpendicular velocity $v_\perp^2 = v_x^2 + v_y^2$.

perturbations are initialized. This means that the only deviation from the equilibrium state is the small amplitude noise induced by energetic particles which are loaded uniformly in real space and according to (4.5) in velocity space (parameters $\zeta_s(s) = 1$, $v_{\text{th}}(s) = v_{\text{th}}$, $v_{0x} = v_{0y} = 0$ and $v_{0z} = v_0$ in the probability density function (3.132)).

Figure 4.3 a) shows the simulated evolution of the wave magnetic field energy $\tilde{\mathcal{H}}_B$ for four different toroidal mode numbers and the corresponding analytical growth rates from the dispersion relation (2.57) (dashed lines). It is evident that the instability develops out of a short and noisy initial phase and that the numerical growth rates agree well with the analytical ones. Only the case of the smallest mode number $n = 8$ (blue curve) slightly underestimates the growth rate. This might be due to the fact that the resonant velocity $v_R \approx 3.3$ is located quite at the tail of the Maxwellian, which means that there are very few particles resulting in a poor numerical resolution. Figure 4.3 b) and c) show the evolution of the wave magnetic field components $B_{h,x}$ and $B_{h,y}$ in the t-z-plane for the generic mode number $n = 10$. Since there is clearly a phase shift of 90° between the two components, a circularly polarized wave with frequency $\omega = B_0 n / R_0 \approx 1.88$ is forming out of the noisy initial phase. Moreover, one can easily check that the direction of rotation is such that it is a right-handed circularly wave (R-wave). This is in agreement with the analytical theory developed in Section 2.4 because it predicts higher growth rates for R-waves than for L-waves.

To get further insights in the wave-particle interaction mechanism, snapshots of the parallel

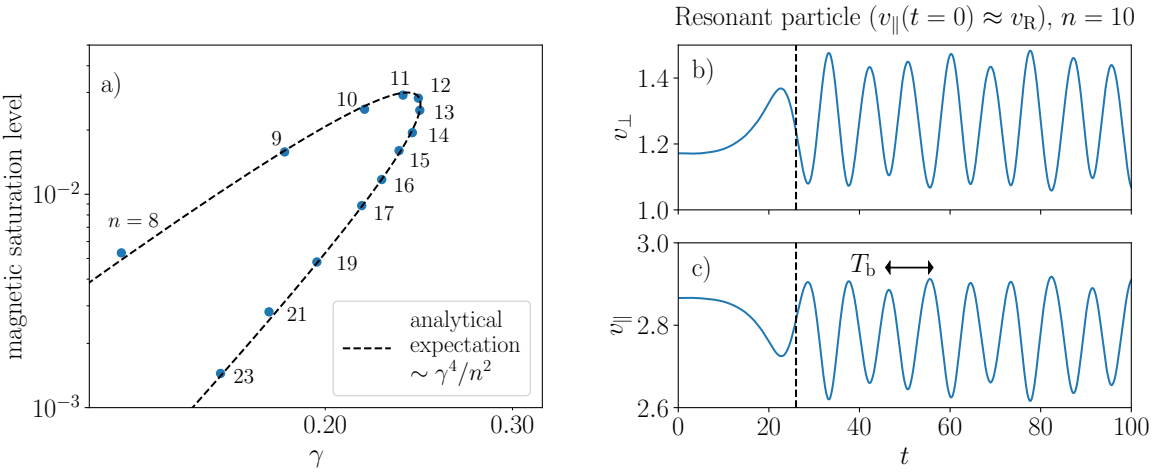

Figure 4.5: Cyclotron interaction of a shear Alfvén wave with full-orbit energetic ions: a) Saturation levels of the wave magnetic field energy with respect to the linear growth rate γ and comparison to the analytically expected dependence (dashed lines) b) Time evolution of the perpendicular velocity of a resonant particle in the linear and non-linear phase (separated by dashed lines). c) Same for parallel velocity; also the expected bounce period $T_\mathrm{b} = 2\pi/\omega_\mathrm{b}$ resulting from magnetic trapping is depicted.

EP distribution function

$$f_{\mathrm{h},\parallel}(v_z) := \int_0^1 \int_0^1 \int_0^1 \int_{-\infty}^{\infty} \int_{-\infty}^{\infty} f_\mathrm{h}\, \mathrm{d}v_x\, \mathrm{d}v_y\, \mathrm{d}s\, \mathrm{d}\chi\, \mathrm{d}\varphi\,, \tag{4.6}$$

are depicted in Figure 4.4 for mode numbers $n = 10$ (upper row) and $n = 15$ (lower row) at two different times in the linear phase. One observes a strong distortion of the distribution functions at the vicinity of the respective resonant velocities $v_\mathrm{R} = B_0\,(1 + \kappa Z_\mathrm{h}/A_\mathrm{h} k) \approx 2.86$ ($n = 10$) and $v_\mathrm{R} \approx 2.24$ ($n = 15$) (see expression (2.59) for the resonant velocity). More resonant particles are decelerated than accelerated in parallel direction, which is clearly visible in the middle column of Figure 4.4. To check that this leads to a net energy transfer from EPs to the wave, the right column shows the measured wave-particle power exchange[1]

$$P_\mathrm{h}(v_\parallel, v_\perp) := \nu_\mathrm{h} \frac{Z_\mathrm{h}}{A_\mathrm{b}}\, \kappa \int_0^1 \int_0^1 \int_0^1 (\mathbf{v} \cdot \mathbf{E})\, f_\mathrm{h}\, 2\pi\, v_\perp\, \mathrm{d}s\, \mathrm{d}\chi\, \mathrm{d}\varphi\,, \tag{4.7}$$

in $v_\parallel$-$v_\perp$-space. The additional resolution in the perpendicular velocity reveals that the net loss in energy in parallel direction is larger than possible net gains in perpendicular direction. Therefore, the overall energy exchange is such that energy is transferred from resonant particles to the wave.

Finally, the subsequent non-linear saturation phase is investigated. Previous works on electron Whistler instabilities [98, 99, 100] suggest that resonant particles in cyclotron interaction processes get trapped in the wave magnetic field for sufficiently large amplitudes and that this is the responsible mechanism for the saturation of instabilities. This magnetic trapping caused by $\mathbf{v} \times \mathbf{B}$ forces leads to a bouncing of resonant particles within the wave fields with the bounce frequency

$$\omega_\mathrm{b} = \sqrt{k v_\perp \frac{Z_\mathrm{h}\, \kappa |\mathbf{B}|_\mathrm{sat}}{A_\mathrm{h}}}\,, \tag{4.8}$$

[1] This expression follows from the change of the EP energy (2.33) after appropriate normalization.

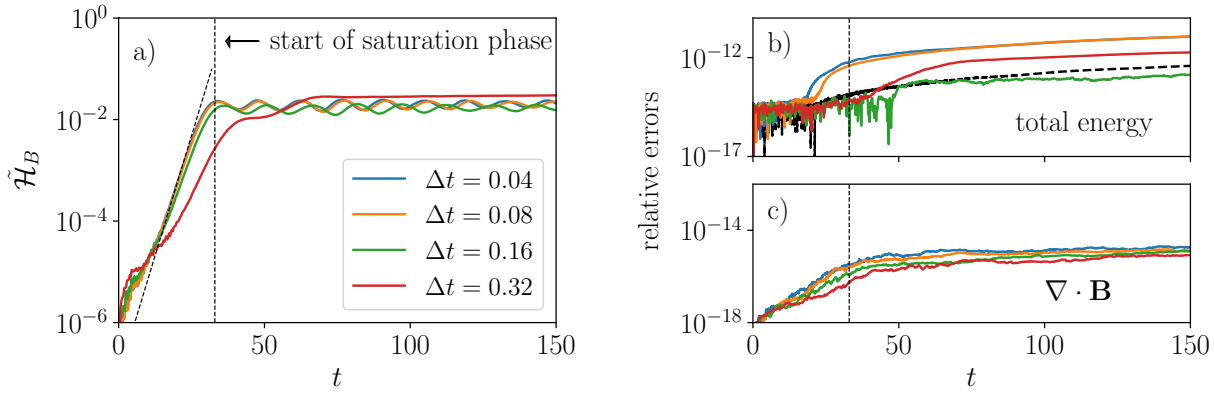

Figure 4.6: Cyclotron interaction of a shear Alfvén wave with full-orbit energetic ions: a) Time evolution of the wave magnetic field energy $\tilde{\mathcal{H}}_B$ for different numerical time steps Δt. b) Corresponding evolution of the relative error in the conservation of the total energy $\tilde{\mathcal{H}}_h$ (3.93). The black dashed line is the case $\Delta t = 0.04$ and a stop tolerance of 1×10^{-14} in the iterative linear solvers. In all other runs, the stop tolerance is 1×10^{-12}. c) Corresponding evolution of the divergence of the magnetic field.

where $|\mathbf{B}|_{\text{sat}}$ is the saturated wave magnetic field amplitude and $k = n/R_0$ the wave number. Moreover, it is expected that the bounce frequency is proportional to the linear growth rate γ such that a relation between the saturation level of the wave magnetic field energy and the linear growth rate can be derived:

$$\omega_{\text{b}} = \sqrt{k v_\perp \frac{Z_{\text{h}} \kappa |\mathbf{B}|_{\text{sat}}}{A_{\text{h}}}} \sim \gamma \quad \Rightarrow \quad |\mathbf{B}|^2_{\text{sat}} \sim \gamma^4 / n^2 \,. \tag{4.9}$$

Figure 4.5 a) shows the measured saturation levels of STRUPHY runs for a wide range of mode numbers $n = 8 - 23$ and the comparison to the analytical expectation (4.9). It is evident that there is an excellent agreement for all mode numbers. To further verify that magnetic trapping is the responsible saturation mechanism, Figure 4.5 b) and c) show time traces of the perpendicular and parallel velocity, respectively, of a particle whose initial parallel velocity is close to the resonance velocity. One can see that the parallel velocity decreases and the perpendicular one increases in the linear phase up to $t \approx 25$. This is followed by oscillations in the non-linear phase where the two velocities are phase shifted by 180°. Plugging in the values $k = n/R_0 = 10/3$, $\kappa \approx 12.42$ (recall that $\kappa = \bar{\Omega}_{\text{cp}} \tau_{\text{A}}$, see Section 2.2), $Z_{\text{h}} = 1$, $A_{\text{h}} = 2$, $|\mathbf{B}|_{\text{sat}} \approx 0.02$ (see Figure 4.3) and the perpendicular velocity $v_\perp \approx 1.3$ at the beginning of the non-linear phase yields $\omega_{\text{b}} \approx 0.73$ with results in a bounce period of $T_{\text{b}} \approx 8.56$. This is in perfect agreement with the measured bounce period in the simulations depicted in Figure 4.5 c).

Finally, numerical properties of STRUPHY runs with a focus on conservation properties are investigated. In all simulations shown so far, a very small time step of $\Delta t = 0.02$ has been used. For the chosen set of physical parameters, the EP cyclotron frequency is $\Omega_{\text{ch}} = Z_{\text{h}} \kappa \, B_0 / A_{\text{h}} \approx 6.21$ resulting in a cyclotron period of about $2\pi/\Omega_{\text{ch}} \approx 1.01$. Hence, the time step $\Delta t = 0.02$ results in about 50 steps per cyclotron period which is a very high temporal resolution. Figure 4.6 a) shows the evolution of the wave magnetic field energy for the case $n = 10$, four different time steps up to $\Delta t = 0.32$ (3 steps per cyclotron period) and mesh parameters $N_{\text{el}} = (16, 2)$ and $p = (3, 1)$. The increased spatial resolution is used to demonstrate that STRUPHY's good conservation properties are independent of numerical parameters. Regarding the evolution of the wave magnetic field energy, it can be seen that there is almost no difference for the time

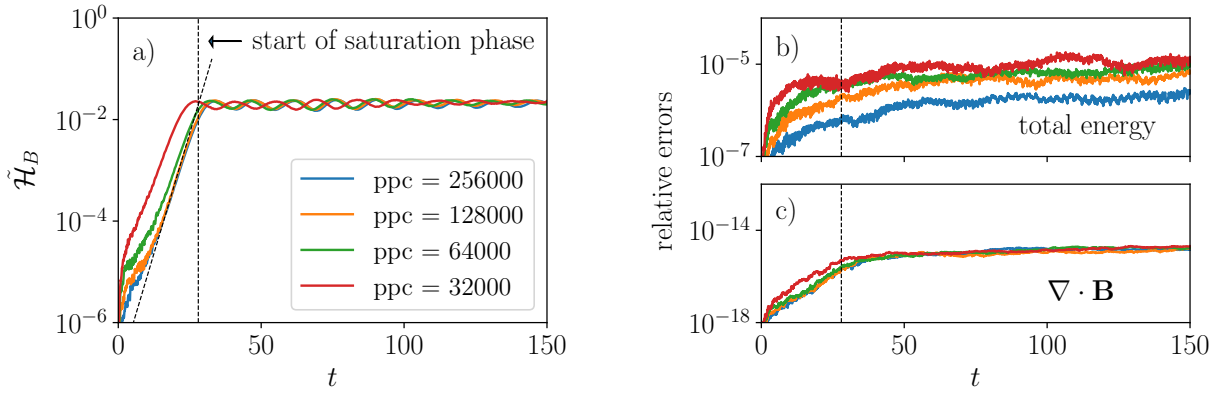

Figure 4.7: Cyclotron interaction of a shear Alfvén wave with full-orbit energetic ions with finite plasma pressure: a) Time evolution of the wave magnetic field energy $\tilde{\mathcal{H}}_B$ for different numbers of particles per cell (ppc). b) Corresponding evolution of the relative error in the conservation of the total energy $\tilde{\mathcal{H}}_h$ (3.93). c) Corresponding evolution of the divergence of the magnetic field.

steps $\Delta t = 0.04$ and $\Delta t = 0.08$ compared to the high resolution case $\Delta t = 0.02$. The time step $\Delta t = 0.16$ still gives a reasonable result but a slight reduction of the growth rate is already visible and lastly, $\Delta t = 0.32$ clearly underestimates the growth rate although the qualitative trend (growth phase in linear phase and non-linear saturation phase) is still captured correctly. However, the small frequency oscillations in the saturation phase caused by trapped particles are completely gone. The right column in Figure 4.6 shows the measured evolution of the relative errors in the conservation of the total energy $\tilde{\mathcal{H}}_h = \tilde{\mathcal{H}}_U + \tilde{\mathcal{H}}_B + \tilde{\mathcal{H}}_p + \tilde{\mathcal{H}}_\mathrm{h}$ (see (3.93) for its definition) and the divergence of the numerical magnetic field. The errors of the latter are close to machine precision ($\approx 1 \times 10^{-16}$ in case of double precision) throughout the entire simulation which is a direct consequence of the conforming finite element spaces used in STRUPHY (discrete de Rham complex with $\mathbb{C}\,\mathbb{D} = 0$). Regarding the energy error, there is a very small (maximum 1×10^{-11}) but finite error which is due to the fact that iterative solvers are used in the solution of all linear systems in the implicit time integration scheme. This means that the linear systems are not solved exactly but up to some given stop tolerance. For all runs in Figure 4.6, this relative stop tolerance is 1×10^{-12}. To show that the finite error is caused by the iterative solvers, an additional run with a smaller stop tolerance 1×10^{-14} is shown in Figure 4.6 b) for the $\Delta t = 0.04$ case (dashed line). Indeed, this results in an error that is reduced by about two orders of magnitude (blue curve vs. black dashed curve).

In all runs presented so far, the bulk plasma had zero pressure because of the absence of magnetic shear ($q_0 = q_1$) and since we set the parameter $\beta = 0$ (plasma beta at $x = 0$). Therefore, as last runs, a finite plasma pressure is included by setting $\beta = 10\,\%$ in the pressure profile in (4.1) and additionally a scan with respect to the number of particles is performed. The latter has been $N_\mathrm{p} = 8 \times 10^6$ until now. Other numerical parameters are $N_\mathrm{el} = (16, 2)$, $p = (3, 1)$ and $\Delta t = 0.04$. With this particular choice of number of elements, the number of particles per element (or cell) ppc ≈ 256000. The results for decreasing number of particles are shown in Figure 4.7. It can be seen that the instability can in principle be simulated with much less particles but the initial noise levels becomes larger as the number of particles is decreased. This reduces the time period of the exponential growth phase but the saturation dynamics remains unchanged. In the right column of Figure 4.7 one observes that the total energy $\tilde{\mathcal{H}}_h$ is not conserved as well as for the case without pressure, but the error is still bounded below 1×10^{-5}. The breakdown of the energy conservation property can be understood as follows: Although

we are simulating a shear Alfvén instability which is non-perturbative in pressure, the particle noise induces small amplitude pressure perturbations such that $\mathrm{d}\tilde{\mathcal{H}}/\mathrm{d}t \neq 0$ in the continuous, undiscretized model (see (2.39)). This is a consequence of the linearized MHD model currently used in STRUPHY.

Chapter 5

Treatment of the magnetic axis

5.1 Mappings with polar singularity

Up to this point we have assumed the mapping $F : (s, \chi, \varphi) \mapsto (x, y, z) = F(s, \chi, \varphi)$ introduced in Section 3.1 to be such that a) the corresponding metric tensor is independent of φ (axial symmetry) and b) it is invertible eyerywhere. In what follows, we shall relax the second assumption by allowing for a polar singularity at $s = 0$, i.e. for fixed $\varphi = \varphi_0$ the function $F(0, \chi, \varphi_0)$ is independent of χ such that the Jacobian determinant $\sqrt{g}\,(s = 0, \chi) = 0$ but $\sqrt{g}\,(s > 0, \chi) > 0$. This is in particular the case for the cylindrical and toroidal mapping (3.123) and (3.124), respectively. In both cases the "poloidal" mapping F_{pol} is such that

$$F_{\text{pol}} : (s, \chi) \mapsto (R, Y)\,, \qquad DF_{\text{pol}}\big|_{s=0} = \left[\begin{array}{cc} \dfrac{\partial R}{\partial s} & \dfrac{\partial R}{\partial \chi} \\ \dfrac{\partial Y}{\partial s} & \dfrac{\partial Y}{\partial \chi} \end{array}\right]\Bigg|_{s=0} = \left[\begin{array}{cc} \left.\dfrac{\partial R}{\partial s}\right|_{s=0} & 0 \\ \left.\dfrac{\partial Y}{\partial s}\right|_{s=0} & 0 \end{array}\right], \tag{5.1}$$

i.e. the second column of the Jacobian matrix is equal to zero at the pole $s = 0$. Of course, this property not only holds for the two generic mappings (3.123) and (3.124), but for every mapping with polar-like flux aligned coordinates. With regards to differential forms that are obtained by the pull-back operations in Table 3.1 under polar mappings with this property, one can easily deduce the following properties for differential forms at the pole:

$$\text{polar 0-forms :} \qquad f^0_k(s = 0, \chi) = const.\,, \tag{5.2a}$$

$$\text{polar 1-forms :} \qquad E^1_{2,k}(s = 0, \chi) = 0 \qquad \forall\, \chi\,, \quad E^1_{3,k}(s = 0, \chi) = const.\,, \tag{5.2b}$$

$$\text{polar 2-forms :} \qquad B^2_{1,k}(s = 0, \chi) = 0 \qquad \forall\, \chi\,, \quad B^2_{3,k}(s = 0, \chi) = 0 \qquad \forall\, \chi\,, \tag{5.2c}$$

$$\text{polar 3-forms :} \qquad p^3_k(s = 0, \chi) = 0 \qquad \forall\, \chi\,. \tag{5.2d}$$

Elements of the standard tensor product B-spline spaces (3.42) resp. (3.54) do **not** make sure that these constraints are satisfied. The *polar spline framework for discrete differential forms* laid out in [82], however, is designed in way that the constraints (5.2) are satisfied on the discrete level while keeping at the same time the discrete cochain complex property (3.52). Moreover, the push-forward of a polar spline is then sufficiently regular across the pole ($\mathcal{C}^1$ for 0-forms in this work for instance but arbitrary $\mathcal{C}^k$-regularity for $k > 1$ would in principle be possible, too).

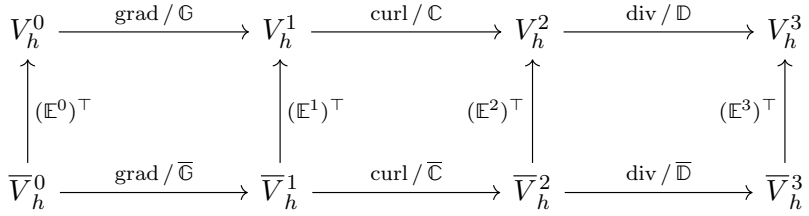

Figure 5.1: Commuting diagram for Sobolev spaces of discrete differential forms on polar domains. Upper row: standard tensor product spaces, bottom row: polar subspaces with built-in constraints (5.2). Both rows form discrete de Rham complexes and are connected via the transposed polar extraction operators $(\mathbb{E}^k)^\top$ $(0 \leq k \leq 3)$.

5.2 Discrete differential forms on polar domains

The basic structure of the polar spline framework for discrete differential forms is shown in Figure 5.1. The upper row is the de Rham complex consisting of the standard tensor product spaces V_h^k while the bottom row is a complex consisting of new *polar* subspaces $\overline{V}_h^k$. The appeal of the polar spline framework is the fact that the bases of these polar spaces are given by linear combinations of the tensor product bases making the polar spaces subspaces of the tensor product spaces. The linear combination is done via so-called *polar extraction operators* $\mathbb{E}^k$ such that the polar spaces

$$\overline{V}_h^k := \operatorname{span}\left(\overline{\boldsymbol{\Lambda}}^k := \mathbb{E}^k \boldsymbol{\Lambda}^k\right) \quad k = 0, 3\,, \qquad \overline{V}_h^k := \operatorname{span}\left(\vec{\overline{\boldsymbol{\Lambda}}}^k := \mathbb{E}^k \vec{\boldsymbol{\Lambda}}^k\right) \quad k = 1, 2\,, \tag{5.3}$$

have smaller dimensions $\overline{n}^k := \dim \overline{V}_h^k$ than the tensor product spaces $n^k = \dim V_h^k$. However, since the polar spaces are subspaces of the tensor product spaces, it is always possible to express a polar spline function in the tensor product basis because

$$V_h^0 \ni f_h^0 = \overline{\mathbf{f}}^\top \overline{\boldsymbol{\Lambda}}^0 = \overline{\mathbf{f}}^\top \mathbb{E}^0 \boldsymbol{\Lambda}^0 = \left[\,(\mathbb{E}^0)^\top \overline{\mathbf{f}}\,\right]^\top \boldsymbol{\Lambda}^0 = \mathbf{f}^\top \boldsymbol{\Lambda}^0\,. \tag{5.4}$$

Consequently, for given polar FE coefficients $\overline{\mathbf{f}}$, the corresponding tensor product FE coefficients are obtained via $\mathbf{f} = (\mathbb{E}^0)^\top \overline{\mathbf{f}}$. It should be noted that the inverse operation, i.e. going from $\mathbf{f}$ to $\overline{\mathbf{f}}$, is not unique and can be achieved through any kind of projection $V_h^0 \to \overline{V}_h^0$; such a projection has for instance been identified in [101]. The polar space $\overline{V}_h^0$ is a subspace of V_h^0 comprised of those elements with FE coefficients of the form $\mathbf{f} = (\mathbb{E}^0)^\top \overline{\mathbf{f}}$ for any $\overline{\mathbf{f}} \in \mathbb{R}^{\overline{n}^0}$. Finally, the framework results in modified polar derivative matrices $\overline{\mathbb{G}}$, $\overline{\mathbb{C}}$ and $\overline{\mathbb{D}}$ satisfying

$$\mathbb{G}\,(\mathbb{E}^0)^\top = (\mathbb{E}^1)^\top\,\overline{\mathbb{G}}\,, \qquad \mathbb{C}\,(\mathbb{E}^1)^\top = (\mathbb{E}^2)^\top\,\overline{\mathbb{C}}\,, \qquad \mathbb{D}\,(\mathbb{E}^2)^\top = (\mathbb{E}^3)^\top\,\overline{\mathbb{D}}\,, \tag{5.5}$$

which means that the diagram in Figure 5.1 is once more a commuting diagram [102].

Moreover, the polar spline framework is based on the usage of an IGA mapping of the form (3.125) meaning that the mapping F_{pol} (5.1) must be represented in the *same* B-spline basis that is used to construct the elements in the finite element space V_h^0.

5.2.1 Discrete polar 0-forms

The details of constructing the $\mathcal{C}^1$-continuous polar basis for the V_h^0-space from spline mappings such as (3.125) are given in [80] and will not be repeated here. We start directly from the result and review the derivation of basis functions for the other spaces in the discrete de Rham

sequence. These spaces will be $\mathcal{C}^0$ at the pole $s = 0$ because a) first derivatives are, and b) mixed first derivatives will turn out to be zero. According to [80], the Fourier component $f^0_{h,k}$ of a $\mathcal{C}^1$-continuous polar differential 0-form is given by

$$f^0_{h,k}(s,\chi) = \sum_{\ell=0}^{2} f_{(\ell k)} \underbrace{\sum_{i=0}^{1}\sum_{j=0}^{n_\chi-1} \xi^\ell_{ij}\, N^{p_s}_i(s) N^{p_\chi}_j(\chi)}_{=:\,\overline{\Lambda}^0_\ell(s,\chi)} + \sum_{i>1,j} f_{(\overline{ijk})} N^{p_s}_i(s) N^{p_\chi}_j(\chi)\,, \tag{5.6}$$

where the meaning of the polar flattened-index notation $(\overline{ijk})$ is given in (5.11). The three new polar basis functions $(\,\overline{\Lambda}^0_0, \overline{\Lambda}^0_1, \overline{\Lambda}^0_2\,)$ with indices $\ell = 0, 1, 2$ are obtained by linear combination of $i = 0$ and $i = 1$ tensor product basis functions. The dimension of the first polar subspace is thus $\overline{n}^0 = 2\,[\,(n_s - 2)\,n_\chi + 3\,]$ (the first 2 accounts for the two toroidal Fourier components $k = 0$ and $k = 1$). Using the abbreviations $\Delta R_{1j} := c^R_{(1j)} - R_0$ and $\Delta Y_{1j} := c^Y_{(1j)} - Y_0$, the polar extraction coefficients are given by

$$\ell = 0: \qquad \xi^0_{0j} := \frac{1}{3}\,, \qquad \xi^0_{1j} := \frac{1}{3} + \frac{2}{3\tau}\Delta R_{1j}, \tag{5.7a}$$

$$\ell = 1: \qquad \xi^1_{0j} := \frac{1}{3}\,, \qquad \xi^1_{1j} := \frac{1}{3} - \frac{1}{3\tau}\Delta R_{1j} + \frac{\sqrt{3}}{3\tau}\Delta Y_{1j}, \tag{5.7b}$$

$$\ell = 2: \qquad \xi^2_{0j} := \frac{1}{3}\,, \qquad \xi^2_{1j} := \frac{1}{3} - \frac{1}{3\tau}\Delta R_{1j} - \frac{\sqrt{3}}{3\tau}\Delta Y_{1j}\,. \tag{5.7c}$$

They are the barycentric coordinates of the control points $c^R_{(ij)}$) and $c^Y_{(ij)}$ with indices $i = 0$ and $i = 1$ with respect to an equilateral triangle with vertices

$$v_1 := (\tau + R_0, 0), \quad v_2 := \left(R_0 - \frac{\tau}{2}, Y_0 + \frac{\sqrt{3}}{2}\tau\right), \quad v_3 := \left(R_0 - \frac{\tau}{2}, Y_0 - \frac{\sqrt{3}}{2}\tau\right). \tag{5.8}$$

The parameter τ is chosen such that the triangle encloses the pole (R_0, Z_0) and the first ring of control points $(c^R_{(1j)}, c^Y_{(1j)})$. This leads to the definition

$$\tau := \max\left[\max_j\left(-2\Delta R_{1j}\right), \max_j\left(\Delta R_{1j} - \sqrt{3}\,\Delta Y_{1j}\right), \max_j\left(\Delta R_{1j} + \sqrt{3}\,\Delta Y_{1j}\right)\right]. \tag{5.9}$$

The three new basis functions are plotted in Figure 5.2 for cubic B-splines both on the logical (upper row) and physical (lower row) domain using the mapping (3.123) (cylinder). Unlike pure tensor product basis functions, each of the new polar basis functions has a support that overlaps the pole. Moreover, using the property (3.22) of clamped B-splines, it is easily verified that (5.6) satisfies

$$f^0_{h,k}(s = 0, \chi) = \frac{1}{3}\,(f_{(0k)} + f_{(1k)} + f_{(2k)}). \tag{5.10}$$

Discrete polar 0-forms are therefore by construction single-valued at the pole such that the first requirement (5.2a) is met. Similar to the tensor product basis functions (3.38) we introduce the stacking notation

$$\begin{gathered}\overline{\mathbf{\Lambda}}^0 := \left(\overline{\Lambda}^0_{(\ell k)},\, \overline{\Lambda}^0_{(\overline{ijk})}\right) \in \mathbb{R}^{\overline{n}^0}\,, \qquad \overline{\Lambda}^0_{(\ell k)} := \overline{\Lambda}^0_\ell\, \mathcal{F}^n_k\,, \\ \text{with} \quad (\overline{ijk}) = 2\,[\,n_\chi\,(i-2) + j + 3\,] + k\,, \qquad 1 < i < n_s\,.\end{gathered} \tag{5.11}$$

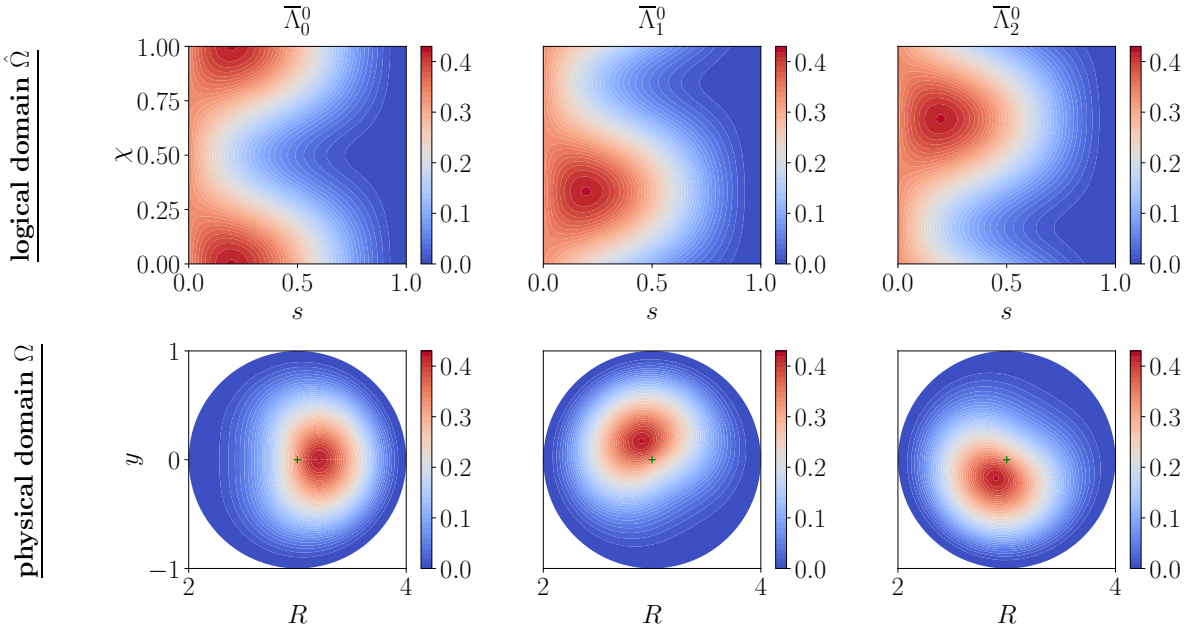

Figure 5.2: The three new basis functions $\overline{\Lambda}^0_0$, $\overline{\Lambda}^0_1$ and $\overline{\Lambda}^0_2$ for the example $p_s = p_\chi = 3$, $n_s = 4$ and $n_\chi = 12$ on the logical domain (upper row) and physical domain (lower row) using the mapping (3.123) with parameters $a = 1$ and $R_0 = 3$. Any linear combination of these three basis functions is single-valued at the pole and continuously differentiable across the pole. The pole $(R_0, 0)$ is marked with a cross.

Hence, the new set of basis functions $\overline{\boldsymbol{\Lambda}}^0$ contains as its first six entries the new polar basis functions $(\overline{\Lambda}^0_{(\ell k)})$ followed by standard tensor product basis functions $(\,\overline{\Lambda}^0_{(\overline{ijk})} = N^{p_s}_i N^{p_\chi}_j \mathcal{F}^n_k\,)$ with index $i > 1$. Based on this new set of basis functions, similar to (3.43), a discrete polar 0-form $f_h \in \overline{V}^0_h$ can compactly be written as

$$f^0_h = \overline{\mathcal{S}}_0[\,\overline{\mathbf{f}}\,] = \overline{\mathbf{f}}^\top \overline{\boldsymbol{\Lambda}}^0\,, \qquad \overline{\mathbf{f}} := \left(f_{(\ell k)}, f_{(\overline{ijk})}\right) \in \mathbb{R}^{\overline{n}^0}\,. \tag{5.12}$$

Finally, the first polar extraction operator $\mathbb{E}^0 \in \mathbb{R}^{\overline{n}^0 \times n^0}$ is given by

$$\mathbb{E}^0 := \begin{bmatrix} \mathbb{X}^0 & 0 \\ 0 & \mathbb{1}_{(n_s-2)n_\chi} \end{bmatrix} \otimes \mathbb{1}_2\,, \qquad \mathbb{X}^0 \in \mathbb{R}^{3\times 2n_\chi}\,, \quad \mathbb{X}^0_{\ell j} := \begin{cases} \xi^\ell_{0j} & 0 \le j < n_\chi\,, \\ \xi^\ell_{1(j-n_\chi)} & n_\chi \le j < 2n_\chi\,, \end{cases} \tag{5.13}$$

where the matrix $\mathbb{X}^0$ performs the linear combination of the first $2n_\chi$ tensor product basis functions in $\boldsymbol{\Lambda}^0$ corresponding to one of the two toroidal Fourier components to yield the three new polar splines $(\,\overline{\Lambda}^0_0, \overline{\Lambda}^0_1, \overline{\Lambda}^0_2\,)$.

5.2.2 Discrete polar gradient operator and 1-forms

When applying the gradient to a polar 0-form, the result must be a polar 1-form whose coefficients are obtained via the application of the *polar gradient matrix* $\overline{\mathbb{G}}$, formally

$$\hat{\nabla} f^0_h = (\,\overline{\mathbb{G}}\,\overline{\mathbf{f}}\,)^\top \vec{\overline{\boldsymbol{\Lambda}}}^1\,. \tag{5.14}$$

The goal of this section is to identify on the one hand the suitable basis $\vec{\overline{\boldsymbol{\Lambda}}}^1$ and on the other hand the form of the polar gradient matrix $\overline{\mathbb{G}}$.

Let us start by computing the partial derivatives of (5.6). Using the recursion formulae (3.23) and (3.24) in both directions s and χ we obtain

$$\frac{\partial f^0_{h,k}}{\partial s} = \sum_{\ell=0}^{2} f_{(\ell k)} \sum_{i=0}^{1} \sum_{j=0}^{n_\chi - 1} \xi^\ell_{ij} (D^{p_s}_{i-1} - D^{p_s}_i) N^{p_\chi}_j + \sum_{i>1,j} f_{(\overline{ijk})} (D^{p_s}_{i-1} - D^{p_s}_i) N^{p_\chi}_j \,, \tag{5.15}$$

$$\frac{\partial f^0_{h,k}}{\partial \chi} = \sum_{\ell=0}^{2} f_{(\ell k)} \sum_{i=0}^{1} \sum_{j=0}^{n_\chi - 1} \xi^\ell_{ij} N^{p_s}_i (D^{p_\chi}_{j-1} - D^{p_\chi}_j) + \sum_{i>1,j} f_{(\overline{ijk})} N^{p_s}_i (D^{p_\chi}_{j-1} - D^{p_\chi}_j) \,. \tag{5.16}$$

We can sort this in terms of tensor product basis functions that span the space V^1_h:

$$\begin{aligned} \frac{\partial f^0_{h,k}}{\partial s} = &\sum_{\ell=0}^{2} f_{(\ell k)} \sum_{j=0}^{n_\chi - 1} (\xi^\ell_{1j} - \xi^\ell_{0j}) D^{p_s}_0 N^{p_\chi}_j + \sum_{j=0}^{n_\chi - 1} \left(f_{(\overline{2jk})} - \sum_{\ell=0}^{2} f_{(\ell k)} \xi^\ell_{1j} \right) D^{p_s}_1 N^{p_\chi}_j \\ &+ \sum_{i>1,j} (f_{(\overline{i+1jk})} - f_{(\overline{ijk})}) D^{p_s}_i N^{p_\chi}_j \,, \end{aligned} \tag{5.17}$$

$$\frac{\partial f^0_{h,k}}{\partial \chi} = \sum_{\ell=0}^{2} f_{(\ell k)} \sum_{i=0}^{1} \sum_{j=0}^{d_\chi - 1} (\xi^\ell_{ij+1} - \xi^\ell_{ij}) N^{p_s}_i D^{p_\chi}_j + \sum_{i>1,j} (f_{(\overline{ij+1k})} - f_{(\overline{ijk})}) N^{p_s}_i D^{p_\chi}_j \,. \tag{5.18}$$

Before further simplifying these expressions, we note some important properties of the extraction coefficients (5.7):

$$1. \quad \xi^\ell_{0j+1} - \xi^\ell_{0j} = 0 \qquad \forall\, j,\, \ell \,, \tag{5.19}$$

$$2. \quad \sum_{\ell=0}^{2} f_{(\ell k)} \, (\xi^\ell_{1j} - \xi^\ell_{0j}) = \sum_{\ell=1}^{2} (f_{(\ell k)} - f_{(0k)}) \, (\xi^\ell_{1j} - \xi^\ell_{0j}) \qquad \forall\, j,\, k \,, \tag{5.20}$$

$$3. \quad \sum_{\ell=0}^{2} f_{(\ell k)} \, (\xi^\ell_{1j+1} - \xi^\ell_{1j}) = \sum_{\ell=1}^{2} (f_{(\ell k)} - f_{(0k)}) \, (\xi^\ell_{1j+1} - \xi^\ell_{1j}) \qquad \forall\, j,\, k \,, \tag{5.21}$$

$$4. \quad \sum_{\ell=0}^{2} \xi^\ell_{1j} = 1 \qquad \forall\, j \,. \tag{5.22}$$

By substituting the first three relations (5.19)-(5.21) into the derivatives (5.17) and (5.18), the first two components of the gradient of f_h can be written as

$$\begin{aligned} \begin{bmatrix} \partial_s f^0_{h,k} \\ \partial_\chi f^0_{h,k} \end{bmatrix} = &\sum_{\ell=1}^{2} (f_{(\ell k)} - f_{(0k)}) \sum_{j=0}^{n_\chi - 1} \begin{bmatrix} (\xi^\ell_{1j} - \xi^\ell_{0j}) D^{p_s}_0 N^{p_\chi}_j \\ (\xi^\ell_{1j+1} - \xi^\ell_{1j}) N^{p_s}_1 D^{p_\chi}_j \end{bmatrix} \\ &+ \sum_{j=0}^{n_\chi - 1} \left(f_{(\overline{2jk})} - \sum_{\ell=0}^{2} f_{(\ell k)} \xi^\ell_{1j} \right) \begin{bmatrix} D^{p_s}_1 N^{p_\chi}_j \\ 0 \end{bmatrix} + \sum_{i>1,j} (f_{(\overline{i+1jk})} - f_{(\overline{ijk})}) \begin{bmatrix} D^{p_s}_i N^{p_\chi}_j \\ 0 \end{bmatrix} \\ &+ \sum_{i>1,j} (f_{(\overline{ij+1k})} - f_{(\overline{ijk})}) \begin{bmatrix} 0 \\ N^{p_s}_i D^{p_\chi}_j \end{bmatrix} . \end{aligned} \tag{5.23}$$

Here, one should keep in mind that $d_\chi = n_\chi$. This representation of the gradient is intuitive because each term is multiplied by a difference of FE coefficients $\bar{\mathbf{f}}$. Due to the property (5.22)

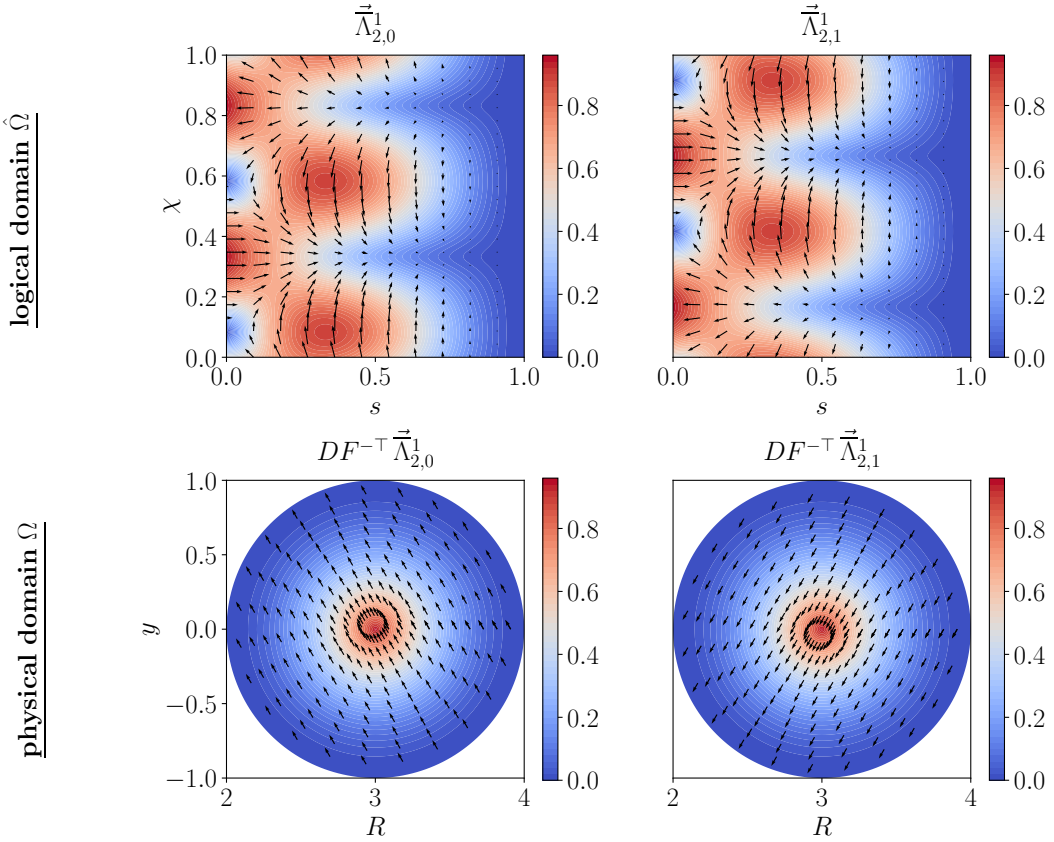

Figure 5.3: The two new vector-valued basis functions $\vec{\Lambda}^1_{2,0}$ (left column) and $\vec{\Lambda}^1_{2,1}$ (right column) (5.24) on the logical domain (uppper row) and physical domain (lower row) for the example $p_s = p_\chi = 3$, $n_s = 4$ and $n_\chi = 12$ using the mapping (3.123) with parameters $a = 1$ and $R_0 = 3$. The arrows' absolute values are color-coded. Arrows on the physical domain are normalized to the same value for better visibility and arrows at $s = 0$ pointing in the negative direction are not visible on the logical domain.

this means that the gradient is evidently zero if all entries of $\overline{\mathbf{f}}$ are identical. From the partition of unity property of B-splines it then follows that constant functions are in the kernel of the polar gradient operator. The first term on the right-hand side of (5.23) leads to the definition of two new basis functions:

$$\vec{\Lambda}^1_{2,0} := \sum_{j=0}^{n_\chi - 1} \begin{bmatrix} (\xi^1_{1j} - \xi^1_{0j}) D_0^{p_s} N_j^{p_\chi} \\ (\xi^1_{1j+1} - \xi^1_{1j}) N_1^{p_s} D_j^{p_\chi} \\ 0 \end{bmatrix}, \qquad \vec{\Lambda}^1_{2,1} := \sum_{j=0}^{n_\chi - 1} \begin{bmatrix} (\xi^2_{1j} - \xi^2_{0j}) D_0^{p_s} N_j^{p_\chi} \\ (\xi^2_{1j+1} - \xi^2_{1j}) N_1^{p_s} D_j^{p_\chi} \\ 0 \end{bmatrix}. \tag{5.24}$$

Note that these basis functions are vector-valued and that we will attribute them to the *second component of polar 1-forms*, which will become clear when discussing projection operators in Section 5.3. The other basis functions are standard tensor product basis functions. The dimensions are thus $\overline{n}^1_1 := 2\,(d_s - 1)\,n_\chi$ for the first component and $\overline{n}^1_2 := 2\,[\,(n_s - 2)\,d_\chi + 2\,]$ for the second component. The two new basis functions are plotted in Figure 5.3 both on the logical (upper row) and physical (lower row) domain (push-forward with $DF^{-\top}$, see Table 3.1) using the mapping (3.123) (cylinder). It is evident that both basis functions have no χ-dependence

on the physical domain. Moreover, we note that

$$\left(\vec{\overline{\Lambda}}^1_{2,0} \cdot \vec{\mathbf{e}}_2\right)(s=0,\chi) = \left(\vec{\overline{\Lambda}}^1_{2,1} \cdot \vec{\mathbf{e}}_2\right)(s=0,\chi) = 0 \qquad \forall\, \chi\,, \tag{5.25}$$

where $\vec{\mathbf{e}}_2 = [\,0,1,0\,]$. Hence, when using these two basis functions for discrete polar 1-forms, they correctly mimic the requirement (5.2b) for the second component of continuous polar 1-forms. The basis for the third component is the same as for 0-forms and similar to the tensor product basis functions (3.39) we introduce the notation

$$\vec{\overline{\mathbf{\Lambda}}}^1 := \left(\vec{\overline{\mathbf{\Lambda}}}^1_1,\, \vec{\overline{\mathbf{\Lambda}}}^1_2,\, \vec{\overline{\mathbf{\Lambda}}}^1_3\right) \begin{cases} \vec{\overline{\mathbf{\Lambda}}}^1_1 := \left(\vec{\overline{\Lambda}}^1_{1,(\overline{ijk})}\right) \in \mathbb{R}^{\overline{n}^1_1}\,, \\ \qquad \text{with} \quad (\overline{ijk}) = 2\,[\,n_\chi\,(i-1)+j\,]+k\,, \qquad 0<i<d_s\,, \\ \vec{\overline{\mathbf{\Lambda}}}^1_2 := \left(\vec{\overline{\Lambda}}^1_{2,(\ell k)},\, \vec{\overline{\Lambda}}^1_{2,(\overline{ijk})}\right) \in \mathbb{R}^{\overline{n}^1_2}\,, \qquad \vec{\overline{\Lambda}}^1_{2,(\ell k)} := \vec{\overline{\Lambda}}^1_{2,\ell}\,\mathcal{F}^n_k\,, \\ \qquad \text{with} \quad (\overline{ijk}) = 2\,[\,d_\chi\,(i-2)+j+2\,]+k\,, \qquad 1<i<n_s\,, \\ \vec{\overline{\mathbf{\Lambda}}}^1_3 := \left(\vec{\overline{\Lambda}}^1_{3,(\ell k)},\, \vec{\overline{\Lambda}}^1_{3,(\overline{ijk})}\right) \in \mathbb{R}^{\overline{n}^0}\,, \qquad \vec{\overline{\Lambda}}^1_{3,(\ell k)} := \overline{\Lambda}^0_{(\ell k)}\,\vec{\mathbf{e}}_3\,, \\ \qquad \text{with} \quad (\overline{ijk}) = 2\,[\,n_\chi\,(i-2)+j+3\,]+k\,, \qquad 1<i<n_s\,, \end{cases} \tag{5.26}$$

where $\vec{\mathbf{e}}_3 = [\,0,0,1\,]$ and basis functions with index $(\overline{ijk})$ are once more standard tensor product basis functions. Based on this new set of basis functions, similar to (3.44), a discrete polar 1-form $\mathbf{E}^1_h \in \overline{V}^1_h$ can compactly be written as

$$\begin{aligned} &\mathbf{E}^1_h = \overline{\mathcal{S}}_1[\,\vec{\overline{\mathbf{e}}}\,] = \vec{\overline{\mathbf{e}}}^{\,\top}\vec{\overline{\mathbf{\Lambda}}}^1\,, \\ &\vec{\overline{\mathbf{e}}} := \left(\overline{\mathbf{e}}_1 := \left(e_{1,(\overline{ijk})}\right),\, \overline{\mathbf{e}}_2 := \left(e_{2,(\ell k)},\, e_{2,(\overline{ijk})}\right),\, \overline{\mathbf{e}}_3 := \left(e_{3,(\ell k)},\, e_{3,(\overline{ijk})}\right)\right) \in \mathbb{R}^{\overline{n}^1}\,. \end{aligned} \tag{5.27}$$

With regards to (5.13), we define in a block-wise fashion the second polar extraction operator $\mathbb{E}^1 \in \mathbb{R}^{\overline{n}^1 \times n^1}$, where

$$\mathbb{E}^1 := \begin{bmatrix} \mathbb{E}^{1,\mathrm{pol}} & 0 \\ 0 & \mathbb{E}^0 \end{bmatrix}\,, \qquad \mathbb{E}^{1,\mathrm{pol}} := \begin{bmatrix} 0 & \mathbb{1}_{(d_s-1)\,n_\chi} & 0 & 0 \\ \mathbb{X}^1_1 & 0 & \mathbb{X}^1_2 & 0 \\ 0 & 0 & 0 & \mathbb{1}_{(n_s-2)\,d_\chi} \end{bmatrix} \otimes \mathbb{1}_2\,. \tag{5.28}$$

The matrix $\mathbb{X}^1_1 \in \mathbb{R}^{2\times n_\chi}$ acts on the first n_χ tensor product basis functions in $\vec{\mathbf{\Lambda}}^1_1$ corresponding to one of the two toroidal Fourier components and $\mathbb{X}^1_2 \in \mathbb{R}^{2\times 2d_\chi}$ acts on the first $2d_\chi$ tensor product basis functions in $\vec{\mathbf{\Lambda}}^1_2$ to yield (5.24). The entries can be deduced from (5.24) and read

$$\mathbb{X}^1_{1,\ell j} := \xi^{\ell+1}_{1j} - \xi^{\ell+1}_{0j}\,, \qquad \mathbb{X}^1_{2,\ell j} := \begin{cases} 0 & 0 \le j < d_\chi\,, \\ \xi^{\ell+1}_{1(j-d_\chi+1)} - \xi^{\ell+1}_{1(j-d_\chi)} & d_\chi \le j < 2d_\chi\,. \end{cases} \tag{5.29}$$

Finally, in view of (5.23), we shall write the gradient of $f^0_h \in \overline{V}^0_h$ compactly as

$$\hat{\nabla} f^0_h = (\,\overline{\mathbb{G}}\,\overline{\mathbf{f}}\,)^\top\,\vec{\overline{\mathbf{\Lambda}}}^1\,, \qquad \overline{\mathbb{G}} := \begin{bmatrix} \overline{\mathbb{D}}^s \\ \overline{\mathbb{D}}^\chi \\ \overline{\mathbb{D}}^\varphi \end{bmatrix}\,, \tag{5.30}$$

with the derivative matrices

$$\overline{\mathbb{D}}^{s} := \begin{bmatrix} \mathbb{D}^{s,\mathrm{pol}} & \mathbb{G}^{s}_{-2} \otimes \mathbb{1}^{\chi} \otimes \mathbb{1}_2 \end{bmatrix} \in \mathbb{R}^{\overline{n}^1_1 \times \overline{n}^0}\,, \qquad \overline{\mathbb{D}}^{\chi} := \begin{bmatrix} \mathbb{D}^{\chi,\mathrm{pol}} & 0 \\ 0 & \mathbb{D}^{\chi} \end{bmatrix} \in \mathbb{R}^{\overline{n}^1_2 \times \overline{n}^0}\,, \tag{5.31}$$
$$\overline{\mathbb{D}}^{\varphi} := \mathbb{1}^{\mathrm{pol}} \otimes \mathbb{G}^{\varphi} \in \mathbb{R}^{\overline{n}^0 \times \overline{n}^0}\,,$$

with blocks

$$\mathbb{D}^{s,\mathrm{pol}} \in \mathbb{R}^{\overline{n}^1_1 \times 6}\,, \qquad \mathbb{D}^{s,\mathrm{pol}}_{(\overline{ijk})(\ell k)} := \begin{cases} -\xi^{\ell}_{1j} & \text{for } i = 1\,, \\ 0 & \text{else}\,, \end{cases} \tag{5.32}$$

$$\mathbb{G}^{s}_{-2} := (\mathbb{G}^{s}_{ij})_{i>0, j>1} \in \mathbb{R}^{(d_s-1)\times(n_s-2)}\,, \tag{5.33}$$

$$\mathbb{D}^{\chi,\mathrm{pol}} \in \mathbb{R}^{4\times 6}\,, \qquad \mathbb{D}^{\chi,\mathrm{pol}} := \begin{bmatrix} -1 & 1 & 0 \\ -1 & 0 & 1 \end{bmatrix} \otimes \mathbb{1}_2\,. \tag{5.34}$$

The matrix $\mathbb{D}^{\chi}$ has been defined in (3.47) and is used here with $\mathbb{1}^{s} = \mathbb{1}_{n_s-2}$. The matrix $\mathbb{G}^{\varphi}$ has been defined in (3.48) and the size of the matrix $\mathbb{1}^{\mathrm{pol}}$ in the definition of $\overline{\mathbb{D}}^{\varphi}$ is adapted to the size of the space it acts on in the following. Here, $\mathbb{1}^{\mathrm{pol}} = \mathbb{1}_{\overline{n}^0/2}$.

5.2.3 Discrete polar curl operator and 2-forms

When applying the curl to a polar 1-form (5.27), the result must be a polar 2-form whose coefficients are obtained via the application of the *polar curl matrix* $\overline{\mathbb{C}}$, formally

$$\hat{\nabla} \times \mathbf{E}^1_h = (\,\overline{\mathbb{C}}\,\vec{\mathbf{e}}\,)^{\top}\,\vec{\overline{\mathbf{\Lambda}}}^2\,. \tag{5.35}$$

The goal of this section is to identify on the one hand the suitable basis $\vec{\overline{\mathbf{\Lambda}}}^2$ and on the other hand the form of the polar curl matrix $\overline{\mathbb{C}}$.

Since $E^1_{h,3} = \overline{\mathbf{e}}_3^{\top}\,\overline{\mathbf{\Lambda}}^0$, we already computed $\partial_s E^1_{h,3}$ and $\partial_\chi E^1_{h,3}$ in (5.23) of the previous section. Therefore,

$$\vec{\overline{\Lambda}}^2_{1,0} := \vec{\overline{\Lambda}}^1_{2,0} \times \vec{\mathbf{e}}_3\,, \qquad \vec{\overline{\Lambda}}^2_{1,1} := \vec{\overline{\Lambda}}^1_{2,1} \times \vec{\mathbf{e}}_3\,. \tag{5.36}$$

Note that unlike polar 1-forms, we attribute these basis functions to the *first component of polar 2-forms*. The dimensions are thus $\overline{n}^2_1 := \overline{n}^1_2$ for the first component and $\overline{n}^2_2 := \overline{n}^1_1$ for the second component. The two new basis functions are plotted in Figure 5.4 both on the logical (upper row) and physical (lower row) domain (push-forward with $DF/\sqrt{g}$, see Table 3.1) using the mapping (3.123) (cylinder). It is evident that both basis functions have no χ-dependence on the physical domain. Moreover, we note that

$$\left(\vec{\overline{\Lambda}}^2_{1,0} \cdot \vec{\mathbf{e}}_1\right)(s=0,\chi) = \left(\vec{\overline{\Lambda}}^2_{1,1} \cdot \vec{\mathbf{e}}_1\right)(s=0,\chi) = 0 \qquad \forall\,\chi\,, \tag{5.37}$$

where $\vec{\mathbf{e}}_1 = [\,1,0,0\,]$. Hence, when using these two basis functions for discrete polar 2-forms, they correctly mimic the requirement (5.2c) for the first component of continuous polar 2-forms.

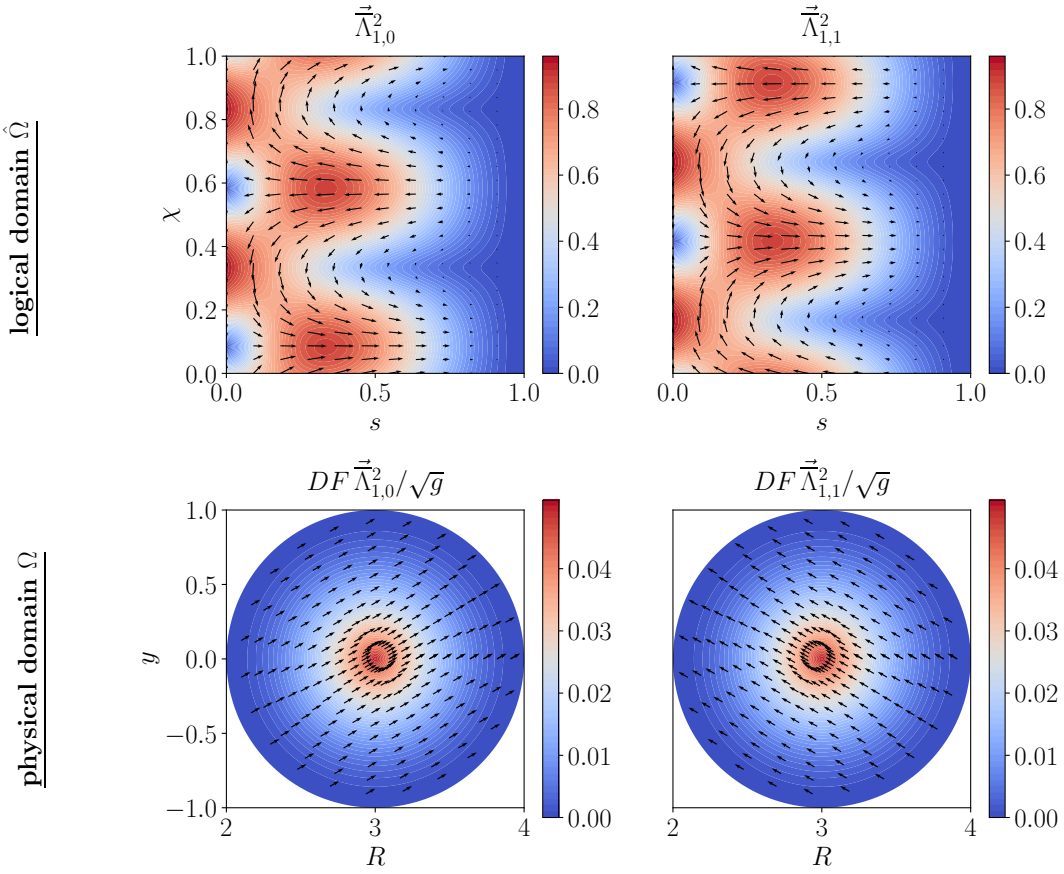

Figure 5.4: The two new vector-valued basis functions $\vec{\Lambda}^2_{1,0}$ (left column) and $\vec{\Lambda}^2_{1,1}$ (right column) (5.36) on the logical domain (uppper row) and physical domain (lower row) for the example $p_s = p_\theta = 3$, $n_s = 4$ and $n_\theta = 12$ using the mapping (3.123) with parameters $a = 1$ and $R_0 = 3$. The arrows' absolute values are color-coded. Arrows on the physical domain are normalized to the same value for better visibility and arrows tangential to the surface $s = 0$ are not visible on the logical domain.

Similar to the tensor product basis (3.40) we introduce the notation

$$\vec{\boldsymbol{\Lambda}}^2 := \left(\vec{\boldsymbol{\Lambda}}^2_1, \vec{\boldsymbol{\Lambda}}^2_2, \vec{\boldsymbol{\Lambda}}^2_3\right) \begin{cases} \vec{\boldsymbol{\Lambda}}^2_1 := \left(\vec{\Lambda}^2_{1,(\ell k)}, \vec{\Lambda}^2_{1,(\overline{ijk})}\right) \in \mathbb{R}^{\overline{n}^2_1}, \quad \vec{\Lambda}^2_{1,(\ell k)} := \vec{\Lambda}^2_{1,\ell}\,\mathcal{F}^n_k\,, \\ \qquad \text{with} \quad (\overline{ijk}) = 2\,[\,d_\chi\,(i-2) + j + 2\,] + k\,, \qquad 1 < i < n_s\,, \\ \vec{\boldsymbol{\Lambda}}^2_2 := \left(\vec{\Lambda}^2_{2,(\overline{ijk})}\right) \in \mathbb{R}^{\overline{n}^2_2}\,, \\ \qquad \text{with} \quad (\overline{ijk}) = 2\,[\,n_\chi\,(i-1) + j\,] + k\,, \qquad 0 < i < d_s\,, \\ \vec{\boldsymbol{\Lambda}}^2_3 := \left(\vec{\Lambda}^2_{3,(\overline{ijk})}\right) \in \mathbb{R}^{\overline{n}^3}\,, \\ \qquad \text{with} \quad (\overline{ijk}) = 2\,[\,d_\chi\,(i-1) + j\,] + k\,, \qquad 0 < i < d_s\,. \end{cases} \tag{5.38}$$

The third component $\vec{\boldsymbol{\Lambda}}^2_3$ has been determined from the third component of the curl of a polar

2-form. The relevant partial derivatives of $\mathbf{E}^1_h$ read

$$\begin{aligned}\frac{\partial E^1_{h,2,k}}{\partial s} &= \sum_{\ell=0}^{1} e_{2,(\ell k)} \sum_{j=0}^{d_\chi-1} (\xi^{\ell+1}_{1j+1} - \xi^{\ell+1}_{1j})(D^{p_s}_0 - D^{p_s}_1) D^{p_\chi}_j + \sum_{i>1,j} e_{2,(\overline{ijk})} (D^{p_s}_{i-1} - D^{p_s}_i) D^{p_\chi}_j \\ &= \sum_{\ell=0}^{1} e_{2,(\ell k)} \sum_{j=0}^{d_\chi-1} (\xi^{\ell+1}_{1j+1} - \xi^{\ell+1}_{1j}) D^{p_s}_0 D^{p_\chi}_j \\ &+ \sum_{j=0}^{d_\chi-1} \left[e_{2,(\overline{2jk})} - \sum_{\ell=0}^{1} e_{2,(\ell k)} (\xi^{\ell+1}_{1j+1} - \xi^{\ell+1}_{1j}) \right] D^{p_s}_1 D^{p_\chi}_j + \sum_{i>1,j} (e_{2,(\overline{i+1jk})} - e_{2,(\overline{ijk})}) D^{p_s}_i D^{p_\chi}_j \,,\end{aligned} \tag{5.39}$$

$$\begin{aligned}\frac{\partial E^1_{h,1,k}}{\partial \chi} &= \sum_{\ell=0}^{1} e_{2,(\ell k)} \sum_{j=0}^{n_\chi-1} (\xi^{\ell+1}_{1j} - \xi^{\ell+1}_{0j}) D^{p_s}_0 (D^{p_\chi}_{j-1} - D^{p_\chi}_j) + \sum_{i>0,j} e_{1,(\overline{ijk})} D^{p_s}_i (D^{p_\chi}_{j-1} - D^{p_\chi}_j) \\ &= \sum_{\ell=0}^{1} e_{2,(\ell k)} \sum_{j=0}^{d_\chi-1} (\xi^{\ell+1}_{1j+1} - \xi^{\ell+1}_{0j+1} - \xi^{\ell+1}_{1j} + \xi^{\ell+1}_{0j}) D^{p_s}_0 D^{p_\chi}_j \\ &\qquad + \sum_{i>0,j} (e_{1,(\overline{ij+1k})} - e_{1,(\overline{ijk})}) D^{p_s}_i D^{p_\chi}_j \\ &= \sum_{\ell=0}^{1} e_{2,(\ell k)} \sum_{j=0}^{d_\chi-1} (\xi^{\ell+1}_{1j+1} - \xi^{\ell+1}_{1j}) D^{p_s}_0 D^{p_\chi}_j + \sum_{i>0,j} (e_{1,(\overline{ij+1k})} - e_{1,(\overline{ijk})}) D^{p_s}_i D^{p_\chi}_j \,,\end{aligned} \tag{5.40}$$

respectively, where we used (5.19) to obtain the last line. Taking the difference yields

$$\begin{aligned}&\frac{\partial E^1_{h,2,k}}{\partial s} - \frac{\partial E^1_{h,1,k}}{\partial \chi} \\ &\qquad = \sum_{j=0}^{d_\chi-1} \left[e_{2,(\overline{2jk})} - \sum_{\ell=0}^{1} e_{2,(\ell k)} (\xi^{\ell+1}_{1j+1} - \xi^{\ell+1}_{1j}) - e_{1,(\overline{1j+1k})} + e_{1,(\overline{1jk})} \right] D^{p_s}_1 D^{p_\chi}_j \\ &\qquad + \sum_{i>1,j} \Big(e_{2,(\overline{i+1jk})} - e_{2,(\overline{ijk})} - e_{1,(\overline{ij+1k})} + e_{1,(\overline{ijk})} \Big) D^{p_s}_i D^{p_\chi}_j \,,\end{aligned} \tag{5.41}$$

which reveals the basis of the third component of 2-forms, namely being standard tensor product basis functions ($\vec{\overline{\Lambda}}^2_{3,(\overline{ijk})} = D^{p_s}_i D^{p_\chi}_j \mathcal{F}^n_k \, \vec{\mathbf{e}}_3$) with index $i > 0$ such that the second requirement in (5.2c) is satisfied and $\overline{n}^3 := 2\,(d_s - 1)\,d_\chi$. Based on this new set of basis functions, similar to (3.45), a discrete polar 2-form $\mathbf{B}^2_h \in \overline{V}^2_h$ can compactly be written as

$$\begin{aligned}&\mathbf{B}^2_h = \overline{\mathcal{S}}_2[\,\vec{\overline{\mathbf{b}}}\,] := \vec{\overline{\mathbf{b}}}^{\top} \vec{\overline{\mathbf{\Lambda}}}^2 \,, \\ &\vec{\overline{\mathbf{b}}} := \Big(\overline{\mathbf{b}}_1 := \Big(b_{1,(\ell k)},\, b_{1,(\overline{ijk})} \Big) \,,\, \overline{\mathbf{b}}_2 := \Big(b_{2,(\overline{ijk})} \Big) \,,\, \overline{\mathbf{b}}_3 := \Big(b_{3,(\overline{ijk})} \Big) \Big) \in \mathbb{R}^{\overline{n}^2} \,.\end{aligned} \tag{5.42}$$

With regards to (5.28), we define in a block-wise fashion the third polar extraction operator $\mathbb{E}^2 \in \mathbb{R}^{\overline{n}^2 \times n^2}$, where

$$\mathbb{E}^2 := \begin{bmatrix} \mathbb{E}^{2,\mathrm{pol}} & 0 \\ 0 & \mathbb{E}^3 \end{bmatrix} \,, \qquad \mathbb{E}^{2,\mathrm{pol}} := \begin{bmatrix} \mathbb{X}^1_2 & 0 & -\mathbb{X}^1_1 & 0 \\ 0 & \mathbb{1}_{(n_s-2)\,d_\chi} & 0 & 0 \\ 0 & 0 & 0 & \mathbb{1}_{(d_s-1)\,n_\chi} \end{bmatrix} \otimes \mathbb{1}_2 \,. \tag{5.43}$$

The matrices $\mathbb{K}_1^1$ and $\mathbb{K}_2^1$ were defined in (5.29) and the extraction operator $\mathbb{E}^3 \in \mathbb{R}^{\overline{n}^3 \times n^3}$ for the third component reads

$$\mathbb{E}^3 := \begin{bmatrix} 0 & \mathbb{1}_{(d_s-1)\, d_\chi} \end{bmatrix} \otimes \mathbb{1}_2 \,. \tag{5.44}$$

Finally, in view of (5.35) and (5.41), we shall write the curl of $\mathbf{E}_h^1 \in \overline{V}_h^1$ compactly as

$$\hat{\nabla} \times \mathbf{E}_h^1 = (\,\overline{\mathbb{C}}\,\vec{\mathbf{e}}\,)^\top \vec{\mathbf{\Lambda}}^2 \,, \qquad \overline{\mathbb{C}} := \begin{bmatrix} 0 & -\overline{\mathbb{D}}^\varphi & \overline{\mathbb{D}}^\chi \\ \overline{\mathbb{D}}^\varphi & 0 & -\overline{\mathbb{D}}^s \\ -\mathbb{D}^\chi & \overline{\mathbb{S}} & 0 \end{bmatrix} , \tag{5.45}$$

where $\mathbb{D}^\chi$ has been defined in (3.47) and is used here with $\mathbb{1}^s = \mathbb{1}_{d_s-1}$ and the derivative matrices $\overline{\mathbb{D}}^s$, $\overline{\mathbb{D}}^\chi$ and $\overline{\mathbb{D}}^\varphi$ have been defined in (5.31), where an appropriate sizes for the identity matrix $\mathbb{1}^{\mathrm{pol}}$ must be used for the latter. Moreover,

$$\overline{\mathbb{S}} := \begin{bmatrix} \mathbb{S}^{s,\mathrm{pol}} & \mathbb{G}^s_{-2} \otimes \mathbb{1}^\chi \otimes \mathbb{1}_2 \end{bmatrix} \in \mathbb{R}^{\overline{n}^3 \times \overline{n}_2^1} \,, \tag{5.46}$$

where

$$\mathbb{S}^{s,\mathrm{pol}} \in \mathbb{R}^{\overline{n}^3 \times 4} \,, \qquad \mathbb{S}^{s,\mathrm{pol}}_{(\overline{ijk})(\ell k)} := \begin{cases} -(\xi^{\ell+1}_{1j+1} - \xi^{\ell+1}_{1j}) & i = 1 \,, \\ 0 & \text{else} \,, \end{cases} \tag{5.47}$$

and $\mathbb{G}^s_{-2}$ has been defined in (5.33).

Proposition 3. *We have* $\overline{\mathbb{C}}\,\overline{\mathbb{G}} = 0$.

Proof. The matrix product of interest reads

$$\overline{\mathbb{C}}\,\overline{\mathbb{G}} = \begin{bmatrix} 0 & -\overline{\mathbb{D}}^\varphi & \overline{\mathbb{D}}^\chi \\ \overline{\mathbb{D}}^\varphi & 0 & -\overline{\mathbb{D}}^s \\ -\mathbb{D}^\chi & \overline{\mathbb{S}} & 0 \end{bmatrix} \begin{bmatrix} \overline{\mathbb{D}}^s \\ \overline{\mathbb{D}}^\chi \\ \overline{\mathbb{D}}^\varphi \end{bmatrix} .$$

The first two rows yield zero immediately. In the last row we must show that $-\mathbb{D}^\chi\,\overline{\mathbb{D}}^s + \overline{\mathbb{S}}\,\overline{\mathbb{D}}^\chi = 0$ where

$$\mathbb{D}^\chi = \mathbb{1}_{d_s-1} \otimes \mathbb{G}^\chi \otimes \mathbb{1}_2 \qquad \in \mathbb{R}^{\overline{n}^3 \times \overline{n}_1^1} \,, \qquad \overline{\mathbb{D}}^s = \begin{bmatrix} \mathbb{D}^{s,\mathrm{pol}} & \mathbb{G}^s_{-2} \otimes \mathbb{1}^\chi \otimes \mathbb{1}_2 \end{bmatrix} \in \mathbb{R}^{\overline{n}_2^2 \times \overline{n}^0} \,,$$

$$\overline{\mathbb{S}} = \begin{bmatrix} \mathbb{S}^{s,\mathrm{pol}} & \mathbb{G}^s_{-2} \otimes \mathbb{1}^\chi \otimes \mathbb{1}_2 \end{bmatrix} \in \mathbb{R}^{\overline{n}^3 \times \overline{n}_2^1} \,, \qquad \overline{\mathbb{D}}^\chi = \begin{bmatrix} \mathbb{D}^{\chi,\mathrm{pol}} & 0 \\ 0 & \mathbb{D}^\chi \end{bmatrix} \qquad \in \mathbb{R}^{\overline{n}_1^2 \times \overline{n}^0} \,,$$

and the single blocks

$$\mathbb{G}^\chi \in \mathbb{R}^{d_\chi \times n_\chi} \,, \quad \mathbb{G}^s_{-2} \in \mathbb{R}^{(d_s-1)\times(n_s-2)} \,, \quad \mathbb{D}^{s,\mathrm{pol}} \in \mathbb{R}^{\overline{n}_2^2 \times 6} \,, \quad \mathbb{S}^{s,\mathrm{pol}} \in \mathbb{R}^{\overline{n}^3 \times 4} \,, \quad \mathbb{D}^{\chi,\mathrm{pol}} \in \mathbb{R}^{4\times 6} \,.$$

Therefore,

$$-\mathbb{D}^\chi\,\overline{\mathbb{D}}^s + \overline{\mathbb{S}}\,\overline{\mathbb{D}}^\chi = -\begin{bmatrix} \mathbb{D}^\chi\,\mathbb{D}^{s,\mathrm{pol}} & \mathbb{G}^s_{-2} \otimes \mathbb{G}^\chi \otimes \mathbb{1}_2 \end{bmatrix} + \begin{bmatrix} \mathbb{S}^{s,\mathrm{pol}}\,\mathbb{D}^{\chi,\mathrm{pol}} & \mathbb{G}^s_{-2} \otimes \mathbb{G}^\chi \otimes \mathbb{1}_2 \end{bmatrix} .$$

It remains to show the equality of the first block:

$$\mathbb{D}^\chi\,\mathbb{D}^{s,\mathrm{pol}}_{(\overline{ijk})(\ell k)} = \mathbb{D}^{s,\mathrm{pol}}_{(\overline{ij+1k})(\ell k)} - \mathbb{D}^{s,\mathrm{pol}}_{(\overline{ijk})(\ell k)} = \begin{cases} -\xi^\ell_{1j+1} + \xi^\ell_{ij} & i = 1 \,, \quad \ell = 0,1,2 \,, \\ 0 & \text{else} \,, \end{cases}$$

$$\mathbb{S}^{s,\mathrm{pol}}\,\mathbb{D}^{\chi,\mathrm{pol}} = \begin{cases} \xi^1_{1j+1} - \xi^1_{ij} + \xi^2_{1j+1} - \xi^2_{ij} & i = 1 \,, \quad \ell = 0 \,, \\ -\xi^\ell_{1j+1} + \xi^\ell_{ij} & i = 1 \,, \quad \ell = 1,2 \,, \\ 0 & \text{else} \,. \end{cases}$$

From the polar extraction coefficients (5.7) follows

$$\xi^1_{1j+1} - \xi^1_{ij} + \xi^2_{1j+1} - \xi^2_{ij} = -\xi^0_{1j+1} + \xi^0_{ij}\,,$$

which completes the proof. □

5.2.4 Discrete polar divergence operator and 3-forms

When applying the divergence to a polar 2-form (5.42), the result must be a polar 3-form whose coefficients are obtained via the application of the *polar divergence matrix* $\overline{\mathbb{D}}$, formally

$$\hat{\nabla} \cdot \mathbf{B}^2_h = (\,\overline{\mathbb{D}}\,\vec{\mathbf{b}}\,)^\top\,\overline{\mathbf{\Lambda}}^3\,. \tag{5.48}$$

The goal of this section is to identify on the one hand the suitable basis $\overline{\mathbf{\Lambda}}^3$ and on the other hand the form of the polar divergence matrix $\overline{\mathbb{D}}$.

The basis is evidently given by the basis of the third component in (5.38). Thus,

$$\begin{aligned} \overline{\mathbf{\Lambda}}^3 &:= \left(\,\overline{\Lambda}^3_{(\overline{ijk})}\right) \in \mathbb{R}^{\overline{n}^3}\,, \qquad \overline{\Lambda}^3_{(\overline{ijk})} := \vec{\overline{\Lambda}}^2_{3,(\overline{ijk})} \cdot \vec{\mathbf{e}}_3\,, \\ &\text{with} \quad (\overline{ijk}) = 2\,[\,d_\chi\,(i-1) + j\,] + k\,, \qquad 0 < i < d_s\,. \end{aligned} \tag{5.49}$$

Based on this new set of basis functions, similar to (3.46), a discrete polar 3-form $p^3_h \in \overline{V}^3_h$ can compactly be written as

$$p^3_h = \overline{\mathcal{S}}_3[\,\overline{\mathbf{p}}\,] = \overline{\mathbf{p}}^\top\,\overline{\mathbf{\Lambda}}^3\,, \qquad \overline{\mathbf{p}} := \left(p_{(\overline{ijk})}\right) \in \mathbb{R}^{\overline{n}^3}\,. \tag{5.50}$$

The corresponding third polar extraction operator $\mathbb{E}^3$ has already been defined in (5.44). In order to compute the polar divergence matrix we note that the sum of the derivatives with respect to s and χ can be easily deduced from (5.41), where we take note of the minus sign in the definition of the polar 2-form basis functions (5.36):

$$\begin{aligned} &\frac{\partial B^2_{h,1,k}}{\partial s} + \frac{\partial B^2_{h,2,k}}{\partial \chi} \\ &\qquad = \sum_{j=0}^{d_\chi - 1} \left[b_{1,(\overline{2jk})} - \sum_{\ell=0}^{1} b_{1,(\ell k)} (\xi^{\ell+1}_{1j+1} - \xi^{\ell+1}_{1j}) + b_{2,(\overline{1j+1k})} - b_{2,(\overline{1jk})} \right] D^{p_s}_1 D^{p_\chi}_j \\ &\qquad + \sum_{i>1,j} \left(b_{1,(\overline{i+1jk})} - b_{1,(\overline{ijk})} + b_{2,(\overline{ij+1k})} - b_{2,(\overline{ijk})} \right) D^{p_s}_i D^{p_\chi}_j\,. \end{aligned} \tag{5.51}$$

The divergence of $\mathbf{B}^2_h \in \overline{V}^2_h$ can then be written compactly as

$$\hat{\nabla} \cdot \mathbf{B}^2_h = (\,\overline{\mathbb{D}}\,\vec{\mathbf{b}}\,)^\top \overline{\mathbf{\Lambda}}^3\,, \qquad \overline{\mathbb{D}} := \left[\; \overline{\mathbb{S}} \;\middle|\; \mathbb{D}^\chi \;\middle|\; \overline{\mathbb{D}}^\varphi \;\right]\,, \tag{5.52}$$

where $\mathbb{D}^\chi$ has been defined in (5.31) and is used here with $\mathbb{1}^s = \mathbb{1}_{d_s - 1}$ and $\overline{\mathbb{S}}$ has been defined in (5.46).

Proposition 4. *We have* $\overline{\mathbb{D}}\,\overline{\mathbb{C}} = 0$.

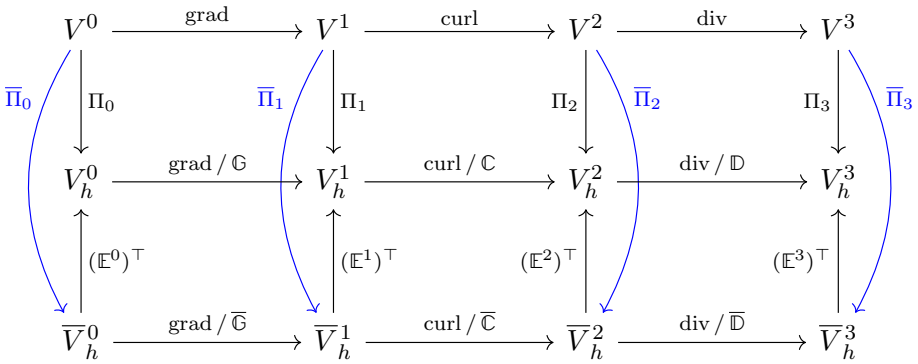

Figure 5.5: Commuting diagrams in three dimensions. Top row: continuous function spaces, middle row: pure tensor product subspaces, bottom row: polar subspaces.

Proof. The matrix product of interest reads

$$\overline{\mathbb{D}}\,\overline{\mathbb{C}} = \left[\begin{array}{c|c|c} \overline{\mathbb{S}} & \mathbb{D}^\chi & \overline{\mathbb{D}}^\varphi \end{array}\right] \begin{bmatrix} 0 & -\overline{\mathbb{D}}^\varphi & \overline{\mathbb{D}}^\chi \\ \overline{\mathbb{D}}^\varphi & 0 & -\overline{\mathbb{D}}^s \\ -\mathbb{D}^\chi & \overline{\mathbb{S}} & 0 \end{bmatrix}.$$

The first two rows yield zero immediately and the relation $\overline{\mathbb{S}}\,\overline{\mathbb{D}}^\chi - \mathbb{D}^\chi\,\overline{\mathbb{D}}^s = 0$ has been proven in Proposition 3. □

Consequently, due to the fact that $\overline{\mathbb{C}}\,\overline{\mathbb{G}} = 0$ and $\overline{\mathbb{D}}\,\overline{\mathbb{C}} = 0$ (see Propositions 3 and 4), we can construct the discrete de Rham complex

$$\overline{V}_h^0 \xrightarrow{\text{grad} / \overline{\mathbb{G}}} \overline{V}_h^1 \xrightarrow{\text{curl} / \overline{\mathbb{C}}} \overline{V}_h^2 \xrightarrow{\text{div} / \overline{\mathbb{D}}} \overline{V}_h^3\,, \tag{5.53}$$

in the same way as in the pure tensor product case (3.52).

5.3 Polar commuting projectors

In this section we derive polar DOFs that guarantee the commuting property shown in Figure 5.5. Figure 5.6 shows the grey tensor product grid with $n_s n_\chi$ interpolation points $(\mathfrak{s}_i, \mathfrak{t}_j)$ on the vertices for the DOFs σ^0 defined in (3.68a). In the polar case, only the blue points/grid are used for interpolation. The number of blue points is $(n_s - 2)\,n_\chi + 3$ which corresponds to the dimension of one Fourier component in $\overline{V}_h^0$. The first two "rings" around the pole $(\mathfrak{s}_0, \mathfrak{t}_j)$ and $(\mathfrak{s}_1, \mathfrak{t}_j)$ are removed and three new points $(\mathfrak{s}_1, \bar{\mathfrak{t}}_0)$, $(\mathfrak{s}_1, \bar{\mathfrak{t}}_1)$ and $(\mathfrak{s}_1, \bar{\mathfrak{t}}_2)$ on the $i = 1$ ring are added for interpolation. The three angles $(\bar{\mathfrak{t}}_0, \bar{\mathfrak{t}}_1, \bar{\mathfrak{t}}_2) \subset \mathfrak{t}$ must be distinct and are here chosen to be part of the tensor product grid for implementation reasons. They account for the three DOFs necessary for the three new polar spline basis functions $(\,\overline{\Lambda}_0^0, \overline{\Lambda}_1^0, \overline{\Lambda}_2^0\,)$ around the pole. In the polar setting, we define the DOFs $\overline{\sigma}^0$ as

$$f^0 \in V^0 : \begin{cases} \overline{\sigma}^0_{(\ell k)}(f^0) := f_k^0(\mathfrak{s}_1, \bar{\mathfrak{t}}_\ell)\,, & \ell = 0, 1, 2\,, \\ \overline{\sigma}^0_{(ijk)}(f^0) := f_k^0(\mathfrak{s}_i, \mathfrak{t}_j)\,, & 1 < i < n_s\,. \end{cases} \tag{5.54}$$

We now aim to construct the DOFs for the space $\overline{V}_h^1$ in a way that the commutation relations (3.72) hold. The proof of Proposition 2 serves as the blue print of how to achieve this. From

Figure 5.6 we see that for $i > 1$ histopolation can be carried out as usual on the blue grid. However, we also need to carry out histopolation between $i = 1$ and $i = 2$ in order to get as many DOFs as basis functions in the space $\overline{V}^1_h$. In order to get the commuting property, we employ a convex combination of the DOFs for $i = 1$ and demand

$$\overline{\sigma}^1_{1,(\overline{1jk})}\left(\frac{\partial f^0}{\partial s}\,\vec{\mathbf{e}}_1\right) = f^0_k(\mathfrak{s}_2, \mathfrak{t}_j) - \sum_{\ell=0}^{2} w_{\ell j} f^0_k(\mathfrak{s}_1, \bar{\mathfrak{t}}_\ell)\,, \quad w_{\ell j} \in \mathbb{R}\,, \quad \sum_{\ell=0}^{2} w_{\ell j} = 1 \quad \forall\, j\,, \tag{5.55}$$

for $f^0 \in V^0$. In the χ-direction we demand

$$\overline{\sigma}^1_{2,(\ell k)}\left(\frac{\partial f}{\partial \chi}\,\vec{\mathbf{e}}_2\right) = f^0_k(\mathfrak{s}_1, \bar{\mathfrak{t}}_{\ell+1}) - f^0_k(\mathfrak{s}_1, \bar{\mathfrak{t}}_0)\,, \qquad \ell = 0, 1\,. \tag{5.56}$$

The conditions (5.55) and (5.56) can be satisfied with the following polar DOFs for the space $\overline{V}^1_h$:

$$\mathbf{E}^1 \in V^1 : \begin{cases} \overline{\sigma}^1_{1,(\overline{1jk})}(\mathbf{E}^1) := \displaystyle\int_{\mathfrak{s}_0}^{\mathfrak{s}_2} E^1_{1,k}(s, \mathfrak{t}_j)\,\mathrm{d}s - \sum_{\ell=0}^{2} w_{\ell j} \int_{\mathfrak{s}_0}^{\mathfrak{s}_1} E^1_{1,k}(s, \bar{\mathfrak{t}}_\ell)\,\mathrm{d}s\,, \\ \overline{\sigma}^1_{1,(\overline{ijk})}(\mathbf{E}^1) := \displaystyle\int_{\mathfrak{s}_i}^{\mathfrak{s}_{i+1}} E^1_{1,k}(s, \mathfrak{t}_j)\,\mathrm{d}s\,, \qquad 1 < i < d_s\,, \\ \overline{\sigma}^1_{2,(\ell k)}(\mathbf{E}^1) := \displaystyle\int_{\bar{\mathfrak{t}}_0}^{\bar{\mathfrak{t}}_{\ell+1}} E^1_{2,k}(\mathfrak{s}_1, \chi)\,\mathrm{d}\chi\,, \qquad \ell = 0, 1\,, \\ \overline{\sigma}^1_{2,(\overline{ijk})}(\mathbf{E}^1) := \displaystyle\int_{\mathfrak{t}_j}^{\mathfrak{t}_{j+1}} E^1_{2,k}(\mathfrak{s}_i, \chi)\,\mathrm{d}\chi \qquad 1 < i < n_s\,, \\ \overline{\sigma}^1_3(\mathbf{E}^1) := \overline{\sigma}^0(E^1_3)\,. \end{cases} \tag{5.57}$$

Let us verify that (5.55) is indeed fulfilled: from the first line in (5.57) we obtain

$$\overline{\sigma}^1_{1,(\overline{1jk})}\left(\frac{\partial f^0}{\partial s}\,\vec{\mathbf{e}}_1\right) = f^0_k(\mathfrak{s}_2, \mathfrak{t}_j) - f^0_k(\mathfrak{s}_0, \mathfrak{t}_j) - \sum_{\ell=0}^{2} w_{\ell j}\left[f^0_k(\mathfrak{s}_1, \bar{\mathfrak{t}}_\ell) - f^0_k(\mathfrak{s}_0, \bar{\mathfrak{t}}_\ell)\right]\,. \tag{5.58}$$

Taking into account that $f^0_k(\mathfrak{s}_0 = 0, \chi)$ ($\mathfrak{s}_0 = 0$ for clamped B-splines) is independent of χ because polar 0-forms are single-valued at the pole and, moreover, that we demanded $\sum_\ell w_{\ell j} = 1$, we obtain relation (5.55). The relation (5.56) follows directly from the third line in (5.57). The polar DOFs for $\mathbf{B} \in V^2$ follow by exchanging the components in (5.57):

$$\mathbf{B}^2 \in V^2 : \begin{cases} \overline{\sigma}^2_1(\mathbf{B}^2) := \overline{\sigma}^1_2(\mathbf{B}^2)\,, \\ \overline{\sigma}^2_2(\mathbf{B}^2) := \overline{\sigma}^1_1(\mathbf{B}^2)\,, \\ \overline{\sigma}^2_3(\mathbf{B}^2) := \overline{\sigma}^3(B^2_3)\,. \end{cases} \tag{5.59}$$

Here, $\overline{\sigma}^3$ is identified by looking at DOFs for $p^3 \in V^3$ which we define to be

$$p^3 \in V^3 : \begin{cases} \overline{\sigma}^3_{(\overline{1jk})}(p^3) := \displaystyle\int_{\mathfrak{s}_0}^{\mathfrak{s}_2} \int_{\mathfrak{t}_j}^{\mathfrak{t}_{j+1}} p^3_k(s, \chi)\,\mathrm{d}s\,\mathrm{d}\chi - \sum_{\ell=0}^{1} a_{\ell j} \int_{\mathfrak{s}_0}^{\mathfrak{s}_1} \int_{\bar{\mathfrak{t}}_0}^{\bar{\mathfrak{t}}_{\ell+1}} p^3_k(s, \chi)\,\mathrm{d}s\,\mathrm{d}\chi\,, \\ \overline{\sigma}^3_{(\overline{ijk})}(p^3) := \displaystyle\int_{\mathfrak{s}_i}^{\mathfrak{s}_{i+1}} \int_{\mathfrak{t}_j}^{\mathfrak{t}_{j+1}} p^3_k(s, \chi)\,\mathrm{d}s\,\mathrm{d}\chi\,, \qquad 1 < i < d_s\,. \end{cases} \tag{5.60}$$

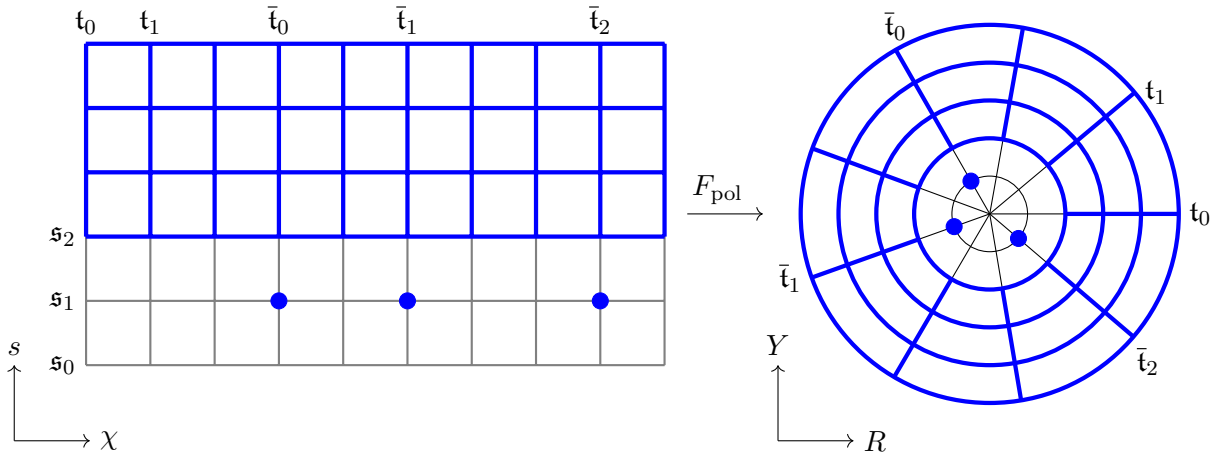

Figure 5.6: Only the three blue points and the vertices of the blue grid are used for interpolation in the polar setting in contrast to the vertices of the grey grid in the tensor product setting. Note that all points on the line at $\mathfrak{s}_0 = 0$ are mapped to the pole (R_0, Y_0) under the mapping F_{pol}. However, no interpolation points are located on this line for the new blue grid.

Here, we introduced the coefficients $a_{0j}, a_{1j} \in \mathbb{R}$ which have to be chosen such that the commuting property holds (see below). Note that the above DOFs are linearly independent and that the number of DOFs matches the dimension of each respective space.

Definition 3. *The projectors $\overline{\Pi}_k : V^k \to \overline{V}_h^k$ are defined via the DOFs* (5.54), (5.57), (5.59) *and* (5.60)*:*

$$\overline{\sigma}^0(\,\overline{\Pi}_0(f^0)\,) = \overline{\sigma}^0(f^0)\,, \qquad \overline{\sigma}^1(\,\overline{\Pi}_1(\mathbf{E}^1)\,) = \overline{\sigma}^1(\mathbf{E}^1)\,, \tag{5.61a}$$

$$\overline{\sigma}^3(\,\overline{\Pi}_3(p^3)\,) = \overline{\sigma}^3(p^3)\,, \qquad \overline{\sigma}^2(\,\overline{\Pi}_2(\mathbf{B}^2)\,) = \overline{\sigma}^2(\mathbf{B}^2)\,. \tag{5.61b}$$

Proposition 5. *Provided that the integrals in* (5.57), (5.59) *and* (5.60) *are exact and that for any* $(f_{(0k)}, f_{(1k)}, f_{(2k)}) \in \mathbb{R}^3$*,*

$$\sum_{\ell=0}^{1} a_{\ell j}(f_{(\ell+1k)} - f_{(0k)}) = \sum_{\ell=0}^{2}(w_{\ell j+1} - w_{\ell j})f_{(\ell k)}\,, \qquad a_{\ell j} \neq 0\,, \qquad \sum_{\ell=0}^{2} w_{\ell j} = 1\,, \tag{5.62}$$

the projectors (5.61) *satisfy the commutation relations*

$$\overline{\Pi}_1\,\mathrm{grad} = \mathrm{grad}\,\overline{\Pi}_0\,, \qquad \overline{\Pi}_2\,\mathrm{curl} = \mathrm{curl}\,\overline{\Pi}_1\,, \qquad \overline{\Pi}_3\,\mathrm{div} = \mathrm{div}\,\overline{\Pi}_2\,.$$

Proof. Let us start with $\overline{\Pi}_1\,\mathrm{grad} = \mathrm{grad}\,\overline{\Pi}_0$. By definition both sides of the equality are in $\overline{V}_h^1$. Since an element in $\overline{V}_h^1$ is uniquely defined by its DOFs, we can apply $\overline{\sigma}^1$ on both sides. The

tensor product part is as usual; the new parts read

$$\begin{aligned}
\overline{\sigma}^1_{1,(\overline{1jk})}\left(\overline{\Pi}_1(\hat{\nabla} f^0)\right) &\overset{(5.61)}{=} \overline{\sigma}^1_{1,(\overline{1jk})}\left(\hat{\nabla} f^0\right) = f^0_k(\mathfrak{s}_2,\mathfrak{t}_j) - f^0_k(\mathfrak{s}_0,\mathfrak{t}_j) \\
&\qquad - \sum_{\ell=0}^{2} w_{\ell j}\left[\, f^0_k(\mathfrak{s}_1,\bar{\mathfrak{t}}_\ell) - f^0_k(\mathfrak{s}_0,\bar{\mathfrak{t}}_\ell)\,\right] = \overline{\sigma}^0_{(\overline{2jk})}\left(f^0\right) - \sum_{\ell=0}^{2} w_{\ell j}\,\overline{\sigma}^0_{(\ell k)}\left(f^0\right)\,, \\
\overline{\sigma}^1_{2,(\ell k)}\left(\overline{\Pi}_1(\hat{\nabla} f^0)\right) &\overset{(5.61)}{=} \overline{\sigma}^1_{2,(\ell k)}\left(\hat{\nabla} f^0\right) = f^0_k(\mathfrak{s}_1,\bar{\mathfrak{t}}_{\ell+1}) - f^0_k(\mathfrak{s}_1,\bar{\mathfrak{t}}_0) = \overline{\sigma}^0_{(\ell+1k)}\left(f^0\right) - \overline{\sigma}^0_{(0k)}\left(f^0\right)\,, \\
\overline{\sigma}^1_{3,(\ell k)}\left(\overline{\Pi}_1(\hat{\nabla} f^0)\right) &\overset{(5.61)}{=} \overline{\sigma}^1_{3,(\ell k)}\left(\hat{\nabla} f^0\right) = -2\pi n \operatorname{sgn}\left(k-\frac{1}{2}\right) f^0_{k+1}(\mathfrak{s}_1,\bar{\mathfrak{t}}_\ell) \\
&= -2\pi n \operatorname{sgn}\left(k-\frac{1}{2}\right)\overline{\sigma}^0_{(\ell k+1)}\,,
\end{aligned}$$

and

$$\begin{aligned}
\overline{\sigma}^1_{1,(\overline{1jk})}\left(\hat{\nabla}\,\overline{\Pi}_0(f^0)\right) &= \left[\,\overline{\Pi}_0(f^0)\,\right]_k(\mathfrak{s}_2,\mathfrak{t}_j) - \left[\,\overline{\Pi}_0(f^0)\,\right]_k(\mathfrak{s}_0,\mathfrak{t}_j) \\
&\qquad - \sum_{\ell=0}^{2} w_{\ell j}\left\{\,\left[\,\overline{\Pi}_0(f^0)\,\right]_k(\mathfrak{s}_1,\bar{\mathfrak{t}}_\ell) - \left[\,\overline{\Pi}_0(f^0)\,\right]_k(\mathfrak{s}_0,\bar{\mathfrak{t}}_\ell)\right\} \\
&= \overline{\sigma}^0_{(\overline{2jk})}(\,\overline{\Pi}_0(f^0)\,) - \sum_{\ell=0}^{2} w_{\ell j}\,\overline{\sigma}^0_{(\ell k)}(\,\overline{\Pi}_0(f^0)\,) \\
&\overset{(5.61)}{=} \overline{\sigma}^0_{(\overline{2jk})}(f^0) - \sum_{\ell=0}^{2} w_{\ell j}\overline{\sigma}^0_{(\ell k)}(f^0)\,, \\
\overline{\sigma}^1_{2,(\ell k)}\left(\hat{\nabla}\,\overline{\Pi}_0(f^0)\right) &= \left[\,\overline{\Pi}_0(f^0)\,\right]_k(\mathfrak{s}_1,\bar{\mathfrak{t}}_{\ell+1}) - \left[\,\overline{\Pi}_0(f^0)\,\right]_k(\mathfrak{s}_1,\bar{\mathfrak{t}}_0) \\
&= \overline{\sigma}^0_{(\ell+1k)}(\,\overline{\Pi}_0(f^0)\,) - \overline{\sigma}^0_{(0k)}(\,\overline{\Pi}_0(f^0)\,) \overset{(5.61)}{=} \overline{\sigma}^0_{(\ell+1k)}(f^0) - \overline{\sigma}^0_{(0k)}(f^0)\,, \\
\overline{\sigma}^1_{3,(\ell k)}\left(\hat{\nabla}\,\overline{\Pi}_0(f^0)\right) &= -2\pi n \operatorname{sgn}\left(k-\frac{1}{2}\right)\left[\,\overline{\Pi}_0(f^0)\,\right]_{k+1}(\mathfrak{s}_1,\bar{\mathfrak{t}}_\ell) \\
&= -2\pi n \operatorname{sgn}\left(k-\frac{1}{2}\right)\overline{\sigma}^0_{(\ell k+1)}(\,\overline{\Pi}_0(f^0)\,) \overset{(5.61)}{=} -2\pi n \operatorname{sgn}\left(k-\frac{1}{2}\right)\overline{\sigma}^0_{(\ell k+1)}(f^0)\,.
\end{aligned}$$

In order to prove the second and the third commutation relation, we just need to prove the commutation for the third component of the second relation (which corresponds to the divergence of the vector curl in 2d); everything else then follows in a straightforward manner. Hence, let us look at the third component of $\overline{\Pi}_2(\operatorname{curl}\mathbf{E}^1) = \operatorname{curl}\overline{\Pi}_1(\mathbf{E}^1)$. As usual, we can apply $\overline{\sigma}^2_3$ on both

sides. The tensor product part is as usual; the new parts read

$$\begin{aligned}
\overline{\sigma}^2_{3,(\overline{1jk})}\left(\overline{\Pi}_2(\,\hat{\nabla}\times\mathbf{E}^1\,)\right) &\overset{(5.61)}{=} \overline{\sigma}^2_{3,(\overline{1jk})}\left(\hat{\nabla}\times\mathbf{E}^1\right) = \overline{\sigma}^3_{(\overline{1jk})}\left(\frac{\partial E^1_{2,k}}{\partial s} - \frac{\partial E^1_{1,k}}{\partial \chi}\right) \\
&= \int_{\mathfrak{t}_j}^{\mathfrak{t}_{j+1}} \left[E^1_{2,k}(\mathfrak{s}_2,\chi) - E^1_{2,k}(\mathfrak{s}_0,\chi)\right] \mathrm{d}\chi - \sum_{\ell=0}^{1} a_{\ell j} \int_{\bar{\mathfrak{t}}_0}^{\bar{\mathfrak{t}}_{\ell+1}} \left[E^1_{2,k}(\mathfrak{s}_1,\chi) - E^1_{2,k}(\mathfrak{s}_0,\chi)\right] \mathrm{d}\chi \\
&- \int_{\mathfrak{s}_0}^{\mathfrak{s}_2} [E^1_{1,k}(s,\mathfrak{t}_{j+1}) - E^1_{1,k}(s,\mathfrak{t}_j)]\,\mathrm{d}s + \sum_{\ell=0}^{1} a_{\ell j} \int_{\mathfrak{s}_0}^{\mathfrak{s}_1} [E^1_{1,k}(s,\bar{\mathfrak{t}}_{\ell+1}) - E^1_{1,k}(s,\bar{\mathfrak{t}}_0)]\,\mathrm{d}s \\
&= \int_{\mathfrak{t}_j}^{\mathfrak{t}_{j+1}} E^1_{2,k}(\mathfrak{s}_2,\chi)\,\mathrm{d}\chi - \sum_{\ell=0}^{1} a_{\ell j} \int_{\bar{\mathfrak{t}}_0}^{\bar{\mathfrak{t}}_{\ell+1}} E^1_{2,k}(\mathfrak{s}_1,\chi)\,\mathrm{d}\chi \\
&- \int_{\mathfrak{s}_0}^{\mathfrak{s}_2} [E^1_{1,k}(s,\mathfrak{t}_{j+1}) - E^1_{1,k}(s,\mathfrak{t}_j)]\,\mathrm{d}s + \sum_{\ell=0}^{2} (w_{\ell j+1} - w_{\ell j}) \int_{\mathfrak{s}_0}^{\mathfrak{s}_1} E^1_{1,k}(s,\bar{\mathfrak{t}}_\ell)\,\mathrm{d}s \\
&= \overline{\sigma}^1_{2,(\overline{2jk})}\left(\mathbf{E}^1\right) - \sum_{\ell=0}^{1} a_{\ell j}\, \overline{\sigma}^1_{2,(\ell k)}\left(\mathbf{E}^1\right) - \overline{\sigma}^1_{1,(\overline{1j+1k})}\left(\mathbf{E}^1\right) + \overline{\sigma}^1_{1,(\overline{1jk})}\left(\mathbf{E}^1\right)\,,
\end{aligned}$$

where we used that $E^1_{2,k}(\mathfrak{s}_0 = 0,\chi) = 0 \;\forall\,\chi$. Moreover, when going from the second to the third equality sign we inserted the condition (5.62). By replacing $\mathbf{E}^1 \to \overline{\Pi}_1(\mathbf{E}^1)$ in the last line, we obtain

$$\begin{aligned}
\overline{\sigma}^2_{3,(\overline{ijk})}\left(\hat{\nabla}\times\overline{\Pi}_1(\mathbf{E}^1)\right) &= \overline{\sigma}^3_{(\overline{1jk})}\left((\hat{\nabla}\times\overline{\Pi}_1(\mathbf{E}^1))\cdot\vec{\mathbf{e}}_3\right) \\
&= \overline{\sigma}^1_{2,(\overline{2jk})}\left(\overline{\Pi}_1(\mathbf{E}^1)\right) - \sum_{\ell=0}^{1} a_{\ell j}\, \overline{\sigma}^1_{2,(\ell k)}\left(\overline{\Pi}_1(\mathbf{E}^1)\right) - \overline{\sigma}^1_{1,(\overline{1j+1k})}\left(\overline{\Pi}_1(\mathbf{E}^1)\right) + \overline{\sigma}^1_{1,(\overline{1jk})}\left(\overline{\Pi}_1(\mathbf{E}^1)\right) \\
&\overset{(5.61)}{=} \overline{\sigma}^1_{2,(\overline{2jk})}\left(\mathbf{E}^1\right) - \sum_{\ell=0}^{1} a_{\ell j}\, \overline{\sigma}^1_{2,(\ell k)}\left(\mathbf{E}^1\right) - \overline{\sigma}^1_{1,(\overline{1j+1k})}\left(\mathbf{E}^1\right) + \overline{\sigma}^1_{1,(\overline{1jk})}\left(\mathbf{E}^1\right)\,.
\end{aligned}$$

□

By comparing coefficients of $f_{(\ell k)}$ it is easy to see that the equations (5.62) are satisfied if

$$a_{\ell j} = w_{\ell+1 j+1} - w_{\ell+1 j}\,, \qquad \ell = 0, 1\,. \tag{5.63}$$

This leads to the relation (5.21) if we set $w_{\ell j} = \xi^\ell_{1j}$.

In the tensor product setting, projection onto the spaces V^k_h $(0 \le k \le 3)$ means inverting the respective inter-/histopolation matrices $\mathcal{I}^k$, as written in (3.74). We will now identify the corresponding linear systems for the previously introduced polar projectors $\overline{\Pi}_k$. The starting point is the Definition 3 of the polar projectors via the DOFs. By expressing the projected function in the respective basis that spans $\overline{V}^k_h$, the left-hand side can be expressed in terms of new *polar inter-/histopolation matrices* $\overline{\mathcal{I}}^k$,

$$\overline{\mathcal{I}}^0\,\overline{\mathbf{f}} = \overline{\sigma}^0(f^0)\,, \qquad \overline{\mathcal{I}}^1\,\vec{\overline{\mathbf{e}}} = \overline{\sigma}^1(\mathbf{E}^1)\,, \qquad \overline{\mathcal{I}}^2\,\vec{\overline{\mathbf{b}}} = \overline{\sigma}^2(\mathbf{B}^2)\,, \qquad \overline{\mathcal{I}}^3\,\overline{\mathbf{p}} = \overline{\sigma}^3(p^3)\,. \tag{5.64}$$

In order to determine the matrices $\overline{\mathcal{I}}^k$, we note that the polar DOFs are linear combinations of the tensor product DOFs. Therefore, let us write the projection problems in the tensor product

bases, restrict the solution to the polar subspaces via the transpose extraction operators $(\mathbb{E}^k)^\top$, and project the DOFs to get square matrices:

$$\mathbb{P}^0\,\mathcal{I}^0\,(\mathbb{E}^0)^\top\,\overline{\mathbf{f}} = \mathbb{P}^0\,\sigma^0(f^0)\,, \qquad \mathbb{P}^1\,\mathcal{I}^1\,(\mathbb{E}^1)^\top\,\vec{\overline{\mathbf{e}}} = \mathbb{P}^1\,\sigma^1(\mathbf{E}^1)\,, \tag{5.65}$$

$$\mathbb{P}^3\,\mathcal{I}^3\,(\mathbb{E}^3)^\top\,\overline{\mathbf{p}} = \mathbb{P}^3\,\sigma^3(p^3)\,, \qquad \mathbb{P}^2\,\mathcal{I}^2\,(\mathbb{E}^2)^\top\,\vec{\overline{\mathbf{b}}} = \mathbb{P}^2\,\sigma^2(\mathbf{B}^2)\,. \tag{5.66}$$

Here, we introduced the matrices $\mathbb{P}^k \in \mathbb{R}^{\overline{n}^k \times n^k}$ that map tensor product DOFs to polar DOFs, $\overline{\sigma}^k(\cdot) = \mathbb{P}^k\sigma^k(\cdot)$. These matrices perform linear combinations of tensor product DOFs and thus play a similar role as the extraction matrices for basis functions $\mathbb{E}^k$. However, while $\mathbb{E}^k$ always act on tensor product basis functions, $\mathbb{P}^k$ always act on tensor product DOFs. Their explicit form follow directly from the definitions of the polar DOFs from the previous section. From (5.54) we obtain

$$\mathbb{P}^0 := \begin{bmatrix} \mathbb{Y}^0 & 0 \\ 0 & \mathbb{1}_{(n_s-2)\,n_\chi} \end{bmatrix} \otimes \mathbb{1}_2\,, \qquad \mathbb{Y}^0 \in \mathbb{R}^{3\times 2n_\chi}\,, \quad \mathbb{Y}^0_{\ell j} := \begin{cases} 1 & j = n_\chi + \overline{j}_\ell\,, \\ 0 & \text{else}\,, \end{cases} \tag{5.67}$$

where $\overline{j}_\ell$ is the local index of the interpolation point $\overline{\mathfrak{t}}_\ell$ on the $i = 1$ ring such that $\mathbb{Y}^0$ selects the three interpolation points $(\,\overline{\mathfrak{t}}_0, \overline{\mathfrak{t}}_1, \overline{\mathfrak{t}}_2\,)$ from the complete set of interpolation points. From (5.57) we obtain

$$\mathbb{P}^1 := \begin{bmatrix} \mathbb{P}^1_1 & 0 & 0 \\ 0 & \mathbb{P}^1_2 & 0 \\ 0 & 0 & \mathbb{P}^0 \end{bmatrix}\,, \qquad \mathbb{P}^1_1 \in \mathbb{R}^{\overline{n}^1_1 \times 2d_s n_\chi}\,, \qquad \mathbb{P}^1_2 \in \mathbb{R}^{\overline{n}^1_2 \times 2n_s d_\chi}\,, \tag{5.68}$$

with blocks

$$\mathbb{P}^1_1 := \begin{bmatrix} \mathbb{Y}^1_1 & 0 \\ 0 & \mathbb{1}_{(d_s-2)\,n_\chi} \end{bmatrix} \otimes \mathbb{1}_2\,, \qquad \mathbb{P}^1_2 := \begin{bmatrix} \mathbb{Y}^1_2 & 0 \\ 0 & \mathbb{1}_{(n_s-2)\,n_\chi} \end{bmatrix} \otimes \mathbb{1}_2\,, \tag{5.69}$$

where $\mathbb{Y}^1_1 \in \mathbb{R}^{n_\chi \times 2n_\chi}$ acts on the first $2n_\chi$ tensor product DOFs $(\sigma^1_{1,(ijk)})$ corresponding to one of the two toroidal Fourier components and $\mathbb{Y}^1_2 \in \mathbb{R}^{2\times 2d_\chi}$ acts on the first $2d_\chi$ tensor product DOFs $(\sigma^1_{2,(ijk)})$:

$$\mathbb{Y}^1_{1,ij} := \begin{cases} \delta_{ij} - \sum_{\ell=0}^{2} \delta_{j\overline{j}_\ell} w_{\ell i} & 0 \le j < n_\chi\,, \\ \delta_{i(j-n_\chi)} & n_\chi \le j < 2n_\chi\,, \\ 0 & \text{else}\,, \end{cases} \quad \mathbb{Y}^1_{2,\ell j} := \begin{cases} 1 & d_\chi + \overline{j}_0 \le j < d_\chi + \overline{j}_{\ell+1}\,, \\ 0 & \text{else}\,. \end{cases} \tag{5.70}$$

From (5.59) and (5.60) we obtain

$$\mathbb{P}^2 := \begin{bmatrix} \mathbb{P}^1_2 & 0 & 0 \\ 0 & \mathbb{P}^1_1 & 0 \\ 0 & 0 & \mathbb{P}^3 \end{bmatrix}\,, \qquad \mathbb{P}^3 := \begin{bmatrix} \mathbb{Y}^3 & 0 \\ 0 & \mathbb{1}_{(d_s-2)\,d_\chi} \end{bmatrix} \in \mathbb{R}^{\overline{n}^3 \times n^3}\,, \tag{5.71}$$

where $\mathbb{Y}^3 \in \mathbb{R}^{d_\chi \times 2d_\chi}$ acts on the first $2d_\chi$ tensor product DOFs $(\sigma^{2,3}_{(ijk)}) = (\sigma^3_{(ijk)})$,

$$\mathbb{Y}^3_{ij} := \begin{cases} \delta_{ij} & 0 \le j < \overline{j}_0 \quad \text{and} \quad \overline{j}_2 \le j < d_\chi\,, \\ \delta_{ij} - (a_{0i} + a_{1i}) & \overline{j}_0 < j \le \overline{j}_1\,, \\ \delta_{ij} - a_{1i} & \overline{j}_1 < j \le \overline{j}_2\,, \\ \delta_{i(j-d_\chi)} & d_\chi \le j < 2d_\chi\,, \\ 0 & \text{else}\,. \end{cases} \tag{5.72}$$

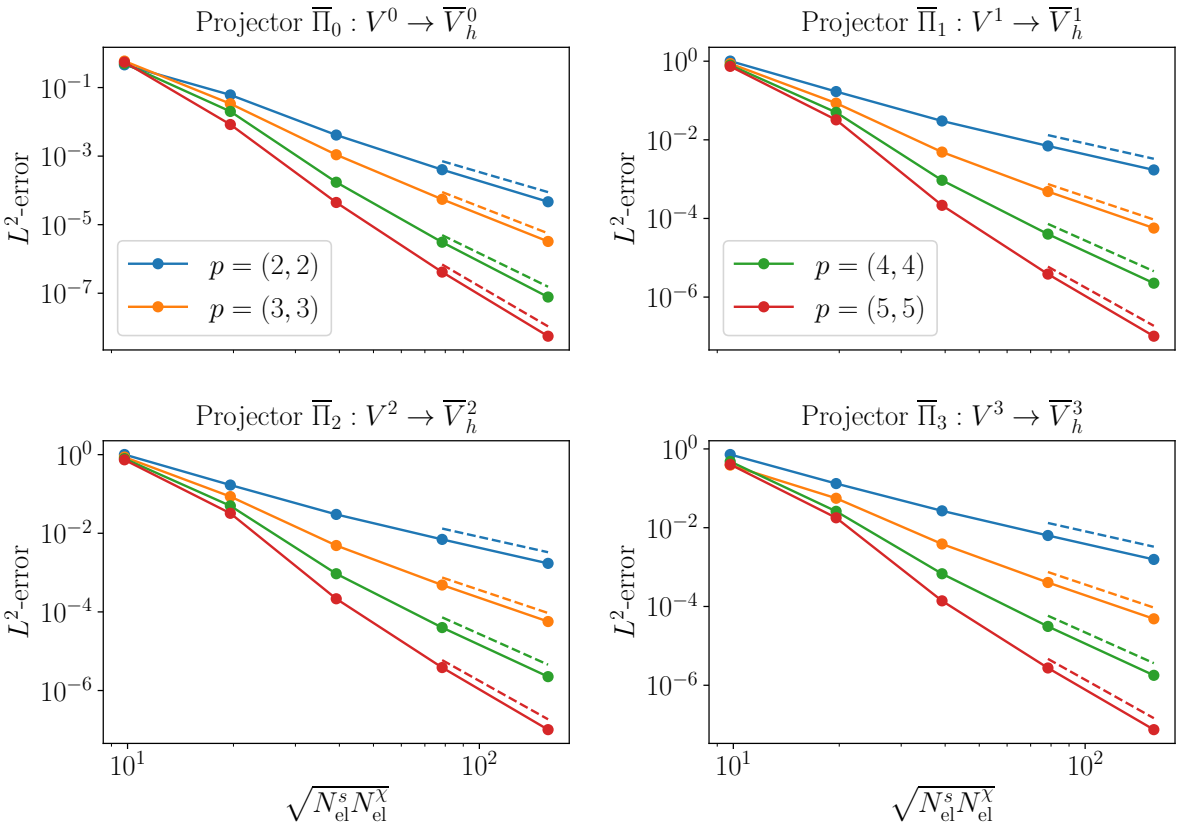

Figure 5.7: L^2-errors of projected polar differential k-forms ($0 \leq k \leq 3$) corresponding to the fields (5.73) for different spline degrees $p = (p_s, p_\chi)$ and different number of elements $N^s_{\text{el}} = n_s - p_s$ and $N^\chi_{\text{el}} = n_\chi$ (solid lines). Dashed lines are expected convergence rates h^{p_s+1} for $\overline{\Pi}_0$ and h^{p_s} for $\overline{\Pi}_k$ ($0 < k \leq 3$).

Finally, we investigate the performance of the introduced polar projection operators $\overline{\Pi}_k$ ($0 \leq k \leq 3$). For this, we conduct an L^2-convergence test by increasing the number of splines both in s- and χ- direction on the one hand and increasing the spline degrees on the other hand. This is done for the (exact) scalar- and vector-valued functions

$$f_{\text{ex}}(x, y) = (1 - x^2 - y^2) \cos(2\pi x) \cos(2\pi y)\,, \tag{5.73a}$$

$$\mathbf{V}_{\text{ex}}(x, y) = f_{\text{ex}}(x, y)\, \mathbf{e}_x + f_{\text{ex}}(x, y)\, \mathbf{e}_z\,, \tag{5.73b}$$

respectively. First, these fields are transformed to differential k-forms via the pull-back operations listed in Table 3.1 under the mapping (3.123) (cylinder) such that the resulting differential forms are functions of s and χ only with means that the toroidal mode number $n = 0$. This is followed by projections on the spaces $\overline{V}^k_h$ ($0 \leq k \leq 3$) using the polar projection operators introduced in the previous section. The errors compared to the exact forms corresponding to the fields (5.73) are then measured in the L^2-norm based on the L^2-scalar products (3.8). The resulting errors are shown in Figure 5.7 for each of the four projectors using spline degrees $p_s = p_\chi = 2, 3, 4, 5$ (solid lines). The same convergence behavior as for the pure tensor product case is observed: h^{p_s+1}-convergence for the $\overline{\Pi}_0$ projector which is based on pure interpolation and h^{p_s}-convergence for the other three projectors which are based on either mixed inter- and histopolation in case of $\overline{\Pi}_1$ and $\overline{\Pi}_2$ or pure histopolation in case of $\overline{\Pi}_3$. The parameter

$h = 1/\sqrt{N_{\text{el}}^s N_{\text{el}}^\chi}$ is the geometric mean of the 1d element lengths $h_s = 1/N_{\text{el}}^s$ and $h_\chi = 1/N_{\text{el}}^\chi$ on the logical domain, where $N_{\text{el}}^s = n_s - p_s$ and $N_{\text{el}}^\chi = n_\chi$ are the number of elements in the s- and χ-direction, respectively.

5.4 Modified discrete MHD eigenvalue problem

A difference of polar domains with the pole at $s = 0$ compared to non-polar domains is that the domain boundary of the latter is located at $s = 1$ while the "surface" at $s = 0$ collapses to the pole and is therefore part of the domain and not a boundary. To account for this, we must modify the continuous spaces (3.11) and exclude the conditions at $s = 0$ which are then imposed on the discrete level by the polar splines. We denote these continuous spaces by $\overline{V}_0^k$ $(0 \leq k \leq 3)$:

$$\overline{V}_0^0 := \left\{ f^0 \in V^0,\ f_k^0(s = 1, \chi) = 0 \quad \forall\, \chi,\, k \right\} , \tag{5.74a}$$

$$\overline{V}_0^1 := \left\{ \mathbf{V}^1 \in V^1,\ V_{2,k}^2(s = 1, \chi) = V_3^2(s = 1, \chi) = 0 \quad \forall\, \chi,\, k \right\} , \tag{5.74b}$$

$$\overline{V}_0^2 := \left\{ \mathbf{V}^2 \in V^2,\ V_{1,k}^2(s = 1, \chi) = 0 \quad \forall\, \chi,\, k \right\} , \tag{5.74c}$$

$$\overline{V}_0^3 := V^3 . \tag{5.74d}$$

With regards to the pure tensor product boundary operators (3.56) and (3.57), we introduce modified boundary operators $\overline{\mathbb{B}}^k$ to incorporate the boundary conditions at $s = 1$ on the discrete level. As in the pure tensor product case (3.54) we therefore define

$$\overline{V}_{0,h}^k := \operatorname{span}\left(\overline{\mathbb{B}}^k \overline{\mathbf{\Lambda}}^k \right) \quad k = 0, 3 , \qquad \overline{V}_{0,h}^k := \operatorname{span}\left(\overline{\mathbb{B}}^k \vec{\overline{\mathbf{\Lambda}}}^k \right) \quad k = 1, 2 . \tag{5.75}$$

The boundary operators once more have a simple form and just have to make sure that basis functions of the spaces $\overline{V}_h^k$ having contributions from $N_{n_s-1}^{p_s}$ are eliminated. Since these basis function are standard tensor product basis functions even in the polar spline setting, there are $n_\chi = d_\chi$ functions to be removed (for one toroidal Fourier component). The dimensions $\overline{n}_0^k := \dim \overline{V}_{0,h}^k$ are thus $\overline{n}_0^0 := \overline{n}^0 - 2n_\chi$, $\overline{n}_0^1 := \overline{n}^1 - 2d_\chi - 2n_\chi$, $\overline{n}_0^2 := \overline{n}^2 - 2d_\chi$ and $\overline{n}_0^3 := \overline{n}^3$ and the boundary operators read

$$\overline{\mathbb{B}}^0 := \begin{bmatrix} \mathbb{1}_{\overline{n}^0 - 2n_\chi} & 0 \end{bmatrix} , \qquad \overline{\mathbb{B}}^1 := \begin{bmatrix} \mathbb{1}_{\overline{n}_1^1} & 0 & 0 & 0 \\ 0 & \mathbb{1}_{\overline{n}_2^1 - 2d_\chi} & 0 & 0 \\ 0 & 0 & 0 & \overline{\mathbb{B}}^0 \end{bmatrix} , \tag{5.76}$$

$$\overline{\mathbb{B}}^3 := \mathbb{1}_{\overline{n}^3} , \qquad \overline{\mathbb{B}}^2 := \begin{bmatrix} \mathbb{1}_{\overline{n}_1^2 - 2d_\chi} & 0 & 0 & 0 \\ 0 & 0 & \mathbb{1}_{\overline{n}_2^2} & 0 \\ 0 & 0 & 0 & \overline{\mathbb{B}}^3 \end{bmatrix} , \tag{5.77}$$

and the sizes of the zero blocks can be deduced from the sizes of the identity matrices and the boundary operators $\overline{\mathbb{B}}^k \in \mathbb{R}^{\overline{n}_0^k \times \overline{n}^k}$ themselves. As in the pure tensor product case (3.61), the discrete derivatives linking the spaces $\overline{V}_{0,h}^k$ via a discrete de Rham complex are given by

$$\overline{\mathbb{G}}_0 := \overline{\mathbb{B}}^1 \, \overline{\mathbb{G}} \, (\overline{\mathbb{B}}^0)^\top , \qquad \overline{\mathbb{C}}_0 := \overline{\mathbb{B}}^2 \, \overline{\mathbb{C}} \, (\overline{\mathbb{B}}^1)^\top , \qquad \overline{\mathbb{D}}_0 := \overline{\mathbb{B}}^3 \, \overline{\mathbb{D}} \, (\overline{\mathbb{B}}^2)^\top . \tag{5.78}$$

The modified discrete MHD eigenvalue problem for polar domains is then obtained by first replacing the spaces V_0^k in (3.13) with the spaces $\overline{V}_0^k$ (5.74) followed by performing the same

spatial discretization as in the tensor product case with the discrete spaces $\overline{V}^k_{0,h}$ (5.75). This leads to the following formulation: find non-trivial $\omega \in \mathbb{C}$ and $(\vec{\mathbf{u}}, \overline{\mathbf{p}}, \vec{\mathbf{b}}) \in \mathbb{R}^{\overline{n}^2_0} \times \mathbb{R}^{\overline{n}^3} \times \mathbb{R}^{\overline{n}^2_0}$ such that

$$-i\omega\, \overline{\mathbb{M}}^{n_\flat}_0\, \vec{\mathbf{u}} = \overline{\mathbb{D}}^\top_0\, \overline{\mathbb{M}}^3_0\, \overline{\mathbf{p}} + \overline{\mathcal{T}}^\top_0\, (\overline{\mathcal{I}}^1_0)^{-\top}\, \overline{\mathbb{C}}^\top_0\, \overline{\mathbb{M}}^2_0\, \vec{\mathbf{b}} + \overline{\mathbb{M}}^J_0\, \vec{\mathbf{b}}\,, \tag{5.79a}$$

$$-i\omega\, \overline{\mathbf{p}} = -\overline{\mathbb{D}}_0\, (\overline{\mathcal{I}}^2_0)^{-1}\, \overline{\mathcal{F}}_0\, \vec{\mathbf{u}} - (\gamma - 1)\, (\overline{\mathcal{I}}^3_0)^{-1}\, \overline{\mathcal{K}}_0\, \overline{\mathbb{D}}_0\, \vec{\mathbf{u}}\,, \tag{5.79b}$$

$$-i\omega\, \vec{\mathbf{b}} = -\overline{\mathbb{C}}_0\, (\overline{\mathcal{I}}^1_0)^{-1}\, \overline{\mathcal{T}}_0\, \vec{\mathbf{u}}\,. \tag{5.79c}$$

The mass matrices, interpolation matrices and DOF matrices are obtained from the pure tensor product ones by

$$\begin{aligned} &\overline{\mathbb{M}}^k_0 := \overline{\mathbb{B}}^k\, \mathbb{E}^k\, \mathbb{M}^k\, (\mathbb{E}^k)^\top (\overline{\mathbb{B}}^k)^\top\,, \quad \overline{\mathcal{I}}^k_0 := \overline{\mathbb{B}}^k\, \mathbb{P}^k\, \mathcal{I}^k\, (\mathbb{E}^k)^\top (\overline{\mathbb{B}}^k)^\top\,, \\ &\overline{\mathcal{T}}_0 := \overline{\mathbb{B}}^k\, \mathbb{P}^k\, \mathcal{T}\, (\mathbb{E}^k)^\top (\overline{\mathbb{B}}^k)^\top\,, \end{aligned} \tag{5.80}$$

and accordingly for the weighted mass matrices $\overline{\mathbb{M}}^{n_\flat}_0$ and $\overline{\mathbb{M}}^J_0$ and the other DOF matrices $\overline{\mathcal{F}}_0$ and $\overline{\mathcal{K}}_0$. The final form of the discrete MHD eigenvalue problem for polar domains is once more obtained by inserting (5.79b) and (5.79c) in (5.79a) which leads to the compact form

$$\begin{cases} \overline{\mathbb{F}}\, \vec{\mathbf{u}} = -\omega^2\, \overline{\mathbb{M}}^{n_\flat}_0\, \vec{\mathbf{u}} & (5.81a) \\ \overline{\mathbb{F}} := -\overline{\mathbb{D}}^\top_0\, \overline{\mathbb{M}}^3_0 \left[\, \overline{\mathbb{D}}_0\, (\overline{\mathcal{I}}^2_0)^{-1}\, \overline{\mathcal{F}}_0 + (\gamma - 1)\, (\overline{\mathcal{I}}^3_0)^{-1}\, \overline{\mathcal{K}}_0\, \overline{\mathbb{D}}_0 \right] - \overline{\mathbb{A}} - \overline{\mathbb{M}}^J_0\, \overline{\mathbb{C}}_0\, (\overline{\mathcal{I}}^1_0)^{-1}\, \overline{\mathcal{T}}_0\,, & (5.81b) \\ \overline{\mathbb{A}} := \overline{\mathcal{T}}^\top_0\, (\overline{\mathcal{I}}^1_0)^{-\top}\, \overline{\mathbb{C}}^\top_0\, \overline{\mathbb{M}}^2_0\, \overline{\mathbb{C}}_0\, (\overline{\mathcal{I}}^1_0)^{-1}\, \overline{\mathcal{T}}_0\,, & (5.81c) \end{cases}$$

which has the same structure as (3.81).

Lastly, it is worth mentioning that all new operators related to the polar spline framework were implemented in the class `TensorSplineSpace` given in Table 3.3. This means that there are additional (optional) input parameters `ck`, `cR` and `cY`, where `ck` is the smoothness at the pole, i.e. the default value for the standard tensor product case is `ck=-1`, while the $\mathcal{C}^1$-continuous framework can be obtained by setting `ck=1`. In this case, the control points `cR` and `cY` of the poloidal mapping must be additionally passed in order to assemble the spline extraction operators $\mathbb{E}^k$, which are then attributes of an object created from the class `TensorSplineSpace`. Moreover, the extraction operators $\mathbb{P}^k$ for the degrees of freedom are part of the class `ProjectorsGlobal3D`. In fact, if the standard tensor product case if chosen (`ck=-1`), these two types of operators are simply identity matrices which leads to a compact implementation with easy switching between the standard tensor product framework and the new polar framework.

Chapter 6

Simulation results in tokamak-like geometries

This chapter is concerned with results obtained with the extended polar spline framework introduced on the previous chapter. First, results in a straight tokamak configuration will be presented followed by results in a tokamak configuration with finite toroidal curvature. In both cases, comparison studies between the standard tensor product framework and the polar spline framework will be discussed along with physics results.

6.1 Straight tokamak geometry

Due to the fact that a straight tokamak can be considered as a tokamak with an infinitely large aspect ratio, it is actually a cylindrical configuration which means that the mapping (3.123) is used in the following. However, as explained in the previous section, the polar spline framework relies on the usage of an isogeometric analysis (IGA) type of mapping. To obtain such, the functions $R = R(s, \chi)$ and $Y = Y(s, \chi)$ are simply interpolated on the V_h^0 FEM B-spline space in order to obtain the needed control points $\mathbf{c}^R$ and $\mathbf{c}^Y$ in (3.125). Moreover, the general MHD equilibrium

$$\begin{array}{l} \text{Straight tokamak} \\ x = r\cos\theta + R_0 \\ y = r\sin\theta \end{array} \quad : \quad \left\{ \begin{array}{l} \mathbf{B}_{\text{eq}} = B_0 \left(\mathbf{e}_z + \dfrac{r}{q(r) R_0} \, \mathbf{e}_\theta \right) , \quad q(r) = q_0 + (q_1 - q_0) \dfrac{r^2}{a^2} , \\ \\ p_{\text{eq}} = \left\{ \begin{array}{ll} \dfrac{B_0^2 a^2 q_0}{2 R_0^2 (q_1 - q_0)} \left(\dfrac{1}{q^2} - \dfrac{1}{q_1^2} \right) & \text{if } \; q_1 \neq q_0 \, , \\ \\ \dfrac{\beta B_0^2}{2} & \text{else} \, , \end{array} \right. \\ \\ n_{\text{b,eq}} = (1 - n_a) \left(1 - \left(\dfrac{r}{a} \right)^{n_1} \right)^{n_2} + n_a \, , \end{array} \right. \tag{6.1}$$

with fixed on-axis magnetic field $B_0 = 1$ is used.

6.1.1 Magnetosonic eigenmodes

For parameters $q_0 = q_1 \to \infty$, $n_1 = n_2 = 0$ and $n_a = 1$, i.e. a homogeneous plasma that is placed in a constant axial magnetic field, analytical solutions to the ideal MHD eigenvalue problem can

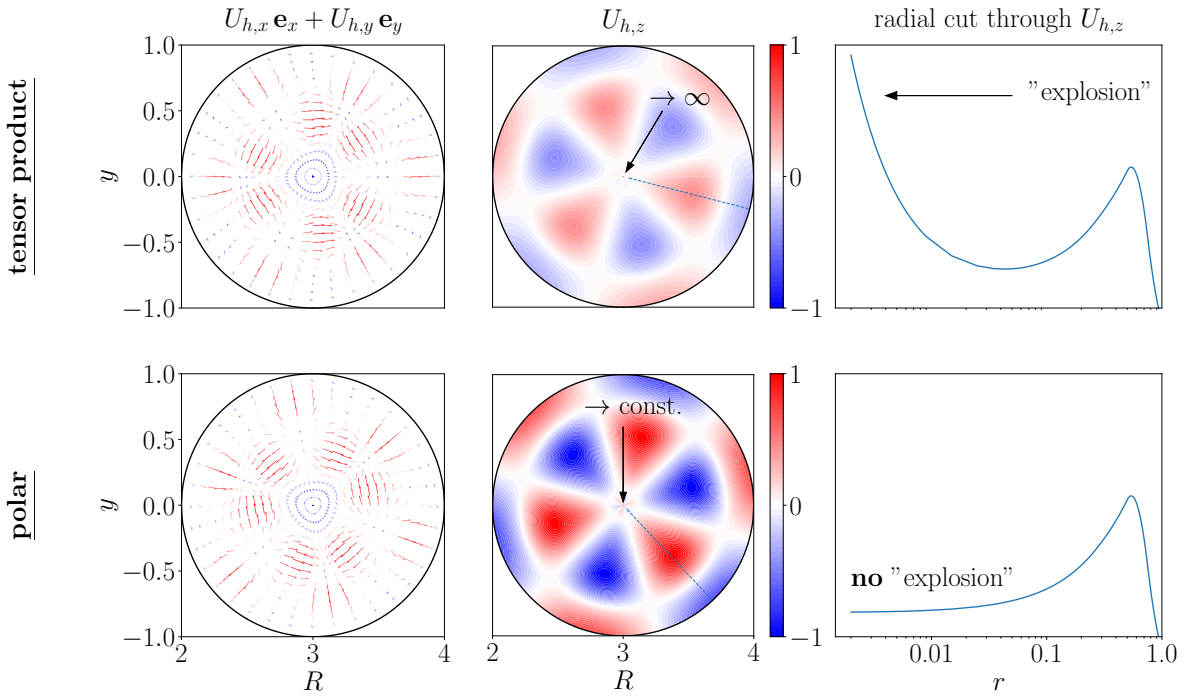

Figure 6.1: Slow magnetosonic eigenmode with mode numbers $l = 2$ and $|m| = 3$ in straight tokamak geometry with a pure axial magnetic field $\mathbf{B}_{\text{eq}} = B_0\mathbf{e}_z$ using pure tensor product splines (upper row) and polar splines (lower row). Numerical parameters are $N_{\text{el}} = (4, 12)$ and $p = (3, 3)$. The axial component $U_{\text{h,z}}$ is normalized to its respective maximum absolute value. The right most column shows radial cuts through $U_{\text{h,z}}$ for a fixed angle χ.

be derived [72]. This yields two types of solutions which eigenfrequencies

$$\omega^2 = \begin{cases} v_{\text{A}}^2 k^2\,, \\ \dfrac{1}{2}\left(k^2 + \dfrac{\alpha_{ml}^2}{a^2}\right)\left((v_{\text{A}}^2 + v_{\text{S}}^2) \pm \sqrt{(v_{\text{A}}^2 + v_{\text{S}}^2)^2 - 4v_{\text{A}}^2 v_{\text{S}}^2 k^2 / \left(k^2 + \dfrac{\alpha_{ml}^2}{a^2}\right)}\right)\,, \end{cases} \tag{6.2}$$

where $k = n/R_0$ is once more the toroidal (axial) wave number and α_{ml} is the l-th zero of the first derivative of the m-th Bessel function J_m. The characteristic velocities are the Alfvén velocity $v_{\text{A}}^2 = B_0^2$ and the speed of sound $v_{\text{S}}^2 = \gamma p_0$, where $p_0 = \beta B_0^2/2$. Hence, shear Alfvén waves are not affected by the presence of a cylindrical wall and therefore exhibit a spectrum with infinitely degenerate eigenfrequencies $\omega^2 = v_{\text{A}}^2 k^2$. In contrast to that, fast (+) and slow (−) magnetosonic waves exhibit a discrete spectrum of eigenfrequencies characterized by two integer mode numbers $l > 0$ and $|m| \geq 0$, where m is once more the poloidal (azimuthal) mode number. It is straightforward to show that in the limit $a \to \infty$ the second expression in (6.2) collapses to the standard dispersion relation for magnetosonic waves propagating parallel to the magnetic field in an infinitely extended plasma. In this case, the fast waves (+) propagate with the Alfvén velocity and the slow waves (−) (which are then ordinary sound waves) with the speed of sound.

For parameters $a = 1$, $R_0 = 3$, $n = 1$, and $\beta = 10\,\%$, we compute numerical solutions to the MHD eigenvalue problem according to (5.81) and compare it to the numerical spectrum obtained when using pure tensor product splines. For the latter, boundary conditions at the pole ($s = 0$) must be supplemented. In the pure tensor product spline de Rham complex (3.52)

Table 6.1: Comparison of analytical (see (6.2)) and numerical eigenfrequencies for the $l = 2$, $|m| = 3$ slow magnetosonic eigenmode obtained with pure tensor product splines and polar splines ($\omega_\mathrm{A} = B_0/R_0$).

	$(\omega^2 - \omega_\infty^2)/\omega_\mathrm{A}^2$	relative error
analytical	$9.432\,61 \times 10^{-6}$	-
pure tensor product splines	$9.408\,55 \times 10^{-6}$	$2.550\,57 \times 10^{-3}$
polar splines	$9.407\,21 \times 10^{-6}$	$2.692\,79 \times 10^{-3}$

it is possible to impose the boundary conditions (5.2a), (5.2b) and the first condition in (5.2c) at $s = 0$ but not the second condition in (5.2c) and the condition (5.2d) for 3-forms. For $\mathcal{C}^1$-smooth polar splines, by contrast, the latter two are satisfied as well. To highlight the consequence of this, we investigate the $l = 2$, $|m| = 3$ slow magnetosonic eigenmode which is found in both numerical spectra. Numerical parameters are $N_\mathrm{el} = (4, 12)$ and $p = (3, 3)$. It can be shown that the eigenfrequencies (6.2) corresponding to the slow magnetosonic eigenmodes converge towards the accumulation point $\omega_\infty^2 = v_\mathrm{A}^2\, v_\mathrm{S}^2\, k^2/(v_\mathrm{A}^2 + v_\mathrm{S}^2)$ for $l \to \infty$. Hence, rather than the absolute values, differences to this point are taken as a measure of accuracy.

The resulting numerical eigenfrequencies listed in Table 6.1 agree well with the analytical one (relative error $< 3 \times 10^{-3}$) and the difference between the pure tensor product result and the polar spline result is small. The slightly larger error for the polar splines might be due to the reduced solution space. However, if the resulting eigenfunctions are plotted on the physical domain using the push-forward operation for 2-forms shown in Table 3.1, a very different behavior is found close to the magnetic axis for the axial component $U_{h,z}$. This is shown in Figure 6.1 where the resulting $U_{h,x}\mathbf{e}_x + U_{h,y}\mathbf{e}_y$ vector field (left column) and $U_{h,z}$-component (middle column) are plotted using pure tensor product splines (upper row) and polar splines (lower row). While for the former the axial component diverges close to the pole due to the $1/\sqrt{g}$ factor in the push-forward operation for 2-forms ($\sqrt{g} \to 0$ for $s \to 0$), this is not the case for the polar splines where regularity in the push-forward is guaranteed. The point where the tensor product solution explodes can be pushed towards the pole $s = 0$ by increasing the resolution of the spline basis; however, this is not a viable solution when eigenfunctions need to be evaluated arbitrarily close to the pole, as for instance in particle-in-cell codes such as STRUPHY [103].

6.1.2 Global Alfvén eigenmode and internal kink mode

In Section 4, we discussed continuous Alfvén spectra whose eigenfunctions are singular, i.e. infinitely narrow at a certain radial location. However, even in the simplified straight tokamak geometry, where poloidal harmonics are decoupled, global Alfvén eigenmodes (GAEs) [104, 105] with a non-singular, radially extended mode structure can exist below or above extremum points in the continuous Alfvén spectrum [15]

$$\omega^2(r) = \frac{B_0^2}{n_\mathrm{b,eq}(r)} \frac{1}{R_0^2} \left(n + \frac{m}{q(r)} \right)^2 . \tag{6.3}$$

Besides stable eigenmodes characterized by eigenfrequencies $\omega^2 > 0$, unstable $m = 1$ internal kink modes with $\omega^2 < 0$ exist if the resulting on-axis safety factor $q_0 < 1/|n|$ [106].

These two features are obtained with STRUPHY simultaneously for parameters $n = -1$, $q_0 = 0.8$, $q_1 = 1.85$, $a = 1$ and $R_0 = 5$. Moreover, the number density profile in (6.1) is endowed with parameters $n_1 = 4$, $n_2 = 3$ and $n_a = 0$, such that the number density drops to zero at the

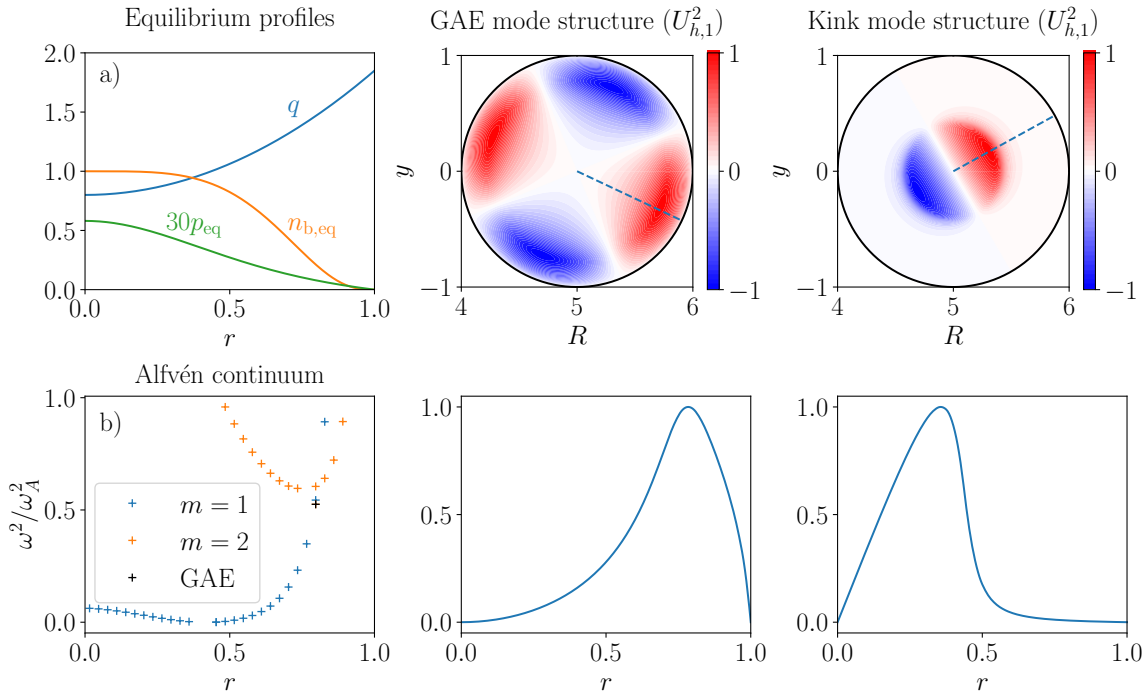

Figure 6.2: Global Alfvén eigenmode (middle column) and internal kink mode (right column) in straight tokamak geometry with toroidal mode number $n = -1$ and equilibrium profiles shown in a). The numerical eigenfrequencies corresponding to $m = 1$ and $m = 2$ Alfvén continuua are shown in b) together with the location of the global Alfvén eingenmode (GAE) below the $m = 2$ branch. Numerical parameters are $N_{\mathrm{el}} = (32, 24)$ and $p = (2, 3)$.

boundary. The safety factor, equilibrium number density profile and pressure profile are shown in Figure 6.2 a), where the pressure is multiplied by a scaling factor in order to make it visible. The number density profile is not chosen randomly but in a way that the continuous Alfvén spectrum (6.3) for the poloidal mode number $m = 2$ possesses a minimum at $r \approx 0.8$. Calculating the complete ideal MHD spectrum with parameters $N_{\mathrm{el}} = (32, 24)$ and $p = (2, 3)$ indeed results in a $m = 2$ branch with a minimum as shown in Figure 6.2 b). Below that minimum, a GAE with $\omega^2/\omega_{\mathrm{A}}^2 \approx 0.52523$ is found whose mode structure (first component of the 2-form eigen-velocity $\mathbf{U}_{\mathrm{h}}$) is shown in the middle column of Figure 6.2. It is clearly evident that the mode structure is global which means that it would not be subjected to continuum damping if it was excited. Finally, since the on-axis safety factor $q_0 < 1$, an $m = 1$ internal kink mode with eigenfrequency $\omega^2/\omega_{\mathrm{A}}^2 \approx -2.05 \times 10^{-3}$ is found in the same numerical spectrum. Its mode structure is shown in Figure 6.2 in the right column and shows the characteristic drop to zero at the location where $q = 1$. Since the first component of a 2-form contains the Jacobian determinant $\sqrt{g} \sim r$ in contrast to the first component of a contravariant vector, we have $U^2_{h,1} \sim r\,\hat{U}_{h,1}$. Therefore, $\hat{U}_{h,1}$ is nearly a step function. Lastly, in order to benchmark STRUPHY against literature values, an additional internal kink mode computation with parameters given on page 53 f. in Gruber's book [72] is performed ("Test case F"). The parameters are $n = -1$, $q_0 = 0.7$, $q_1 = 2.1286$, $a = 1$, $R_0 = 5$, $n_1 = 0$, $n_2 = 0$ and $n_a = 1$. The resulting eigenfrequency $\omega^2/\omega_{\mathrm{A}}^2 \approx -1.48 \times 10^{-3}$ calculated with STRUPHY with a rather high resolution, $N_{\mathrm{el}} = (48, 24)$ and $p = (3, 3)$ to ensure convergence, is in excellent agreement with Gruber's result $\omega^2/\omega_{\mathrm{A}}^2 \approx -1.47 \times 10^{-3}$ although very different numerical schemes are used.

6.2 Toroidal geometry

6.2.1 Toroidal Alfvén eigenmodes

As a next step, we include effects caused by toroidal curvature. The main difference compared to the straight case is the symmetry breaking in the poloidal plane due to the characteristic $1/R$ behavior of the toroidal magnetic field resulting in a high-field side on the inner side of the torus and a low-field side on the outer side. This symmetry breaking can lead to coupling of different poloidal harmonics which in turn can result in frequency gaps, i.e. "forbidden" zones for continuum modes, with possible global modes within these gaps (toroidal Alfvén eigenmodes - TAEs) [16]. To model this feature, we take as the geometry a simplified tokamak with circular concentric flux surfaces with minor radius a and major radius R_0 described by the straight field line mapping (3.124). The corresponding ad hoc equilibrium fields are given by

$$\begin{aligned} &\text{Tokamak (ad hoc)} \\ &x = R\cos\theta\cos\phi \\ &y = r\sin\theta \\ &z = R\cos\theta\sin\phi \\ &R = R_0 + r\cos\theta \end{aligned} \quad : \quad \begin{cases} \mathbf{B}_{\mathrm{eq}} = \dfrac{B_0 R_0}{R}\left(\mathbf{e}_\phi + \dfrac{r}{\bar{q}(r)R_0}\,\mathbf{e}_\theta\right), \quad \bar{q}(r) = q(r)\sqrt{1-\dfrac{r^2}{R_0^2}}\,, \\ \qquad\qquad\qquad\qquad q(r) = q_0 + (q_1 - q_0)\dfrac{r^2}{a^2}\,, \\ p_{\mathrm{eq}} = \dfrac{\beta B_0^2}{2}\left(1 - p_1\dfrac{r^2}{a^2} - p_2\dfrac{r^4}{a^4}\right), \\ n_{\mathrm{b,eq}} = (1-n_a)\left(1-\left(\dfrac{r}{a}\right)^{n_1}\right)^{n_2} + n_a\,. \end{cases} \tag{6.4}$$

These fields are implemented in STRUPHY (see Section 3.7.3). In the following, however, only results for a flat pressure and density profile are presented and discussed. Hence, $p_1 = p_2 = 0$, $n_1 = n_2 = 0$ and $n_a = 1$ in (6.4).

With regards to (6.3), it is easily verified that continuum branches for poloidal mode numbers m and $m+1$ may intersect (see Figure 6.2 b) for instance). This degeneracy is lifted if poloidal mode coupling is present, such that the location of the frequency gap and a possible TAE within the gap is readily obtained by

$$k_m = -k_{m+1} \quad \Rightarrow \quad q_{\mathrm{TAE}} = \frac{m+1/2}{n}\,, \tag{6.5}$$

i.e. the TAE is located at $r = r_0$ for which $q(r_0) = q_{\mathrm{TAE}}$. Moreover, it can be shown that the width of the frequency gap is approximately given by [107]

$$\Delta \approx \frac{4n^2 r_0/R_0}{(r_0^2/R_0^2 - 1)(2m+1)^2}\,. \tag{6.6}$$

All this features are obtained with STRUPHY for the toroidal mode number $n = -2$ and parameters $B_0 = 5$, $q_0 = 1.15$, $q_1 = 1.60$, $a = 1$, $R_0 = 5$ and $\beta = 0.2\,\%$ in (6.4). The results for numerical parameters $N_{\mathrm{el}} = (32, 48)$ and $p = (3, 3)$ are shown in the upper two rows of Figure 6.3 both for standard tensor product splines and polar splines. Shown are from left to right the Alfvén continuum branches for poloidal mode numbers $m = 2$ and $m = 3$ in the range $0.1 < \omega^2/\omega_{\mathrm{A}}^2 < 0.25$, the full TAE mode structure in the poloidal plane (first component of $\mathbf{U}_h$) and the poloidally averaged absolute values of the dominant TAE Fourier components ($m = 1 - 4$). Firstly, from a numerical point of view, it should be noted that there is no visible

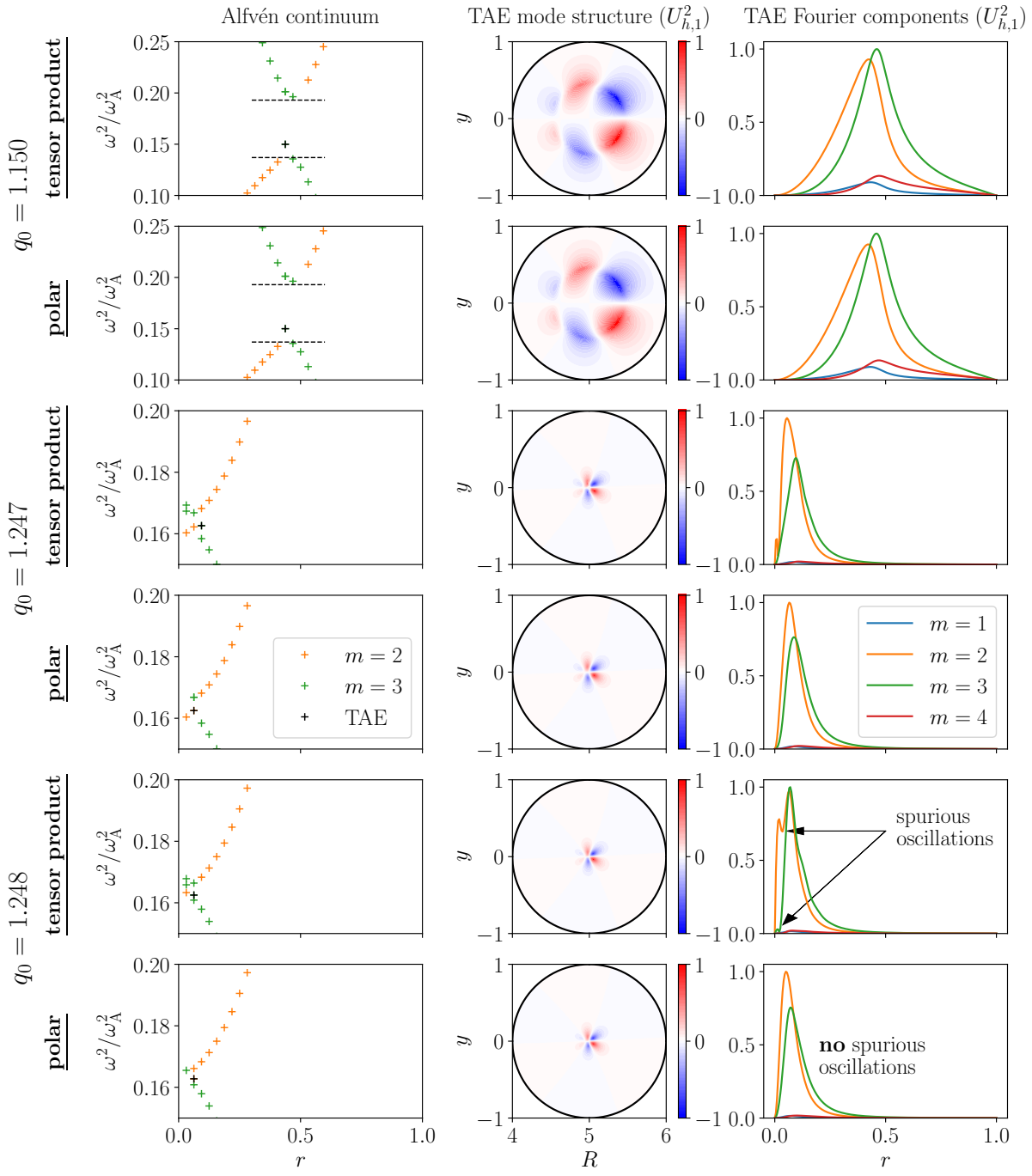

Figure 6.3: Comparison study between standard tensor product splines and polar splines for TAEs which are located very close to the magnetic axis. The toroidal mode number $n = -2$ and $q_{\text{TAE}} = 1.25$ in all cases. Numerical parameters are $N_{\text{el}} = (32, 48)$ and $p = (3, 3)$.

difference between the tensor product and polar spline framework. This is not very surprising since the polar spline framework only change the admissible solution space at the very vicinity of the magnetic axis at which, for this example, there are neither continuum modes nor the TAE. Secondly, from a physical point of view, the frequency gap is forming at the correct location, namely at the intersection point of the $m = 2$ and $m = 3$ continuum branches. This means that $q_{\text{TAE}} = 1.25$ and therefore $r_0 \approx 0.47$ according to (6.5). Moreover, the measured width of

the gap $\Delta \approx 0.056$ (see dashed lines in Figure 6.3) agrees well with the analytical prediction $\Delta \approx 0.061$ according to (6.6). Due to coupling of $m = 2$ and $m = 3$ poloidal harmonics, the TAE mode structure in the middle column of Figure 6.3 exhibits a ballooning-like mode structure, i.e. there is an asymmetry between the high-field side and low-field side. Finally, the separated Fourier components in the right column reveal that the TAE indeed consists most dominantly of $m = 2$ and $m = 3$ harmonics.

To investigate differences in the tensor product and polar spline frameworks, q_{TAE} is now moved closer and closer to the magnetic axis by moving the on-axis safety factor $q_0 \to q_{\mathrm{TAE}} = 1.250$. The results for this are shown in the third and fourth row of Figure 6.3 for $q_0 = 1.247$ and in the fifth and sixth row for $q_0 = 1.248$. In both cases it is evident that the standard tensor product framework has problems with properly resolving the continuous spectrum close to the magnetic axis. First, the formation of a frequency gap is not clearly visible anymore (especially for $q_0 = 1.248$) and second, there are spurious eigenmodes which pollute the spectrum. Additionally, the TAE Fourier harmonics show spurious oscillations close to the axis. In contrast to that, all these problems are gone if the polar spline modifications are used. The frequency gaps can still be identified in a satisfactory way and also the TAE Fourier components are smooth and exhibit no spurious oscillations.

6.2.2 Energetic particle drive

The next test case is taken from [108], where a benchmark study between different codes was performed for the case of a TAE which is destabilized by resonant energetic ions with a radial pressure gradient. It is once more characterized by a tokamak with circular concentric flux surfaces. The simulation parameters are $n = -6$, $B_0 = 3$, $q_0 = 1.71$, $q_1 = 1.87$, $a = 1$, $R_0 = 10$ and $\beta = 0.179\,\%$, such that $q_{\mathrm{TAE}} = 1.75$ and $r_0 = 0.5$. First, the MHD part of STRUPHY is tested for the bulk plasma without EPs. The results for numerical parameters $N_{\mathrm{el}} = (48, 96)$ and $p = (3, 3)$ are shown in Figure 6.4, where in the upper row the Alfvén continuous spectra for poloidal mode numbers $m = 9 - 12$ are shown in the range $0 < \omega/\omega_{\mathrm{A}} \leq 1$. The gap at the intersection point of the $m = 10$ and $m = 11$ branches is clearly visible and also a TAE is found within the gap. The lower row of Figure 6.4 shows the TAE mode structure of the three components of the 2-form eigen-velocity $\mathbf{U}_h^2$. As in the previous case, an asymmetric mode structure with respect to the high-field side and low-field side is observed and additionally, it can be seen that the third component is very small compared to the first and second component; a fact that is used in reduced MHD models. In order to convert the calculated TAE eigenfrequency to physical units, we additionally specify the bulk plasma to be composed of hydrogen ions ($A_{\mathrm{b}} = 1$) with number density $\bar{n}_{\mathrm{b}} = 2 \times 10^{19}\,\mathrm{m}^{-3}$. This results in the TAE frequency $\omega = 4.14 \times 10^5\,\mathrm{rad/s}$ which is in good agreement with other codes that calculate TAE frequencies in the range $\omega \approx 4.10 \times 10^5\,\mathrm{rad/s} - 4.16 \times 10^5\,\mathrm{rad/s}$ (see graphs corresponding to *MHD: no background pressure gradient* in plot (a) of Figure 2 in [108]).

Based on the result that the $m = 10, 11$ TAE is contained in the numerical eigenspectrum and that it is well resolved with the chosen numerical parameters, an EP distribution with a negative pressure gradient in radial direction is now added to the system. This setup should drive the TAE unstable. The EPs are chosen to be deuterons, i.e. $Z_{\mathrm{h}} = 1$ and $A_{\mathrm{h}} = 2$. From a computational point of view, it is important to note that compared to previous simulations (see [108]), this test case is very challenging with the current version of STRUPHY. This is for two reasons: first, the full cyclotron motion of the EPs is resolved which means that a rather small time step compared to the Alfvén time is needed and second, a full-f description requires far more particles compared to a delta-f description. In fact, for all time-dependent runs in the following, the time step is set to $\Delta t = 0.025$ which corresponds to about 1/12 of

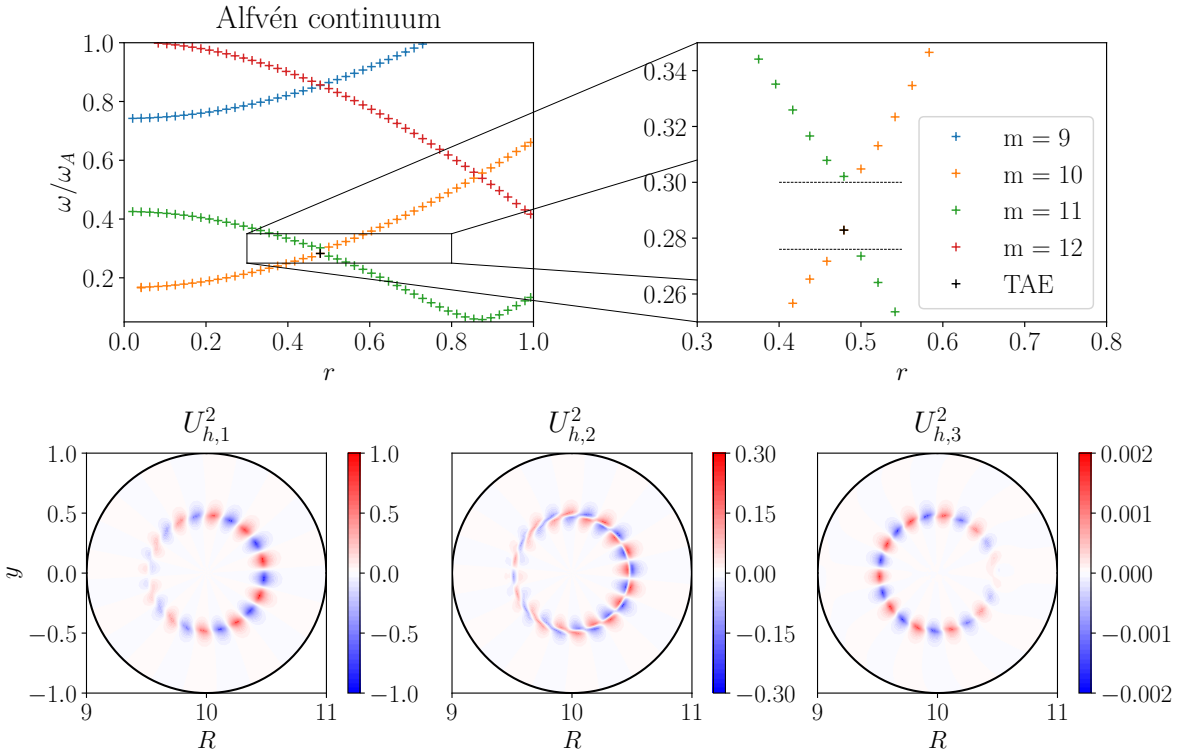

Figure 6.4: MHD results for the ITPA TAE case ($n = -6$): $m = 9-12$ Alfvén continuous spectra (upper row) and mode structure of the $m = 10, 11$ TAE (lower row). Numerical parameters are $N_{\mathrm{el}} = (48, 96)$ and $p = (3, 3)$.

the on-axis gyro-period but about 1/740 of a single TAE period. This choice of time step is based on the result in Chapter 4 that it still resolves the cyclotron motion in a satisfactory way. Moreover, $N_{\mathrm{p}} = 5 \times 10^6$ uniformly loaded particles (in real space) are used which turned out to be a satisfactory compromise between numerical noise on the one hand and computing time on the other hand. However, there is still quite some noise left which may be reduced by using more particles. The initial EP distribution function is taken to be an isotropic Maxwellian in velocity space supplemented with a monotonically decreasing number density distribution in radial direction in real space. On the logical domain it is given by

$$f^0_{\mathrm{h}}(s, \mathbf{v}, t = 0) = c_3 \exp\left(-\frac{c_2}{c_1} \tanh\frac{s - c_0}{c_2}\right) \frac{1}{\pi^{3/2} v^3_{\mathrm{th}}} \exp\left(\frac{v_x^2 + v_y^2 + v_z^2}{v^2_{\mathrm{th}}}\right), \tag{6.7}$$

where the thermal velocity is set to be constant such that there is no radial EP temperature gradient. In the following, $v_{\mathrm{th}} = 1.27$ which translates to a temperature of 400 keV in physical units. As in chapter 4, the particles are loaded uniformly in logical space and according to the isotropic Maxwellian in (6.7) in velocity space. The EP number density

$$n_{\mathrm{h}}(s) = \int_0^1 \int_0^1 \int f^0_{\mathrm{h}} \, \mathrm{d}^3 v \, \mathrm{d}\chi \, \mathrm{d}\varphi \,, \tag{6.8}$$

for the parameters given in [108] ($c_0 = 0.49123$, $c_1 = 0.298228$, $c_2 = 0.198739$, $c_3 = 0.521298$) is plotted in Figure 6.5 a) (back dashed line). Recall that $s \simeq r$ with the present choice of coordinates.

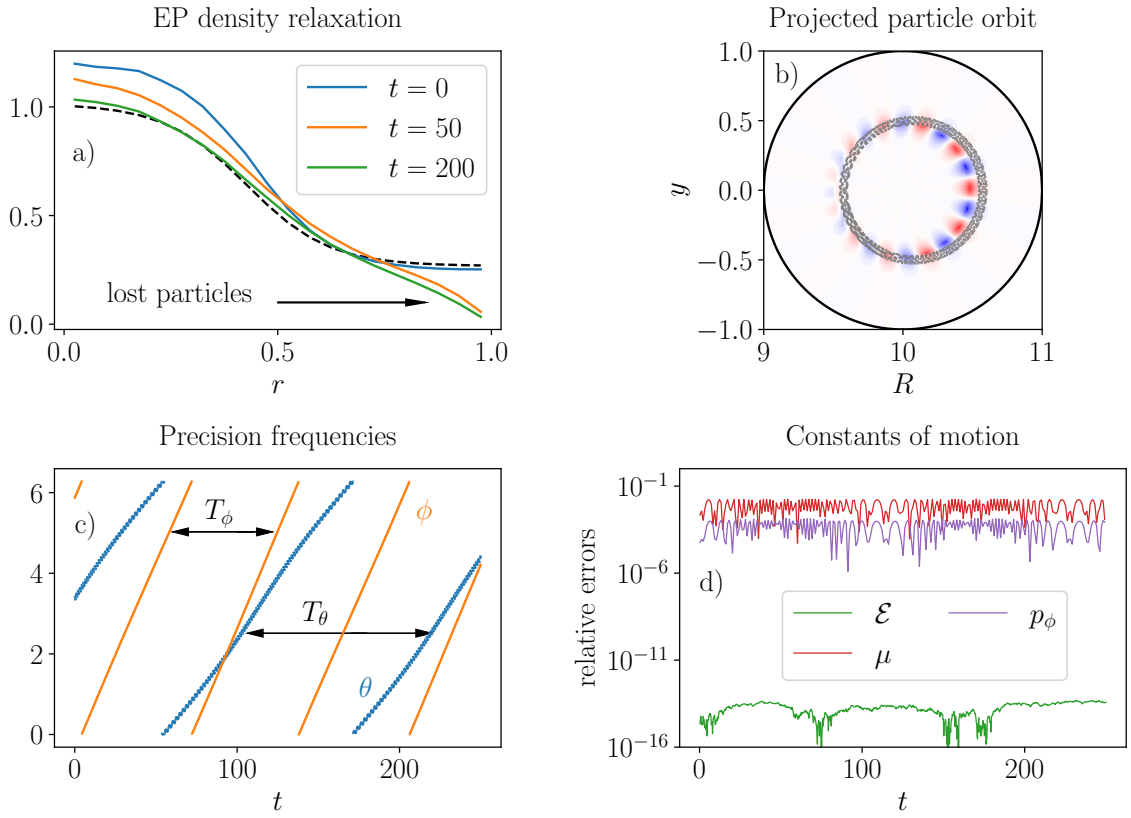

Figure 6.5: Relaxation of the full-f EP distribution function in the ITPA TAE case and particle orbit analysis for a co-passing particle close to TAE resonance: a) Evolution of the EP density with respect to time and comparison to the distribution used in [108] (black dashed line). b) Poloidally projected full orbit (cyclotron + drift orbit) of an EP with $v_\parallel \approx v_\mathrm{A}/3$ together with the TAE mode structure from Figure 6.4. c) Particle's poloidal (θ) and toroidal (ϕ) angle with respect to time and respective precision periods $T_\theta = 2\pi/\omega_\theta$ and $T_\phi = 2\pi/\omega_\phi$. d) Evolution of the relative errors of the particle's kinetic energy $\mathcal{E}$, magnetic moment μ and canonical toroidal angular momentum p_ϕ.

When performing the first simulations with these parameters, it was observed that the full-f EP distribution shows a relaxation to some steady-state distribution in a way that the density gradient at $r \approx 0.5$ is reduced. This observed relaxation states that

$$\mathbf{v} \cdot \nabla f_\mathrm{h}(t=0) + (\mathbf{v} \times \mathbf{B}_\mathrm{eq}) \cdot \nabla_\mathbf{v} f_\mathrm{h}(t=0) \neq 0\,, \tag{6.9}$$

which means that (6.7) does **not** constitute an equilibrium distribution function satisfying $\partial f_\mathrm{h}/\partial t = 0$. To remove the "damping" caused by the relaxation during the expected TAE mode drive, an EP distribution with a steeper initial gradient was chosen in a way that the relaxed distribution is as close as possible to the default one. Moreover, during the relaxation, the coupling terms between the bulk plasma and EPs were switched off. The relaxation of the distribution function (6.7) supplemented with new parameters $c_0 = 0.515792$, $c_1 = 0.238582$, $c_2 = 0.188802$ and $c_3 = 0.547363$ is shown in Figure 6.5 a) in the time range $t = 0 - 250$. It is evident that the initial density distribution (blue curve) approximately relaxes at $t = 200$ (green line) to the distribution in [108] (black dashed line). The drop of the density close to the boundary is due to particles that hit the wall at $r = 1$ and which are removed from the simulation

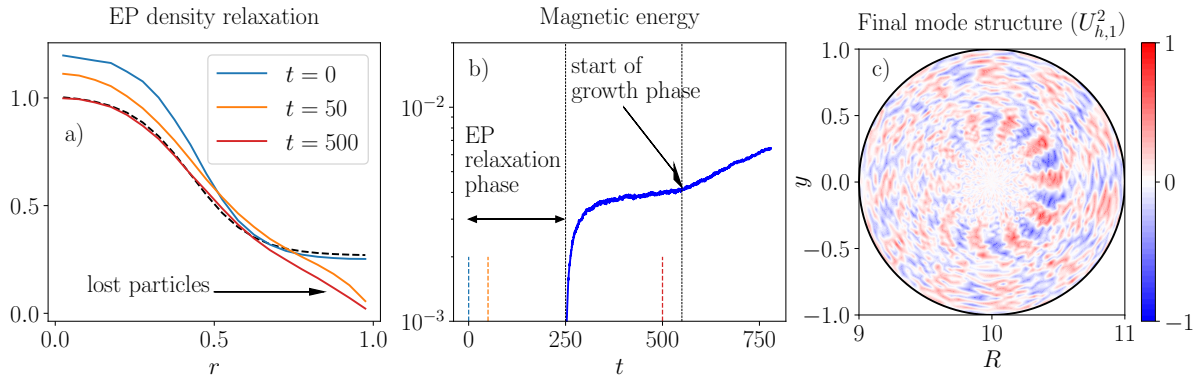

Figure 6.6: ITPA TAE case: a) Evolution of the EP density with respect to time and comparison to the distribution used in [108] (black dashed line). b) Evolution of the magnetic field energy $\tilde{\mathcal{H}}_B$ after switching on the coupling terms between MHD and EP Vlasov equations at $t = 250$. c) Final mode structure that developed out of particle induced noise.

domain. Due to the finite EP Lamor radii in the current version of STRUPHY, generally more particles hit the wall than in a drift-kinetic code, because there narrower guiding-center orbits are of interest. However, since the mode drive is expected to happen at $r \simeq 0.5$, this density drop is expected not to have a significant impact on the mode drive.

The relaxation phase in the time range $t = 0 - 250$ is also used to investigate whether particle orbits are calculated correctly. Numerical orbit calculations are principle a non-trivial task and it is known that standard ODE solver like the fourth order Runge-Kutta method fail to correctly compute orbits in long-tern simulations due to artificial energy accumulation or dissipation; see [109] for illustrative examples. Figure 6.5 b) shows the poloidally projected orbit of a co-passing particle in the relaxation phase which is close to TAE resonance $v_\parallel = v_\mathrm{A}/3$, where $v_\mathrm{A} = B_0 = 3$. In the range $t = 0 - 250$, the particle moves about three times around the torus in poloidal direction and four times in toroidal direction. This can be seen in Figure 6.5 c), where the temporal evolution of the particle's poloidal angle (θ) and toroidal angle (ϕ) is plotted. The measured periods $T_\theta = 2\pi/\omega_\theta \approx 117.25$ and $T_\phi = 2\pi/\omega_\phi \approx 65.75$ agree very well with the analytical approximations [12]

$$\omega_\theta \approx \frac{v_\parallel}{qR_0}\,, \qquad \omega_\phi \approx \frac{v_\parallel}{R_0}\,, \tag{6.10}$$

which result in $T_\theta = 2\pi/\omega_\theta \approx 117.96$ and $T_\phi = 2\pi/\omega_\phi \approx 67.70$ for the initial parallel velocity $v_\parallel \approx 0.93$ and safety factor at the particle position $q \approx 1.74$. Finally, the relative errors of the (normalized) kinetic energy, magnetic moment and canonical toroidal angular momentum

$$\mathcal{E} = \frac{1}{2}A_\mathrm{h}\left(v_x^2 + v_y^2 + v_z^2\right), \qquad \mu = \frac{A_\mathrm{h}v_\perp^2}{2B}\,, \qquad p_\phi = A_\mathrm{h}R\,v_\phi + Z_\mathrm{h}\Psi\,, \tag{6.11}$$

with respect to time are measured in Figure 6.5 d). In (6.11), $v_\phi = -v_x\sin\phi + v_z\cos\phi$ is the particle's velocity in toroidal direction and Ψ is the poloidal magnetic flux. While the energy of a particle in a magnetic field is always a conserved quantity, the canonical toroidal angular momentum p_ϕ is a conserved quantity specific for tokamak-like configurations with toroidal symmetry. The magnetic moment is not an exact conserved quantity but an adiabatic invariant. It is approximately conserved if the magnetic field variation $B/|\nabla B|$ is small compared to the particle's gyro-radius which is the case in the present setup. In Figure 6.5 d), it can be seen that

the energy is conserved almost to machine precision (green line); a direct consequence of the exact analytical solution (3.113) of the $\mathbf{v} \times \mathbf{B}$ force term in the particles' equations of motion. In contrast to that, μ and p_ϕ also depend on the particle's spatial position and therefore have finite, but bounded errors of about 1.79 % and 0.14 %.

After having let the EP distribution function relax to a steady-state distribution until $t = 250$, Figure 6.6 b) shows the evolution of the magnetic energy from the point where all coupling terms between the MHD bulk and EPs are switched on. In this regard, it should be noted that no other initial perturbations apart from particle noise is imposed. One can see that once the coupling is switched on, there is a sudden increase in the energy to a first plateau. This can be identified with the noise introduced by numerical particles. At $t \approx 550$, an instability starts to build up and the final mode structure in Figure 6.6 c) reveals that the $m = 10, 11$ TAE at $r_0 \approx 0.5$ is excited. However, the result is still quite noisy which is probably due to the rather low number of particle used in the present case. Moreover, a quantitative analysis and benchmark of the growth rate is at this stage quite difficult because of the relaxation of EP distribution function which changes the density and its gradient at the TAE location. A quantitative analysis, a better understanding of the relaxation phenomenon and finally, a higher numerical resolution runs after further code performance optimization is therefore left for future work.

Chapter 7

Conclusions and Outlook

This thesis presented the newly developed hybrid MHD-kinetic code STRUPHY for investigating interactions between MHD waves and energetic particles in fusion plasmas. In the version presented in this thesis, the code solves 3d linearized, ideal MHD equations, coupled non-linearly to fully kinetic 6d Vlasov equations via a current-coupling scheme. It was verified that STRUPHY is able to reproduce various ideal MHD results in slab, cylindrical and toroidal geometry and that coupling effects to a kinetic minority species are captured correctly both in the ion cyclotron frequency regime as well as in the low-frequency regime of large scale MHD modes. With the significant numerical improvements listed below, it is believed that STRUPHY brings several new qualities to the already existing arsenal of hybrid codes. This is mainly because of the following features:

- The newly developed algorithm in Chapter 3 provably conserves energy and $\nabla \cdot \mathbf{B} = 0$ irrespective of metric, grid spacing, chosen spline degree and degree of time splitting. This is a consequence of the finite element exterior calculus framework and the resulting skew-symmetry of the matrix in (3.98) which is subjected to a skew-symmetric, energy-preserving splitting. It is believed that these built-in conservation properties improve long-time stability, especially in strongly non-linear simulations.

- The use of B-spline basis function of arbitrary degree results in a high-order method which guarantees accuracy, the implicit nature of the time integration enables large time steps in the MHD part and the use of full MHD provides the possibility of exploring the whole range of MHD waves in contrast to reduced MHD.

- The novel numerical strategy for treating computational domains with a unique singular pole (edge that is mapped onto a single point) suppresses spurious oscillations at the pole that may propagate to other regions in the domain and pollute the simulation.

In more detail, the new approach for handling polar singularities combines discrete differential forms with the IGA-based polar spline framework introduced by Toshniwal et al. [80, 82]. The former provides a natural discretization of grad-, curl- and div-operators in curvilinear coordinates that preserves the de Rham cochain complex on the discrete level. The latter leads to continuous eigenfunctions on the mapped domain, including the pole. Based on this framework, new commuting projectors were constructed in Chapter 5 for the extended de Rham diagram 5.5 (blue arrows therein). These projectors were defined via so-called polar degrees of freedom (DOFs), obtained as linear combinations of existing tensor product DOFs. Several sufficient conditions on these linear combinations were stated in order to achieve commutativity and, moreover, explicit, block-wise representations of all needed extraction/reduction matrices were

given. In Chapter 6, the new framework was tested by means of a magnetosonic eigenmode in cylindrical geometry for analytical comparison and toroidal Alfvén eigenmode (TAE) calculations in toroidal geometry; the correct behavior of the eigenfunctions near the pole was demonstrated, in contrast to the standard tensor product solver usually used in other codes.

Finally, on the physics side, STRUPHY was verified in slab geometry by calculating shear Alfvén and slow sound continuous spectra and conducting phase mixing test cases with resulting continuum damping. Additionally, an instability in the ion cyclotron frequency regime was successfully compared to a linear, analytical theory developed in Chapter 2 and the non-linear saturation mechanism was identified by analyzing the motion of resonant particles. Additionally, the good conservation properties of STRUPHY were demonstrated and it was shown that these particularly hold in the non-linear phase. Besides this, global Alfvén eigenmode and internal kink mode calculations were conducted in cylindrical geometry and all features of continuous shear Alfvén spectra in toroidal geometry, in particular gap formation and gap size, were demonstrated. Moreover, a particular $n = -6$ TAE case was benchmarked with other codes and it was shown that the full-f, full-orbit (6d) treatment of EPs in STRUPHY is able to simulate TAE mode drive leading to instability.

Outlook

In the version presented in this thesis, STRUPHY features a hybrid MPI/OpenMP parallelization of the kinetic PIC part, which allows the distribution of particles on up to several hundreds of CPUs on the available computing cluster. However, no considerable effort has been put into performance of assembling and solving the large linear systems yet. They appear because of the implicit nature of the used time integration scheme. As a consequence of that, STRUPHY is currently limited to a single toroidal mode number and therefore to axisymmetric systems in order to keep the linear systems relatively small. Nevertheless, having proved in this work the feasibility of the novel algorithm, further development steps include:

1. Implementation of a drift-kinetic particle pusher for more efficiently simulating low-frequency phenomena. The suitable Hamiltonian model has been developed in [40].

2. Creation of an interface to MHD equilibrium codes such as VMEC [110] for the purpose of loading realistic tokamak and stellarator equilibria.

3. Implementation of Hamiltonian pressure-coupling schemes [39] and comparison of simulation results to the currently implemented current-coupling scheme.

4. Extension to fully non-linear MHD.

Some of these efforts (especially points 2 and 3) are already on the way. Once the full OpenMP/MPI hybrid parallelization (including the MHD part) is in place, detailed benchmark studies with other hybrid codes such as MEGA [29], HMGC [32, 33] and the hybrid MHD-kinetic extension of JOREK [37] are planned. Moreover, the capability of solving larger linear systems will then allow for the usage of another B-spline basis in toroidal direction (instead of a Fourier basis) which will ultimately lead to a full three-dimensional version of STRUPHY.

Finally, due to STRUPHY's major improvements regarding the treatment of polar singularities, it can serve as a novel numerical tool that is able to accurately simulate so-called "fishbone" instabilities and sawtooth cycles in fusion devices. This is due to the fact that both phenomena occur in the core region of fusion plasmas at the very vicinity of the magnetic axis. Fishbones are $(1, 1)$-kink-like modes that resonantly interact with trapped energetic particles coming from e.g. neutral beam injection [111]. In this regard, the instability can lead to a degradation of

energetic particle confinement and consequently to a reduced heating power [112]. Sawtooth cycles are periodic reconnection events inside the $q = 1$ surface that lead to sudden drops of the core temperature and prevent the current profile from strong central peaking [113]. Due to the involved magnetic reconnection, a shift of the magnetic axis away from its original position can happen.

Bibliography

[1] A. Piel. *Plasma Physics: An Introduction to Laboratory, Space, and Fusion Plasmas*. Springer International Publishing AG, 2 edition, 2017.

[2] Y. Horibe and N. Ogura. Deuterium content as a parameter of water mass in the ocean. *Journal of Geophysical Research (1896-1977)*, 73(4):1239–1249, 1968.

[3] G. Federici, L. Boccaccini, F. Cismondi, M. Gasparotto, Y. Poitevin, and I. Ricapito. An overview of the EU breeding blanket design strategy as an integral part of the DEMO design effort. *Fusion Engineering and Design*, 141:30–42, 2019.

[4] U. Stroth. *Plasmaphysik: Phänomene, Grundlagen und Anwendungen*. Springer Spektrum, Berlin, Heidelberg, 2018.

[5] F. F. Chen. *Introduction to Plasma Physics and Controlled Fusion*. Springer, Cham, 3 edition, 2016.

[6] H. S. Bosch and G. M. Hale. Improved formulas for fusion cross-sections and thermal reactivities. *Nuclear Fusion*, 32(4):611–631, 1992.

[7] J. D. Lawson. Some Criteria for a Power Producing Thermonuclear Reactor. *Proceedings of the Physical Society. Section B*, 70(1):6–10, 1957.

[8] D. Keefe. Inertial Confinement Fusion. *Annual Review of Nuclear and Particle Science*, 32(1):391–441, 1982.

[9] O. A. Hurricane, D. A. Callahan, D. T. Casey, P. M. Celliers, C. Cerjan, E. L. Dewald, T. R. Dittrich, T. Döppner, D. E. Hinkel, L. F. Berzak Hopkins, J. L. Kline, S. Le Pape, T. Ma, A. G. MacPhee, J. L. Milovich, A. Pak, H.-S. Park, P. K. Patel, B. A. Remington, J. D. Salmonson, P. T. Springer, and R. Tommasini. Fuel gain exceeding unity in an inertially confined fusion implosion. *Nature*, 506(7488):343–348, 2014.

[10] ITER Physics Basis Editors and ITER Physics Expert Group Chairs an Co-Chairs and ITER Joint Central Team and Physics Unit. Chapter 1: Overview and summary. *Nuclear Fusion*, 39(12):2137–2174, 1999.

[11] J. Nührenberg, W. Lotz, P. Merkel, C. Nührenberg, U. Schwenn, E. Strumberger, and T. Hayashi. Overview on Wendelstein 7-X Theory. *Fusion Technology*, 27(3T):71–78, 1995.

[12] W. W. Heidbrink. Basic physics of Alfvén instabilities driven by energetic particles in toroidally confined plasmas. *Physics of Plasmas*, 15(5):055501, 2008.

[13] P. Lauber. Super-thermal particles in hot plasmas—Kinetic models, numerical solution strategies, and comparison to tokamak experiments. *Physics Reports*, 533(2):33–68, 2013.

[14] L. Chen and F. Zonca. Physics of Alfvén waves and energetic particles in burning plasmas. *Rev. Mod. Phys.*, 88:015008, 2016.

[15] K. Appert, R. Gruber, and J. Vaclavik. Continuous spectra of a cylindrical magnetohydrodynamic equilibrium. *The Physics of Fluids*, 17(7):1471–1472, 1974.

[16] C. Z. Cheng and M. S. Chance. Low-n shear Alfvén spectra in axisymmetric toroidal plasmas. *The Physics of Fluids*, 29(11):3695–3701, 1986.

[17] S. E. Sharapov, B. Alper, H. L. Berk, D. N. Borba, B. N. Breizman, C. D. Challis, A. Fasoli, N. C. Hawkes, T. C. Hender, J. Mailloux, S. D. Pinches, and D. Testa. Alfvén wave cascades in a tokamak. *Physics of Plasmas*, 9(5):2027–2036, 2002.

[18] H. Kimura, Y. Kusama, M .Saigusa, G. J. Kramer, K. Tobita, M. Nemoto, T. Kondoh, T Nishitani, O. Da Costa, T. Ozeki, T. Oikawa, S. Moriyama, A. Morioka, G. Y. Fu, C. Z. Cheng, and V. I. Afanas'ev. Alfvén eigenmode and energetic particle research in JT-60U. *Nuclear Fusion*, 38(9):1303–1314, 1998.

[19] R. Betti and J. P. Freidberg. Stability of Alfvén gap modes in burning plasmas. *Physics of Fluids B: Plasma Physics*, 4(6):1465–1474, 1992.

[20] A. Fasoli, J. B. Lister, S. E. Sharapov, S. Ali-Arshad, G. Bosia, D. Borba, D. J. Campbell, N. Deliyanakis, J. A. Dobbing, C. Gormezano, H. A. Holties, G. T. A. Huysmans, J. Jacquinot, A. Jaun, W. Kerner, P. Lavanchy, J. M. Moret, L. Porte, A. Santagiustina, and L. Villard. Overview of Alfven eigenmode experiments in JET. *Nuclear Fusion*, 35(12):1485–1495, 1995.

[21] R. G. Littlejohn. Hamiltonian formulation of guiding center motion. *The Physics of Fluids*, 24(9):1730–1749, 1981.

[22] R. G. Littlejohn. Hamiltonian perturbation theory in noncanonical coordinates. *Journal of Mathematical Physics*, 23(5):742–747, 1982.

[23] R. G. Littlejohn. Variational principles of guiding centre motion. *Journal of Plasma Physics*, 29(1):111–125, 1983.

[24] J. R. Cary and R. G. Littlejohn. Noncanonical Hamiltonian mechanics and its application to magnetic field line flow. *Annals of Physics*, 151(1):1–34, 1983.

[25] P. Lauber, S. Günter, A. Könies, and S. D. Pinches. LIGKA: A linear gyrokinetic code for the description of background kinetic and fast particle effects on the MHD stability in tokamaks. *Journal of Computational Physics*, 226(1):447–465, 2007.

[26] S. Jolliet, A. Bottino, P. Angelino, R. Hatzky, T. M. Tran, F. Mcmillan, B., O. Sauter, A. Appert, Y. Idomura, and L. Villard. A global collisionless PIC code in magnetic coordinates. *Computer Physics Communications*, 177(5):409–425, 2007.

[27] G. Jost, T. M. Tran, W. A. Cooper, L. Villard, and K. Appert. Global linear gyrokinetic simulations in quasi-symmetric configurations. *Physics of Plasmas*, 8(7):3321–3333, 2001.

[28] W. Park, S. Parker, H. Biglari, M. Chance, L. Chen, C. Z. Cheng, T. S. Hahm, W. W. Lee, R. Kulsrud, D. Monticello, L. Sugiyama, and R. White. Three-dimensional hybrid gyrokinetic-magnetohydrodynamics simulation. *Physics of Fluids B: Plasma Physics*, 4(7):2033–2037, 1992.

[29] Y. Todo and T. Sato. Linear and nonlinear particle-magnetohydrodynamic simulations of the toroidal Alfvén eigenmode. *Physics of Plasmas*, 5(5):1321–1327, 1998.

[30] E. V. Belova, R. E. Denton, and A. A. Chan. Hybrid Simulations of the Effects of Energetic Particles on Low-Frequency MHD Waves. *Journal of Computational Physics*, 136(2):324–336, 1997.

[31] W. Park, E. V. Belova, G. Y. Fu, X. Z. Tang, H. R. Strauss, and L. E. Sugiyama. Plasma simulation studies using multilevel physics models. *Physics of Plasmas*, 6(5):1796–1803, 1999.

[32] S. Briguglio, G. Vlad, F. Zonca, and C. Kar. Hybrid magnetohydrodynamic-gyrokinetic simulation of toroidal Alfvén modes. *Physics of Plasmas*, 2(10):3711–3723, 1995.

[33] X. Wang, S. Briguglio, L. Chen, C. Di Troia, G. Fogaccia, G. Vlad, and F. Zonca. An extended hybrid magnetohydrodynamics gyrokinetic model for numerical simulation of shear Alfvén waves in burning plasmas. *Physics of Plasmas*, 18(5):052504, 2011.

[34] G. T. A. Huysmans and O. Czarny. MHD stability in X-point geometry: simulation of ELMs. *Nuclear Fusion*, 47(7):659–666, 2007.

[35] O. Czarny and G. Huysmans. Bézier surfaces and finite elements for mhd simulations. *Journal of Computational Physics*, 227(16):7423–7445, 2008.

[36] M. Hoelzl, G. T. A. Huijsmans, S. J. P. Pamela, M. Bécoulet, E. Nardon, F. J. Artola, B. Nkonga, C. V. Atanasiu, V. Bandaru, A. Bhole, D. Bonfiglio, A. Cathey, O. Czarny, A. Dvornova, T. Fehér, A. Fil, E. Franck, S. Futatani, M. Gruca, H. Guillard, J. W. Haverkort, I. Holod, D. Hu, S. K. Kim, S. Q. Korving, L. Kos, I. Krebs, L. Kripner, G. Latu, F. Liu, P. Merkel, D. Meshcheriakov, V. Mitterauer, S. Mochalskyy, J. A. Morales, R. Nies, N. Nikulsin, F. Orain, J. Pratt, R. Ramasamy, P. Ramet, C. Reux, K. Särkimäki, N. Schwarz, P. Singh Verma, S. F. Smith, C. Sommariva, E. Strumberger, D. C. van Vugt, M. Verbeek, E. Westerhof, F. Wieschollek, and J. Zielinski. The JOREK non-linear extended MHD code and applications to large-scale instabilities and their control in magnetically confined fusion plasmas. *Nuclear Fusion*, 61(6):065001, 2021.

[37] A. Dvornova. *Hybrid fluid-kinetic MHD simulations of the excitation of Toroidal Alfvén Eigenmodes by fast particles and external antenna*. PhD thesis, Eindhoven University of Technology, 2021.

[38] P. J. Morrison and J. M. Greene. Noncanonical Hamiltonian Density Formulation of Hydrodynamics and Ideal Magnetohydrodynamics. *Phys. Rev. Lett.*, 45:790–794, 1980.

[39] C. Tronci. Hamiltonian approach to hybrid plasma models. *Journal of Physics A: Mathematical and Theoretical*, 43(37):375501, 2010.

[40] J. W. Burby and C. Tronci. Variational approach to low-frequency kinetic-MHD in the current coupling scheme. *Plasma Physics and Controlled Fusion*, 59(4):045013, 2017.

[41] C. Tronci, E. Tassi, E. Camporeale, and P. J. Morrison. Hybrid Vlasov-MHD models: Hamiltonian vs. non-Hamiltonian. *Plasma Physics and Controlled Fusion*, 56(9):095008, 2014.

[42] P. J. Morrison. Structure and structure-preserving algorithms for plasma physics. *Physics of Plasmas*, 24(5):055502, 2017.

[43] S. Markidis and G. Lapenta. The energy conserving particle-in-cell method. *Journal of Computational Physics*, 230(18):7037–7052, 2011.

[44] G. Chen, L. Chacón, and D. C. Barnes. An energy- and charge-conserving, implicit, electrostatic particle-in-cell algorithm. *Journal of Computational Physics*, 230(18):7018–7036, 2011.

[45] C. K. Birdsall and A. B. Langdon. *Plasma Physics via Computer Simulation*. Series in Plasma Physics. Taylor and Francis Group, 2004.

[46] J. Squire, H. Qin, and W. M. Tang. Geometric integration of the Vlasov-Maxwell system with a variational particle-in-cell scheme. *Physics of Plasmas*, 19(8):084501, 2012.

[47] Y. He, H. Qin, Y. Sun, J. Xiao, R. Zhang, and J. Liu. Hamiltonian time integrators for Vlasov-Maxwell equations. *Physics of Plasmas*, 22(12):124503, 2015.

[48] H. Qin, J. Liu, J. Xiao, R. Zhang, Y. He, Y. Wang, Y. Sun, J. W. Burby, L. Ellison, and Y. Zhou. Canonical symplectic particle-in-cell method for long-term large-scale simulations of the Vlasov-Maxwell equations. *Nuclear Fusion*, 56(1):014001, 2015.

[49] J. Xiao, H. Qin, J. Liu, and R. Zhang. Local energy conservation law for a spatially-discretized Hamiltonian Vlasov-Maxwell system. *Physics of Plasmas*, 24(6):062112, 2017.

[50] J. Xiao, H. Qin, and J. Liu. Structure-preserving geometric particle-in-cell methods for Vlasov-Maxwell systems. *Plasma Science and Technology*, 20(11):110501, 2018.

[51] G. Chen and L. Chacón. An energy- and charge-conserving, nonlinearly implicit, electromagnetic 1D-3V Vlasov–Darwin particle-in-cell algorithm. *Computer Physics Communications*, 185(10):2391–2402, 2014.

[52] E. G. Evstatiev and B. A. Shadwick. Variational formulation of particle algorithms for kinetic plasma simulations. *Journal of Computational Physics*, 245:376–398, 2013.

[53] J. Xiao and H. Qin. Field theory and a structure-preserving geometric particle-in-cell algorithm for drift wave instability and turbulence. *Nuclear Fusion*, 59(10):106044, 2019.

[54] Y. Zhou, H. Qin, J. W. Burby, and A. Bhattacharjee. Variational integration for ideal magnetohydrodynamics with built-in advection equations. *Physics of Plasmas*, 21(10):102109, 2014.

[55] S. M. Mamdouh, N. H. Anil, and S. Ravi. Discrete exterior calculus discretization of incompressible Navier–Stokes equations over surface simplicial meshes. *Journal of Computational Physics*, 312:175–191, 2016.

[56] Y. He, Y. Sun, H. Qin, and J. Liu. Hamiltonian particle-in-cell methods for Vlasov-Maxwell equations. *Physics of Plasmas*, 23(9):092108, 2016.

[57] M. Kraus, K. Kormann, P. J. Morrison, and E. Sonnendrücker. GEMPIC: geometric electromagnetic particle-in-cell methods. *Journal of Plasma Physics*, 83(4):905830401, 2017.

[58] A. Buffa, G. Sangalli, and R. Vázquez. Isogeometric analysis in electromagnetics: B-splines approximation. *Computer Methods in Applied Mechanics and Engineering*, 199:1143–1152, 2010.

[59] A. Buffa, J. Rivas, G. Sangalli, and R. Vázquez. Isogeometric Discrete Differential Forms in Three Dimensions. *SIAM Journal on Numerical Analysis*, 49(2):818–844, 2011.

[60] D. N. Arnold, R. S. Falk, and R. Winther. Finite element exterior calculus, homological techniques, and applications. *Acta Numerica*, 15:1–155, 2006.

[61] D. N. Arnold, R. S. Falk, and R. Winther. Finite element exterior calculus: from Hodge theory to numerical stability. *Bulletin of the American mathematical society*, 47(2):281–354, 2010.

[62] D. N. Arnold. *Finite element exterior calculus*, volume 93. SIAM, 2018.

[63] D. Boffi, F. Brezzi, and M. Fortin. *Mixed Finite Element Methods and Applications*, volume 44. Springer Series in Computational Mathematics, 2013.

[64] A. Stanier, L. Chacón, and G. Chen. A fully implicit, conservative, non-linear, electromagnetic hybrid particle-ion/fluid-electron algorithm. *Journal of Computational Physics*, 376:597–616, 2019.

[65] K. Kormann and E. Sonnendrücker. Energy-conserving time propagation for a structure-preserving particle-in-cell Vlasov–Maxwell solver. *Journal of Computational Physics*, 425:109890, 2021.

[66] B. Perse, K. Kormann, and E. Sonnendrücker. Geometric Particle-in-Cell Simulations of the Vlasov–Maxwell System in Curvilinear Coordinates. *SIAM Journal on Scientific Computing*, 43(1):B194–B218, 2021.

[67] J. Crank and P. Nicolson. A practical method for numerical evaluation of solutions of partial differential equations of the heat-conduction type. *Mathematical Proceedings of the Cambridge Philosophical Society*, 43(1):50–67, 1947.

[68] H. F. Trotter. On the Product of Semi-Groups of Operators. *Proceedings of the American Mathematical Society*, 10(4):545–551, 1959.

[69] G. Strang. On the construction and comparison of differences schemes. *Journal on Numerical analysis*, 5:506–517, 1968.

[70] R. I. McLachlan and G. R. W. Quispel. Splitting methods. *Acta Numerica*, 11:341–434, 2002.

[71] J. P. Freidberg. Ideal magnetohydrodynamic theory of magnetic fusion systems. *Rev. Mod. Phys.*, 54:801–902, 1982.

[72] R. Gruber and J. Rappaz. *Finite Element Methods in Linear Ideal Magnetohydrodynamics*. Springer, Berlin, Heidelberg, 1985.

[73] R. C. Grimm, J. M. Greene, and J. L. Johnson. Computation of the Magnetohydrodynamic Spectrum in Axisymmetric Toroidal Confinement Systems. In JOHN KILLEEN, editor, *Controlled Fusion*, volume 16 of *Methods in Computational Physics: Advances in Research and Applications*, pages 253–280. Elsevier, 1976.

[74] R. Gruber, F. Troyon, D. Berger, L. C. Bernard, S. Rousset, R. Schreiber, W. Kerner, W. Schneider, and K. V. Roberts. Erato stability code. *Computer Physics Communications*, 21(3):323–371, 1981.

[75] L. C. Bernard, F. J. Helton, and R. W. Moore. GATO: An MHD stability code for axisymmetric plasmas with internal separatrices. *Computer Physics Communications*, 24(3):377–380, 1981.

[76] L. Degtyarev, A. Martynov, S. Medvedev, F. Troyon, L. Villard, and R. Gruber. The KINX ideal MHD stability code for axisymmetric plasmas with separatrix. *Computer Physics Communications*, 103(1):10–27, 1997.

[77] B Van der Holst, A. J. C. Beliën, J. P. Goedbloed, M. Nool, and A. Van der Ploeg. Calculation of resistive magnetohydrodynamic spectra in tokamaks. *Physics of Plasmas*, 6(5):1554–1561, 1999.

[78] A. Bondeson, G. Vlad, and H. Lütjens. Resistive toroidal stability of internal kink modes in circular and shaped tokamaks. *Physics of Fluids B: Plasma Physics*, 4(7):1889–1900, 1992.

[79] W. Kerner, J. P. Goedbloed, G. T. A Huysmans, S. Poedts, and E. Schwarz. CASTOR: Normal-Mode Analysis of Resistive MHD Plasmas. *Journal of Computational Physics*, 142(2):271–303, 1998.

[80] D. Toshniwal, H. Speleers, R. R. Hiemstra, and T. J. R. Hughes. Multi-degree smooth polar splines: A framework for geometric modeling and isogeometric analysis. *Computer Methods in Applied Mechanics and Engineering*, 316:1005–1061, 2017. Special Issue on Isogeometric Analysis: Progress and Challenges.

[81] J. A. Cottrell, T. J. R. Hughes, and Y. Bazilevs. *Isogeometric analysis: toward integration of CAD and FEA*. John Wiley & Sons, 2009.

[82] D. Toshniwal and T. J. R. Hughes. Isogeometric discrete differential forms: Non-uniform degrees, Bézier extraction, Polar splines and flows on surfaces. *Computer Methods in Applied Mechanics and Engineering*, 376:113576, 2021.

[83] M. Brambilla. *Kinetic Theory of Plasma Waves: Homogeneous Plasmas*. Oxford University Press, 1998.

[84] C. Negulescu and S. Possanner. Closure of the Strongly Magnetized Electron Fluid Equations in the Adiabatic Regime. *Multiscale Modeling & Simulation*, 14(2):839–873, 2016.

[85] S. I. Braginskii. Transport processes in a plasma. *Reviews of Plasma Physics*, pages 205–311, 1965.

[86] J. P. Freidberg. *Ideal MHD*. Cambridge University Press, 2014.

[87] B. D. Fried and S. D. Conte. *The Plasma Dispersion Function*. Academics Press, 1961.

[88] B. T. Tsurutani and G. S. Lakhina. Some basic concepts of wave-particle interactions in collisionless plasmas. *Reviews of Geophysics*, 35(4):491–501, 1997.

[89] T. Frankel. *The Geometry of Physics: An Introduction*. Cambridge University Press, 3 edition, 2011.

[90] C. de Boor. *A Practical Guide to Splines*. Springer New York, NY, 2 edition, 2001.

[91] T. Lyche, C. Manni, and H. Speleers. Foundations of Spline Theory: B-Splines, Spline Approximation, and Hierarchical Refinement. In T. Lyche, C. Manni, and H. Speleers, editors, *Splines and PDEs: From Approximation Theory to Numerical Linear Algebra*, pages 1–76. Springer, Cham, 2018.

[92] G. Farin. *Curves and Surfaces for Computer-Aided Geometric Design*. Academic Press, 1993.

[93] A. Y. Aydemir. A unified Monte Carlo interpretation of particle simulations and applications to non-neutral plasmas. *Physics of Plasmas*, 1(4):822–831, 1994.

[94] X. Lapillonne, S. Brunner, T. Dannert, S. Jolliet, A. Marinoni, L. Villard, T. Görler, F. Jenko, and F. Merz. Clarifications to the limitations of the $s-\alpha$ equilibrium model for gyrokinetic computations of turbulence. *Physics of Plasmas*, 16(3):032308, 2009.

[95] M. R. Hestenes and E. Stiefel. Methods of conjugate gradients for solving linear systems. *Journal of Research of the National Bureau of Standards*, 49(6):409, 1952.

[96] Y. Saad and M. H. Schultz. Gmres: A generalized minimal residual algorithm for solving nonsymmetric linear systems. *SIAM Journal on Scientific and Statistical Computing*, 7(3):856–869, 1986.

[97] S. A. Dupree and S. K. Fraley. *Monte Carlo Sampling Techniques*, pages 21–56. Springer US, 2002.

[98] C. F. Kennel and H. E. Petschek. Limit on stably trapped particle fluxes. *Journal of Geophysical Research (1896-1977)*, 71(1):1–28, 1966.

[99] R. F. Lutomirski and R. N. Sudan. Exact Nonlinear Electromagnetic Whistler Modes. *Phys. Rev.*, 147:156–165, 1966.

[100] S. L. Ossakow, E. Ott, and I. Haber. Nonlinear Evolution of Whistler Instabilities. *The Physics of Fluids*, 15(12):2314–2326, 1972.

[101] H. Speleers and D. Toshniwal. A General Class of C^1 Smooth Rational Splines: Application to Construction of Exact Ellipses and Ellipsoids. *Computer-Aided Design*, 132:102982, 2021.

[102] F. Patrizi. Isogeometric de Rham complex discretization in solid toroidal domains. *arXiv preprint arXiv:2106.10470*, 2021.

[103] F. Holderied, S. Possanner, and X. Wang. MHD-kinetic hybrid code based on structure-preserving finite elements with particles-in-cell. *Journal of Computational Physics*, 433:110143, 2021.

[104] K. Appert, R. Gruber, F. Troyuon, and J. Vaclavik. Excitation of global eigenmodes of the Alfven wave in Tokamaks. *Plasma Physics*, 24(9):1147–1159, 1982.

[105] L. Villard and J. Vaclavik. Alfvén frequency modes and global Alfvén eigenmodes. *Nuclear Fusion*, 37(3):351–360, 1997.

[106] M. N. Rosenbluth, R. Y. Dagazian, and P. H. Rutherford. Nonlinear properties of the internal $m = 1$ kink instability in the cylindrical tokamak. *The Physics of Fluids*, 16(11):1894–1902, 1973.

[107] H. Qin. *Gyrokinetic theory and computational methods for electromagnetic perturbations in tokamaks*. PhD thesis, Princeton University, 1998.

[108] A. Könies, S. Briguglio, N. Gorelenkov, T. Fehér, M. Isaev, P. Lauber, A. Mishchenko, D. A. Spong, Y. Todo, W. A. Cooper, R. Hatzky, R. Kleiber, M. Borchardt, G. Vlad, A. Biancalani, and A. Bottino. Benchmark of gyrokinetic, kinetic MHD and gyrofluid codes for the linear calculation of fast particle driven TAE dynamics. *Nuclear Fusion*, 58(12):126027, 2018.

[109] H. Qin, S. Zhang, J. Xiao, J. Liu, Y. Sun, and W. M. Tang. Why is boris algorithm so good? *Physics of Plasmas*, 20(8):084503, 2013.

[110] S. P. Hirshman and J. C. Whitson. Steepest-descent moment method for three-dimensional magnetohydrodynamic equilibria. *The Physics of Fluids*, 26(12):3553–3568, 1983.

[111] L. Chen, R. B. White, and M. N. Rosenbluth. Excitation of Internal Kink Modes by Trapped Energetic Beam Ions. *Phys. Rev. Lett.*, 52:1122–1125, 1984.

[112] W. W. Heidbrink and G. Sager. The fishbone instability in the DIII-D tokamak. *Nuclear Fusion*, 30(6):1015–1025, 1990.

[113] S. von Goeler, W. Stodiek, and N. Sauthoff. Studies of internal disruptions and $m = 1$ oscillations in tokamak discharges with soft—x-ray tecniques. *Phys. Rev. Lett.*, 33:1201–1203, 1974.

Acknowledgements

First of all, I would like to thank Prof. Dr. Sibylle Günter for the academic supervision of my dissertation, for giving me the opportunity to carry out this thesis at IPP and for the trust and freedom I was offered during this time. This enabled me to find and develop my own strengths and interests and to get in touch with people from many different fields.

Second of all, I would like to thank my scientific supervisors Dr. Xin Wang, Dr. Stefan Possanner as well as Dr. Philipp Lauber for the excellent supervision, their steadily open doors and the joyful and encouraging discussions about physics, mathematics and coding we had throughout the time. Their joy of science, enthusiasm and constant motivation has always been inspiring to me.

Third of all, thank you to all members of the MHD and fast particles group and the numerical methods department at IPP for the always calm and productive working atmosphere and for any support I got during the thesis, in particular solving computer problems, debugging code, giving feedback to presentations, pointing to references or just having fruitful discussions or having a coffee together. In this regard, many thanks to Dr. Thomas Hayward-Schneider, Dr. Zhixin Lu, Andrej Lier, Rohan Ramasamy, Erwin Walter, Nina Schwarz, Prof. Dr. Eric Sonnendrücker, Dr. Yaman Güçlü, Dr. Martin Campos-Pinto, Dr. Florian Hindenlang, Mario Räth, Tobias Blickhan, Benedikt Brantner, Nils Schild and Frederick Schnack.

And finally, many thanks to my family. Without its constant support my entire studies and consequently this thesis would not have been possible.